# 2D NANOLAMELLAR MATERIALS TOWARD

# WATER-ENERGY NEXUS APPLICATIONS

Dissertation
zur Erlangung des Grades
des Doktors der Naturwissenschaften
der Naturwissenschaftlich-Technischen Fakultät
der Universität des Saarlandes

von

**Mohammad Torkamanzadeh**

Saarbrücken, 2023

| | |
|---|---|
| **Tag des Kolloquiums:** | 09. Februar 2024 |
| **Dekan:** | Prof. Dr. Ludger Santen |
| **Berichterstatter:** | Prof. Dr. Volker Presser<br>Priv.-Doz. Dr.-Ing. Guido Falk |
| **Vorsitz:** | Prof. Dr. Christian Motz |
| **Akad. Beisitzer:** | Dr.-Ing. Frank Aubertin |

**Acknowledgments**

# Contents

## Abstract

Electrochemical water desalination is an emerging technology known for its high efficiency and low energy consumption in removing ions from aqueous media. The present thesis begins by explaining the fundamentals of a typical electrochemical water desalination system and presenting relevant performance metrics. The significance and limitations of the latter metrics are then discussed based on the generations of the electrodes developed during the past few decades.

This report seeks to expand the scope by investigating MXene (titanium carbide) as a purely pseudocapacitive material characterized by a capacitor-like electric response achieved through ion intercalation. Afterward, the merit of MXene when utilized as an electrode in electrochemical desalination is investigated for both single-salt and multi-salt aqueous solutions, ultimately establishing qualitative insights into the relationship between MXene properties and its electrochemical desalination behavior.

Finally, the thesis goes beyond MXene and explores its sibling materials, such as MBene (transition metal boride), for lithium-ion battery electrodes. As another application of 2D nanolamellar materials at the water-energy nexus, we have explored MXene conversion into transition metal dichalcogenides by sulfidation heat treatment and its merit as electrodes for hydrogen electrocatalysis. These findings can contribute to developing more efficient and sustainable energy storage, conversion, and desalination technologies.

## Zusammenfassung

Elektrochemische Wasserentsalzung ist eine vielversprechende Technologie, die für ihre hohe Effizienz und ihren geringen Energieverbrauch bei der Entfernung von Ionen aus wässrigen Medien bekannt ist. Die vorliegende Arbeit beginnt mit der Erläuterung der Grundlagen eines typischen elektrochemischen Wasserentsalzungssystems und der Darstellung relevanter Leistungskennzahlen. Die Bedeutung und Einschränkungen der letztgenannten Metriken werden dann anhand der in der Vergangenheit entwickelten Generationen von Elektroden diskutiert.

Die vorliegende Arbeit untersucht MXene (Titankarbid) als rein pseudokapazitives Material, das durch eine kondensatorähnliche elektrische Reaktion gekennzeichnet ist, die durch Ioneninterkalation erreicht wird. Anschließend wird der Nutzen von MXene bei der Verwendung als Elektrode bei der elektrochemischen Entsalzung sowohl für wässrige Lösungen mit einem Salz als auch mit mehreren Salzen untersucht, um schließlich qualitative Erkenntnisse über die Beziehung zwischen den Eigenschaften von MXen und seinem elektrochemischen Entsalzungsverhalten zu gewinnen.

Letztlich erforscht die Arbeit auch MBene (Übergangsmetallborid) sowie die Derivatisierung von MXenen hin zu Übergangsmetalldichalkogeniden durch Sulfidierung für den Einsatz in der Wasserstoffelektrokatalyse untersucht. Die Ergebnisse dieser Studien können zur Entwicklung effizienterer und nachhaltigerer Technologien zur Energiespeicherung, -umwandlung und -entsalzung beitragen.

## 1. Motivation

The worldwide water scarcity crisis has become one of the most pressing challenges of our time. The ever-increasing population, climate change, and industrial development have led to an alarming depletion of freshwater resources. In response, developing sustainable methods for treating these dwindling reserves becomes crucial to our continued existence.

The United Nations Sustainable Development Goal 6 aims to ensure the global availability and sustainable management of water and sanitation by 2030, highlighting the urgency of addressing water scarcity worldwide.[1] The urgency to find efficient and sustainable water treatment solutions partly arises because traditional desalination technologies, such as reverse osmosis, suffer from high energy consumption and environmental drawbacks. As energy represents a critical component in the water treatment process, the need for energy-efficient techniques has become imperative. **Figure 1** shows an ecosystem where energy is converted or consumed to produce freshwater from saline sources. A sustainable approach to such an ecosystem would require clean, efficient, and durable materials and processes across the entire water-energy sphere.
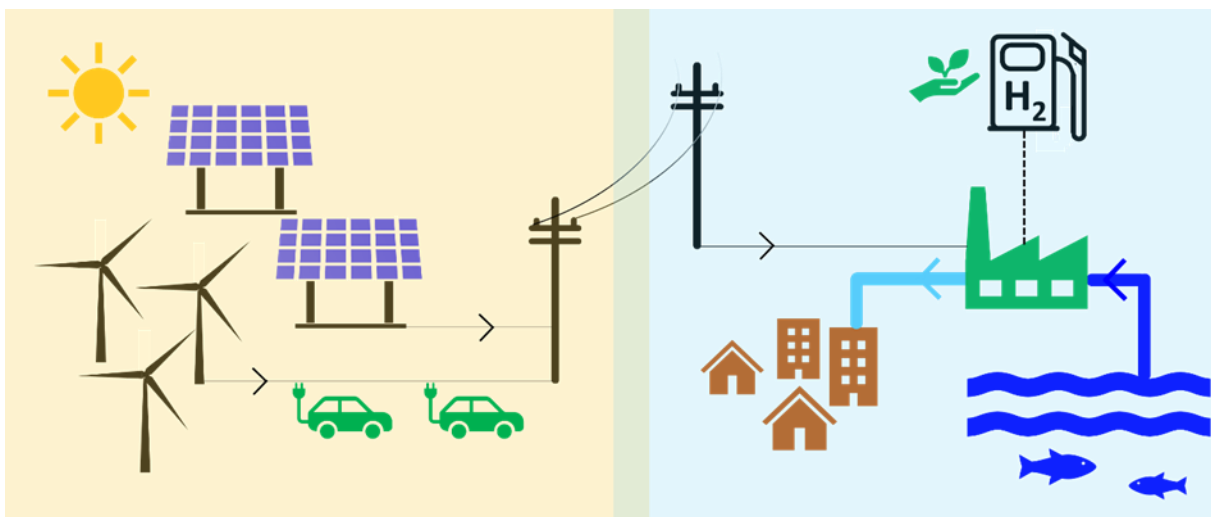


**Figure 1:** Schematic illustration of an ecosystem of energy generation via renewable sources, its conversion into energy carriers such as hydrogen, or its consumption to produce freshwater.

Nanomaterials hold much promise toward possible solutions that can help tackle global crises around water-energy nexus, particularly in electrochemical water desalination. Especially those nanomaterials with 2D nanolamellar architecture offer unique advantages due to their atomically thin structure and tunable properties. These materials have so far shown great promise for energy storage, which is an integral component of sustainable water treatment systems. In recent years, substantial progress has been made in the synthesis and application of various 2D nanolamellar materials, including graphene,[2, 3] transition metal dichalcogenides,[4-6], and MXenes[7, 8] in electrochemical water desalination. These materials offer remarkable properties such as high electrical conductivity, mechanical flexibility, or ion selectivity.[6] Their unique attributes make them suitable candidates for enhancing the performance and efficiency of electrochemical desalination systems, leading to the development of advanced water desalination technologies.

Among many water desalination technologies, electrochemical desalination has emerged as a promising option, as it can effectively remove ions from saline water using an electrical potential difference, leading to lower energy requirements than conventional desalination techniques.[9, 10] Electrochemical desalination also has the potential for selective separation, which plays a crucial role in the success of any desalination technology.[11] The latter feature is particularly relevant to present-day challenges, such as the shortage of lithium reserves and the ever-increasing demand for lithium by lithium-ion battery manufacturing industries. As such, an electrochemical desalination system capable of selective capture and recovery of dilute concentrations of lithium ions in the oceanwater (0.17 ppm) could tap into the virtually unlimited amount of lithium in marine reserves (~230 billion tons).[12] This could address the increasing demand for lithium while reducing dependence on limited terrestrial lithium reserves, besides the geopolitical edge of developing such a strategic technology.

The present thesis aims to explore the potential of 2D nanolamellar materials in the context of the water-energy nexus, with a specific focus on their application for electrochemical water desalination. The work will investigate their synthesis methods, characterization techniques, desalination capacity, efficiency, stability, and selectivity performance. Through this research, we aspire to contribute to developing sustainable and cost-effective water treatment technologies, addressing the global water scarcity challenge.

## 2.   Theoretical Background

### 2.1.   Water desalination technologies

Desalination technologies can be categorized into groups based on their processes, such as thermal, membrane, chemical, or physical process.[13] Thermal processes involve using heat to evaporate water, leaving the salts behind in the brine and further condensing the water vapor into liquid (**Figure 2A**).[14] In contrast, membrane processes employ pressure or electricity to drive water through a semi-permeable membrane, effectively blocking salts and other dissolved solids from passing through (**Figure 2B**).[15]
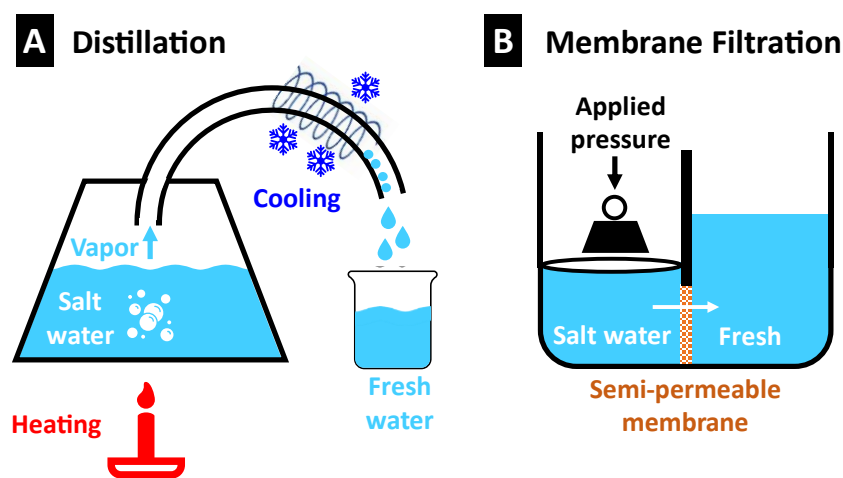


**Figure 2:** Schematic representation of the working principles of two major desalination technologies: (A) distillation and (B) membrane filtration processes, adapted with permission from Ref.[16]

### 2.1.1.   Thermal processes

Thermal desalination processes utilize heat to separate freshwater from saline water through evaporation and condensation. In large-scale desalination plants, efforts are made to make the most use of invested energy[17] and enhance process automation.[18, 19] As such, steady-state processes are used instead of the schematically shown batch distillation process shown in **Figure 2A** (also known as differential distillation), such as the one shown in **Figure 3**. In the latter processes, saline water flows into the system while the distillate (fresh water) and condensate (brine) leave the system.[20] For maximum energy efficiency, the hot vapor produced in one step is used to pre-warm the incoming saline water in the following steps.[21] The latter principle is the foundation of several types of thermal desalination processes,

including multi-stage flash distillation (MSF), multiple-effect distillation (MED), and vapor compression distillation (VCD).[14]

MSF is the most widely used thermal desalination process.[22, 23] It involves heating saline water under reduced pressure to a temperature higher than its boiling point, flash evaporation.[24] The heated water then passes through a series of chambers or 'stages' at progressively lower pressures, causing it to flash into steam. The steam is then condensed to produce freshwater. The flow chart for an MSF process with 3 stages is shown in **Figure 3**. MSF plants may have 20-40 stages.[25] MSF distillation requires significant energy and is typically operated using waste heat from the neighboring power plants.[26, 27]
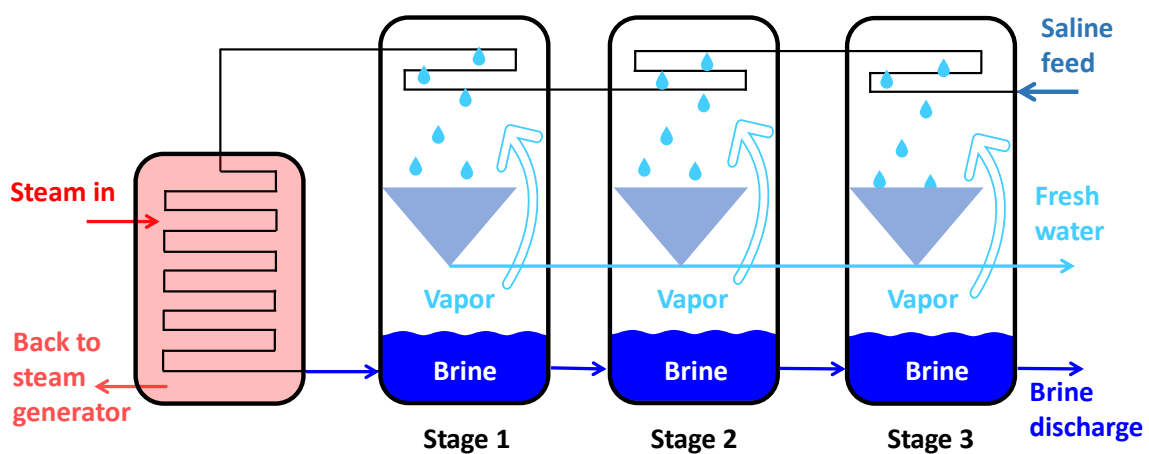


**Figure 3:** Flow chart of the multi-stage flash distillation process.

MED is similar to MSF distillation but operates at lower temperatures and pressures, making it the most thermodynamically efficient thermal desalination technology.[28] It consists of multiple stages, known as effects, where each effect operates at a progressively lower pressure. In contrast to MSF, the pre-warmed seawater is sprayed onto the hot tubes carrying steam. In each effect, heat is transferred from the steam to evaporate more saline water. The steam is then condensed to produce freshwater. MED is known for its energy efficiency,[29] and it can be powered by various heat sources, such as waste heat and exhaust steam from power station turbines, for more economical desalination.[30]

VCD is a thermal desalination process that utilizes mechanical compressors to increase water vapor pressure generated by evaporation. Compressing the vapor increases its temperature and energy content following the classic adiabatic compression process.[31] The seawater that gets in contact with the high-temperature vapor (steam) tubes evaporates, allowing the vapor inside the tube to be condensed and recovered as freshwater.[32] VCD is known for its simplicity and compactness and could be a viable option for small to medium-sized desalination plants with production capacities of around 1500-5000 $m^3$/day.[33, 34] The high energy consumption to operate the compressors and costly maintenance might limit considerations regarding the VCD option.[34]

### 2.1.2. Membrane filtration processes

Reverse membrane filtration processes typically utilize selective and permeable membranes, that is, permselective, to separate freshwater from saline water. Based on the pore sizes, membranes could be categorized from larger to smaller into microfiltration, ultrafiltration, nanofiltration, and reverse osmosis, as illustrated in **Figure 4**. Microfiltration removes larger particles and bacteria, and ultrafiltration separates macromolecules such as proteins or colloidal particles, though neither method effectively removes salt ions.[35] In contrast, nanofiltration can remove divalent salt ions like calcium, magnesium, and sulfate.[36, 37]
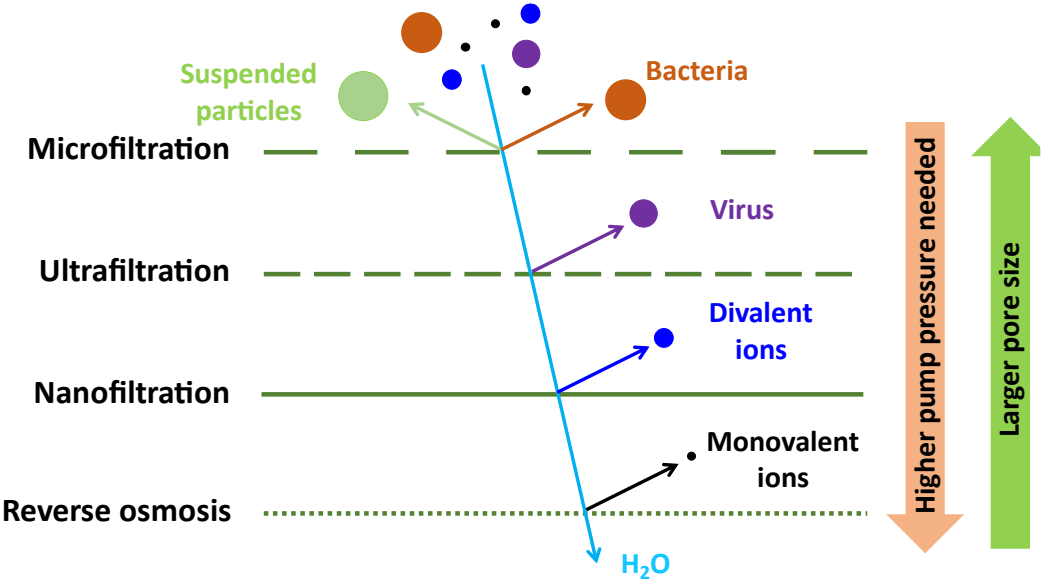


**Figure 4:** Classification of membrane filtration processes concerning the membrane pore size and permeability of different water impurities, adapted with permission from Refs.[38, 39]

Reverse osmosis (RO) membranes possess the smallest pores, typically around 0.1-1.0 nm.[40, 41] They can strip water from impurities at the molecular level, such as removing ions, molecules, and even some bacteria and viruses. As such, RO is the most widely used desalination technology at municipal and industrial levels. As shown in **Figure 4**, a higher purification degree requires more powerful pumps to provide higher transmembrane pressures, increasing the system's energy consumption. For RO, such pressure typically ranges between 60-80 bar.[42]

### 2.1.3. Electrochemical desalination processes

Thermal and membrane filtration processes rely on temperature and pressure as the driving forces to remove the water from a saline solution. In contrast, electrochemical desalination relies upon electrical potential as the driving force to remove the salt ions from the saline media. A significant advantage of electrochemical desalination is its low energy consumption compared to other technologies.[43] It operates at low voltages and does not require high-pressure pumps or thermal energy. Electrochemical desalination systems are also up-scalable,[44-46] modular,[46, 47] and can be customized to suit various applications, ranging from brackish water[48-50] to seawater[51, 52] desalination to industrial wastewater treatment.[53, 54]

**Figure 5A** schematically shows the simplest form of an electrochemical desalination cell that consists of a pair of electrodes to which an electrical potential is applied. Upon polarization of the electrodes, dissolved salt ions are attracted to the electrodes and immobilized, resulting in a less salty effluent. When the electrodes are made of carbon materials, such a process could be called capacitive deionization (CDI), as the carbon electrodes store the charge capacitively.[55] **Figure 5B** depicts a CDI module consisting of several carbon electrode pairs stacked in parallel for a more significant desalination throughput.
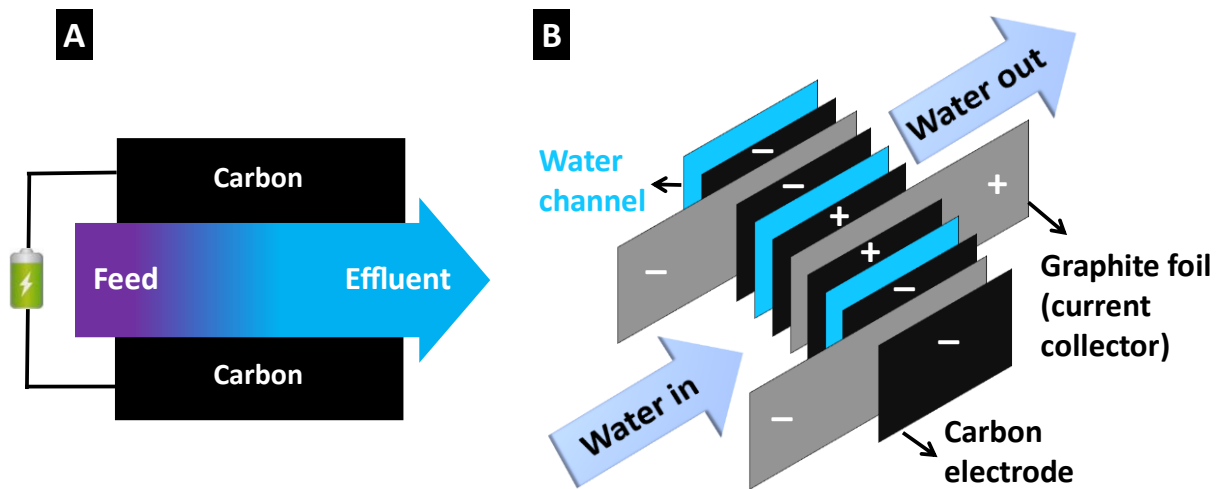
**Figure 5:** (A) Schematic representation of a single electrochemical desalination cell and (B) an electrochemical desalination module consisting of multiple cells stacked in parallel.

Electrodialysis (ED) is another effective electrothermal desalination method consisting of membranes. The reason is that, as outlined previously, in a typical membrane filtration process, water passes through a permselective membrane while blocking salt ions. In ED, on the contrary, the membranes allow the salt ions with specific signs to pass through the membrane while blocking the counter ions and the water.[56, 57]

In an ED system like the one shown in **Figure 6**, water containing salt ions is directed into separate chambers, partitioned by membranes that selectively permeate cations or anions.[58] When an electric voltage is applied, anions migrate toward the positive pole, while cations move toward the negative pole. By arranging the membranes alternately, only one type of ion can pass through each membrane, while the adjacent membrane blocks its passage. This configuration creates a series of alternating chambers containing concentrated and desalinated water, which can be extracted through separate tube systems.[59]

The ED system described above can be used in reverse to generate electricity. Reverse electrodialysis (RED) is the latter process, which can harness the energy generated by the salinity gradient between two solutions to create an electrical potential.[60, 61]
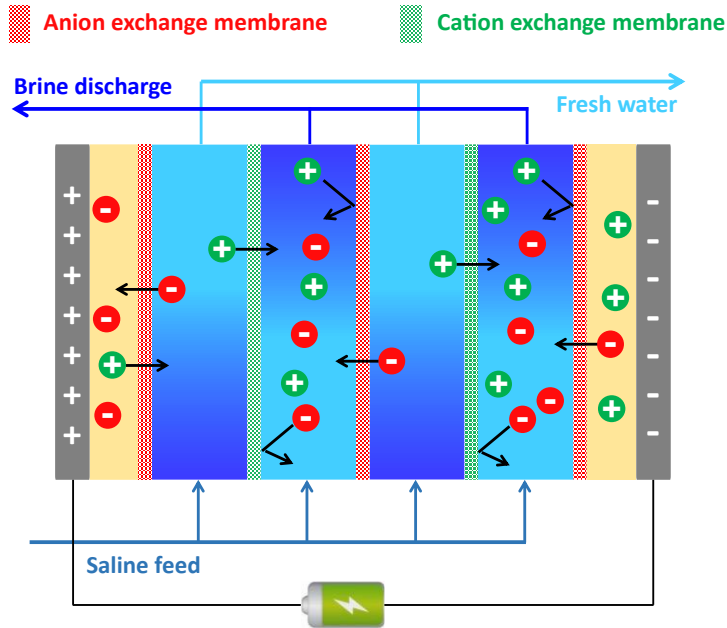
**Figure 6:** Illustration of the principle of an electrodialysis system, adapted with permission from Ref.[62]

### 2.1.4. Prevalence, energy consumption, and water recovery ratios of each desalination technology

Regardless of the desalination technology, or the trajectory traveled by water going from a saline solution to a freshwater solution, the minimum theoretical (thermodynamic) energy to accomplish desalination will be the same, assuming zero losses.[63] The minimum specific energy consumption (SEC$_{min}$) to perform desalination follows the expression in **Eq. (1)** (Ref. [64]):

$$SEC_{min} = -\frac{\pi_f}{R_w} \ln(1 - R_w) \qquad \text{(Eq. 1)}$$

where $\pi_f$ is the osmotic pressure of the feedwater (Pa), and R$_W$ is the water recovery ratio. Water recovery ratio, or percent recovery, is a unitless value between 0 to 1, defined as the fraction (volume) of desalinated water produced from the feedwater.[65] As inferred from **Eq. (1)**, the minimum specific energy consumption (joules per liter freshwater) solely depends on the osmotic pressure of the feedwater and the water recovery ratio. The osmotic pressure of a solution is calculated following **Eq. (2)** (Ref.[66]):

$$\pi = C_M RT \qquad \text{(Eq. 2)}$$

where $C_M$ is the molarity of the solution, R is the ideal gas constant (8.314 $\frac{J}{Kmol}$), T is the absolute temperature (K), and $\pi$ is the osmotic pressure (Pa). Given the latter expression, one

can plot the osmotic pressure of aqueous saline solutions with different NaCl concentrations, as shown in **Figure 7A**, assuming the solutions are at room temperature (25 °C).
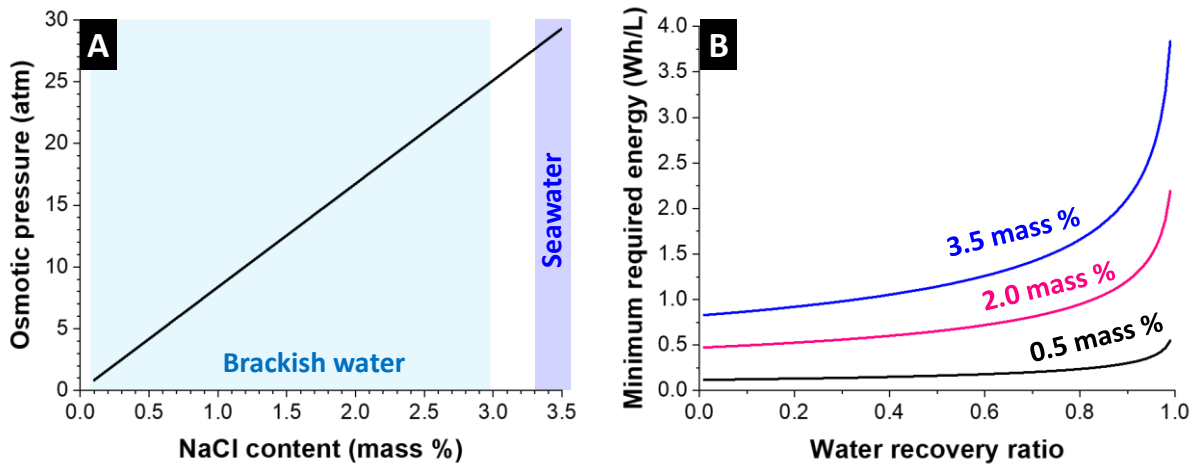


**Figure 7**: (A) Osmotic pressure of aqueous saline solutions with different NaCl salt contents and (B) thermodynamic energy consumption analysis of converting aqueous saline solutions with three NaCl salt contents into pure water (100 % salt rejection) across various water recovery ratios, calculated based on the expressions reported in Ref.[64]

**Figure 7A** shows that the osmotic pressure of saline water has a direct linear relationship with its dissolved salt content and illustrates how it increases going from brackish water regimes to seawater-level concentrations of NaCl. Substitution of the osmotic pressures obtained in **Eq. (2)** in **Eq. (1)** then gives the minimum thermodynamic energy to convert a saline solution of a particular concentration into ideally pure water at a given water recovery ratio, as demonstrated by **Figure 7B**. As observed, the energy consumption increases exponentially as the water recovery ratio increases, particularly when the water recovery ratio approaches unity.

**Table 1** shows the sanity levels of different water sources, ranging from potable freshwater to the highly saline brine solutions ejected from mining activities and their potential applications.[67] The freshwater salt content is less than 500 ppm[68, 69] or less than 1000 ppm.[70] The salinity level of ocean water is generally established as 35 g salts per liter, where the NaCl salt constitutes the major component among all other salt species.[71]

**Table 1**: Salinity levels and potential uses of various water sources.[67-70]

| | Fresh water | Brackish water | Saline water | Brine |
|---|---|---|---|---|
| **Salt content (mass %)** | < 0.05 | 0.05-3 | 3-5 | > 5 |
| **Concentration (g/L)** | < 0.5 | 0.5-30 | 30-50 | > 50 |
| **Concentration (mM)** | < 10 | 10-500 | 500-900 | > 900 |
| **Typical sources** | Desalinated water, ponds, rivers. | River/underground water, lakes | Sea/ocean Water, salt lakes | Desalination plants/mining rejection |
| **Uses** | Drinking and all irrigation | Irrigation of certain crops Useful for most livestock | Limited use for certain livestock | Mining |

As outlined above, the theoretical thermodynamic energy requirements depend only on the osmotic pressure of the feedwater, its temperature, and the target water recovery ratio one has in mind. In practice, however, every desalination technology has its losses associated inherently with the system components involved in that technology. In membrane filtration processes, for instance, the losses occurring in the non-ideal operation of the high-pressure pumps, the resistances of membranes to fluid permeation, and friction losses in the fluid channels will significantly add to overall energy consumption.[72] Likewise, the heat losses associated with the reboiler and condenser units of thermal desalination processes add to their energy consumption.[73] In addition, the thermodynamic minimum energy calculations are based on infinitesimally slow processes to approach a reversible process (that is, quasi-static), which in practice will not be economically feasible.[63]

**Table 2** shows practical energy consumption values for the desalination technologies introduced earlier from real-life desalination plants for the desalination of different water types.

**Table 2**: Energy consumption and water recovery ratio metrics of various water desalination technologies. N/A: not available.

| Desalination technology | Water type | Energy consumption (Wh/L or kWh/m³) | Desalination capacity (m³/day freshwater produced) | Water recovery ratio (%) | Location | Ref. |
|---|---|---|---|---|---|---|
| MSF | Seawater | 20-38 | N/A | N/A | Kuwait | [74] |
| MED | Seawater | 19.2 | 17,616 | N/A | Qatar | [75] |
| VCD | Seawater | 10-11 | 500 | 45 | Canary Islands, Spain | [76] |
| RO | Brackish water | 1.8 | 8,660 | 60 | Adrar, Algeria | [77] |
| RO | Seawater | 3.4-3.8 | 41,000 | 40-60 | Maspalomas, Spain | [78] |
| Electrochemical desalination | Brackish water | 0.55 | 3,600 | 79 | Shanghai, China | [50] |
| Electrochemical desalination | Brackish water | 0.1-0.2 | ~ 22 | 80 | Utrecht, The Netherlands | [79] |

**Figure 8** shows the prevalence of each desalination technology in operation worldwide as of 2019, together with their water recovery ratios in desalination of brackish water, seawater, and brine. As expected, the desalination plants generally opt for higher water recovery ratios in the case of low salinity water types and lower water recovery ratios in the case of highly saline water types to avoid the regions of highest energy consumption shown in **Figure 8B**.
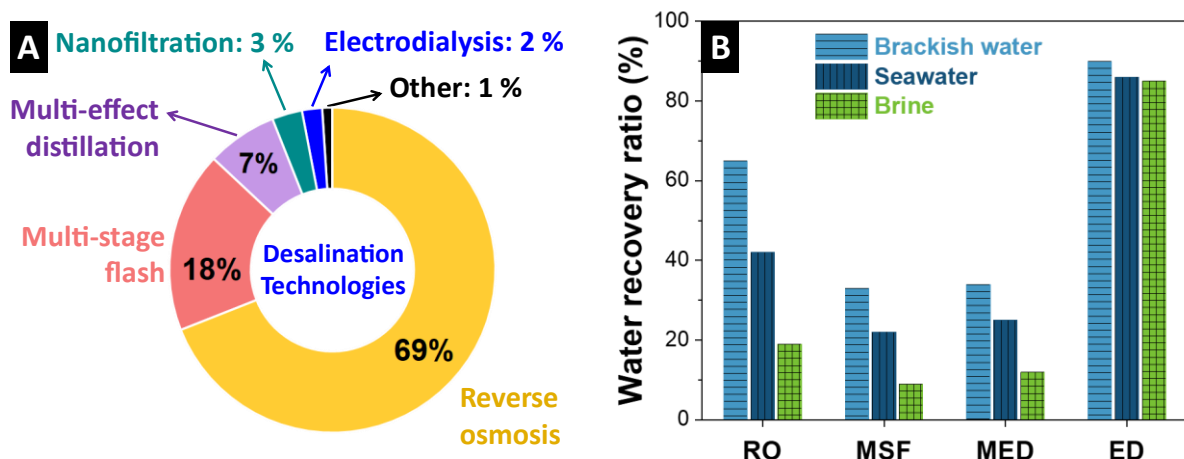


**Figure 8**: (A) Global share of major desalination technologies in operation as of 2019, and (B) their water recovery ratios, adapted with permission from Ref.[80]

## 2.2. Electrochemical water desalination

### 2.2.1. The electrochemical desalination setup

Electrochemical desalination is an emerging water treatment technology that utilizes electrochemical principles to remove ions and impurities from water.[81] In industrial or municipal-level desalination plants, multiple cells can be connected in series or parallel to increase the treatment capacity or adapt to different water quality scenarios.[44] At the laboratory scale experiments, however, just a single cell is typically tested to benchmark its desalination performance merits. **Figure 9** schematically shows the entire electrochemical desalination setup used throughout this thesis.

The electrolyte reservoir (10 L in volume) is de-aerated by constant bubbling with an inert gas such as nitrogen. The goal is to remove the dissolved oxygen from the electrolyte, which could be a source of electro-oxidation of electrodes upon electrochemical cycling. A peristaltic pump circulates the electrolyte through the cell, followed by a conductivity chamber, a pH chamber, and finally, back to the reservoir. An electrochemical workstation provides the user-defined voltage and current values as the driving force to the cell to accomplish desalination. The cell's response data, manifested in conductivity and pH change in its effluent stream, is then recorded and shown in the computer in real-time.
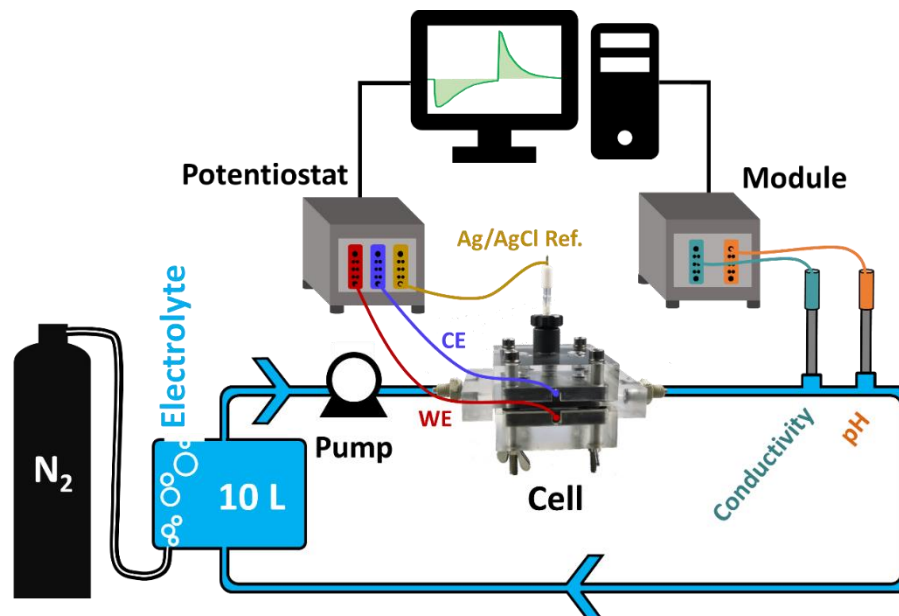


**Figure 9:** (A) Schematic representation of a typical electrochemical desalination setup; WE: working electrode, CE: counter electrode, adapted with permission from Ref.[82]

The cell is at the heart of the electrochemical desalination setup described above. **Figure 10** schematically shows the core components within the cell., which can consist of two carbon electrodes separated by glass fiber separators that provide a pathway for the water stream to move through the cell. Two current collectors (typically graphite foil or graphite plates) bring the current from the power source (electrochemical workstation) to the carbon electrodes, immobilizing positive and negative salt ions in water.
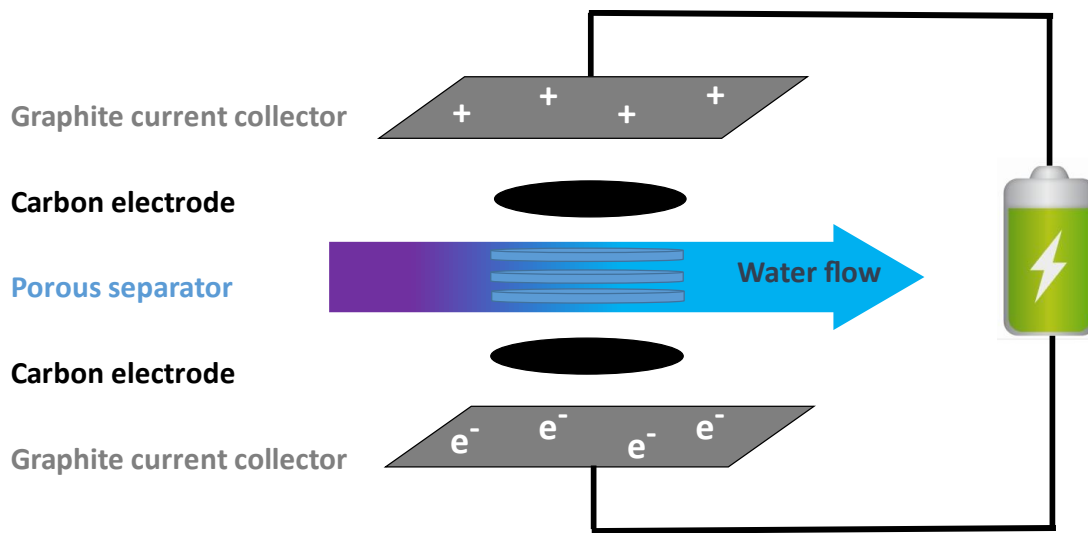


**Figure 10:** Schematic illustration of the key components of a typical electrochemical desalination cell.

**Figure 11** shows a photograph of the cell used in the present study. Two incoming (noted #1 in the figure) and outflowing (#2) flexible tubes circulate the electrolyte in the cell at a flow rate of typically 2 mL/min. The electrolyte reservoir is a tank that contains 10 L. The cell accomplishes desalination by applying a voltage and current carried by two wires connected to the cell (#3). The potential development is then monitored by an Ag/AgCl (3 M NaCl) reference electrode (#4). A transparent cell body (#5) helps to find and resolve possible bubbles or leakages of the cell during operation.
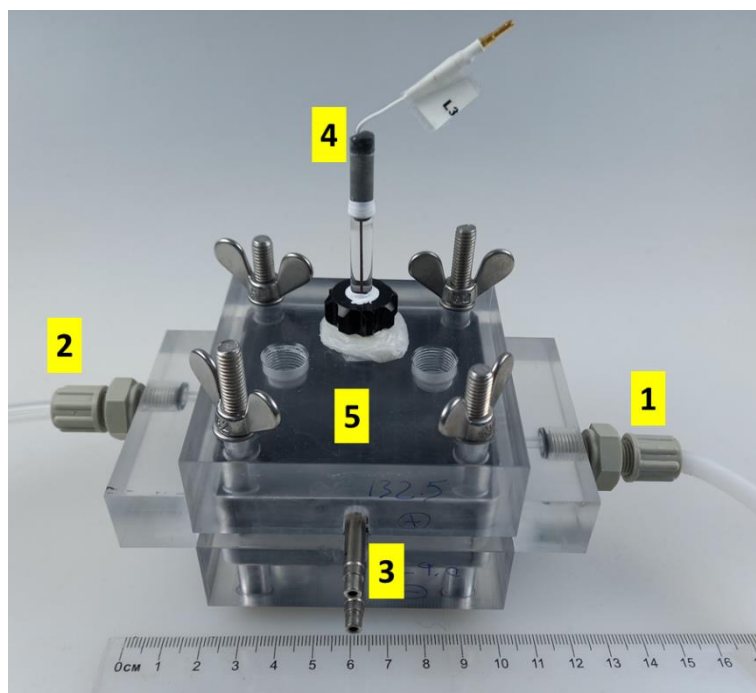
**Figure 11**. A photograph of the electrochemical desalination cell, with the dimensions (L × W × H) of ca. 12 × 8 × 8 cm$^3$.

When the water flows through the cell, an electrical potential is applied between the two electrodes. The positive electrode (or anode) attracts negatively charged ions (anions), while the negative electrode (or cathode) attracts positively charged ions (cations). As a result, ions from the water are immobilized onto the surfaces of the electrodes, forming an electrical double-layer. During the charging step (**Figure 12A**), an electric potential is applied, causing ions in the water to migrate toward the respective electrodes and accumulate in the electrical double-layer. The latter electronic charge separation and ion adsorption create an electrical energy storage mechanism within the cell. The stored energy could be partially recovered in the following discharging step, which is one advantage that makes electrochemical desalination attractive compared to other conventional technologies.[83-85]

The charging process can be understood by considering the behavior of an electrode immersed in an electrolyte solution. The electrode surface has a fixed charge density due to the presence of functional groups or surface defects. When the electric potential is applied, an excess electronic charge is induced on the electrode surface, which makes the ions in the solution experience an electrostatic force that attracts them to the oppositely charged electrode. The carbon-based materials used as electrodes in CDI systems possess a high specific surface area and high pore volume, providing ample ability for ion electrosorption.

The pore structure, consisting of micropores, mesopores, and macropores, influences the salt removal capacity and/or rate.[86, 87]

The international union of pure and applied chemistry (IUPAC) classifies the pore sizes into three regimes: (i) micropores, with pore width less than 2 nm, (ii) mesopores, between 2 nm and 50 nm, and (iii) macropores, larger than 50 nm.[88] Pores' geometry can also differ largely from one material to another. Some typical pore geometries are slit-shaped, cylindrical, and cone-shaped, among others.[89] The pores that are accessible to their surroundings are called 'open' pores. The latter pores could also be only open at one end, in which case they are called 'blind' or 'dead-end' pores. Those pores with no communication with their surroundings are called 'closed' pores.[90] Closed pores are defined as pores that cannot be penetrated by Helium gas at 303 K.[91]

The electrochemical desalination system enters the discharging step once the electrodes are saturated with ions. The electric potential is reduced (shorted or reversed), and the ions adsorbed on the electrodes are released back into the water, as shown in **Figure 12B**. This process allows the removal of the ions from the water, effectively deionizing it.
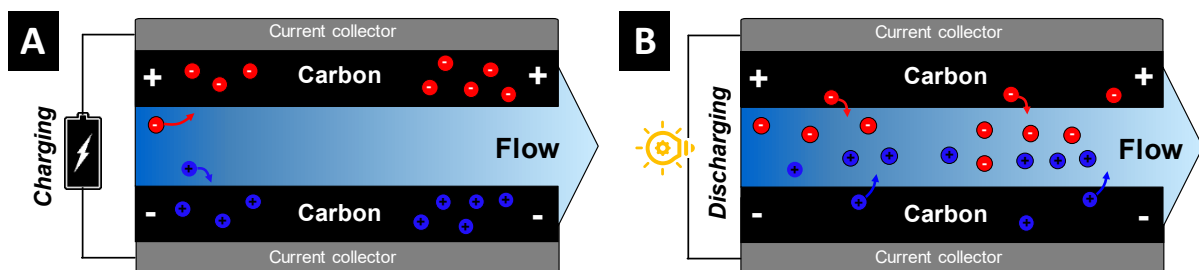


**Figure 12:** Schematic representation of an electrochemical desalination cell (A) during charging, where ions are attracted to the electrodes with an opposite sign, and (B) during discharging, where ions are ejected from the electrodes to the water flow channel.

### 2.2.2. Electrode materials, the underlying mechanisms, and their brief history

Since Blair and Murphy conceptualized the electrochemical desalination technology in 1960,[92] where it was initially called electrochemical demineralization, various materials were examined as electrodes. The latter pioneering work showed that a porous carbon electrode could be paired with a silver-silver chloride (Ag/AgCl) electrode to remove the sodium and chloride ions from an aqueous sodium chloride electrolyte. In the following decades, which consisted of long gaps in the advancement of electrochemical desalination research, carbon-based electrodes dominated the field.[93] As such, carbon materials could

be considered as 'first-generation' materials in electrochemical desalination research. The mechanism behind the ion storage of carbon-based electrodes involves the formation of oppositely charged electronic and ionic charges at the interface between the electrode and electrolyte, respectively, as shown in **Figure 13**.[94] The latter phenomenon, known as electric double-layer capacitance (EDLC), is responsible for immobilizing the ions within the pores of a carbon electrode.[55]
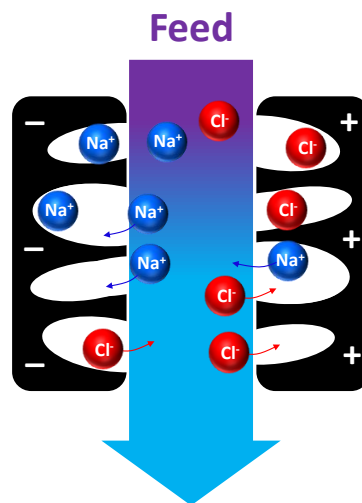


**Figure 13:** Schematic representation of immobilization of salt ions within the porous matrix of carbon electrodes in a symmetric electrochemical desalination cell.

It was not until the beginning of the 21$^{st}$ century that electrochemical desalination research gained significant momentum. In 2003, composites made of carbon and titanium oxide (TiO$_2$) have significantly improved the desalination capacity compared to bare carbon electrodes.[95] However, due to the lack of standardization of the electrochemical desalination metrics back in the time, the latter positive effect has only been shown qualitatively. Quantitate benchmarking of similar electrodes has found that coating carbon electrodes with titanium oxide (TiO$_2$) drastically improves the desalination capacity from 9 mg to 17 mg NaCl per gram electrode.[96] Since the specific capacitance of the TiO$_2$-coated carbon electrode was very close to that of the bare carbon electrode, the enhanced desalination capacity was attributed to the enhanced wettability of carbon electrodes brought by TiO$_2$ coating and, as a result, better ion accessibility of carbon surfaces. TiO$_2$-decorated electrode has also shown an enhanced cycle stability of up to 100 in aqueous media of high oxygen contents.[97] The latter enhanced stability is owing to the electrocatalytic activity of TiO$_2$, which hinders hydrogen peroxide evolution and prevents carbon oxidation.

Another shortcoming of carbon electrodes, apart from their moderate desalination capacity or vulnerability to oxidation, was that they were generally ineffective at high salinity levels, such as in seawater. As such, ion-exchange membranes were introduced in 2006 to remedy the latter issue.[98] Such permselective membranes, commonly made of polymers,[99, 100] cover each carbon electrode's surface, allowing the desired ions to permeate across the membrane and make it to the electrodes.[101] This way, the weakness of carbon electrodes in non-permselectivity can be compensated, though at the cost of adding another rather expensive component to the system: membranes.

The promise shown by electrode materials beyond carbon and the shortcoming of carbon materials in desalination capacity and permselectivity has prompted the electrochemical desalination research community to explore next-generation electrode materials, such as those employed in the adjacent energy storage field. With no carbon materials, a desalination battery was then named an electrochemical cell whose electrodes consisted of sodium manganese oxide ($Na_2Mn_5O_{10}$) and silver-silver chloride (Ag/AgCl), in 2012.[102] The latter membrane-less cell was also sodium-selective among $K^+$, $Mg^{2+}$, and $Ca^{2+}$ competing cations and chloride-selective versus $SO_4^{2-}$ ions. Introducing an anion-exchange membrane to a similar cell made of Prussian Blue and Prussian Blue analogue electrodes in 2017 has demonstrated that such a cell can selectively remove ions during both charging and discharge, giving rise to the 'rocking chair desalination battery'.[103]

Electrochemical desalination with electrode materials previously shown promise in battery research, which could be classified as 'second-generation' materials, has become the subject of numerous studies in the field. Examples include 2D transition metal carbides (MXenes) such as $Ti_3C_2T_x$[104] and $V_2CT_x$[105] that have previously shown promise as Li-ion battery anodes in organic media for electrochemical desalination in aqueous media for the first time in 2016[106] and in the following years.[107, 108] The ion storage mechanism in such materials differs fundamentally from that of carbon materials. In a battery material, Faradaic processes are often at play, which include surface redox reactions such as in 2D $MnO_2$,[109, 110] conversion reactions such as in Ag/AgCl,[111, 112] and Bi/BiOCl,[113, 114] or ion intercalation such as in MXenes,[8, 106] transition metal dichalcogenides,[4, 5] and metal oxides.[115]

Unlike carbons, a high surface area is not necessarily required in the said materials as the electrolyte ions need not adsorb to the surface of electrode materials but rather insert, intercalate, or convert to the electrode.[116] A notable example is the $Ti_3C_2T_x$ MXene with a low surface area of below 10 $m^2/g$,[106, 117] in contrast to the high carbon surface area of around 1600 $m^2/g$.[117]

The combination of first- and second-generation materials has also become a common practice in the electrochemical desalination research community. Such an 'asymmetric' or 'hybrid' cell typically consists of carbon as one electrode and a battery material as the other. The most prominent example is the first electrochemical desalination cell conceptualized in the pioneering study in 1960, where Ag/AgCl was paired with porous carbons.[92] Recent examples include $Ti_3C_2T_x$ MXene employed as the negative electrode and porous activated carbon as the positive electrode for the desalination of aqueous saline media,[117] as shown in **Figure 14**.
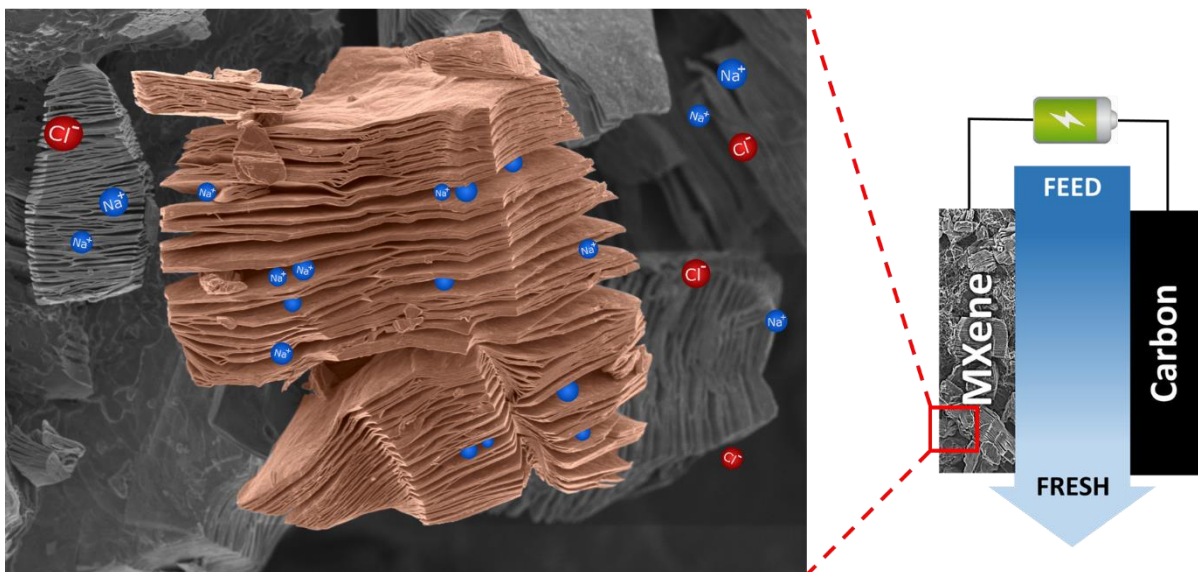


**Figure 14:** Schematic representation of an asymmetric electrochemical desalination cell consisting of MXene as the negative electrode and carbon as the positive electrode, alongside a scanning electron microscopy image of the MXene electrode.

The asymmetric design offers the advantage of capitalizing on the high capacity of the battery material, resulting in higher desalinating capacities, such as in the case of a hybrid $Na_4Mn_9O_{18}$/activated carbon cell, which yields 31 mg/g desalinating capacity compared to 14 mg/g in the case of the symmetric carbon/carbon cell.[118] Asymmetric cells can also show selectivity, often owing to the battery material.[6] However, opting for asymmetric cell design is sometimes inevitable, as certain materials show poor stability upon negative or positive polarizations. The asymmetric $Ti_3C_2T_x$ MXene/activated carbon cell is an example of a scenario since $Ti_3C_2T_x$ MXene electrode quickly degrades (oxidizes) upon positive polarizations in aqueous media.[117]

While the desalination capacities of carbon electrodes are typically in the range of 10-30 mg/g, the battery materials enhanced the capacities to an order of magnitude higher. Examples include 3D insertion materials such as sodium super ionic conductor (NASICON),[119] Prussian Blue,[120] and Prussian Blue analogue[121] electrodes with a desalination capacity of around 100 mg NaCl salt per gram electrode or antimony alloying electrode with nearly 300 mg/g for sodium ion removal.[122]

Desalination capacities above and beyond those values have been recently shown by new cell concepts where electrocatalytic materials are employed or where the active material in the electrode or electrolyte is constantly replenished. An example of an electrocatalytic system includes zinc-air desalination, where an elemental zinc electrode is paired with a $MoS_2$ electrocatalyst that turns the oxygen in the air into hydroxide ions,[123] which shows desalination capacities beyond 1000 mg/g. Other metal-air desalination systems introduced so far include magnesium-air[124] and aluminum-air electrodes,[125, 126] all of which are inspired by the concept of metal-air batteries from the adjacent field of energy storage.[127] Fuel cell desalination is another prominent example, where platinum electrocatalysts turn the hydrogen and oxygen inputs into protons and hydroxide ions to simultaneously desalinate, produce HCl and NaOH as side products, and co-generate electricity.[128] All such materials could be designated as third-generation electrode materials in electrochemical water desalination, which show drastically higher desalination capacities, the possibility for continuous operation, selectivity toward specific ions,[129] and co-generation of electricity, among others. **Figure 15** captures the three generations of electrode materials in electrochemical desalination systems outlined herein.

## Generations of electrochemical desalination electrode materials



**1**

**Electrochemical desalination with carbon materials**
- Electric double-layer capacitance
- Activated porous carbons up to 27 mg/g desalination capacity
- Up to 90 mg/g when paired with membranes

**2**

**Electrochemical desalination with battery materials**
- Faradaic processes such as surface redox, ion inspersion, and conversion reactions
- MXenes, Prussian blue, TMDs, TMOs, Ag/AgCl, etc.
- Up to 300 mg/g desalination capacity

**3**

**Electrochemical desalination with electrocatalytic materials**
- Faradaic processes in presence of an electrocatalyst
- Desalination fuel cell, metal-air desalination, etc.
- 1000 mg/g or beyond, with virtually unlimited capacity via continuous flow systems

**Figure 15:** Classification of electrode materials based on three generations of electrochemical desalination systems introduced in Ref.[81]

### 2.2.3.  Performance metrics

For a reliable and meaningful comparison between the merits of different systems within electrochemical desalination, it becomes necessary to establish precise quantitative criteria for evaluating cell performances. Among the key performance indicators for an electrochemical desalination system are desalination capacity, charge efficiency, energy consumption, and ion selectivity, all of which will be discussed in the following sections. These criteria, including energy consumption, can also be cautiously applied to assess the strengths of electrochemical desalination in comparison to adjacent technologies like membrane filtration or thermal processes.

*Desalination capacity*

The desalination capacity (DC) in electrochemical water desalination refers to the system's ability to remove salt ions from water. It represents the amount of salt that the system can effectively remove or reduce within a given time frame. As such, DC is a key quantitative measure in electrochemical desalination that provides valuable information about the system's performance, water production capabilities, and overall suitability for various water treatment applications. The simple relationship in **Eq. (3)** shows how the DC can be quantified:

$$DC = \frac{Flow\ rate \times Salt\ redcution \times Cycle\ duration}{Electrodes\ mass}$$ (Eq. 3)

The salt reduction refers to the reduction in the concentration of effluent water of an electrochemical desalination cell as a result of voltage application. The product of salt reduction and cycle duration can be graphically calculated by integrating the area under the concentration-time curve, like the one shown in **Figure 16**. The latter area should be, in principle, similar to the next half-cycle, during the cell discharge and brine production. However, due to non-idealities, the latter two areas might be non-equal (up to ~10 % different) in practice, and hence an average amount could be taken for calculations. Alternatively, a DC for the charging step and a DC for the discharging step could be calculated and compared.
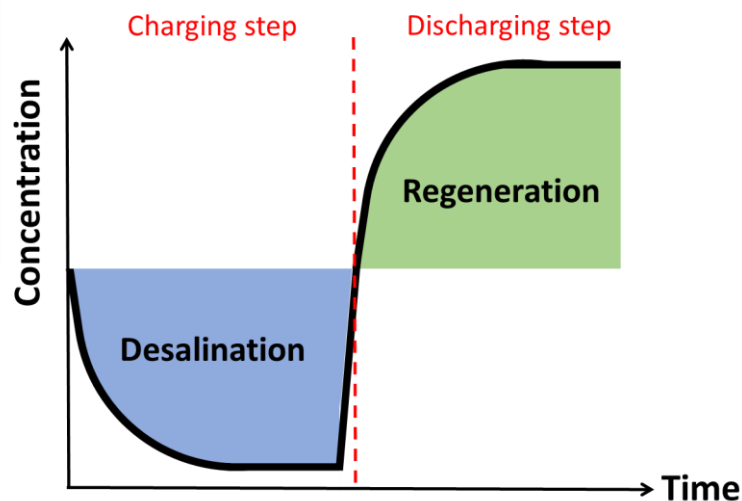


**Figure 16:** Schematic representation of a typical concentration profile of the effluent of an electrochemical desalination cell during charging and discharging half-cycles.

The integrated area in **Figure 16** could then be plugged in **Eq. (4)** to calculate the gravimetric DC:

$$\text{DC} = \frac{v}{m_{total}} \int C \, dt \qquad \text{(Eq. 4)}$$

where $v$ is the flow rate (L/s), $m_{total}$ is the total mass of both electrodes combined (g), and $t$ is the time (s) during which a concentration change (mmol/L or mM) occurs. As such, the gravimetric DC could be obtained as millimoles of salt removed per gram of the electrode or simply mmol/g.

More commonly, however, the latter value is multiplied by the molar mass of the salt under study, as formulated in **Eq. (5):**

$$\text{DC} = \frac{v \, M}{m_{total}} \int C \, dt \qquad \text{(Eq. 5)}$$

where $M$ is the molar mass of the salt (g/mol). As such, the DC will then have the unit of mg/g, that is, milligram salt removed per gram of the electrode.

Analogous to capacitance supercapacitors or charge storage capacity in battery systems, DC can also be calculated in gravimetric, volumetric, or areal forms. One could alternatively report the DC in volumetric form by simply replacing the $m_{total}$ in the denominator of **Eq. (4)** or **Eq. (5)** by volume of the electrodes (say, in cm$^3$), to obtain volumetric DC with the unit of mg/cm$^3$. Similarly, areal DC (such as in mg/cm$^2$) can be calculated by normalizing the area of the electrodes exposed to the flow channel. The latter form is beneficial in reporting the desalination capacity of electrochemical desalination systems comprised of third-generation electrodes, such as metal-air desalination.[123-126] In such a system, the exact mass of the metal electrode participating in the desalination process is often challenging to know. In contrast, the geometric area of the electrode utilized in the process is easily measurable.

*Charge efficiency*

The effectiveness of electrical energy utilization for ion removal from water is measured by a crucial parameter known as charge efficiency (CE) in electrochemical water desalination. This parameter indicates the proportion of electrical energy dedicated to ion removal compared to the total electrical energy input to the system. Therefore, charge efficiency is essential in electrochemical desalination, offering valuable information about energy efficiency and system performance. It is vital in optimizing system operation and assessing overall system effectiveness.

The following simple relationship shows how the CE can be quantified via **Eq. (6)**:

$$CE = \frac{\text{electronic charge that contributed to } \textit{desalination}}{\textit{total electronic charge } \text{invested}}$$ (Eq. 6)

As such, CE is a unitless value between zero to unity. Alternatively, CE is also reported in percentage.

The nominator of the latter relationship is equivalent to the total number of salt molecules removed, which was previously calculated by **Eq. (4)**. To match the units with the nominator, the denominator should also be represented as the number of electronic charge (that is, the number of electrons in moles). As such, the above relationship could then be formulated as **Eq. (7)**:

$$CE\ (\%) = \frac{DC}{Q/F} \times 100$$ (Eq. 7)

where DC is mmol/g, F is the Faraday constant (96485 C/mol), and Q is the gravimetric electronic charge (C/g) stored in the electrodes normalized to the total mass of both electrodes combined.

*Energy consumption*

It is crucial to analyze the energy consumption of electrochemical desalination to determine the most energy-efficient system components, such as electrode materials, cell configurations, or electrolyte concentrations. For instance, energy consumption calculations can reveal that carbon electrodes exhibit higher energy consumption at higher electrolyte concentrations. At the same time, Faradaic materials like 2D transition metal sulfides or MXenes maintain a relatively constant energy consumption across wide concentration ranges.[5, 8, 117]

One approach to calculating the consumed energy would be to consider the watt-hours (Wh) required to produce a certain volume of freshwater, commonly reported as Wh/L. The freshwater is typically defined as less than 500 ppm (< 9 mM NaCl)[68] or less than 1000 ppm (< 17 mM NaCl).[70] While the Wh/L values are commonly reported in RO technology, they should be cautiously applied to electrochemical desalination systems. In a general RO process, over 99 % of the salt content is removed from the product water. In contrast, in electrochemical desalination at the lab scale, only a small percentage of the salt content is removed in each charging half-cycle in a single-pass mode of operation.[130]

Therefore, calculating energy consumption for complete salt removal through electrochemical desalination might require extrapolation calculations, assuming that the system consumes energy at the same rate even at very low salt content. However, this assumption could be incorrect since electrolytes with lower concentrations exhibit higher solution resistance, resulting in higher energy consumption as the concentration decreases.

Another approach to reporting energy consumption in an electrochemical desalination system would be to break down the energy to every salt molecule removed from the saline media. **Eq. (8)** can be used to calculate the energy invested in removing a single salt molecule from the saline stream:

$$\text{Energy consumption per ion} = \frac{\frac{U_{charge}}{m_{total}}}{\frac{DC}{M_{NaCl}}} \tag{Eq. 8}$$

In the latter expression, the numerator provides the consumed energy normalized to the mass of both electrodes combined (Wh/g), and the denominator gives the moles of salt ions removed normalized to the mass of both electrodes combined (mmol/g). However, the energy of the molecular systems is given by the product of Boltzmann constant and temperature ($k_B T$). At 25 C, 1 Wh would then be equal to $8.75 \times 10^{23}$ $k_B T$, Multiplication of $8.75 \times 10^{23}$ to the value obtained by **Eq. (8)** will then give the energy consumed for the removal of each salt molecule, such as NaCl from the saline media.


*Selectivity*

Electrochemical desalination systems can be designed in a way to preferentially remove certain species from the aqueous environment.[11, 131] The latter feature is of high value and interest for a host of industrial, mining, or municipal activities where certain toxic elements are present in the wastewater, such as lead[132-134] and cadmium.[135] Selective separation is also becoming more and more relevant for recovery and recycling of value-added elements, such as lithium, nickel, cobalt, and manganese ions, contributing toward a circular Li-ion batteries economy.[136-138]

The selective behavior of an electrochemical desalination system can be typically tuned by controlling the electric potential,[6] optimizing the electrode materials,[139-141] or kinetics of the electrochemical process.[142-145] The latter time-dependent selectivity allows for tailored water treatment based on the desired water quality, such as removal of monovalent ions during early operation times of the electrochemical desalination system, followed by the removal of divalent ions in later operation times.[143-146] The scheme in **Figure 17** captures

such a selective behavior when separating a target ion from a mixture of cations in aqueous media.
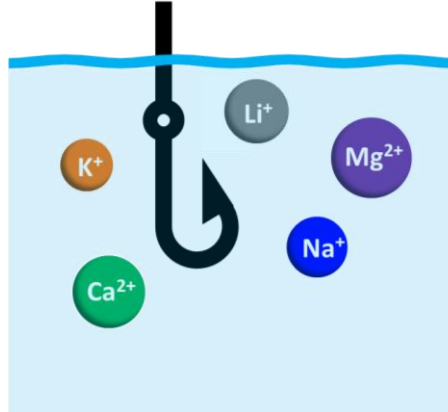


**Figure 17:** Schematic representation of targeted removal of ions from aqueous media.

The preferential removal of certain ions by an electrochemical desalination system can be quantified by defining a new performance metric known as separation factor. When the ion A is removed from a mixture of A + B ions, the separation factor, $\beta$, can be expressed following **Eq. (9)**:

$$\beta_{A/B} = \left(\frac{C_{A,initial} - C_{A,final}}{C_{B,initial} - C_{B,final}}\right)\left(\frac{C_{B,initial}}{C_{A,initial}}\right) \tag{Eq. 9}$$

where $C_{A,initial}$ and $C_{A,final}$ refer to the concentrations of A ions in the beginning and at the end of the process, respectively; and $C_{B,initial}$ and $C_{B,final}$ refer to the concentrations of B ions in the beginning and at the end of the process, respectively.[147] The latter expression simplifies to **Eq. (10)** when there are equimolar concentrations of the ionic species in the feed solution.

$$\beta_{A/B} = \left(\frac{C_{A,initial} - C_{A,final}}{C_{B,initial} - C_{B,final}}\right) \tag{Eq. 10}$$

A separation factor value near unity, therefore, means that the system is non-selective and removes both A and B ions indiscriminately. Values of $\beta_{A/B}$ larger than one indicates a favorable removal toward A compared to B.

## 2.3. Harnessing 2D materials for electrochemical water desalination and energy applications

In pursuing novel materials and technologies enabling sustainable water treatment or energy storage and conversion systems, 2D nanolamellar materials have emerged as promising candidates.[148-151] Owing to their anisotropic nature that the properties in one direction differ from those in another direction,[152] 2D materials offer unique properties and advantages over their conventional bulk (3D) counterparts, as is the case for graphene and graphite.[153, 154] Also, due to the proximity of all atoms to the surface in a 2D material, their properties can be significantly altered and tuned.[155] The latter can be accomplished using surface functionalization, such as the conversion of graphene to graphene acid (G-COOH),[156, 157] or heteroatom doping, such as in nitrogen doping of the latter two species.[158]

The proximity of atoms to the surface also exposes the layers of a 2D material (electrode) to their immediate surroundings (electrolyte), maximizing the interactions between the two. The latter, which potentially also increases the electrochemically active specific surface area of 2D materials, could be capitalized particularly in (electro)catalytic applications.[159-161] The extraordinarily high surface area of 2630 $m^2$/g for graphene,[162] as compared with ~12 $m^2$/g of its 3D bulk counterpart graphite or 100-400 $m^2$/g in the case of multi-walled carbon nanotubes (CNTs),[163] attests such a surface area enhancement in the 2D form. Similar enhancements also occur in terms of mechanical and electronic properties. In the graphene example, since the layers have strong in-plane bonds and are at the same time thin[155] (that is, a large surface-to-volume ratio), they tend to show high mechanical strength and flexibility[164] while possessing beneficial processability.[165]

### 2.3.1. MXene for electrochemical desalination

MXenes are a relatively new class of 2D materials that have garnered significant attention due to their excellent mechanical, electrical, and thermal properties.[166] These materials comprise transition metal atoms sandwiched between carbon and/or nitrogen atoms. MXenes have shown potential for various applications in the water-energy nexus, including water remediation[7] and energy storage.[167] For instance, MXene-based membranes have shown promising performance in water desalination,[168-170] while MXene-based electrodes have been widely used for lithium-ion batteries.[171]

MXenes are produced from their parent material MAX phase. MAX phases are a family of layered ternary compounds that consist of a transition metal (M), an element from group A (A), and carbon or nitrogen (X). The name "MAX" is derived from the first letters of the chemical symbols representing the components. Since their discovery, one of the most widely studied MAX phase and MXene have been $Ti_3AlC_2$ and $Ti_3C_2T_x$, respectively. **Figure 18** schematically shows the synthesis route to fabricate $Ti_3AlC_2$ MAX phase from its elemental precursors and its further processing to obtain $Ti_3C_2T_x$ MXene and subsequent delamination.
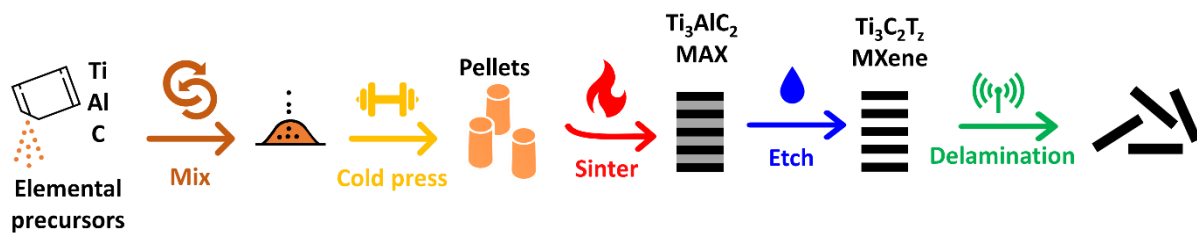


**Figure 18:** Processing of titanium, aluminum, and carbon elemental precursors to obtain $Ti_3AlC_2$ MAX phase, $Ti_3C_2T_x$ MXene, and finally delaminated $Ti_3C_2T_x$ MXene sheets.

To better understand the MXene properties, it is imperative to know how MXene ins obtained from its parent MAX phase material. MAX phase compounds have a unique crystal structure, typically with alternating layers of M-X atoms separated by layers of A atoms, as schematically shown in **Figure 19**. The synthesis of MXenes typically involves selectively etching aluminum (A) layers from various MAX phases using aqueous hydrofluoric acid (HF) at room temperature.[172, 173] As shown in **Figure 19**, upon HF treatment of the MAX phase, the aluminum layer is selectively removed from the stack, leaving behind M-X layers, MXenes.[174] The process of removing the A (in this case, Aluminum) atoms from the MAX phase and its concomitant layer opening is called exfoliation.

During the latter process, the dangling bonds on the surface of MXene sheets cling to the species present in the reaction environment, such as -O, -OH, and -F, in case the reaction media is aqueous. The said surface terminations are often collectively represented by $T_x$ in MXene's stoichiometric formula, such as $Ti_3C_2T_x$ in the case of titanium carbide MXene. The -O and -OH bonds on the MXene surface (weakly) hold together its layered structure via hydrogen and van der Waals bonds. As such, MXenes can be easily delaminated when a bulky organic molecule is intercalated in between its layers, such as DMSO, Hydrazine,[175] or TBAOH.[176] The delamination process is not to be confused with exfoliation, though they are sometimes used interchangeably in the literature. As outlined earlier, exfoliation means opening up the layers during acid (commonly HF) treatment of the MAX phase, turning them into stacks of multilayered accordion-like MXene structures. Delamination, however, refers to breaking the weak bonds between the latter MXene layers, turning them into single or few-layered MXene sheets.
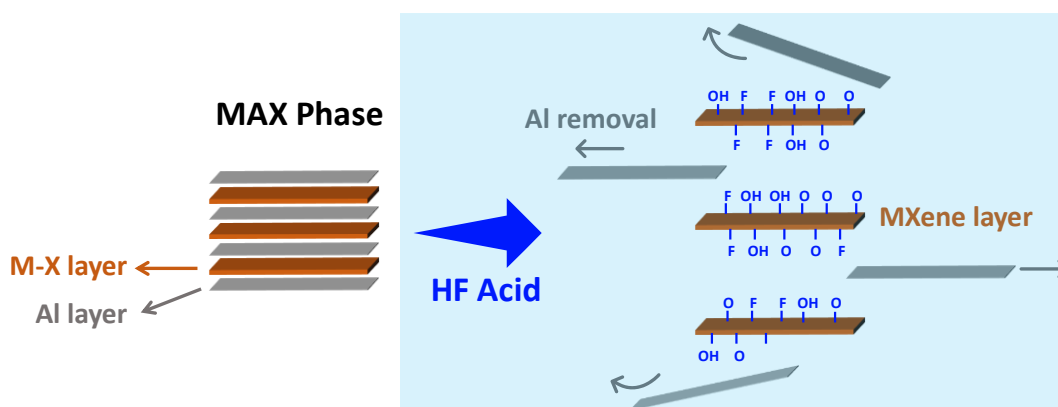


**Figure 19:** Schematic representation of MXene synthesis via acid treatment of a MAX phase in aqueous media and the simultaneous formation of surface terminations.

Furthermore, owing to the -O and -OH bonds, MXenes exhibit hydrophilicity and can be processed into films[177] or inks to print electrodes.[178] MXenes also inherit a number of their properties from their parent MAX phases. Among the most prominent features is their high electrical conductivity, making them suitable as electrodes for electrochemical systems. For $Ti_3C_2T_x$ MXene, for instance, very high values for electrical conductivities of up to 9800 S/cm have been reported.[179] Much of the MXenes properties are dictated by the interlayer spacing, lateral size, and surface terminations,[180] which depend on the MXene synthesis route.[172] **Table 3** lists several $Ti_3C_2T_x$ MXene fabrication routes from its parent MAX phase $Ti_3AlC_2$.

In addition to making MXene surfaces hydrophilic, the -O/-OH surface terminations are also redox-active and contribute toward enhanced charge storage capacities. Surface termination engineering of $Ti_3C_2T_x$ MXene has shown that higher contents of -O functional groups lead to almost a two-fold increase in gravimetric capacitance of $Ti_3C_2T_x$ MXene as supercapacitor electrodes in 1 M $H_2SO_4$ electrolyte.[181] The latter engineering techniques to maximize the ratio of -O to -F functional groups include, among others, etching of the MAX phase with lower HF concentrations,[181] LiF-HCl etching instead of HF etching,[182] and alkalization of the synthesized MXene (treatment with KOH, for instance).[183] In lithium-sulfur batteries, the redox-active hydroxyl surface groups and Ti sites break down the polysulfide species, thereby hindering the parasitic polysulfide shuttling effect,[184] as confirmed by studies on $Ti_2CT_x$,[185] $Ti_3C_2T_x$,[186] and $Ti_3CNT_x$ MXenes.[187]

While the -O/-OH surface terminations are beneficial toward enhanced energy storage capabilities and stability, the -F surface terminations have shown to be detrimental in that regard, as the -F surface terminations block electrolyte ion transport,[188] and make the MXene surface hydrophobic.[189] As such, even though MXenes with fluorine-rich surfaces are not promising electrodes for energy storage, they have shown promise in energy harvesting and energy conversion. Fluorine-rich and hydroxyl-free terminated $Ti_3C_2T_x$ MXene, for instance, has been used as additives in perovskite solar cells with improved performance,[189] in triboelectric generation,[190] or in hydrogen evolution electrocatalysis.[191]

**Table 3**: Summary of different etching methods to convert $Ti_3AlC_2$ MAX into $Ti_3C_2T_x$ MXene.

| Etching Method | Etchant | Conditions | $T_x$ | Ref. |
|---|---|---|---|---|
| Wet chemical etching | HF (50 mass %)<br>HCl (6 M) + LiF<br>HF (10 mass %) + LiCl | 25 °C, 2 h<br>40 °C, 45 h<br>25 °C, 24 h | -OH, -O, -F | [192]<br>[193]<br>[194] |
| Molten salt | $CuCl_2$<br>$ZnCl_2$ | 750 °C, 24 h<br>550 °C, 5 h | $-Cl_2$ | [195]<br>[196] |
| Ionic liquid | $EMIMBF_4$ | 80 °C, 20 h | -O, -OH (after wash) | [197] |
| Halogen etching | $I_2$ (s)<br>$I_2$ (s), $Br_2$ (l), Icl (l), Ibr (s) | 100 °C, 4 d<br>-78-70 °C, 4-8 h | -O, -OH (after wash)<br>-I, -Br | [198]<br>[199] |
| Electrochemical | 2 M aqueous HCl | -0.6 V, 5 d | -Cl, -OH, -O | [200] |
| Alkali etching | 27.5 M NaOH | 270 °C, 12 h | -OH, -O | [201] |

Most of the etching techniques listed in **Table 3** can also be employed to etch MAX phases other than $Ti_3AlC_2$, such as HF etching of $Ti_2AlC$ MAX into $Ti_2CT_x$ MXene,[171] HCl + LiF etching of $V_2AlC$ MAX into $V_2CT_x$ MXene,[202] or molten salt etching of $Nb_2AlC$ MAX into $Nb_2CT_x$ MXene,[203] among many others. The etching conditions must be adjusted for each MAX phase composition to achieve successful conversion due to varying bond strengths between the metal elements and A layers.[204] Within one composition, two slightly different etching routes can result in distinct physicochemical properties of the resulting MXene. The latter is best shown in the $Ti_3AlC_2$ MAX phase when treated with HF etching and HCl + LiF etching routes. Nuclear magnetic resonance studies on the resulting $Ti_3C_2T_x$ MXenes show a majority of F-terminated surfaces in the former route and a majority of O-terminated surfaces in the latter route. XRD analysis also shows a significantly different interlayer spacing between the two synthesis routes, with a c-lattice parameter of 25 Å for the HCl + LiF etched sample compared to that of HF-etched MXene at around 19-20 Å.[182]

Once the MXene is synthesized, it can be readily employed in its multilayered form or can undergo further post-processing techniques to alter its surface chemistry, interlayer spacing, and lateral size of the flakes or to be delaminated.[205] Surface chemistry modifications include minimizing the population of F surface terminations and maximizing O/OH populations since the latter is redox-active and can bring enhancements for battery applications. Such techniques include hydrogen heat treatment,[206] vacuum heat treatment,[207] or alkalization, such as the treatment of MXene with KOH.[183, 208, 209] The alkalization technique simultaneously can increase the interlayer spacing, boosting the capacity/capacitance of the MXene electrodes by enabling more ions to be accommodated within the MXene galleries. It has been shown that an interlayer expansion of KOH-treated MXene from a c-lattice parameter of 19.2 Å to 25.0 Å has resulted in a three-fold increase in the capacitance of MXene supercapacitor compared to the untreated MXene.[183] Other ways to significantly increase the MXene interlayer spacing, apart from KOH treatment ($K^+$ pre-intercalation), include pillaring of MXene with large inorganic atoms. An example is $SiO_2$-pillared $Ti_3C_2T_x$ MXene, which has shown a four-fold increase in the capacity of MXene electrodes for Li-ion batteries.[210]

The lateral size of MXene can also play a key role in the kinetics of the ion intercalation, which is of high importance when it comes to energy storage systems,[211] as well as non-electrochemical systems such as ion-sieving applications of MXenes.[170, 212] The electrolyte ions in the immediate surroundings of an MXene electrode interact with shallow and deep sites along the layers of MXenes.[213] The deep sites of MXene layers with ultra-large lateral sizes are more challenging to reach. As such, the diffusion path lengths will increase, leading to a more sluggish charge storage kinetics.[211] Control over the desired lateral size becomes vital to optimize the electrochemical performance of energy storage devices made of MXene electrodes.

Similar to MXene's surface chemistry outlined earlier, MXene's lateral size is also highly dependent on the synthesis route of MXene from the MAX phase and any post-processing that MXene undergoes afterward. In the case of MXene's lateral size, however, the preceding step, MAX synthesis, also dictates the upper limit of MXene's lateral size. It has been shown that longer sintering times result in MAX phases of significantly larger lateral sizes. Heat treatment of $Ti_3AlC_2$ MAX phase precursors at 1400 °C,[214] instead of commonly 2 h,[215] has resulted in MAX phase flake sizes of up to 75 μm. Since the MXene flakes, once synthesized, cannot be fused to constitute larger flakes, efforts should be made to translate the lateral size of the parent MAX phase into individual MXene sheets. **Figure 20** summarizes the experimental techniques used to control the flake sizes of MXenes. As shown, the MXene sheets maintain the largest lateral sizes by application of mechanical energy with the least intensity, such as gentle manual shaking.
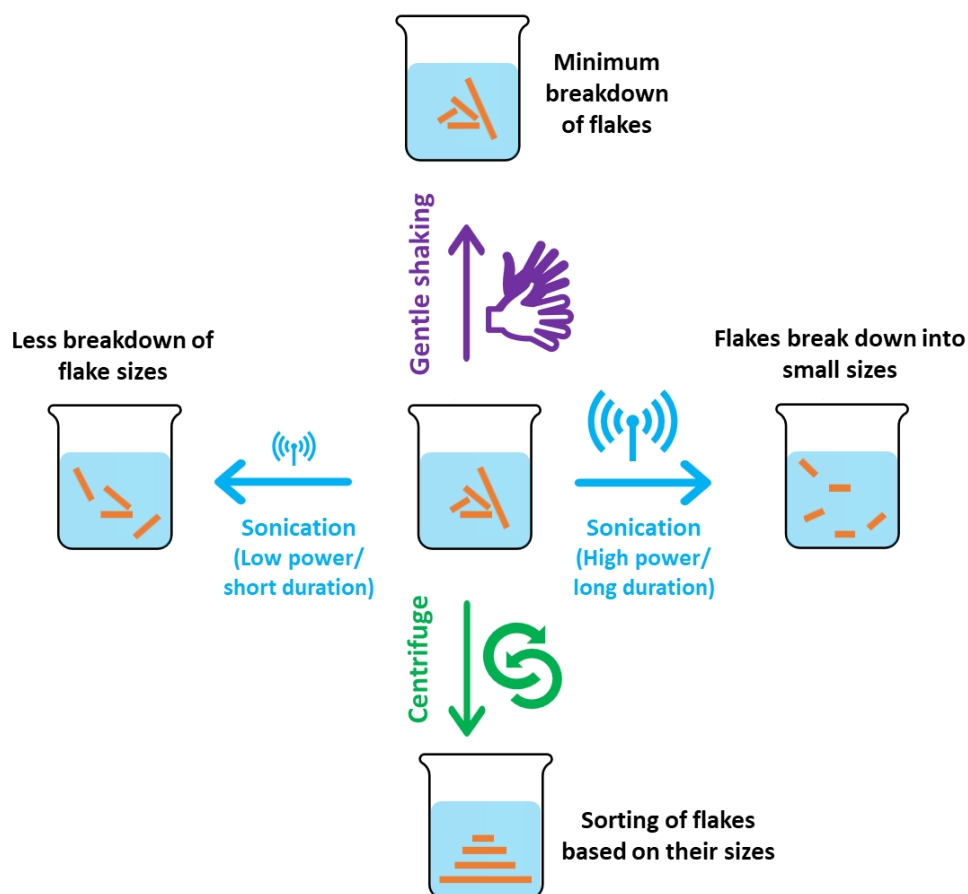
**Figure 20**: Schematic representation of the degree of control over MXene's lateral size by the magnitude of mechanical energy applied after etching with HCl/LiF.

Due to the high tunability of MXene properties, such as its interlayer spacings, lateral sizes, surface chemistry, and generally high electrical conductivity, MXene has become the subject of many electrochemical systems. Electrochemical desalination with MXene electrodes has been the subject of several studies during the past few years.[106, 216-218] MXene was first explored in 2016 as electrodes for electrochemical desalination of NaCl solutions of low molarity.[106] In the latter report, symmetric electrodes made of multilayered $Ti_3C_2T_x$ MXene (HF-etched $Ti_3AlC_2$) were shown to have been effective in stable electrochemical desalination of 5 mM NaCl solutions for over 30 cycles, with an average desalination capacity of 13±2 mg/g.[106] Numerous studies have then employed modification techniques on $Ti_3C_2T_x$ MXene to increase its desalination capacity, such as nitrogen doping,[219] argon plasma treatment,[220] freeze-drying,[108] or delamination.[108]

**Table 4** and **Table 5** list a number of studies that employed MXenes as symmetric and asymmetric electrodes, respectively, for electrochemical desalination, along with their operational parameters and key results.

**Table 4:** Comparison of different MXene electrode types and systems for electrochemical desalination with symmetric MXene/MXene electrodes. N/A: not available.

| Electrode material | Additive (mass%) | BET SSA (m²/g) | DC (mg/g) | NaCl concentration (mM) | Electrolyte flow rate (mL/min) | Cell voltage (V) | Layered status | Membrane | Ref. |
|---|---|---|---|---|---|---|---|---|---|
| $Ti_3C_2T_x$ | - | 6 | 13 | 5 | 22 | 1.2 | Multilayered | - | [106] |
| $Mo_{1.33}CT_x$ | CNT: 10 | 30 | 5/9/15 | 5/50/600 | 15 | 0.8 | Delaminated by TBAOH* | - | [8] |
| Cryo-dried $Ti_3C_2T_x$ | Super P: 10 PVDF: 10 | 293 | 45 | 171 | 40 | 1.2 | Delaminated by chloroform | - | [108] |
| LiF/HCL-etched $Ti_3C_2T_x$ | - | 2 | 68 | 10 | 20 | 1.2 | Delaminated by LiF/HCl | - | [221] |
| N-doped $Ti_3C_2T_x$ | Super P: 10 PVDF: 10 | 369 | 44 | 86 | 30 | 1.2 | Delaminated by chloroform | - | [219] |
| Pre-conditioned $Ti_3C_2T_x$ | OLC**: 10 PTFE: 5 | N/A | 9.2 (max) | 10 | 5-20 | 1.2 | Multilayered | AEM + CEM*** | [222] |

*TBAOH: tetrabutylammonium hydroxide

**OLC: onion-like carbon

***AEM: anion exchange membrane, CEM: cation exchange membrane.

**Table 5:** Comparison of different MXene electrode types and systems for electrochemical desalination with asymmetric electrodes with MXene as cathode (negative electrode). N/A: not available.

| Cathode (negative electrode) | Additives for cathode (mass %) | Anode (positive electrode) | Additives for anode (mass %) | BET SSA of cathode (m²/g) | DC (mg/g) | CE (%) | NaCl concen-tration (mM) | Electrolyte flow rate (mL/min) | Cell voltage (V) | Layered status | Membrane | Ref. |
|---|---|---|---|---|---|---|---|---|---|---|---|---|
| $Ti_3C_2T_x$ | - | Activated carbon | Acetylene black: 10 PVDF: 10 | N/A | 72 | N/A | 5 | 50 | 1.6 | Delaminated by LiF/HCl + DMSO* | AEM + CEM | [223] |
| $Ti_3C_2T_x$ | CNT: 10 | Activated carbon | PTFE: 5 | 7 | 12/8 | 85 | 20/600 | 2 | 0.9 (0.3-1.2) | Multilayered | w & w/o AEM | [117] |
| NaOH-intercalated $Ti_3C_2T_x$ | Super P: 10 PVDF: 10 | Activated carbon | Super P: 10 PVDF: 10 | N/A | 12/16 | 83/77 | 2/9 | 25 | 1.2 | Multilayered | - | [224] |
| NaOH-intercalated $Ti_3C_2T_x$ | PTFE: 5 | Activated carbon | N/A | 49 | 16 | 80 | 2 | N/A | 1.2 | Delaminated by LiF/HCl + freeze-dried | - | [217] |
| NaOH-intercalated $Ti_3C_2T_x$ | Carbon black: 10 PTFE: 5 | Activated carbon | N/A | N/A | 15 | 81 | 2 | 10 | 1.2 | Multilayered | - | [218] |

* DMSO: dimethyl sulfoxide

As observed in the latter tables, $Ti_3C_2T_x$ MXene in its multilayered form has shown a desalination capacity of around 10-15 mg/g across a wide range of electrolyte concentrations tested,[216, 222] while the delaminated MXene can boost the desalination capacity up to around 70 mg/g. This is most probably because the delamination minimizes that portion of layers inaccessible to the electrolyte in the multilayered form and maximizes their exposure to the salt ions to interact with them. Delaminated MXene sheets have also shown promise to be used as flowing electrode cells for removing and recovering elements from water.[225] Other efforts have revolved around the hybridization of MXene with heterostructures that can facilitate better ion transport through its interlayers, enhance conductivity, and prevent oxidation, such as MXene-polydopamine[226] or organic framework-bound MXene,[227] MXene/metal oxides[228-230] or MXene/Prussian Blue analogue[231] composites.

### 2.3.2. MBene for energy storage

The discovery of MXenes in 2011 has spurred extensive research in two-dimensional (2D) materials beyond graphene.[232, 233] Among these materials are MBenes, or transition metal borides (such as MoB), which bear structural similarities to MXenes but differ in stoichiometry and layer arrangement.[234] While the synthesis of non-2D metal borides has been documented for several decades,[235, 236] it was only in 2021 that a top-down synthesis approach for producing 2D metal borides (MBenes or Boridenes) from their parent MAB phases was first reported.[237]. In the typical MAB phase, similar to a MAX phase, early transition metal atoms (M) form bonded layers with boron atoms (B), which are periodically interleaved by mono- or bi-layers of aluminum (A). The M-A bonds display metallic properties, while the M-B bonds possess a mixed metallic/ionic/covalent character, enabling aluminum etching: MAB, $M_2AB_2$, $M_2A_2B_2$, $M_3AB_4$, and $M_4AlB_6$.[234, 238] However, only a limited number of MAB phases have been (partially) etched to form MBenes thus far.[239, 240]

Like in the case of MAX phase synthesis, MAB phases are typically fabricated through high-temperature sintering of the precursors, as illustrated in **Figure 21** for the synthesis of MoAlB as a model MAB phase. One of the advantages of MBenes over MXenes is the less harsh etching conditions required for their fabrication. Dilute HCl has been proven efficient in a near-complete Al removal from $Cr_2AlB_2$ MAB,[241, 242] whereas highly toxic HF acid is a common etchant for MAX phases.[243] NaOH has also been reported as an etchant to partially remove aluminum from various Mo-Al-B MAB phases.[244-246] In contrast to MAX phases, where complete removal of the aluminum layer sandwiched between M-X octahedral blocks is commonly achieved, etching of MAB phases can leave cavities and stacking faults in its structure,[239, 245] as shown schematically in **Figure 22**.
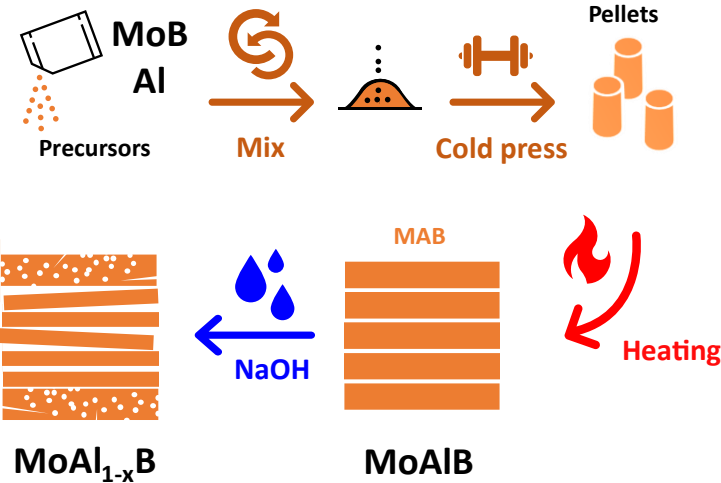


**Figure 21:** Step-by-step representation of MoAlB synthesis procedure and subsequent NaOH etching.
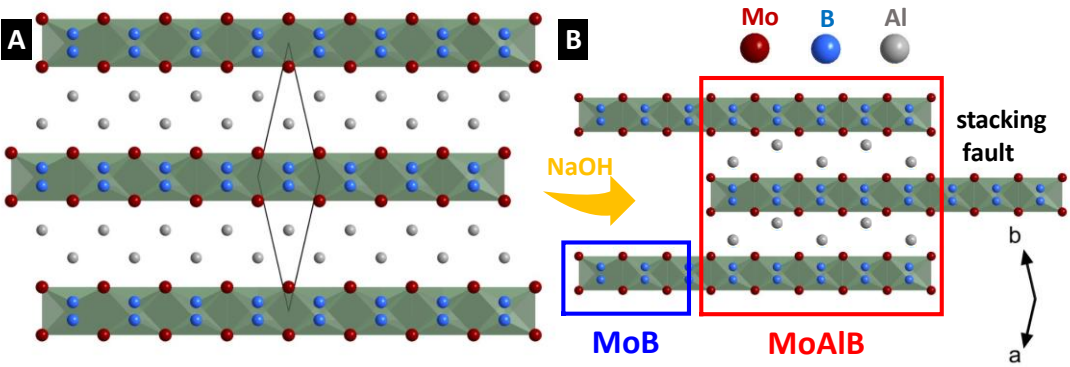


**Figure 22:** (A) Schematic representation of MoAlB (MAB phase) crystal structure and (B) its interaction with NaOH, resulting in a structure with cavities and stacking faults of co-existing Al-deficient MAB species (MoAl1-xB) and MAB phase.

**Figure 23A** shows the scanning electron microscopy images of the as-synthesized MoAlB MAB phase with tightly stacked layers, reminiscent of MAX phases.[247] We have then treated the MoAlB MAB phase with aqueous NaOH solutions (10 mass %) for one day at room temperature. As shown by the NaOH-1d sample in **Figure 23B**, the tightly packed layers of MoAlB exfoliate while forming cavities. We performed energy-dispersive X-ray (EDX) analysis (**Table 6**) on the MoAlB parent material and the derived NaOH-treated materials. EDX shows a clear decreasing trend in aluminum content from 1 day to 4 days of NaOH treatment. The aluminum is only partially removed, suggesting that some of the aluminum double layers in the parent material are deintercalated to become single layers.[248] The stoichiometry of the resulting structures can thus be written as $MoAl_{1-x}B$, where x could be 0.1, 0.2, and 0.3 for samples treated for 1 d, 2 d, and 4 d, respectively, according to the findings in **Table 6**.



**Figure 23:** Scanning electron micrographs of (A) pristine MoAlB MAB, and after etching with NaOH for (B) 1 day and (C) 2 days.

**Table 6:** Elemental composition of pristine and NaOH-treated MAB samples.

| (at %) | Al | Mo | O | F |
|---|---|---|---|---|
| MAB | 46±4 | 46±4 | 8±6 | - |
| NaOH-1d | 40±3 | 44±3 | 16±5 | - |
| NaOH-2d | 34±4 | 44±5 | 19±4 | <3 |
| NaOH-4d | 31±5 | 43±7 | 25±12 | - |

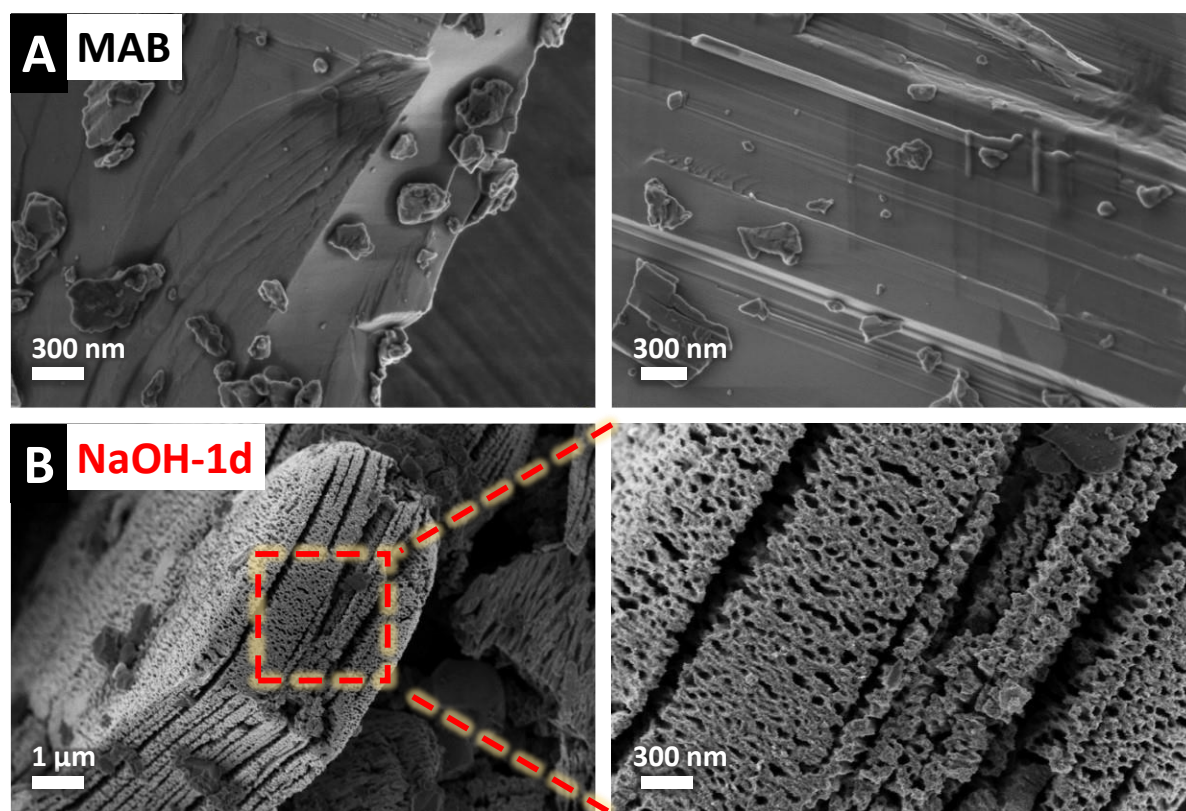Although the MoAlB MAB phase shows negligible ion storage properties[238] due to their minimal population of ion intercalation sites, the cavity-rich morphology of the derived MBene species could give rise to an ion-accessible electrode, potentially enhancing charge storage performances.[249] We have evidenced the latter by performing half-cell cyclic voltammetry measurements with electrodes made of the MAB phase and its 1-day and 2-day NaOH-treated derivatives. As observed in **Figure 24**, there is a mild increase in the capacitance going from untreated MAB phase to its 1-day-treated derivative to its 2-day-treated derivative.
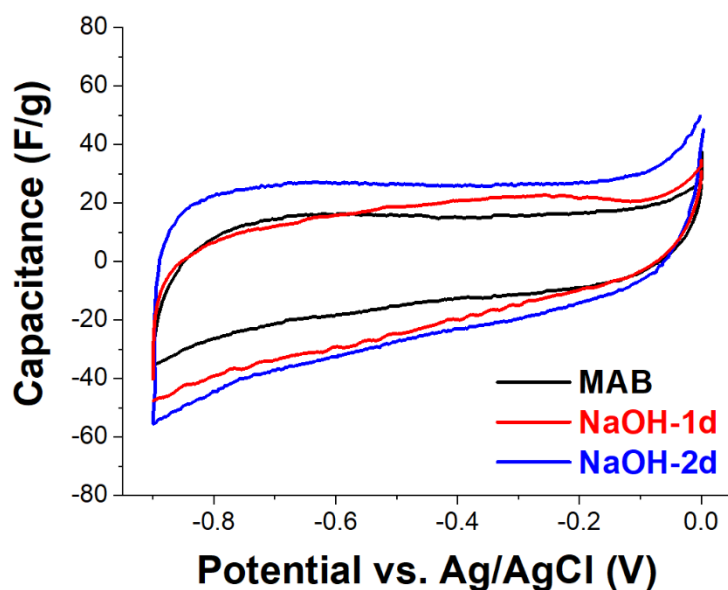


**Figure 24:** Effect of longer etching durations on electrochemical stability window and pristine MAB phase capacitance after NaOH treatment for 1 day and 2 days. All measurements used 1 M aqueous NaCl solution as an electrolyte at 1 mV/s scan rate.

### 2.3.3. TMD for energy conversion

As outlined before, the water-energy nexus consists of an ecosystem of water desalination technologies hand in hand with energy generation, conversion, and storage systems (**Figure 1**). However, energy generation systems such as wind or solar energy sources have an intermittent nature, which is often asynchronous with the energy demands of human activities during the day and night.[250] Consequently, converting the generated energy and its sustainable storage becomes imperative to buffer the mismatch between energy supply and demand.[251]

Until this date, the most common hydrogen production method is via steam reforming of hydrocarbons in the oil and gas industry.[252, 253] Electrochemical production of hydrogen gas could be a promising route to convert and store excess electrical energy as chemical energy.[254] In such a method, an electric potential is applied to an electrochemical cell of two electrodes immersed in an aqueous electrolyte. The electronic charge passed through the external circuit will transfer from the electrode surface to the electrolyte ions, such as protons in the electrolyte, reducing them into hydrogen gas at the negative electrode (cathode). Similarly, water molecules adjacent to the positive electrode (anode) give up their electrons, evolving oxygen gas and the generation of protons used by the negative electrode.[255] **Figure 25** shows an electrochemical cell that works with such mechanisms (an electrolyzer cell) and the electrodes in such a cell (electrocatalysts).



**Figure 25:** Schematic illustration of an electrolyzer cell's hydrogen and oxygen evolution reactions, adapted with permission from Ref.[233]
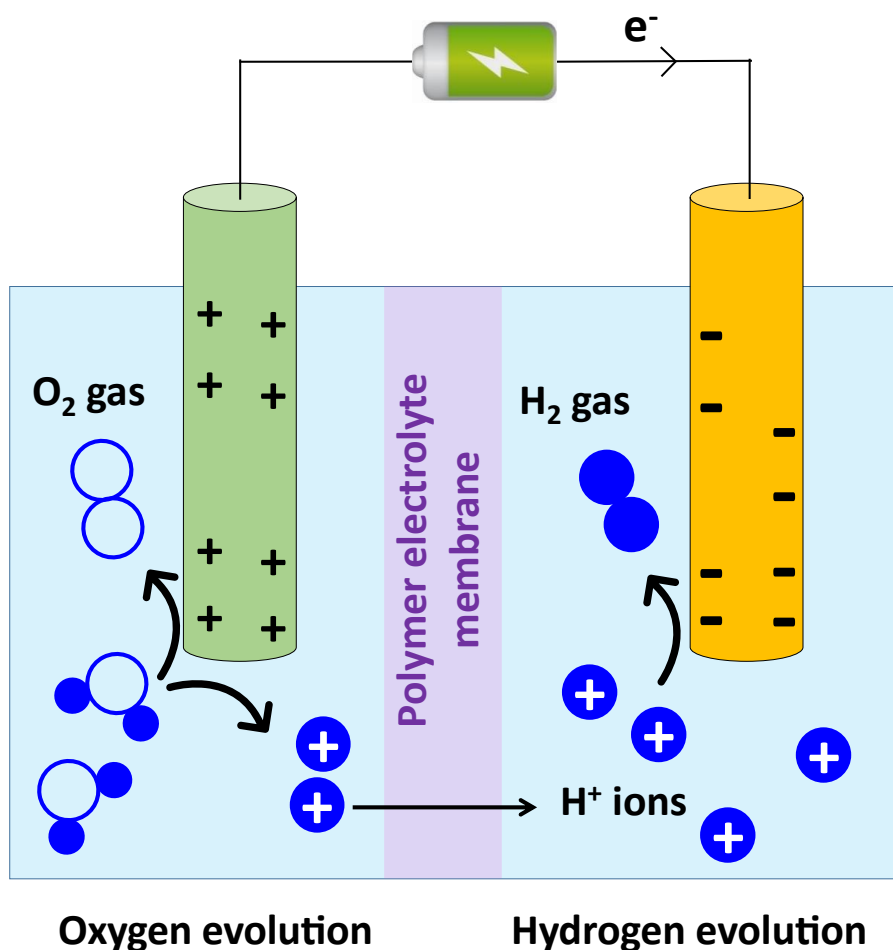
In pursuit of earth-abundant and non-precious materials suitable for electrocatalysis, MXenes[256-261] and transition metal dichalcogenides (TMDs)[262, 263] have shown promise for both hydrogen evolution reaction (HER) and oxygen evolution reaction (OER). What makes MXenes a good candidate for HER are, among others, their high electrical conductivity, their hydrophilic nature, and the tunability of their catalytically active surface groups at their basal planes.[264, 265] For instance, tuning the surface chemistry (that is, $T_x$) of $Ti_3C_2T_x$, $Ti_2CT_x$, $Mo_2CT_x$ MXenes, has shown that electrocatalytic activities significantly improve by minimizing fluorine groups and maximizing oxygen groups.[264] Delamination of $Mo_2CT_x$ MXene has been shown to further increase its electrocatalytic activity by exposing a more significant proportion of its basal planes to the electrolyte ions.[266]

TMDs, like MXenes, also offer rich chemistry and high structural and electronic tunability for electrocatalytic applications. In a pioneering work in 2005,[267] $MoS_2$ was theoretically studied, and it was found that hydrogen atoms can bind to $MoS_2$ with energy barriers close to platinum. Since then, numerous have studied the latter material and other TMDs, in an attempt to boost their electrocatalytic performances. Defect engineering of $MoS_2$, for instance, has shown that a high level of sulfur vacancies increased the HER activity.[268, 269] There are, in general, two kinds of surface sites on TMD sheets: the unsaturated edge sites of the sheets, which are active, and the inactive terrace sites at the basal planes.[270-272] As such, nano-structuring of TMDs so that the maximum number of edge sites of TMD sheets are exposed has shown to be very effective in boosting electrocatalytic activities.[271, 273]

Moreover, while TMDs offer outstanding versatility in their chemistry and attractive electrocatalytic activities that make them a promising candidate for energy conversion applications, they commonly suffer from poor electrical conductivities (both in bulk and exfoliated forms) for use as electrodes. For example, $MoS_2$ shows an in-plane conductivity of as low as 0.2 S/cm in its 2H phase (trigonal prismatic, semiconducting) and 10-100 S/cm in its 1T phase (octahedral, metallic).[274] Therefore, to approach their maximum performances, bulk (3D) TMDs are commonly exfoliated into their 2D nanosheets and/or integrated into a carbon network, such as graphene[275, 276] or CNTs.[277, 278] Hence, TMDs' performance could be boosted by their intimate mixing with a highly conductive backbone that can provide efficient charge transfer and expose the maximum number of TMDs active sites. MXenes as highly conductive 2D materials (up to $24 \cdot 10^3$ S/cm in the case of $Ti_3C_2T_x$[279]) can fulfill the latter criteria.

Hydrothermal synthesis of TMDs onto MXenes[187, 280, 281], vacuum-assisted co-filtration of TMDs and MXene dispersions[282, 283], and vapor deposition of MXene on TMD[284] are among various techniques recently employed to fabricate MXene/TMD composites. Each hybridization method has different complexity and labor intensity, resulting in specific morphologies.[285, 286] One-step synthesis methods often offer more simplicity and a higher potential for industrial-scale manufacturing. The one-step sacrificial conversion of MXene into TMD via in-situ thermal sulfidation is a facile hybridization method that requires no TMD precursors (unlike hydrothermal and vapor deposition methods), and results in a morphology that is highly accessible to electrolytes and allows for fast charge transfer.[287-289]

In this method, MXene is sacrificially transformed into its respective TMD under a flow of $H_2S$ gas or through sulfur sublimation (**Figure 26**). The degree of MXene-to-TMD conversion depends on the treatment temperature and duration. Hybrid MXene/TMD heterostructures of $Mo_2TiC_2T_x$/$MoS_2$,[290] $Mo_2CT_x$/$MoS_2$,[291] and $Ti_3C_2T_x$/$TiS_2$[287, 288] have been produced via the MXene sulfidation technique. These MXene-derived TMDs are distributed in the matrix of parent MXene, resulting in intimate contact between the two phases and providing strong adhesion and a nanohybrid interface.[291]
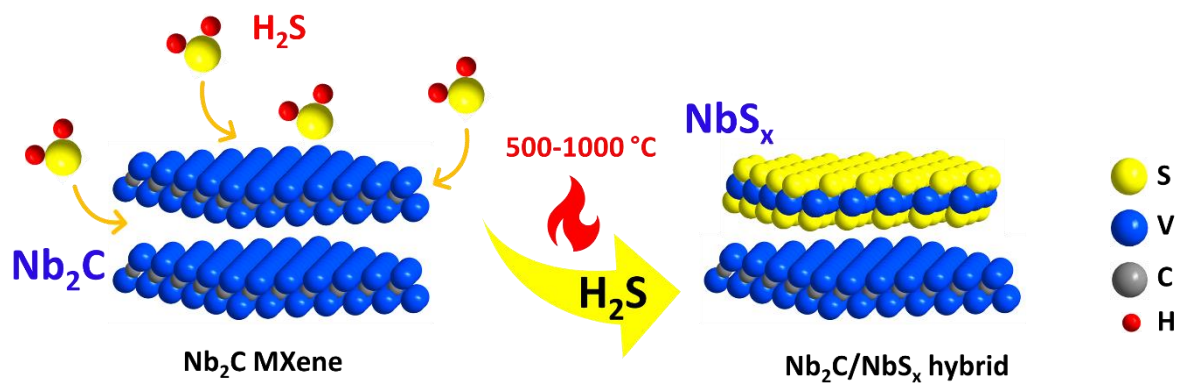


**Figure 26:** Direct sacrificial conversion of $Nb_2C$ MXene into niobium sulfide upon heat treatment of MXene under $H_2S$ gas.

### 2.3.4. High-entropy 2D materials

High-entropy materials are a specific category comprised of multiple principal elements in roughly equal atomic percentages, in contrast to conventional alloys with only one or two principal elements. Even though the definition of a high-entropy has been the subject of controversy,[292] two main definitions are commonly used: (I) when an alloy consists of at least five major metal elements, with each having an atomic content in the range of 5-35 %; (II) when an alloy possesses a configurational entropy greater than 1.5R (the latter border line was previously set as 0.69R and 1.61R[293]). Definition (II) can be expressed as **Eq. (11)** [294, 295]:

$$\Delta S_{config} = -R \sum_i x_i \, lnx_i \qquad \text{(Eq. 11)}$$

where R is the ideal gas constant, and $x_i$ is the mole fraction of the $i^{th}$ metallic component. Examples include multi-principal-element high-entropy $M_4C_3T_x$ MXenes such as $TiVNbMoC_3T_x$ and $TiVCrMoC_3T_x$ that have been fabricated by high-temperature sintering of their mixed metal elemental precursors,[296] as opposed to the conventual heat treatment of single transition metal element. **Figure 27** schematically shows a spectrum where a regular low-entropy 2D material can be turned into multi-principal 2D material with medium or high configurational entropy by introducing more atomic species to its structure.



**Figure 27:** Schematic illustration of 2D materials with low to high configurational entropies, adapted with permission from Ref.[233]

The intricate composition of high-entropy materials brings about distinct properties and characteristics that set them apart from traditional materials.[297] High-entropy materials have emerged as a relatively new field and thus offer new possibilities for research in various applicatio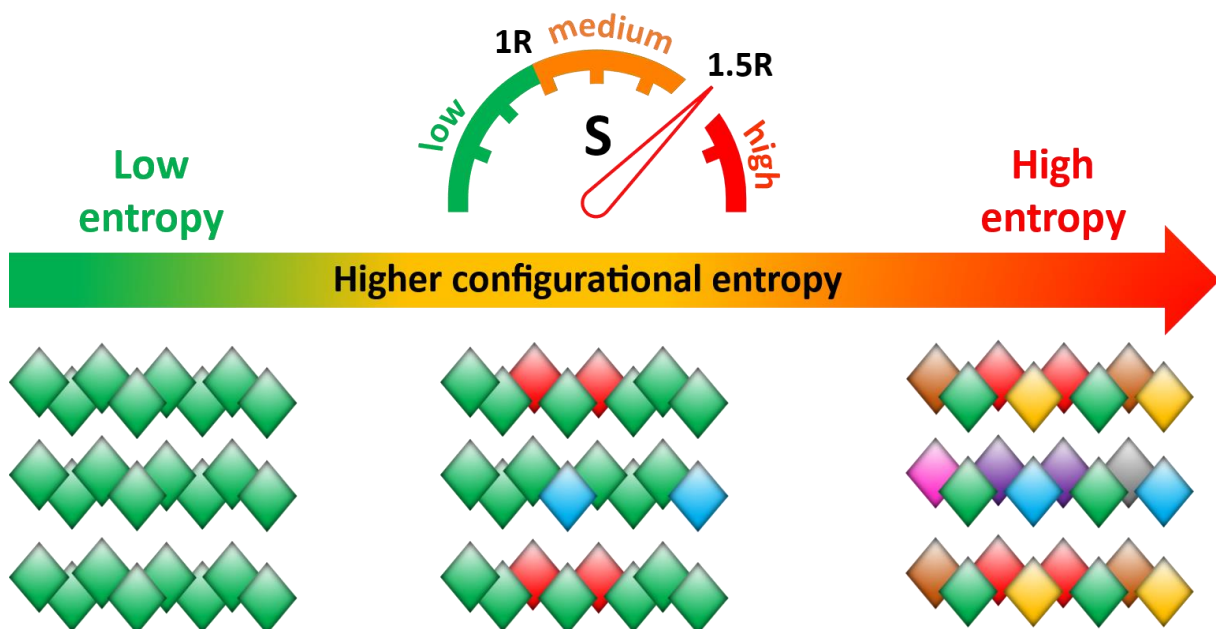ns.[298] Specifically, a key property enhancement lies within energy conversion,[299-302] where high-entropy 2D materials potentially exhibit clear advantages over traditional 2D materials.

A successful electrocatalyst for breaking water into hydrogen gas is a material that possesses, among others, the most exposed active sites for the HER reaction to take place.[303-305] Through the high-entropy strategy, the HER activity of a metal phosphorus trichalcogenides such as $CoPS_3$ is tuned by optimizing the sulfur sites on the edges and phosphorus sites on the basal planes of its high-entropy counterpart, that is, $Co_{0.6}(VMnNiZn)_{0.4}PS_3$.[306] As a result, $Co_{0.6}(VMnNiZn)_{0.4}PS_3$ was found to exhibit over 15 times enhanced catalytic activity for the HER compared to $CoPS_3$, with overpotential values decreased from around 200 mV for the latter to 66 mV for the former (at a current density of 10 mA/cm$^2$). Besides increasing its catalytically active sites, the diversification of metal sites on a 2D material also facilitates the kinetics of adsorption-desorption of reaction intermediates formed during electrocatalysis. Similar enhancements have been reported for the high-entropy 2D transition metal dichalcogenide $MoWVNbTaS_2$, for electrocatalytic $CO_2$ capture and its conversion into CO.[307] It has been shown that when a $CO_2$ molecule approaches the surface, it strongly binds to the transition metal, forming COOH* and CO* reaction intermediates. The presence of neighboring diverse metal atoms in the high-entropy material reduces the energy barrier for desorption, facilitating the breakage of the CO bond.

The high-entropy strategy can also be beneficial for energy storage systems, whether in the choice of electrode materials[308, 309] or electrolyte compositions.[310-312] Since an energy storage system's gravimetric charge storage capacity is often a highly sought-after performance metric, diversifying principal elements in the electrode by incorporating heavy metal atoms might result in negligible or even adverse effects in the latter metric. That was observed when the high-entropy $Ti_{1.1}V_{0.7}Cr_xNb_{1.0}Ta_{0.6}C_3T_x$ MXene was employed as a lithium-ion battery anode with a first-cycle capacity of only 126 mAh/g (at 0.01 A/g) whereas that has been 410 mAh/g for regular low-entropy $Ti_3C_2T_x$ MXene (at a rate of 1C),[313] though the high-entropy MXene showed improved cycle stability.[314]

As such, a promising design of a high-entropy energy storage system would be to capitalize on the conversion reactions of such a 2D material since the charge storage capacity contribution from the intercalation of such materials could be limited.[315] For instance, a high-entropy MXene could effectively utilize the high theoretical capacity of multistep sulfur conversion processes for improved energy storage (1672 mAh/g for sulfur).[316] This led to higher capacities of around 900 mAh/g (at a rate of 1C) and an improved rate capability of 702 mAh/g (at a rate of 4C), along with promising cycling stability for $(Ti_{1/3}V_{1/6}Zr_{1/6}Nb_{1/6}Ta_{1/6})_2C_xN_{1-x}$ MXene.[317]

## 3. Approach and Overview

The research section of this thesis consists of 6 chapters that explore advanced materials for addressing challenges in the water-energy nexus, as summarized in **Figure 28**.

In **Chapter 1**, we explore the best practices for generating and analyzing data in the field of electrochemical water desalination. The chapter focuses on the experimental setup, data processing, and calculations of relevant metrics employed in a typical electrochemical desalination study. Here, we discuss the challenges associated with data interpretation and provide recommendations for accurate and reliable data generation and analysis in this field.

**Chapter 2** then explores the field of electrochemical water desalination using MXene/activated carbon hybrids. We begin by introducing the unique properties of MXene and activated carbon, highlighting the merit of MXene as a 2D nanolamellar material capable of desalination at seawater-level saline solutions without using any ion-exchange membranes. We show that the latter 'forced permselectivity' of an asymmetric MXene/activated carbon cell contrasts sharply with a symmetric activated carbon/activated carbon cell where virtually no ion removal is accomplished in saline media of such high molar strengths. We further investigate the stability of MXene electrodes up to 100 cycles of operation and show how performance decay over time is linked to the MXene electrode degradation, that is, titanium oxide formation on titanium carbide layers.

**Chapter 3** focuses on the time-dependent cation selectivity of titanium carbide MXene in an aqueous solution of several alkaline and alkaline earth cations and explores the underlying mechanisms behind the observed selectivity changes throughout long-term desalination. Online monitoring of desalination data via plasma spectroscopy and in-situ X-ray characterization is presented to support our analysis. We also discuss the implications of time-dependent cation selectivity for various applications, such as water softening or separation of value-added elements such as lithium.

**Chapter 4** investigates the synthesis and characterization of layered nano-mosaic structures of niobium sulfide heterostructures by direct sulfidation of niobium carbide MXenes, and their potential application as electrocatalysts for hydrogen evolution reaction. This chapter focuses on the facile fabrication process of sacrificial conversion of MXene into transition metal dichalcogenides and the degree of control over the said conversion degree by adjustment of heat treatment temperature and durations. We then show how the sulfidation of two MXene types with similar atomic compositions but different slab thicknesses, namely $Nb_2CT_x$ and $Nb_4C_3T_x$, can result in heterostructures with significantly different morphologies. We investigate the electrocatalytic properties of those niobium MXene-niobium sulfide heterostructures for hydrogen evolution reactions and discuss the potential for their utilization in sustainable energy conversion systems.

**Chapter 5** discusses the development of layered molybdenum borides (MoAlB and $Mo_2AlB_2$), which are structurally similar to MXenes, as potential battery electrode materials, specifically targeting Li-ion and Na-ion batteries. Here, it is highlighted that the environmental-friendliness of sodium hydroxide as the etchant to fabricate layered borides, as opposed to HF, which is the highly toxic etchant to fabricate MXenes. After delving into the structural characterization of layered molybdenum borides, their performance testing as Li-ion and Na-ion battery electrode materials shows their promise for sustainable energy storage applications.

**Chapter 6** explores the emerging field of functional two-dimensional high-entropy materials. We begin by introducing the concept of high-entropy materials, the tunability of such materials, and the added value brought by the high-entropy strategy. The chapter focuses on these materials' functional properties and potential applications in various fields, such as energy storage and conversion. This section provides the prospects and challenges in this rapidly evolving research area.

**Water**

**1**
**Electrochemical water desalination data analysis**
- Establishing the best practice
- Calculation of desalination metrics

κ, T
pH

**2**
**Electrochemical water desalination with MXene**
- Asymmetric MXene/carbon cell
- Stable membrane-less desalination of seawater

MXene Layers
Porous carbon

**3**
**Time-dependent ion selectivity with MXene**
- Mixed electrolyte of alkali and alkali metal ions
- Effect of charge density and hydration energy barrier

**4**
**MXene-sulfide heterostructures for energy conversion**
- Sacrificial conversion of MXenes into transition metal sulfides
- Electrocatalytic hydrogen evolution

$H_2S$

**5**
**2D metal borides for energy storage**
- Partial NaOH etching of MAB phase
- Anodes for Na-ion and Li-ion battery

MoB
Al

**6**
**2D high-entropy materials for energy storage and conversion**
- Tunability of 2D high-entropy materials
- Functional properties

*Entropy*

**Energy**

**Figure 28:** An outline of the following 6 chapters with results and discussions around advanced materials for addressing challenges in the water-energy nexus, adapted with permission from Refs.[82, 117, 233]

# 4. Results and Discussion

## 4.1. Best practice for electrochemical water desalination data generation and analysis

*Mohammad Torkamanzadeh,[1,2] Cansu Kök,[1,2] Peter Rolf Burger,[1,2] Panyu Ren,[1,2] Yuan Zhang,[1,3] Juhan Lee,[1,4] Choonsoo Kim,[5] and Volker Presser[1,2,6,*]*

[1]  *INM - Leibniz Institute for New Materials, D2 2, 66123, Saarbrücken, Germany*

[2]  *Department of Materials Science & Engineering, Saarland University, Campus D2 2, 66123, Saarbrücken, Germany*

[3]  *Department of Materials Science and Engineering and A.J. Drexel Nanotechnology Institute, Drexel University, Philadelphia, Pennsylvania 19104, USA*

[4]  *Heraeus Battery Technology GmbH, Reinhard-Heraeus-Ring 23, 63801 Kleinostheim, Germany*

[5]  *Department of Environmental Engineering with Institute of Energy/Environment Convergence Technologies and Department of Future Convergence Engineering, Kongju National University, 1223-24, Cheonan-daero, Cheonan-si 31080, Republic of Korea*

[6]  *Saarene, Saarland Center for Energy Materials and Sustainability, Campus C4 2, 66123 Saarbrücken, Germany*

\*      Corresponding author

Own contributions:

Investigation, Conceptualization, Data curation, Visualization, Supervision, Writing - Original Draft, Writing - Review & Editing.

**Article**

# Best practice for electrochemical water desalination data generation and analysis



Electrochemical desalination shows promise for ion-selective, energy-efficient water desalination. Torkamanzadeh et al. provide a step-by-step guide on acquiring, processing, and calculating raw desalination data, emphasizing informative and reliable figures of merit.

Mohammad Torkamanzadeh, Cansu Kök, Peter Rolf Burger, ..., Juhan Lee, Choonsoo Kim, Volker Presser

volker.presser@leibniz-inm.de

**Highlights**

Detailed guide for acquiring and processing desalination data

Thorough demonstration for calculating critical desalination metrics

Insight on avoiding inaccuracies from leakage current and probe aging

Checklist and spreadsheet tools for enhanced test planning and accuracy

## Cell Reports
## Physical Science

✌ CellPress
OPEN ACCESS

### Article

# Best practice for electrochemical water desalination data generation and analysis

Mohammad Torkamanzadeh,[1,2] Cansu Kök,[1,2] Peter Rolf Burger,[1,2] Panyu Ren,[1,2] Yuan Zhang,[1,3] Juhan Lee,[1,4] Choonsoo Kim,[5] and Volker Presser[1,2,6,7,*]

### SUMMARY

**Electrochemical desalination shows promise for ion-selective, energy-efficient water desalination. This work reviews performance metrics commonly used for electrochemical desalination. We provide a step-by-step guide on acquiring, processing, and calculating raw desalination data, emphasizing informative and reliable figures of merit. A typical experiment uses calibrated conductivity probes to relate measured conductivity to concentration. Using a standard electrochemical desalination cell with activated carbon electrodes, we demonstrate the calculation of desalination capacity, charge efficiency, energy consumption, and ion selectivity metrics. We address potential pitfalls in performance metric calculations, including leakage current (charge) considerations and aging of conductivity probes, which can lead to inaccurate results. The relationships between pH, temperature, and conductivity are explored, highlighting their influence on final concentrations. Finally, we provide a checklist for calculating performance metrics and planning electrochemical desalination tests to ensure accuracy and reliability. Additionally, we offer simplified spreadsheet tools to aid data processing, system design, estimations, and upscaling.**

### INTRODUCTION

Electrochemical water desalination is a promising technology that removes the salt ions from aqueous saline media by applying electrical potential as the driving force. Electrodialysis and capacitive deionization are two powerful electrochemical desalination techniques that have the potential toward ion-selective,[1,2] low-energy-consuming,[3] high water recovery,[4] and economical[5] water remediation. In filtration processes such as reverse osmosis, by contrast, pressure serves as the driving force for ion migration; in thermal processes such as distillation processes, heat is the driving force that draws the water molecules out of a saline stream. In contrast, the fundamentally different driving force in electrothermal water desalination is the electrical field that draws the salt molecules out of a saline stream. As such, what makes electrochemical water desalination particularly interesting, among other factors, is that its energy consumption strongly depends on the initial salt concentration of the feed water, unlike other conventional thermal- or pressure-driven processes.[6,7] Comprehensive techno-economic analysis indicates that for a threshold between 3,000 and 30,000 ppm NaCl concentration levels in feedwater, a crossover point occurs for electrochemical water desalination and reverse osmosis. That is, electrochemical water desalination technologies below the mentioned threshold have become increasingly more economically attractive than reverse osmosis.[7]

[1]INM - Leibniz Institute for New Materials, D2 2, 66123 Saarbrücken, Germany

[2]Department of Materials Science & Engineering, Saarland University, Campus D2 2, 66123 Saarbrücken, Germany

[3]Department of Materials Science and Engineering and A.J. Drexel Nanotechnology Institute, Drexel University, Philadelphia, PA 19104, USA

[4]Heraeus Battery Technology GmbH, Reinhard-Heraeus-Ring 23, 63801 Kleinostheim, Germany

[5]Department of Environmental Engineering with Institute of Energy/Environment Convergence Technologies and Department of Future Convergence Engineering, Kongju National University, 1223-24 Cheonan-daero, Cheonan-si 31080, Republic of Korea

[6]Saarene, Saarland Center for Energy Materials and Sustainability, Campus C4 2, 66123 Saarbrücken, Germany
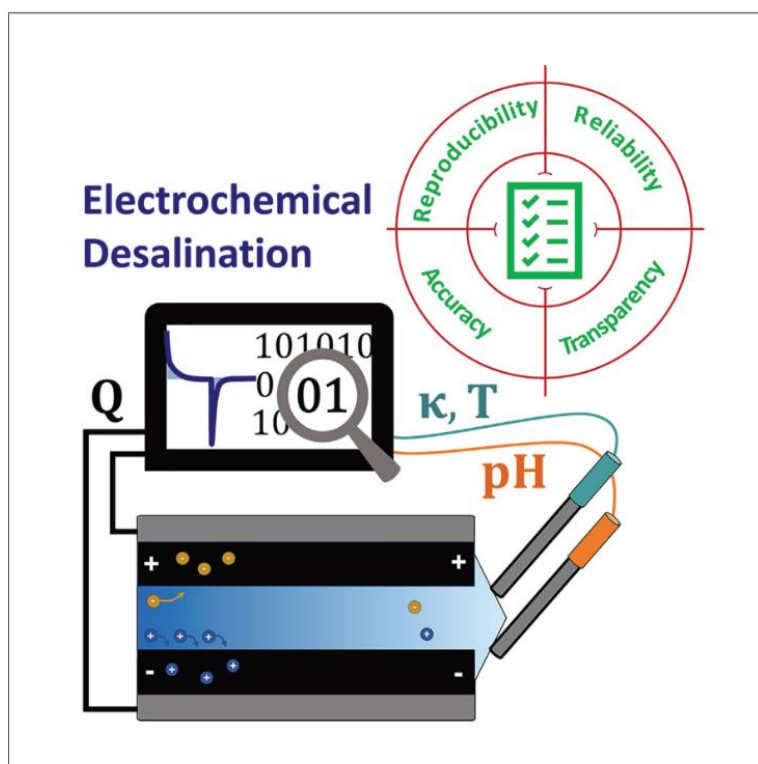
[7]Lead contact

*Correspondence: volker.presser@leibniz-inm.de

https://doi.org/10.1016/j.xcrp.2023.101661

**CellPress**
OPEN ACCESS

**Cell Reports**
**Physical Science**
Article

The energy and cost efficiency,[8] along with many other attractive unique capabilities, such as partially recovering the invested energy[9] or selective separation of ions,[2,10,11] have made electrochemical desalination the subject of numerous studies during the past two decades.[12–15] The key to making those studies reliable, comparable, and reproducible are clear guidelines on how electrochemical desalination data are acquired, processed, and reported. Yet such best-practice studies are limited in the literature, which could limit the rapid advancement of electrochemical desalination technology.

In a typical electrochemical desalination cell, a voltage is applied to a pair of electrodes, and an aqueous saline medium, commonly NaCl, is the electrolyte that continuously flows in and out of the cell. As such, an electrochemical desalination cell could be considered a supercapacitor/battery, only different in that the electrolyte flows through an electrochemical desalination cell. In contrast, it is stagnant in regular supercapacitors/batteries. The standard and probably simplest form of an electrochemical desalination cell is where the water stream passes between and tangentially to the two electrodes, known as the flow-by configuration (Figure S1). Upon polarization of carbon electrodes by applying a charging or discharging voltage, the system's response is commonly recorded in the form of the following key variables: (1) the amount of electric charge stored in the electrodes and (2) the change in the conductivity of the outflowing water. Depending on the available infrastructure, one might record additional variables, such as pH and temperature of outflowing water.

In the present study, we first deal with the conversion of the measured conductivity and pH data into actual salt concentration. We then establish the design of a typical electrochemical water desalination setup consisting of an electrochemical desalination cell with a pair of symmetric activated carbon electrodes in its core and conductivity and pH probes placed downstream of the cell. We show how the obtained conductivity and pH data can be related to the concentration and how the latter concentration obtained is further processed into commonly reported desalination performance metrics in the literature,[16] namely, desalination capacity, charge efficiency, and energy consumption. With the aid of an online elemental monitoring apparatus, we also investigate electrochemical desalination with a mixed-salt electrolyte and show how the preferential removal of specific ions could be quantified and reported in terms of selectivity metrics.

We then systematically investigate the effects of temperature and the aging of the conductivity probe over a 6-month period and how that influences the final reported desalination performance metrics. Finally, we recommend to the community of electrochemical water desalination researchers when and how to best calibrate the conductivity probes to avoid skewing the results. We also provide several simplified and easy-to-use spreadsheets that readily enable the synchronization between pH and concentration data, calculation of concentrations, conversion of standard concentration units (mg L$^{-1}$, ppm, mmol L$^{-1}$) into one another, calculation of the electrode mass needed to achieve a desired water quality, and much more.

## RESULTS AND DISCUSSION

### Description of a typical desalination setup and experiment

Figure 1A schematically shows a typical electrochemical desalination setup. An electrolyte tank (in our case, typically 10 L) provides a practically constant concentration of saline water fed into the cell. However, the size of the tank needs to be adjusted for
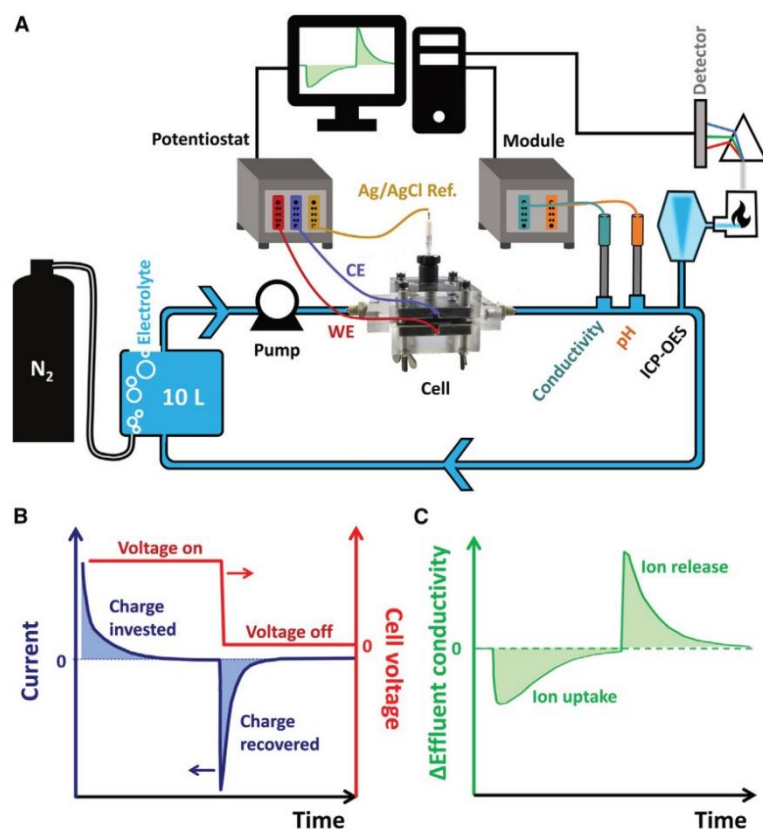
**Cell Reports
Physical Science**
Article

*CellPress*
OPEN ACCESS



**Figure 1. Electrochemical desalination setup and real-time response of the cell**
(A) Schematic representation of a typical electrochemical desalination setup; WE, working electrode; CE, counter electrode.
(B) The applied cell voltage profile and the current response of the cell.
(C) The corresponding conductivity profile during one full electrochemical desalination cycle.

the size of the desalination cell, and one must also consider the possible water evaporation over time during long-term operation. Such a setup is known as a single-pass mode of operation, in contrast to the batch mode.[12] A peristaltic pump continuously circulates the electrolyte from the tank to the cell through the conductivity and pH chambers and directs the electrolyte back to the tank. A nitrogen gas tube is inserted into the tank to constantly bubble the electrolyte with a small nitrogen gas flow to remove the air, and particularly the dissolved oxygen, from the water. The latter measure was taken to minimize carbon oxidation and performance degradation, since the dissolved oxygen in the electrolyte can take part in parasitic oxygen reduction reaction and peroxide formation during charge and discharge.[17,18]

As outlined before, two key datasets are commonly recorded in an electrochemical desalination experiment: (1) electrochemical data provided by the electrochemical workstation, which can include current-time ($I$-$t$), cell voltage-time ($V$-$t$), electrode potential-time ($E$-$t$), or energy-time ($U$-$t$) data, among others, and (2) the cell's effluent electrolyte properties provided by the probes installed at the downstream side of the cell, which can include conductivity-time, pH-time, or temperature-time data, among others.

Figure 1B shows the cell voltage applied during charge and discharge, together with the current response of the cell. As will be shown later, the electric charge stored in the carbon electrodes can be calculated by integrating the area under the *I-t* curve presented here. In a single-pass mode of operation, the concentration-time profile of the outflowing water from the cell resembles the scheme shown in Figure 1C. In the latter mode of operation, there is a quasi-infinite abundance of salt ions present in the circulating electrolyte, which is more than sufficient for the electrodes to take up. As a result, after applying a cell voltage for a while, the electrodes saturate with an overabundance of the present salt ions and reach their maximum (equilibrium) capacities, and the salt concentration of the water flowing out of the cell will finally reach the level of the water that flew into the cell. Likewise, the stored salt ions in the electrodes are ejected back to the circulating electrolyte (brine solution) upon applying the discharge voltage.

The conductivity change is translated into concentration change (see the section "calibration of conductivity probes"), and the integrated area under the concentration-time curve measures the capacity of the electrodes to remove salt ions, a merit called desalination capacity (DC). The electrode's capacity to remove salt ions can then be compared with its capacity to store electric charge in the same cycle. A measure that reports the fraction of the former to the latter is called charge efficiency (CE). CE is not to be confused with Coulombic efficiency, which states the fraction of electric charge obtained during discharging to that while charging an electrochemical cell, a standard metric reported in battery research.

Finally, the energy consumed during the charging of the electrodes could be reported as normalized to the number of ions removed. Assuming no other losses, the net consumed energy in one complete cycle could be envisioned as the sum of the enthalpies of demixing the saline feed water into the desalinated solution produced during charging and the brine solution produced during discharging.[19] The consumed energy for demixing can be harvested again upon mixing the two latter solutions (the capmix process), giving rise to the concept of blue energy or osmotic power.[20]

## Calibration of conductivity probes

To calculate standard desalination performance metrics, such as desalination capacity, one has to convert the obtained conductivity-time data (Figure 1C) into concentration-time data. As a first step, the conductivity probes should be calibrated (or standardized) using several NaCl stock solutions with known concentrations. Figure 2A shows a conductivity probe calibrated with 17 stock solutions of NaCl in pure water, ranging from 1 mmol $L^{-1}$ to 1,000 mmol $L^{-1}$. For accuracy, the conductivity probes are best calibrated with stock solutions with concentrations around the target electrolyte desired to be tested in an electrochemical desalination experiment. In this study, since the target electrolyte for the subsequent electrochemical desalination tests is 20 mmol $L^{-1}$ NaCl, the calibration curve is constructed for the concentration regime of 1–50 mmol $L^{-1}$ (Figure 2B), resulting in a good coefficient of determination ($R^2$) of 0.999 between conductivity and concentration values. Similarly, if an electrolyte simulating seawater-level concentrations of NaCl ($\sim$600 mmol $L^{-1}$) is to be used, a calibration curve between 500 and 1,000 mmol $L^{-1}$ can be constructed (Figure 2C) and used.

Using the concentration-conductivity equation in Figure 2B, the conductivity data obtained in an electrochemical desalination experiment (Figure 3A) could be converted into concentration data (Figure 3B), enabling further calculations on the desalination capacity and CE.
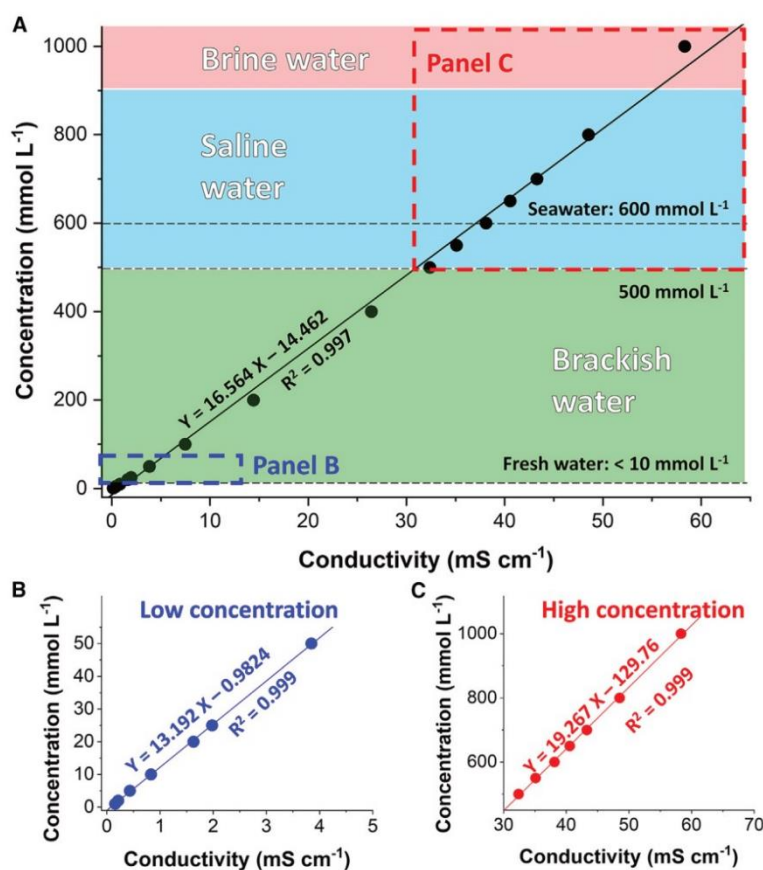
**Cell Reports**
**Physical Science**
Article

**Figure 2. Construction of the calibration curves relating the conductivity to the concentration**
Calibration curves were constructed to convert the measured conductivity into concentration in (A) the entire 1–1,000 mmol L$^{-1}$ range, (B) a low-concentration regime of 1–50 mmol L$^{-1}$, and (C) a high-concentration regime of 500–1,000 mmol L$^{-1}$.

## Desalination capacity

Figure 3A shows the conductivity variations of a standard single-pass electrochemical desalination experiment during several cycles. In this study, we have used a symmetric cell composed of two activated carbon electrodes, charged and discharged at 1.2 V and 0.3 V, respectively. The experimental procedures section details the experimental and operational conditions used in the latter test. Figure 3B shows the typical concentration variations upon cycling of an electrochemical desalination cell. As illustrated in Figure 1A, the electrolyte solution is constantly bubbled by nitrogen gas to remove the dissolved oxygen, accelerating the electrolyte's evaporation over time. As a result, the concentration slightly increases and, hence, the feed concentration of ~22 mmol L$^{-1}$ is reached in Figure 3B instead of the initially made 20 mmol L$^{-1}$. To alleviate electrolyte evaporation, one might pre-wet the dry nitrogen flow by passing it through a gas-washing water bottle.

For the sake of simplicity, the x axis (time) in Figure 3B could be converted to cycle number by dividing the time by the cycle duration (a peak-to-peak separation), which is 7,220 s in the present case, as illustrated in Figure S2. Based on the
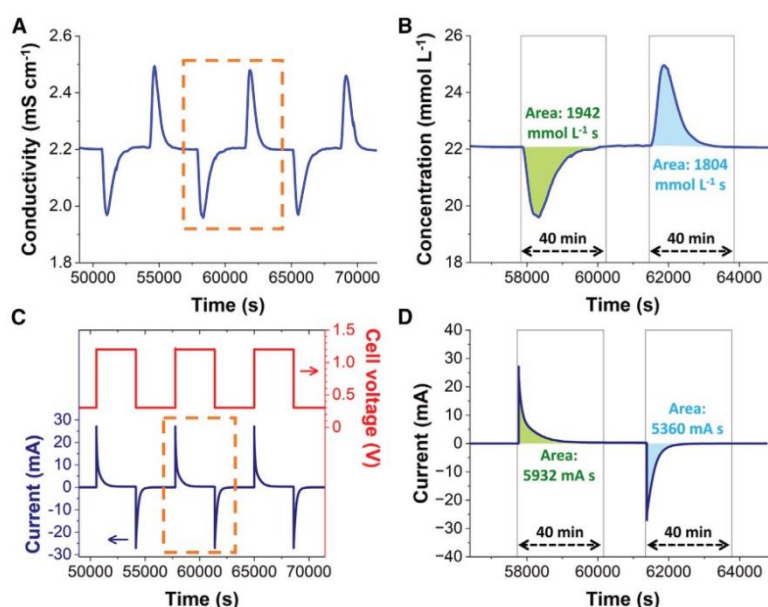
**Figure 3. Integration of the area under the curves of concentration-time and current-time profiles**
(A and B) Processing steps for converting the (A) raw conductivity-time data into (B) concentration-time data and the integration of the area under the curve for charging and discharging half-cycles.
(C) The applied cell voltage during charge and discharge and the current response.
(D) The integration of the area under the current-time curve for charging and discharging half-cycles.

decrease/increase in concentration curve versus time (Figure 3B), induced by charging/discharging of the cell by the electrochemical workstation, the DC (mg$_{salt}$ g$_{electrode}^{-1}$) is then calculated following Equation 1:

$$DC = \frac{\nu\, M_{NaCl}}{m_{total}} \int C\, dt, \qquad \text{(Equation 1)}$$

where $\nu$ is the flow rate (L s$^{-1}$), $M_{NaCl}$ is the molar mass of NaCl (58.44 g mol$^{-1}$), $m_{total}$ is the total mass of both electrodes combined (g), and $t$ is the time (s) during which a concentration change (mmol L$^{-1}$) occurs.

However, one commonly deals with more practical units at laboratory-scale electrochemical desalination, namely, mL min$^{-1}$ for flow rate ($\nu$) and mg for electrode mass ($m_{total}$). Also, the collective term $\int C\, dt$, with the unit mmol L$^{-1}$ s, is obtained by integrating the area under each half-cycle in concentration-time curves. In this case, Equation 1 must be divided by 60 as a conversion factor to give Equation 2:

$$DC\left(\frac{mg\ NaCl}{g_{electrode}}\right) = \frac{\nu\left(\frac{mL}{min}\right) \times 58.44\left(\frac{g\ NaCl}{mol\ NaCl}\right)}{60\, m_{total}(mg)} \int C\, dt\left(\frac{mmol\ s}{L}\right), \quad \text{(Equation 2)}$$

which further simplifies into Equation 3:

$$DC\left(\frac{mg\ NaCl}{g_{electrode}}\right) = \frac{0.974\, \nu\left(\frac{mL}{min}\right)}{m_{total}(mg)} \int C\, dt\left(\frac{mmol\ s}{L}\right), \qquad \text{(Equation 3)}$$

Substituting in Equation 3 1.6 mL min$^{-1}$ for the flow rate, 270.6 mg for the total mass of both electrodes (137.1 mg + 133.5 mg), and 1,873 mmol L$^{-1}$ s as the average of

## Cell Reports
## Physical Science
### Article

CellPress
OPEN ACCESS

integrated areas under the two charging and discharging half-cycles in concentration-time curves $\left(\frac{1,942+1,804}{2}\right)$, will result in DC = 10.8 mg NaCl removal capacity per gram of electrode, or 10.8 mg g$^{-1}$ in short.

In some cases, mainly where selectivity toward certain cations or anions is involved,[11] total NaCl salt removal capacity (DC) may be less relevant than specific removal capacities toward certain ions. If those ions are sodium and chloride,[21] the DC can be broken down to sodium removal capacity and chloride removal capacity following Equations 4 and 5, respectively.

Na$^+$ removal capacity:

$$\left(\frac{\text{mg Na}^+}{\text{g}_{\text{electrode}}}\right) = DC \left(\frac{\text{mg NaCl}}{\text{g}_{\text{electrode}}}\right) \times \frac{\text{mol NaCl}}{58.44 \text{ mg NaCl}} \times \frac{1 \text{ mol Na}^+}{1 \text{ mol NaCl}} \times \frac{22.99 \text{ mg Na}^+}{1 \text{ mol Na}^+} = 0.39 \, DC,$$

(Equation 4)

Cl$^-$ removal capacity:

$$\left(\frac{\text{mg Na}^+}{\text{g}_{\text{electrode}}}\right) = DC \left(\frac{\text{mg NaCl}}{\text{g}_{\text{electrode}}}\right) \times \frac{\text{mol NaCl}}{58.44 \text{ mg NaCl}} \times \frac{1 \text{ mol Cl}^-}{1 \text{ mol NaCl}} \times \frac{35.45 \text{ mg Cl}^-}{1 \text{ mol Cl}^-} = 0.61 \, DC,$$

(Equation 5)

For the example above, Na$^+$ and Cl$^-$ removal capacities would then be 4.2 mg g$^{-1}$ and 6.6 mg g$^{-1}$, respectively. Adjustments must be made if a different salt system is investigated, such as KCl or NaSO$_4$.

### Charge efficiency

After DC, another key metric of an electrochemical desalination system, not always reported in the literature, is the CE. CE is a unitless value between zero and unity (commonly given in percent) that gauges the portion of the invested electric charge that contributes to removing salt ions from the saline stream. The closer the CE to unity (or to 100%), the less the system suffers from parasitic losses. The latter parasitic losses stem from co-ion expulsion phenomena and electrode-electrolyte faradic side reactions.[22] As a result, side processes that do not contribute to the electrochemical desalination bottom line, that is, maximum net salt removal, will decrease the CE value. For a review of different sources of parasitic losses, readers are referred to other studies.[12,23,24]

The CE (%) can be formulated as Equation 6:

$$CE \, (\%) = \frac{\frac{DC}{M_{\text{NaCl}}}}{\frac{Q}{F}} \times 100\%,$$

(Equation 6)

where $F$ is the Faraday constant and $Q$ is the average of total charge stored in the two electrodes normalized to the total mass of both electrodes combined. In Equation 6, the nominator expresses the population of salt ions taken up by the electrode, and the denominator expresses the population of invested electric charge. A critical point that needs to be stressed here is that the charge substituted in the CE formula should be obtained from the same cycle and the duration from which the DC was obtained. As such, the charge capacity/capacitance of the electrodes obtained via any other techniques performed prior to desalination experiments, such as cyclic voltammetry or charge/discharge, will be irrelevant to use here.

62

For practical reasons, the term $Q$ in Equation 6 can be defined as $Q = \frac{q}{m_{total}}$, where $q$ is obtained by integrating the area under each half-cycle in current-time curves or readily obtained by the electrochemical workstation software (EC-Lab in this work). More discussion on the significance of employing either of the latter methods for calculating charge will follow later in this article (see the section "leakage current subtraction"). One might find the following units convenient to use at the laboratory-scale tests: $96,485$ C mol$^{-1}$ for the Faraday constant ($F$), mg for electrodes mass ($m_{total}$), mA s for charge ($Q$), and $58.44$ g mol$^{-1}$ for the molar mass of NaCl ($M_{NaCl}$). In that case, Equation 6 must be divided by $1,000$ as a conversion factor to turn into Equation 7:

$$CE\ (\%) = \frac{DC\left(\frac{mg\ NaCl}{g_{electrode}}\right) \times 96,485\left(\frac{C}{mol}\right) \times m_{total}(mg)}{1,000 \times q\ (mA\ s) \times 58.44\left(\frac{g\ NaCl}{mol\ NaCl}\right)} \times 100, \quad \text{(Equation 7)}$$

which simplifies into Equation 8:

$$CE\ (\%) = \frac{165.10\ DC\left(\frac{mg\ NaCl}{g_{electrode}}\right) \times m_{total}(mg)}{q\ (mA\ s)}, \quad \text{(Equation 8)}$$

Substituting in Equation 8 $10.8$ mg g$^{-1}$ for DC, $270.6$ mg for the total mass of both electrodes ($137.1$ mg + $133.5$ mg), and $5,646$ mA s as the average of integrated areas under the two charging and discharging half-cycles in $I$-$t$ curves $\left(\frac{5,932+5,360}{2}\right)$ will result in CE = 85%.

In an ideal case, the DC or CE obtained in the charging half-cycle (desalination) should be equal to that in the discharging half-cycle (regeneration). Because of non-idealities and parasitic losses, such as leakage current (which will be dealt with later in this work), non-equal, but often close, values of DC or CE are obtained for the two half-cycles. In such a case, one might choose to average the two values, as done above. Without averaging, the DC and CE for the charging half-cycle would be $11.2$ mg g$^{-1}$ and 84%, respectively, and the DC and CE for the discharging half-cycle would be $10.4$ mg g$^{-1}$ and 87%, respectively.

As seen, the values calculated herein differ well below 10% between charging and discharging half-cycles. If those two values differ largely, that is, >10%, one might need to check whether the baseline selection for integration of the area under the curves was precise. A simple method to get better baselines is to prolong the holding times for charging and discharging half-cycles (for relevant considerations, see also the section "leakage current subtraction"), which allows the concentration of the cell's effluent water to reach equilibrium. Moreover, one might also entertain the possible presence of detrimental faradic processes present significantly more in one half-cycle and absent in the other half-cycle. The latter phenomenon is often the case during the charging half-cycle, mainly when the cell is not carefully mass-balanced, and the electric potentials developed in one or both electrodes exceed their stability windows.

## Energy consumption

The energy consumed to accomplish the desalination is a key metric for comparing an electrochemical desalination system to other adjacent technologies. Also, within the realm of electrochemical desalination, the energy consumption analysis provides vital insight when comparing different system components, such as electrode materials, cell configurations, or electrolyte concentrations, as to which combination yields the most energy-efficient results. Such energy consumption analysis, for

**Cell Reports**
## Physical Science
### Article

CellPress
OPEN ACCESS

instance, can reveal that while carbon electrodes show an increased energy consumption going toward higher electrolyte concentrations, faradic materials such as 2D transition metal sulfides or MXenes show a rather constant energy consumption across wide concentration ranges.[16,21,25]

Two approaches could be taken for energy consumption analysis: macroscopic and microscopic. The macroscopic approach involves the Wh energy required for producing x liters of freshwater, commonly reported in the unit Wh L$^{-1}$. The salt content of freshwater is variously defined as less than 500 ppm[26] (<9 mmol L$^{-1}$ NaCl) or less than 1,000 ppm[27] (<17 mmol L$^{-1}$ NaCl). The macroscopic approach is more common in reverse osmosis technology, although its application for electrochemical desalination systems must be cautiously employed. In the case of reverse osmosis filtration, more than 99% of the salt content in the feedwater is removed from the product water.[28] In contrast, in electrochemical desalination at the laboratory scale, only a few percent of the salt content is removed in each charging half-cycle in a single-pass mode of operation.[29] As such, calculating energy consumption for complete salt removal via an electrochemical desalination system might require extrapolation calculations which assume that the system consumes the same energy rate all the way down to a very-low-salt-content electrolyte. However, the latter assumption could be erroneous, as electrolytes of lower concentrations would show a higher solution resistance, resulting in more energy consumed as the concentration decreases.

The microscopic approach, however, eliminates the need for extrapolations or unreliable assumptions. The latter approach involves the energy consumed to remove one salt formula unit in a single electrochemical desalination cycle, which will also be dealt with herein. As outlined before, the energy consumed during the charging ($U_{charge}$) of the electrodes are often considered the basis for energy calculations, even though part of that energy could be potentially recovered during the discharging of the electrodes.[9,30] Equation 9 can then be formulated to calculate the energy invested to remove a single salt molecule from the saline stream.

$$\text{Energy consumption per ion} = \frac{\dfrac{U_{charge}}{m_{total}}}{\dfrac{DC}{M_{NaCl}}}, \qquad \text{(Equation 9)}$$

where the nominator in Equation 9 provides the consumed energy normalized to the mass of both electrodes combined (Wh g$^{-1}$), and the denominator gives the moles of salt ions removed normalized to the mass of both electrodes combined (mmol g$^{-1}$).

The practical energy unit that one commonly deals with at laboratory-scale electrochemical desalination tests is Wh for energy consumed, while the desirable energy unit to report the energy values in molecular-scale systems is the product of the Boltzmann constant and temperature ($k_BT$). Given that For $T$ = 298 K, 1 Wh is equal to $8.75 \times 10^{23} k_BT$, the substitution of the Avogadro number yields Equation 10:

$$\text{Energy consumption per ion} \left(\frac{k_BT}{ion}\right) = \frac{\dfrac{U_{charge}\,(\text{Wh})}{m_{total}\,(\text{mg})}}{DC\left(\dfrac{mg}{g}\right)} = \frac{\dfrac{U_{charge}\,(\text{Wh})}{m_{total}\,(\text{mg})} \times \dfrac{1,000\,mg}{1\,g} \times \dfrac{8.75 \times 10^{23}\,k_BT}{1\,\text{Wh}}}{58.44\left(\dfrac{g}{mol}\right) \times \dfrac{1,000\,mg}{1\,g} \times \dfrac{1\,mol}{6.02214076 \times 10^{23}}},$$

$$\text{(Equation 10)}$$

**CellPress**
OPEN ACCESS

**Cell Reports**
**Physical Science**
Article

which, upon further simplification, yields Equation 11:

$$\text{Energy consumption per ion } \left(\frac{k_B T}{\text{ion}}\right) = \frac{8.49 \times 10^7 \; U_{\text{charge}} \; (\text{Wh})}{m_{\text{total}} \; (\text{mg}) \times \text{DC} \left(\frac{\text{mg}}{\text{g}}\right)}, \qquad \text{(Equation 11)}$$

Referring to the electrochemical workstation software, the $U_{\text{charge}}$ for the cycle studied above (Figure 3B) is $2.08 \times 10^{-3}$ Wh. Substituting the latter value in Equation 11, along with 10.8 mg g$^{-1}$ for DC and 270.6 mg for the total mass of both electrodes, will result in 60.4 $k_B T$ per single salt molecule (NaCl) removed.

### Ion selectivity

There has been an ever-growing interest in the electrochemical desalination research toward selective separation and recovery of ions from aqueous media, either to remove toxic/undesired species from water streams or to capture valuable elements.[2,31] Table 1 lists several works that have reported the selective electrochemical removal of certain ionic species from aqueous media in the presence of other competing ions in a cyclic manner. Lithium, nickel, cobalt, and manganese, for instance, are among the value-added elements that can be recovered from the leaching solution of spent lithium-ion batteries,[32–34] contributing toward a circular economy. The target ionic species in Table 1 are highlighted in a periodic system of elements with their significance and critical applications, as illustrated in Figure 4. As can be seen, the electrochemical desalination world is no longer limited to mere sodium chloride removal. Still, it has expanded in scope for selective removal of cations or anions of various types.

To calculate the performance metrics of an electrochemical desalination system, one has to determine the change in the concentrations of ionic species flowing out of the cell. However, when there is more than one salt species involved, the concentration cannot be related to the conductivity of the effluent water stream, as the measured conductivity is a product of the contribution of multiple ionic species (Figure 5A). Developing methods to quantify the individual ion concentration in a mixed-salt electrolyte is crucial in studying the system's selectivity. Inductively coupled plasma optical emission spectroscopy (ICP-OES), for instance, is a powerful and accurate tool that can individually quantify many ionic species simultaneously.

Techniques such as ICP-OES,[71] inductively coupled plasma mass spectrometry,[72] or ion chromatography[37,45,73] are methods to monitor individual ionic species. Alternatives include the EDTA titration of mixtures of $Ca^{2+}$ and $Mg^{2+}$ ions,[74] or the colorimetric method for determining $Pb^{2+}$ ions in the presence of alkali metal and alkaline earth metal ions.[75] The latter process required the treatment of lead ions with sulfide ions to convert the colorless lead ions into adsorptive lead sulfide, followed by UV-visible-near-infrared (UV-vis-NIR) spectrophotometry.

Ion-selective electrodes have been used when dual-salt electrolytes are involved. An example of the latter is surfactant-functionalized activated carbon electrodes developed to demonstrate a high affinity for $NO_3^-$ compared to $Cl^-$ ions.[73] Combined use of ion-selective electrodes and conductivity/pH measurements have also been shown for mixtures of $Na^+$ and $Ca^{2+}$ ions[53,76] using the extended Onsager-Fuoss model.[77] The latter theoretical foundation helps to predict the complex conductivity changes that occur with concentration changes. This theoretical guidance provides calibration methods that consider the impact of ionic association on conductivity assessments, ensuring that accuracy and precision are maintained over a wide range of concentrations.[78]

**Cell Reports
Physical Science**
Article

CellPress
OPEN ACCESS

**Table 1. Overview of electrochemical desalination research on selective recovery of ions from aqueous media**

| Target element | Competing ions | Electrode material | References |
|---|---|---|---|
| $Li^+$ | $Na^+$, $K^+$, $Mg^{2+}$ | $LiFePO_4$ | Trócoli et al.,[35,36] Pasta et al.[35,36] |
| $Li^+$ | $Na^+$, $K^+$, $Mg^{2+}$, $Ca^{2+}$ | $\lambda$-$MnO_2$ | Lee et al.,[37–39] Trócoli et al.,[37–39] Kim et al.[37–39] |
| $Li^+$ | $Na^+$, $K^+$, $Mg^{2+}$ | flow electrodes of ($Fe[CN]_6^{4-}$/$Fe[CN]_6^{3-}$) redox pair + LISICON membrane | Wang et al.[8] |
| $Li^+$ | $Co^{2+}$ | activated carbon fiber + MXene-based ion-sieving membrane | Jiang et al.[40] |
| $Na^+$ | $Mg^{2+}$, $Ca^{2+}$ | nickel hexacyanoferrate (NiHCF Prussian blue analog) | Singh et al.[41] |
| $Cs^+$ | $Na^+$, $Sr^{2+}$ | copper hexacyanoferrate (CuHCF Prussian blue analog) | Lee et al.[42] |
| $NH_4^+$ | $Na^+$, $K^+$, $Mg^{2+}$, $Ca^{2+}$ | nickel hexacyanoferrate (NiHCF Prussian blue analog) | Tsai et al.[43] |
| $ClO_4^-$ | $Cl^-$ | activated carbon cloth | Xing et al.[44] |
| $PO_4^{3-}$ | $Cl^-$, $NO_3^-$, $SO_4^{2-}$ | layered double hydroxide-reduced graphene oxide composite | Hong et al.[45] |
| $NO_3^-$ | $Cl^-$, $SO_4^{2-}$ | hierarchical carbon aerogel monoliths | Hawks et al.[46] |
| $SO_4^{2-}$ | $Cl^-$ | amine functionalized activated carbon | Zuo et al.[47] |
| $Cl^-$ | $SO_4^{2-}$ | Bi | Chang et al.[48] |
| $Br^-$ | $Cl^-$ | activated carbon + ion-exchange membranes | Li et al.[49] |
| $I^-$ | $Cl^-$ | flow electrodes of activated carbon | Liu et al.[50] |
| $F^-$ | $SO_4^{2-}$ | activated carbon + monovalent anion selective membrane | Pan et al.[51] |
| $F^-$ | $Cl^-$, $NO_3^-$ | graphene oxide-hydroxyapatite composite | Park et al.[52] |
| $Ca^{2+}$ | $Na^+$ | $H_2SO_4$-treated activated carbon cloths | Uwayid et al.[53] |
| $Sr^{2+}$ | $Na^+$ | aryl diazonium salt-modified porous carbon | Xiang et al.[54] |
| $Cu^{2+}$ | $Na^+$ | flow electrodes of activated carbon | Zhang et al.[55] |
| $Fe^{3+}$ | $Na^+$, $Mg^{2+}$, $Ca^{2+}$ | graphene nanoflakes | Li et al.[56] |
| $Ni^{2+}$ | – | conductive graphite adhesive-activated ion-exchange resin composite | Wang et al.[57] |
| $Co^{2+}$ | $Li^+$, $Ni^{2+}$ | electrodialysis with polymeric ion-exchange membranes | Siekierka and Yalcinkaya[58] |
| $Mn^{2+}$ | – | flow electrodes of dilute $H_2SO_4$ with polymeric ion-exchange membranes | Soysüren et al.[59] |
| $Zn^{2+}$ | – | activated carbon cloth | Tang et al.[60] |
| $Pb^{2+}$ | $Mg^{2+}$, $Ca^{2+}$ | thiol-functionalized graphene oxide-activated carbon composite | Huang et al.[61] |
| $Pb^{2+}$ | $Co^{2+}$, $Ni^{2+}$ | FeOOH | Wang et al.[62] |
| $Cd^{2+}$ | – | flow electrodes of $\delta$-$MnO_2$ | Peng et al.[63] |
| $V^{5+}$ (as $VO^{3-}$) | $SO_4^{2-}$, $PO_4^{3-}$, $SiO_3^{2-}$ | resin-activated carbon composite | Bao et al.[64] |
| $Cr^{6+}$ (as $Cr_2O_7^{2-}$) | $Cl^-$, $ClO_4^-$ | poly(vinyl)ferrocene-carbon nanotubes composite | Su et al.[65] |
| $As^{5+}$ (as $AsO_4^{3-}$) | $Cl^-$ | poly(vinyl)ferrocene-carbon nanotubes composite | Su et al.[65] |
| $Sc^{3+}$ | $Na^+$, $K^+$, $Mg^{2+}$, $Ca^{2+}$, $Zn^{2+}$, $Al^{3+}$, $Fe^{3+}$ | electrodialysis with polymeric ion-exchange membranes | Li et al.[66] |
| $Sm^{3+}$ | $Ag^+$, $Cd^{2+}$, $Co^{2+}$, $Mn^{2+}$, $Al^{3+}$, $Cr^{3+}$, $Fe^{3+}$, $Cu^{2+}$, $Pb^{2+}$, $Hg^{2+}$, $Ni^{2+}$, $Zn^{2+}$, $NH_4^+$, $Na^+$, $K^+$, $Mg^{2+}$, $Ca^{2+}$ | $B_{12}S$ nanoflakes | Xiang et al.[67] |
| $La^{3+}$ | $Na^+$, $Ca^{2+}$ | P-doped carbon | Xiong et al.[68] |
| $La^{3+}$, $ND^{3+}$, $Ce^{3+}$ | – | sodium diphenylamine sulfonate-modified activated carbon | Wang et al.[69] |
| $U^{6+}$ (as $UO_2^{2+}$) | seawater (majorly $Na^+$, $K^+$, $Mg^{2+}$, $Ca^{2+}$) | BP nanosheets | Chen and Tong[70] |

The selection of measurement techniques should align with experimental goals to ensure accurate and relevant results in electrochemical desalination investigations. In this work, we have used online ICP-OES monitoring to showcase a selectivity measurement and its relevant considerations and relationships. As outlined previously,
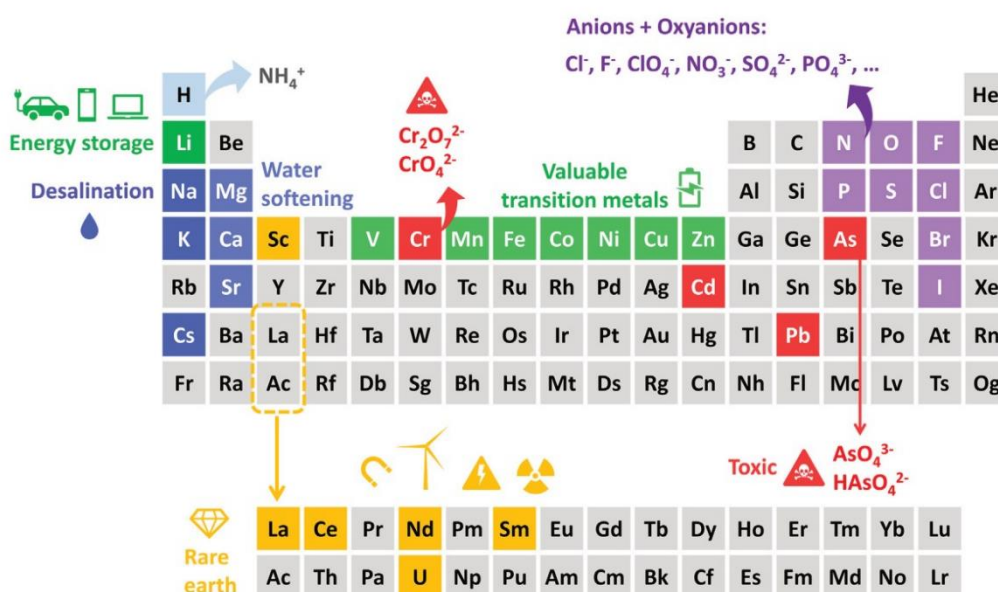
66

**CellPress**
OPEN ACCESS

**Cell Reports**
**Physical Science**
Article



**Figure 4. All elements targeted so far for electrochemical recovery from water**
Periodic table showing elements targeted in electrochemical desalination (capacitive deionization, battery desalination) for selective recovery from aqueous media in a cyclic manner.

an electrochemical desalination cell with symmetric carbon electrodes was charged and discharged. The electrolyte in this case consisted of $CaCl_2$, $KCl$, and $NaCl$, each with 10 mmol $L^{-1}$, instead of the previously examined single-salt NaCl electrolyte.

To enhance the signal-to-noise ratio, one can increase the electrode mass and, if possible, a lower flow rate. The latter measures increase the amplitude of concentration change in each cycle, thereby maximizing the signal-to-noise ratio. A side-by-side comparison of raw ICP-OES data for two cells with carbon electrodes of significantly different masses is included in Figure S3. A noisy raw ICP-OES dataset will translate into less accurate concentration profiles (Figure S4), rendering further integrations and calculations inaccurate.

Further processing of raw ICP-OES data will result in Figures 5B–5D, individually showing the concentration-change profiles of calcium, potassium, and sodium ions. The process to convert raw ICP-OES data into the concentration of ions includes the calibration of the ICP-OES instrument with a set of samples with known concentrations (Figure S5) in the same manner shown previously to convert conductivity data into the concentration of a single-salt electrolyte (Figure 2).

The procedure to calculate the DC will be similar to what has been carried out to calculate the DC of a single-salt system (Figure 3B). For instance, to calculate the desalination capacity of the system for calcium ions ($DC_{Ca}^{2+}$) using Equation 1, one has to substitute the molar mass of calcium ions (40.08 g mol$^{-1}$) instead of the previously used molar mass of NaCl. Also, since the $Ca^{2+}$ ions are attracted to the negative electrodes, the $m_{total}$ in Equation 1 has to be replaced by the mass of only the negative electrode. Substitution of the latter values, the average of integrated areas under the two charging and discharging half-cycles in concentration-time curves, and the flow rate gives $DC_{Ca}^{2+}$ = 7.4 mg g$^{-1}$. Similarly, the desalination
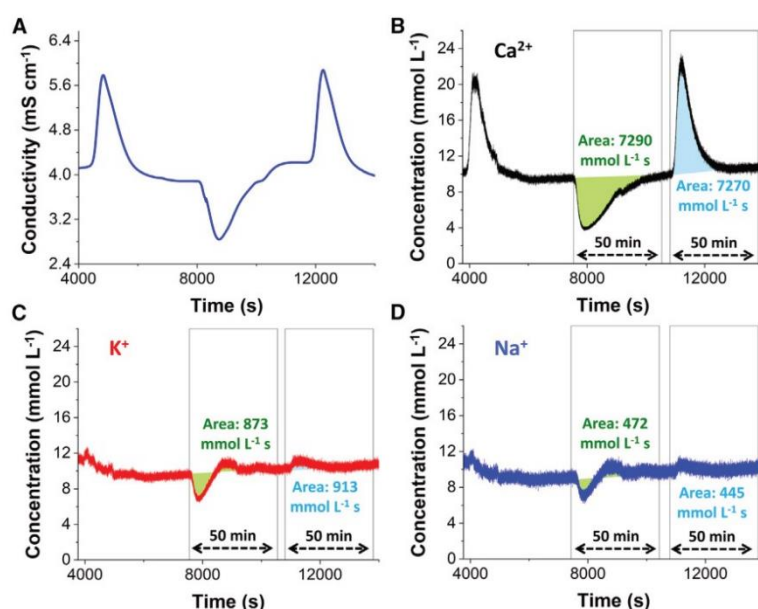
**Figure 5. Online elemental monitoring of the effluent of an electrochemical cell**
(A) Conductivity variations as a result of cycling a carbon/carbon electrochemical cell containing 506 mg of carbon cloth as negative electrode and 501 mg of carbon cloth as positive electrode in a mixed aqueous electrolyte containing $CaCl_2$, KCl, and NaCl, and the corresponding change in the concentration of (B) calcium, (C) potassium, and (D) sodium ions measured online by ICP-OES.

capacity for potassium ions ($DC_K^+$) and desalination capacity for sodium ions ($DC_{Na}^+$) can be calculated by substitution of the respective molar masses and integration areas to result in $DC_K^+ = 0.9$ mg g$^{-1}$ and $DC_{Na}^+ = 0.3$ mg g$^{-1}$.

Figures 5C and 5D show that for K$^+$ and Na$^+$ ions, after an initial dip in concentration induced by charging the electrochemical cell, a slight increase occurs in concentration. This is unlike the case for Ca$^{2+}$ ions in Figure 5B, where the concentration profile is dipped and gradually reaches its past level to the feed concentration. This effect has been observed before in the electrochemical desalination of multicomponent electrolytes via activated carbon electrodes, where the monovalent ions are preferentially adsorbed initially but are gradually replaced by divalent ions.[79] The latter intricate information on such time-dependent ion dynamics is provided exclusively by online monitoring with ICP-OES, as offline manual sampling techniques can hardly reveal such behaviors.[80] For the calculation of $DC_K^+$ and $DC_{Na}^+$ in Figures 5C and 5D, during the charging half-cycle the integrated areas above and under the concentration profiles were subtracted from each other to result in a net removal capacity during the charging half-cycle.

The merit of a system for the preferential removal of a particular element against another elements could be formulated as Equation 12[76]:

$$\beta_{A/B} = \left( \frac{DC_A}{DC_B} \right) \left( \frac{C_{B,feed}}{C_{A,feed}} \right), \qquad \text{(Equation 12)}$$

where $\beta_{A/B}$ is a unitless separation factor for element A with respect to element B, $DC_A$ (mg g$^{-1}$) is the desalination capacity of A ions, $DC_B$ (mg g$^{-1}$) is the desalination capacity of B ions, and $C_{A,feed}$ (mg L$^{-1}$) and $C_{B,feed}$ (mg L$^{-1}$) are the concentration of A

**CelPress**
OPEN ACCESS

and B ions, respectively, at the beginning of the process (that is, their concentrations in feedwater). One must note the use of consistent units in Equation 12 for concentrations and desalination capacities, which were, in this case, mg L$^{-1}$ and mg g$^{-1}$, respectively. Alternatively, one could use mmol L$^{-1}$ for concentrations, which then mandates the use of mmol g$^{-1}$ for desalination capacities.

According to the latter definition, a system that removes both A and B ions indiscriminately, that is, non-selective, will have a separation factor of $\beta_{A/B} = 1$. Any value of $\beta_{A/B}$ greater than unity indicates a favorable removal capacity toward A compared to B. In the example above, to calculate the separation factor for Ca$^{2+}$ ions with respect to Na$^+$ ions ($\beta_{Ca^{2+}/Na^+}$), the following values have to be substituted in Equation 12: $DC_{Ca}{}^{2+} = 7.4$ mg g$^{-1}$, $DC_{Na}{}^+ = 0.3$ mg g$^{-1}$, $C_{Ca}{}^{2+}{}_{,feed} = 400$ mg L$^{-1}$, and $C_{Na}{}^+{}_{,feed} = 230$ mg L$^{-1}$, which results in $\beta_{Ca^{2+}/Na^+} = 14$. Alternatively, one could use the following units to reach the same result: $DC_{Ca}{}^{2+} = 0.185$ mmol g$^{-1}$, $DC_{Na}{}^+ = 0.013$ mmol g$^{-1}$, $C_{Ca}{}^{2+}{}_{,feed} = 10$ mmol L$^{-1}$, and $C_{Na}{}^+{}_{,feed} = 10$ mmol L$^{-1}$.

In a similar fashion, the separation factor for Ca$^{2+}$ ions with respect to K$^+$ ions ($\beta_{Ca^{2+}/K^+}$) will be calculated as 8. This means that the water flowing out of the cell during charging will be calcium deficient, which is relevant for water-softening applications. Similarly, the water flowing out of the cell during discharging will be calcium-rich while being sodium- and potassium-deficient. The volume of the latter flow, the calcium-rich brine, could be minimized by shortening the discharge time for more efficient water softening.

In certain studies, the above process is carried out in a batch mode. In the latter case, the feedwater is introduced into a usually larger cell (also called an electrochemical reactor[81]). After applying the charging voltage and selective uptake of the desired ions from the solution into the electrodes, the solution is exchanged with a fresh solution of lower volume (and of higher purity than feedwater). The discharging is then accomplished in the latter solution, and the ions previously immobilized in the electrodes are released, yielding an enriched solution of the desired ions called the recovery solution. The recovery solution is again exchanged with a fresh feedwater batch, regenerating the cell for a new cycle.
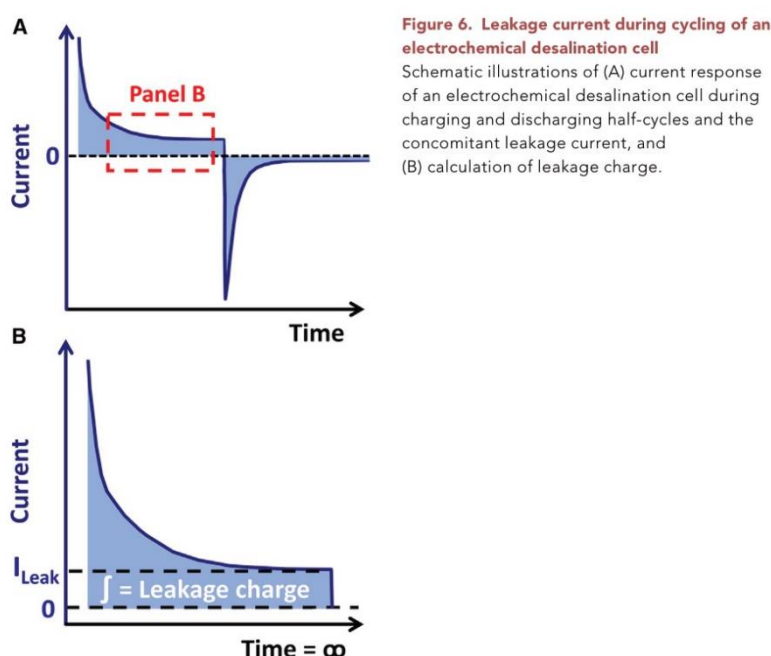
The batch-mode process, though interrupted, eliminates the need for online monitoring of elements, since one only needs to manually collect samples for elemental analysis at certain stages of the process, which are the feedwater and the recovery solutions.[38] In such a case, the separation factor expression can be reformulated as Equation 13:

$$\beta_{A/B} = \left( \frac{C_{A,feed} - C_{A,final}}{C_{B,feed} - C_{B,final}} \right) \left( \frac{C_{B,feed}}{C_{A,feed}} \right), \quad \text{(Equation 13)}$$

where $C_{A,feed}$ and $C_{A,final}$ refer to the concentrations of A ions in the feedwater and the recovery solutions, respectively; and $C_{B,feed}$ and $C_{B,final}$ refer to the concentrations of B ions in the feedwater and the recovery solutions, respectively.[41]

### Parameters affecting accuracy and meaningfulness of desalination performance metrics

Leakage current is one of the leading parasitic losses in the operation of electrochemical desalination cells, leading to energy loss.[82] We consider here the charging mechanism of a capacitor as an analogy to that of an electrochemical desalination cell. When a capacitor is being charged by applying a voltage to its terminals, once the electrodes are fully charged the current passing through the terminals

**Cell Reports**
**Physical Science**
Article

**CellPress**
OPEN ACCESS



**Figure 6. Leakage current during cycling of an electrochemical desalination cell**
Schematic illustrations of (A) current response of an electrochemical desalination cell during charging and discharging half-cycles and the concomitant leakage current, and (B) calculation of leakage charge.

decays to zero. In an electrochemical desalination cell, the latter indicates that the electrodes are fully charged, that the maximum population of salt ions is drawn into the electrode, and that the electrode capacity is fully realized. The rate at which the current decays depends on the time constant ($\tau$) of the capacitor known from classic resistor-capacitor circuits. The latter states that the "natural" current response of a capacitor follows an exponential function of time ($I \propto e^{\frac{-t}{\tau}}$). For instance, the current falls to 37% of its initial value once a period equal to one time constant ($1\tau$) has elapsed since the start of the application of potential bias to its terminals.[83] Likewise, the current should fall to less than 1% of its initial value after a lapse of a period equal to the five times the constant ($5\tau$).

In practice, however, the *I-t* curve of an electrochemical desalination cell typically approaches a non-zero value, known as the leakage current, as schematically shown in Figure 6. In this case, an electrochemical desalination cell can be modeled as an ideal capacitor (or other charge sources such as a battery) paralleled to a leakage resistance element.[84] When a voltage is applied to the cell, a relatively small (leakage) current constantly passes through the cell in the background. One approach to calculating the leakage resistance is to perform impedance spectroscopy measurements. Another approach, which takes less effort, is to prolong the voltage holding time so that the current contribution from the capacitor decays to zero. As a result, the remaining current could be approximated as the leakage current, as shown in Figure 6B.

The origin of the leakage current ($I_{Leak}$) is partly due to the slightly conductive saline electrolyte (in contrast to an insulating dielectric in a capacitor), where the sodium and chloride ions constantly carry (leak) a small fraction of electronic charge across the separator from electrode/current collector on one side to those on the other side upon the polarization of the cell. Another possible origin of the leakage current

could be water splitting, mainly when a cell voltage near 1.2 V is applied and held. More information on other possible sources of leakage current may be found elsewhere.[85,86] As illustrated in Figure 6A, the leakage current is larger during charging than in discharging, since the leakage current is mainly a voltage-dependent phenomenon.[23] As outlined above, one has to prolong the voltage holding time long enough to obtain the leakage current. Integration of the marked rectangular area under the $I$-$t$ curve (Figure 6B) then gives the charge leaked between the electrodes/current collectors via the electrolyte, also known as the leakage charge ($q_{Leak}$).

The leakage charge mentioned above should then be subtracted from the charge stored in the electrodes (obtained by the displacement current passing through the external circuit). Leakage charge considerations do not affect DC values. However, failure to consider the leakage charge in the calculations will result in inaccurate CE values, which follow further.

Zooming in on the $I$-$t$ profiles shown before (Figure 3D) reveals that the leakage current during the discharging half-cycle is insignificant and very close to zero. However, as expected, the leakage current is indeed significant during the charging half-cycle (Figure S6A), and its contribution to the overall charge invested by the power supply needs to be considered. Figure S6B shows how the leakage current is quantified and how the leakage charge can subsequently be obtained by multiplication of the latter to the duration of the cycle in the study, as indicated by the shaded area. Although the $I_{Leak}$ of 0.241 mA may seem small, over time it yields a significant charge of $q_{Leak}$ = 579 mA s relative to the total charge of 5,932 mA s. Subtraction of the latter by the former gives a net charge of 5,353 mA s for the charging half-cycle, which is very close to that for the discharging half-cycle in Figure 3D (5,360 mA s). Averaging the latter two values (5,357 mA s) and substituting them in the CE formula gives a CE of 90%, a 5% increase from previously calculated without consideration of leakage charge.

To shed further light on the complications that might arise from failure to consider leakage charge subtraction, we base the DC and CE calculations this time on a different cycle duration, 60 min instead of 40 min. A glance at concentration-time profiles in Figures 3A and 3B reveals that the electrodes seemingly saturate after 40 min voltage holding time and reach their equilibrium. Calculations based on a 60-min time window for each half-cycle (Figure S7) yield an average CE of 83% and a DC of 10.8 mg g$^{-1}$. Leakage charge corrections, however, will result in the same CE of 90%, previously obtained for a 40-min half-cycle duration. As can be seen, leakage current considerations ensure accurate CE calculations regardless of the duration of the voltage holding step. Otherwise, the more extended voltage holding times will result in lower and lower calculated CE values.

The example above highlights the significance of leakage current considerations, although care must be taken to report it in the proper context. Leakage current is a highly system-dependent value, which depends on cell configuration, electrolyte concentration, and presence or absence of ion-exchange membranes, among others. As such, subtraction of leakage charge would help obtain more precise CE values, which in turn more accurately captures the mechanisms involved, such as the presence of co-ion-expulsion phenomenon or other faradic side reactions (decreasing the CE) or the absence of such phenomena (increasing the CE). Although leakage current considerations are educational within a research context, in a commercial setting where performance benchmarking of an electrochemical cell is being discussed or advertised, one must avoid subtracting the leakage charge.
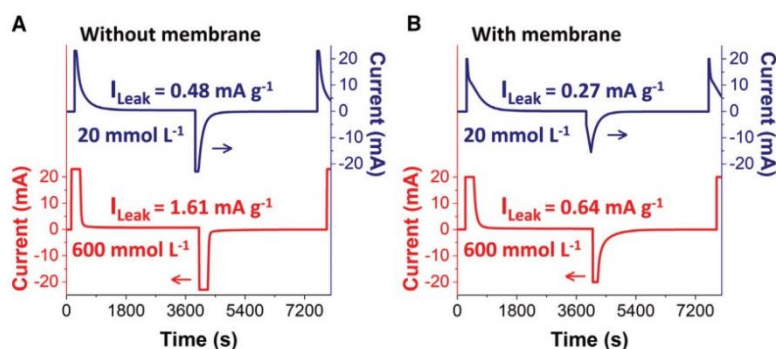
**Cell Reports**
**Physical Science**
Article

**Figure 7. Effect of electrolyte concentration and cell configuration on the magnitude of leakage current**

Current-time profile for one full cycle of electrochemical desalination cells in electrolytes made of 20 mmol L$^{-1}$ and 600 mmol L$^{-1}$ NaCl solutions (A) without any ion-exchange membranes and (B) with anion- and cation-exchange membranes.

Reporting leakage charge-subtracted performance metrics in the latter case might lead to mischaracterization of the actual efficiency of the system.

To investigate the system dependency of leakage current, we have also examined the effect of electrolyte concentration and the presence of ion-exchange membranes in electrochemical desalination cells. Figure 7A shows the specific leakage current magnitude (that is, leakage current normalized to the mass of both carbon electrodes) of a single cell when cycled between 0.3 V and 1.2 V in 20 mmol L$^{-1}$ and 600 mmol L$^{-1}$ aqueous NaCl solutions. Swapping the electrolyte tank from a lower concentration to a higher concentration significantly increases the leakage current during the charging half-cycle. The latter observation is in line with the hypothesis outlined previously, which stated that one source of leakage current could be arising from the conductivity of the saline electrolyte. In 600 mmol L$^{-1}$ aqueous NaCl electrolyte, there will be more leakage of electronic charge from one electrode across the spacer channel to the other electrode.

In a fresh cell (Figure 7B), we introduced polymeric anion- and cation-exchange membranes before positive and negative carbon electrodes. It is seen again that the leakage current magnitudes scale with the concentration level. However, introducing such membranes has resulted in lower magnitudes of specific leakage currents than the membrane-less cell. Even though a barrier such as a membrane could constitute an extra resistive element in the cell, the membranes, which are electrically insulating, probably hinder the passage of electronic charges, resulting in a net diminishing effect on leakage current magnitude. In all cases, the leakage current magnitude during the discharging half-cycle has been shown to be negligible.

Next, we investigate the aging of conductivity probes and test whether it significantly changes the reported desalination metrics. Figure 8A shows two concentration-conductivity calibration curves performed on the same conductivity probe with an interval of 6 months. As understood by the slope change of the latter two curves, the sensitivity of the conductivity probes decreases over time, meaning that lower conductivity values are obtained for the same concentration as the probe ages. This slope change can affect the amplitude of concentration change when applied to an electrochemical desalination dataset. To test this, the linear equations of the fitted calibration curves are applied to the conductivity data shown in
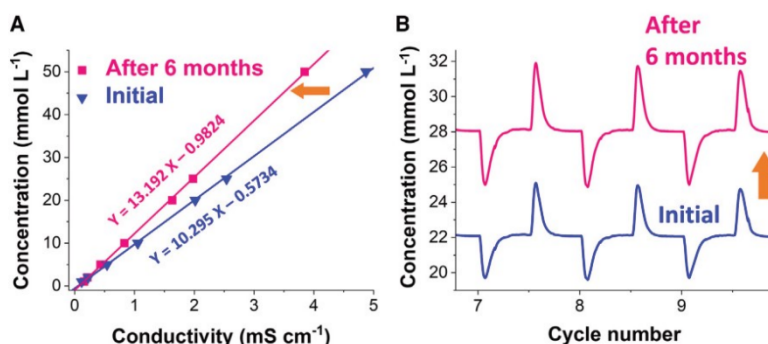
**CellPress**
OPEN ACCESS

**Figure 8. Effect of aging of the conductivity probes**
(A) Calibration curves of the same conductivity probe, performed two times with a 6-month interval in between.
(B) The obtained concentration profiles of an electrochemical cell obtained from the latter two calibration equations.

Figure 2A to construct the concentration data presented in Figure 8B. As observed, two concentration profiles are obtained, which, although they follow the same trend, differ mainly in terms of both baseline concentration values (22 mmol $L^{-1}$ vs. 28 mmol $L^{-1}$) and the amplitude of concentration change.

Performing the same calculations explained previously (Figure 3), DC and CE values of 13.8 mg $g^{-1}$ and 115% (after leakage charge subtraction) are obtained, respectively. The latter values vary primarily with the desalination metrics previously calculated, that is, an overestimation of DC by 3.0 mg $g^{-1}$ and CE by 25%. This pinpoints the importance of regular calibration of the conductivity probes before desalination experiments to avoid such inaccuracies. Assuming a monotonous loss of sensitivity for the conductivity probes tested herein within a 6-month interval, the inaccuracy could be approximated as 0.5 mg $g^{-1}$ per month for DC and around 4% per month for CE. As such, a calibration frequency of at least once per month is recommended to ensure the conductivity probes are fresh enough for reliable calculations.

More calibration curves for low and high-concentration regimes for two different conductivity probes with a 6-month interval may be found in Figure S8. Either of the two approaches may lead to inaccurate calculations: treating the old conductivity data with the equations obtained from a newly calibrated conductivity probe or treating the newly generated conductivity data with the equations obtained from an old formerly calibrated conductivity probe.

### Relationships between pH, temperature, and conductivity

By definition, the conductivity of a solution $\kappa$ (S $m^{-1}$) measures its ability to conduct electricity. The said conductivity of the solution arises from the sum of conductivity contributions of all individual ions present in the solution. As such, one needs to consider the conductivity contributions of pure water and dissolved salt.

The molar conductivity $\Lambda_m$ (S $m^2$ $mol^{-1}$) of an electrolyte solution can be defined[87] as its measured conductivity $\kappa$ (S $m^{-1}$) divided by its molar concentration $C$ (mol $m^{-3}$) following Equation 14:

$$\Lambda_m = \frac{\kappa}{C},$$

(Equation 14)

In the case of an electrolyte with infinitely dilute concentrations of ions, Kohlrausch's law of independent ionic migration[88] can be applied to break down the molar conductivity into its contributions coming from each ion, as expressed in Equation 15:

$$\Lambda_m^{\circ} = \sum_i \nu_i \lambda_i, \qquad \text{(Equation 15)}$$

where $\Lambda_m^{\circ}$ is the molar conductivity at infinite dilution, also known as limiting molar conductivity. $\lambda_i$ is the limiting molar ionic conductivity of ion $i$, and $\nu_i$ is the number of ions $i$ in the formula unit of the electrolyte.

What causes ions to conduct an electric current is their ability to move in a solution, that is, their mobility. As such, the molar ionic conductivity of an ion ($\lambda_i$) is a direct function of its electrical mobility ($\mu_q$) following Equation 16:

$$\lambda_i = F z_i \mu_{q_i}, \qquad \text{(Equation 16)}$$

where $F$ is the Faraday constant, and $z_i$ is the ionic charge (unitless) for the ion $i$. Replacing Equation 16 in Equation 15 gives us Equation 17:

$$\Lambda_m^{\circ} = F \sum_i \nu_i z_i \mu_{q_i}, \qquad \text{(Equation 17)}$$

For a simple A:B electrolyte with monovalent ions, Equation 17 for this electrolyte can be written for $A^+$ and $B^-$ ions as Equation 18:

$$\Lambda_m = F \left( \mu_{q_{A^+}} + \mu_{q_{B^-}} \right), \qquad \text{(Equation 18)}$$

From the Einstein relation (the kinetic theory), we know that the mobility of a particle can be related to its diffusion coefficient via Equation 19:

$$D = \mu k_B T, \qquad \text{(Equation 19)}$$

where $D$ is the diffusion coefficient, $\mu$ is the mobility defined as the ratio of the particle's drift velocity to an applied force, $k_B$ is the Boltzmann constant, and $T$ is the absolute temperature. In the particular case of a particle with electrical charge $q$, the electrical mobility term $\mu_q$ can be related to the generalized mobility $\mu$ in Einstein's relation as Equation 20:

$$\mu = \frac{\mu_q}{q}, \qquad \text{(Equation 20)}$$

where $\mu_q$ is defined as the ratio of the particle's drift velocity per unit electric field.

Combining Equation 19 and Equation 20 gives the Einstein-Smoluchowski equation for the diffusion of charged particles,[89] also known as the electrical mobility equation, as expressed in Equation 21:

$$D = \frac{\mu_q k_B T}{q}, \qquad \text{(Equation 21)}$$

Solving Equation 21 for $\mu_q$ gives Equation 22:

$$\mu_q = \frac{Dq}{k_B T}, \qquad \text{(Equation 22)}$$

The Nernst-Einstein[90] equation can then be written for the AB electrolyte by substitution of Equation 22 in Equation 18 to result in Equation 23:

$$\Lambda_m = F \left( \frac{D_{A^+} q_{A^+}}{k_B T} + \frac{D_{B^-} q_{B^-}}{k_B T} \right), \qquad \text{(Equation 23)}$$

Given that $A^+$ and $B^-$ ions are monovalent ions, $q_{A^+}$ and $q_{B^-}$ will be equal to one elementary charge. Equation 23, thus, upon further simplifications and substitution of $eN_A$ for $F$, becomes Equation 24:

$$\Lambda_m = \frac{Fe}{k_B T}(D_{A^+} + D_{B^-}) = \frac{e^2 N_A}{k_B T}(D_{A^+} + D_{B^-}),$$  (Equation 24)

Replacing Equation 14 in Equation 24 gives Equation 25:

$$\kappa = \frac{e^2 N_A}{k_B T}(C_{A^+} D_{A^+} + C_{B^-} D_{B^-}),$$  (Equation 25)

where $C_{A^+}$ and $C_{B^-}$ are molar concentrations of $A^+$ and $B^-$ ions, respectively.

In the case of hypothetically pure water with absolutely no contaminants, the weak self-ionization of water molecules into protons and hydroxide ions can be formulated as Equation 26:

$$H_2O \rightleftharpoons H^+ + OH^-$$

$$K_w = [H^+][OH^-] = 10^{-14} \text{ at } 25°C$$  (Equation 26)

where $K_w$ is the equilibrium constant for the self-ionization of water. Given that $H^+$ and $OH^-$ ions will be responsible for the electrical conductivity of the electrolyte (water), Equation 25 can be written for them as in the form of Equation 27:

$$\kappa = \frac{e^2 N_A}{k_B T}([H^+]D_{H^+} + [OH^-]D_{OH^-}),$$  (Equation 27)

where $[H^+]$ and $[OH^-]$ in Equation 27 can be related to the pH as Equation 28:

$$[H^+] = 10^{-pH}, \text{ and } [OH^-] = \frac{10^{-14}}{[H^+]} = \frac{10^{-14}}{10^{-pH}} = 10^{pH-14},$$  (Equation 28)

Substitution of the relationships in Equation 28 in Equation 27 then gives Equation 29:

$$\kappa = \frac{e^2 N_A}{k_B T}(10^{-pH}D_{H^+} + 10^{pH-14}D_{OH^-}),$$  (Equation 29)

Equation 29 then provides the relationship between the conductivity, temperature, and water pH.

As expressed by Equation 29, temperature and pH are the only variables influencing the conductivity of ideally pure water. Assuming a constant temperature of 25°C (298 K), the conductivity can then be plotted as a function of pH after substituting all physicochemical constants, as illustrated by Figure S9A. The V-shaped curve shows a weak pH dependency of water conductivity around near-neutral pH regimes. Approaching either of the acidic or basic extreme ends of the pH spectrum results in infinitely large conductivities (Figure S9). At pH 7, a theoretical conductivity of 0.0549 μS cm$^{-1}$ is obtained for ideally pure water free of contaminants, which is very close to the experimentally measured conductivity of ultrapure deionized water reported elsewhere (<0.0555 μS cm$^{-1}$).[91]

The derivation of all the above expressions was based on the assumption that the $H^+$ and $OH^-$ ions are in dilute concentrations. Therefore, far deviations from the near-neutral regimes to either side of the pH range will negate the latter assumption for one of the ionic species and renders the calculations inaccurate. As such, a zoomed-in view of the near-neutral pH regimes (Figures S9B and S9C) would better

**Cell Reports**
# Physical Science
*Article*

**CellPress**
OPEN ACCESS

satisfy the starting assumptions regarding the dilute concentrations of both $H^+$ and $OH^-$ ions. As observed, within the pH range of 5–9, the conductivity is negligibly affected by the pH of the water, with a conductivity change of <0.005 mS cm$^{-1}$ in that pH window. Hence, while working within the pH window of 5–9, one could safely disregard the contribution of pH and be sure that the measured conductivity arises only from the presence of salt ions.

In contrast to pH, temperature variation has a much more complex effect on conductivity. Temperature variations change the self-ionization ($K_w$) of water, as expressed in Equation 26, and shifts the pH values as a result. Consequently, the expression pH + pOH = 14 will no longer hold. Temperature also affects the diffusion coefficients of $H^+$ and $OH^-$ ions in water, further making it less straightforward to plot a theoretical dependence of conductivity on temperature using Equation 25. As such, we measure the temperature dependency of conductivity experimentally in a wide temperature range of 15°C–55°C, as shown in Figure 9.

As expected, a steady increase in conductivity is observed upon increasing the temperature. Elevated temperatures increase the $K_w$ in Equation 26, resulting in more populations of protons and hydroxide ions and thereby increasing the conductivity. The two different conductivity probes show very similar slopes in conductivity-temperature graphs. Going from 15°C to 55°C, we see that the gain in conductivity in the case of a low-concentration NaCl electrolyte (10 mmol L$^{-1}$) is 10%–11%, whereas it is 6%–7% in the case of the high-concentration NaCl electrolyte (600 mmol L$^{-1}$). The slightly higher conductivity gain in the case of low-concentration electrolyte indicates the conductivity contribution coming from the water as a result of temperature change, which becomes only significant when dealing with low-concentration electrodes ($\leq$10 mM NaCl) and upon huge temperature variations such as 40°C. In the case of higher concentrations and slight temperature variations, it can be concluded that the temperature will not significantly influence conductivity and, hence, the concentration obtained.

In summary, the present work has illustrated in a step-by-step manner how a simple electrochemical desalination system is built and operated at the laboratory scale. At the heart of an electrochemical desalination setup, a cell houses a pair of electrodes that cyclically accomplish desalination when being charged and discharged. A conductivity meter monitors the conductivity change downstream of the cell. Once the conductivity meter is freshly calibrated with an array of stock solutions with known concentrations, it can reliably convert the measured conductivity of the cell's effluent water into the salt concentration, from which desalination capacity can be calculated. From the desalination capacity, the CE (and energy consumption) can also be calculated knowing the electronic charge data provided by the electrochemical workstation that applied voltage to the cell. The equations to calculate the said desalination metrics are also presented, which could be minimally modified for systems other than NaCl, such as LiCl.

We have emphasized that the conductivity meter has to be calibrated correctly and on time and have showcased how basing the calculations on 6-month-old calibration data could result in a significant deviation from actual performance metrics, specifically, 25%–30% relative error in final DC and CE values reported. We have additionally shown the significance of leakage current, how it is calculated, and how it could affect the CE values. We finally illustrated the relatively minimal effects of pH and temperature on the measured conductivities. The checklists provided in Notes S1 and S2 are developed to help the researchers have a quick overview of what is
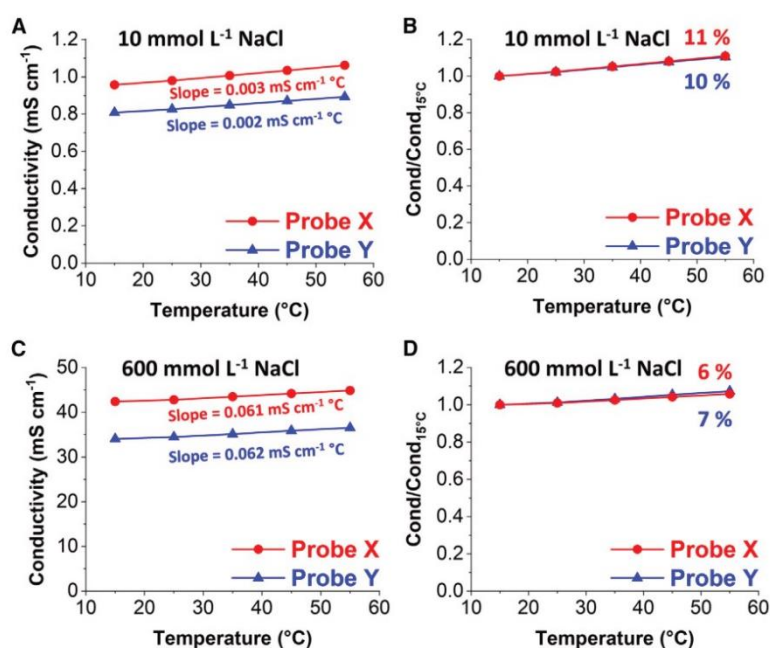
**Figure 9. Wide variation of temperature and its effect on conductivity**
Experimental temperature dependency of the conductivity of two conductivity probes from 15°C to 55°C in (A) low NaCl concentration electrolyte and (B) its normalized gain in conductivity, and (C) high NaCl concentration electrolyte and (D) its normalized gain in conductivity.

needed when designing electrochemical desalination setups and what and how to report once the raw data are generated from such a setup.

## EXPERIMENTAL PROCEDURES

### Resource availability

#### Lead contact

Requests for further information, resources, or materials should be directed to and will be fulfilled by the lead contact, Volker Presser (volker.presser@leibniz-inm.de), upon reasonable request.

#### Materials availability

This study did not generate new unique materials.

#### Data and code availability

The data generated in this study are included in the manuscript and supplemental information and will be made available from the lead contact upon reasonable request.

### Conductivity and pH measurements

Aqueous stock solutions of sodium chloride with concentrations of 1–1,000 mmol $L^{-1}$ were prepared by first making 0.5 L of 1 mol $L^{-1}$ NaCl (VWR Chemicals) parent solution, followed by dilution with deionized water (Milli-Q, Merck Millipore) to the target concentration values. The solutions were kept in plastic centrifuge vials in a climatized chamber (BINDER) at constant temperatures of 25°C overnight to reach the equilibrium temperature before measuring.

## Cell Reports
## Physical Science
### Article

**CellPress**
OPEN ACCESS

The ionic conductivity of each solution was measured by the conductivity probe (Metrohm, 5-ring conductivity measuring cell with integrated Pt1000 temperature sensor) connected to a module (Metrohm, 856 conductivity module), which communicates the data to a desktop computer. Likewise, the pH was measured by a glassy pH probe (Metrohm, 3 mol $L^{-1}$ KCl electrolyte, with an integrated Pt1000 temperature sensor) connected to a module (Metrohm, 867 pH module) that communicates the pH data to the computer. Both conductivity and pH online data are shown in real time on the computer (Tiamo, Metrohm).

For temperature-dependent investigations of conductivity and pH, the aqueous stock solutions were kept in a climatized chamber (BINDER) at constant temperatures of 15°C, 25°C, 35°C, 45°C, and 55°C (each case: ±1°C). At each temperature, the solutions were left in the climatized chamber overnight to equilibrate with the target temperature before the measurements were made.

### Electrode preparation

To prepare free-standing carbon electrodes, we followed the procedure outlined in our previous works.[16,92] Typically, the electrodes were made by adding enough ethanol to activated carbon (type YP-80F, Kuraray) in an agate mortar until it became entirely wet while manually stirring the mixture with a pestle. Once a homogeneous mixture was reached, polytetrafluoroethylene binder (60 mass % dispersion in water, from Sigma-Aldrich) was added to serve as a polymeric binder, using a carbon/binder mass ratio of 9:1. Stirring was continued under the fume hood until ethanol partially evaporated from the mixture to result in a carbon paste, which was further cold-rolled in a rolling machine (MTI HR01, MTI). The free-standing carbon films with a wet thickness of 600 μm were then dried in a vacuum oven (Memmert) at 50°C overnight.

### Electrochemical desalination tests

A pair of round pieces of the free-standing carbon electrodes were cut in 30-mm circular diameter and used as positive and negative electrodes for the electrochemical desalination cell. The carbon electrodes were sandwiched in a custom-made cell,[93] separated by a few round-shaped glass fiber filters (GF/A, Whatman) and nylon mesh pieces to allow the water stream to flow between the electrodes (flow-by configuration). To monitor the potential development in each electrode individually upon charge and discharge, a spectator Ag/AgCl reference electrode (3 M NaCl, BASi) was mounted on the cell near the electrodes. When needed, polymeric ion-exchange membranes with a diameter of 50 mm were cut and soaked into 20 mmol $L^{-1}$ NaCl electrolyte overnight. Anion-exchange membrane (Fumasep FAA-3-20, Fuma-tech) was placed in between the positive electrode and the flow channel, and the cation-exchange membrane (Fumasep FKE-20, Fuma-tech) was placed in between the negative electrode and the flow channel.

Ten liters of 20 mmol $L^{-1}$ aqueous NaCl solution was stored in a tank as the electrolyte, where it is constantly bubbled with a small nitrogen flow to minimize carbon electrode oxidation due to the presence of dissolved oxygen in the electrolyte. The electrolyte was pumped from the tank via a peristaltic pump (Masterflex) at flow rate of ~2 mL $min^{-1}$ into the cell. To ensure that accurate flow-rate values were obtained, the flow was collected manually using a 10-mL graduated cylinder for 5 min after each day of desalination measurements. The water stream flowing out of the cell went further into the chamber containing the conductivity probe, followed by the pH probe chamber, and finally cycled back into the tank to complete the loop (called a single-pass mode of operation). The entire setup was kept in a

climatized chamber at 25°C $\pm$ 1°C to eliminate possible effects from day/night fluctuations in temperature.

Electrochemical testing was then carried out using an electrochemical workstation (Bio-Logic, potentiostat/galvanostat, type VSP300), programmed to repeatedly charge and discharge the cell at the rate of 0.1 A g$^{-1}$ concerning the total mass of both carbon electrodes combined.

For selectivity measurements, a 1-L aqueous electrolyte of KCl (Sigma-Aldrich), NaCl (Roth), and CaCl$_2$ (Sigma-Aldrich), each at 10 mmol L$^{-1}$ concentration, was prepared. The electrolyte was constantly bubbled with nitrogen and pumped via a peristaltic pump (Masterflex Reglo ICC Digital Pump with independent channel control, 3-channel, 8-roller) into an electrochemical cell with symmetric carbon/carbon cloth electrodes (Kynol ACC-5092-20). The water stream flowing out of the cell first went into the chamber containing the conductivity probe and then proceeded to the ICP-OES instrument (ICP-OES, ARCOS FHX22, SPECTRO Analytical Instruments) before finally being discarded. The concentration of each ionic species was determined individually by intensity-concentration equations obtained by calibration of known samples beforehand (Table S1 and Figure S5).

## SUPPLEMENTAL INFORMATION

Supplemental information can be found online at https://doi.org/10.1016/j.xcrp.2023.101661.

## AUTHOR CONTRIBUTIONS

M.T.: investigation, conceptualization, data curation, visualization, supervision, writing – original draft, writing – review & editing. C. Kök: investigation, data curation, writing – review & editing. P.R.B.: investigation, data curation, writing – review & editing. P.R.: writing – review & editing. Y.Z.: supervision, validation, writing – review & editing. J.L.: conceptualization, supervision, validation, writing – review & editing. C. Kim: supervision, validation, writing – original draft, writing – review & editing. V.P.: conceptualization, supervision, validation, resources, visualization, writing – original draft, writing – review & editing, project administration, funding acquisition.

## DECLARATION OF INTERESTS

The authors declare no competing interests.

**CellPress**
OPEN ACCESS

## REFERENCES

1. Shocron, A.N., Roth, R.S., Guyes, E.N., Epsztein, R., and Suss, M.E. (2022). Comparison of ion selectivity in electrodialysis and capacitive deionization. Environ. Sci. Technol. Lett. 9, 889–899. https://doi.org/10.1021/acs.estlett.2c00551.

2. Gamaethiralalage, J.G., Singh, K., Sahin, S., Yoon, J., Elimelech, M., Suss, M.E., Liang, P., Biesheuvel, P.M., Zornitta, R.L., and de Smet, L.C.P.M. (2021). Recent advances in ion selectivity with capacitive deionization. Energy Environ. Sci. 14, 1095–1120. https://doi.org/10.1039/D0EE03145C.

3. Deng, D., Dydek, E.V., Han, J.H., Schlumpberger, S., Mani, A., Zaltzman, B., and Bazant, M.Z. (2013). Overlimiting current and shock electrodialysis in porous media. Langmuir 29, 16167–16177. https://doi.org/10.1021/la4040547.

4. Tian, H., Alkhadra, M.A., Conforti, K.M., and Bazant, M.Z. (2021). Continuous and selective removal of lead from drinking water by shock electrodialysis. ACS ES. T. Water 1, 2269–2274. https://doi.org/10.1021/acsestwater.1c00234.

5. Alkhadra, M.A., Gao, T., Conforti, K.M., Tian, H., and Bazant, M.Z. (2020). Small-scale desalination of seawater by shock electrodialysis. Desalination 476, 114219. https://doi.org/10.1016/j.desal.2019.114219.

6. Sharan, P., Yoon, T.J., Jaffe, S.M., Ju, T., Currier, R.P., and Findikoglu, A.T. (2021). Can capacitive deionization outperform reverse osmosis for brackish water desalination? Cleaner Engineering and Technology 3, 100102. https://doi.org/10.1016/j.clet.2021.100102.

7. Metzger, M., Besli, M.M., Kuppan, S., Hellstrom, S., Kim, S., Sebti, E., Subban, C.V., and Christensen, J. (2020). Techno-economic analysis of capacitive and intercalative water deionization. Energy Environ. Sci. 13, 1544–1560. https://doi.org/10.1039/D0EE00725K.

8. Wang, L., Arnold, S., Ren, P., Wang, Q., Jin, J., Wen, Z., and Presser, V. (2022). Redox flow battery for continuous and energy-effective lithium recovery from aqueous solution. ACS Energy Lett. 7, 3539–3544. https://doi.org/10.1021/acsenergylett.2c01746.

9. Kang, J., Zhang, P., Gao, Z., Zhang, J., Yan, Z., Wang, H., and Chen, R. (2016). Direct energy recovery system for membrane capacitive deionization. Desalination 130, 144–151. https://doi.org/10.1016/j.desal.2016.07.025.

10. Zhang, Y., Ren, P., Wang, L., Pameté, E., Husmann, S., and Presser, V. (2022). Selectivity toward heavier monovalent cations of carbon ultramicropores used for capacitive deionization. Desalination 542, 116053. https://doi.org/10.1016/j.desal.2022.116053.

11. Wang, L., Torkamanzadeh, M., Majed, A., Zhang, Y., Wang, Q., Breitung, B., Feng, G., Naguib, M., and Presser, V. (2022). Time-dependent cation selectivity of titanium carbide MXene in aqueous solution. Advanced Sustainable Systems 6, 2100383. https://doi.org/10.1002/adsu.202100383.

12. Porada, S., Zhao, R., van der Wal, A., Presser, V., and Biesheuvel, P.M. (2013). Review on the science and technology of water desalination by capacitive deionization. Prog. Mater. Sci. 58, 1388–1442. https://doi.org/10.1016/j.pmatsci.2013.03.005.

13. Suss, M.E., Porada, S., Sun, X., Biesheuvel, P.M., Yoon, J., and Presser, V. (2015). Water desalination via capacitive deionization: what is it and what can we expect from it? Energy Environ. Sci. 8, 2296–2319. https://doi.org/10.1039/C5EE00519A.

14. Srimuk, P., Su, X., Yoon, J., Aurbach, D., and Presser, V. (2020). Charge-transfer materials for electrochemical water desalination, ion separation and the recovery of elements. Nat. Rev. Mater. 5, 517–538. https://doi.org/10.1038/s41578-020-0193-1.

15. Wang, L., Zhang, Y., Moh, K., and Presser, V. (2021). From capacitive deionization to desalination batteries and desalination fuel cells. Curr. Opin. Electrochem. 29, 100758. https://doi.org/10.1016/j.coelec.2021.100758.

16. Torkamanzadeh, M., Wang, L., Zhang, Y., Budak, Ö., Srimuk, P., and Presser, V. (2020). MXene/activated-carbon hybrid capacitive deionization for permselective ion removal at low and high salinity. ACS Appl. Mater. Interfaces 12, 26013–26025. https://doi.org/10.1021/acsami.0c05975.

17. Srimuk, P., Zeiger, M., Jäckel, N., Tolosa, A., Krüner, B., Fleischmann, S., Grobelsek, I., Aslan, M., Shvartsev, B., Suss, M.E., and Presser, V. (2017). Enhanced performance stability of carbon/titania hybrid electrodes during capacitive deionization of oxygen saturated saline water. Electrochim. Acta 224, 314–328. https://doi.org/10.1016/j.electacta.2016.12.060.

18. Srimuk, P., Ries, L., Zeiger, M., Fleischmann, S., Jäckel, N., Tolosa, A., Krüner, B., Aslan, M., and Presser, V. (2016). High performance stability of titania decorated carbon for desalination with capacitive deionization in oxygenated water. RSC Adv. 6, 106081–106089. https://doi.org/10.1039/C6RA22800C.

19. Wang, L., Violet, C., DuChanois, R.M., and Elimelech, M. (2020). Derivation of the theoretical minimum energy of separation of desalination processes. J. Chem. Educ. 97, 4361–4369. https://doi.org/10.1021/acs.jchemed.0c01194.

20. Porada, S., Weingarth, D., Hamelers, H.V.M., Bryjak, M., Presser, V., and Biesheuvel, P.M. (2014). Carbon flow electrodes for continuous operation of capacitive deionization and capacitive mixing energy generation. J. Mater. Chem. A Mater. 2, 9313–9321. https://doi.org/10.1039/C4TA01783H.

21. Srimuk, P., Halim, J., Lee, J., Tao, Q., Rosen, J., and Presser, V. (2018). Two-dimensional molybdenum carbide (MXene) with divacancy ordering for brackish and seawater desalination via cation and anion intercalation. ACS Sustain. Chem. Eng. 6, 3739–3747. https://doi.org/10.1021/acssuschemeng.7b04095.

22. Biesheuvel, P., and Van der Wal, A. (2010). Membrane capacitive deionization. J. Membr. Sci. 346, 256–262.

23. Hemmatifar, A., Palko, J.W., Stadermann, M., and Santiago, J.G. (2016). Energy breakdown in capacitive deionization. Water Res. 104, 303–311. https://doi.org/10.1016/j.watres.2016.08.020.

24. Zhang, C., He, D., Ma, J., Tang, W., and Waite, T.D. (2018). Faradaic reactions in capacitive deionization (CDI) - problems and possibilities: A review. Water Res. 128, 314–330. https://doi.org/10.1016/j.watres.2017.10.024.

25. Srimuk, P., Lee, J., Tolosa, A., Kim, C., Aslan, M., and Presser, V. (2017). Titanium disulfide: a promising low-dimensional electrode material for sodium ion intercalation for seawater desalination. Chem. Mater. 29, 9964–9973. https://doi.org/10.1021/acs.chemmater.7b03363.

26. Harb, C., Pan, J., DeVilbiss, S., Badgley, B., Marr, L.C., Schmale, D.G., III, and Foroutan, H. (2021). Increasing freshwater salinity impacts aerosolized bacteria. Environ. Sci. Technol. 55, 5731–5741. https://doi.org/10.1021/acs.est.0c08558.

27. United States Geological Survey (2018). Saline Water and Salinity. https://www.usgs.gov/special-topics/water-science-school/science/saline-water-and-salinity.

28. Bartels, C., Franks, R., Rybar, S., Schierach, M., and Wilf, M. (2005). The effect of feed ionic strength on salt passage through reverse osmosis membranes. Desalination 184, 185–195. https://doi.org/10.1016/j.desal.2005.04.032.

29. Zhang, Y., Ren, P., Liu, Y., and Presser, V. (2022). Particle size distribution influence on capacitive deionization: Insights for electrode preparation. Desalination 525, 115503. https://doi.org/10.1016/j.desal.2021.115503.

30. Długołęcki, P., and van der Wal, A. (2013). Energy recovery in membrane capacitive deionization. Environ. Sci. Technol. 47, 4904–4910. https://doi.org/10.1021/es3053202.

31. Alkhadra, M.A., Su, X., Suss, M.E., Tian, H., Guyes, E.N., Shocron, A.N., Conforti, K.M., de Souza, J.P., Kim, N., Tedesco, M., et al. (2022). Electrochemical methods for water purification, ion separations, and energy conversion. Chem. Rev. 122, 13547–13635. https://doi.org/10.1021/acs.chemrev.1c00396.

32. Vieceli, N., Vonderstein, C., Swiontekc, T., Stopić, S., Dertmann, C., Sojka, R., Reinhardt, N., Ekberg, C., Friedrich, B., and Petranikova, M. (2023). Recycling of Li-ion batteries from industrial processing: upscaled hydrometallurgical treatment and recovery of high purity manganese by solvent extraction. Solvent Extr. Ion Exch. 41, 205–220. https://doi.org/10.1080/07366299.2023.2165405.

33. Mo, D., Yu, G., Zeng, Z., Ni, S., Zhang, S., and Sun, X. (2023). Separation of lithium and transition metals in leaching solution of used lithium ion battery with Sec-octylphenoxyacetic acid. ChemistrySelect 8, e202301036. https://doi.org/10.1002/slct.202301036.

34. Asadi Dalini, E., Karimi, G., and Zandevakili, S. (2021). Treatment of valuable metals from leaching solution of spent lithium-ion batteries.

Miner. Eng. *173*, 107226. https://doi.org/10.1016/j.mineng.2021.107226.

35. Trócoli, R., Battistel, A., and Mantia, F.L. (2014). Selectivity of a lithium-recovery process based on LiFePO$_4$. Chemistry *20*, 9888–9891. https://doi.org/10.1002/chem.201403535.

36. Pasta, M., Battistel, A., and La Mantia, F. (2012). Batteries for lithium recovery from brines. Energy Environ. Sci. *5*, 9487–9491. https://doi.org/10.1039/C2EE22977C.

37. Lee, J., Yu, S.H., Kim, C., Sung, Y.E., and Yoon, J. (2013). Highly selective lithium recovery from brine using a lambda-MnO$_2$-Ag battery. Phys. Chem. Chem. Phys. *15*, 7690–7695. https://doi.org/10.1039/c3cp50919b.

38. Trócoli, R., Erinmwingbovo, C., and La Mantia, F. (2017). Optimized lithium recovery from brines by using an electrochemical ion-pumping process based on λ-MnO$_2$ and nickel hexacyanoferrate. Chemelectrochem *4*, 143–149. https://doi.org/10.1002/celc.201600509.

39. Kim, S., Lee, J., Kang, J.S., Jo, K., Kim, S., Sung, Y.E., and Yoon, J. (2015). Lithium recovery from brine using a lambda-MnO$_2$/activated carbon hybrid supercapacitor system. Chemosphere *125*, 50–56. https://doi.org/10.1016/j.chemosphere.2015.01.024.

40. Jiang, L., Zhu, L., Chen, L., Ding, Y., Zhang, W., and Brice, S. (2022). Coupling hybrid membrane capacitive deionization (HMCDI) with electric-enhanced direct contact membrane distillation (EE-DCMD) for lithium/cobalt separation and concentration. Separ. Purif. Technol. *302*, 122082. https://doi.org/10.1016/j.seppur.2022.122082.

41. Singh, K., Qian, Z., Biesheuvel, P., Zuilhof, H., Porada, S., and de Smet, L.C. (2020). Nickel hexacyanoferrate electrodes for high mono/divalent ion-selectivity in capacitive deionization. Desalination *481*, 114346. https://doi.org/10.1016/j.desal.2020.114346.

42. Lee, S.-H., Choi, M., Moon, J.-K., Kim, S.-W., Lee, S., Ryu, I., Choi, J., and Kim, S. (2022). Electrosorption removal of cesium ions with a copper hexacyanoferrate electrode in a capacitive deionization (CDI) system. Colloids Surf. A Physicochem. Eng. Asp. *647*, 129175. https://doi.org/10.1016/j.colsurfa.2022.129175.

43. Tsai, S.-W., Cuong, D.V., and Hou, C.-H. (2022). Selective capture of ammonium ions from municipal wastewater treatment plant effluent with a nickel hexacyanoferrate electrode. Water Res. *221*, 118786. https://doi.org/10.1016/j.watres.2022.118786.

44. Xing, W., Liang, J., Tang, W., Zeng, G., Wang, X., Li, X., Jiang, L., Luo, Y., Li, X., Tang, N., and Huang, M. (2019). Perchlorate removal from brackish water by capacitive deionization: Experimental and theoretical investigations. Chem. Eng. J. *361*, 209–218. https://doi.org/10.1016/j.cej.2018.12.074.

45. Hong, S.P., Yoon, H., Lee, J., Kim, C., Kim, S., Lee, J., Lee, C., and Yoon, J. (2020). Selective phosphate removal using layered double hydroxide/reduced graphene oxide (LDH/rGO) composite electrode in capacitive deionization. J. Colloid Interface Sci. *564*, 1–7. https://doi.org/10.1016/j.jcis.2019.12.068.

46. Hawks, S.A., Cerón, M.R., Oyarzun, D.I., Pham, T.A., Zhan, C., Loeb, C.K., Mew, D., Deinhart, A., Wood, B.C., Santiago, J.G., et al. (2019). Using ultramicroporous carbon for the selective removal of nitrate with capacitive deionization. Environ. Sci. Technol. *53*, 10863–10870. https://doi.org/10.1021/acs.est.9b01374.

47. Zuo, K., Kim, J., Jain, A., Wang, T., Verduzco, R., Long, M., and Li, Q. (2018). Novel composite electrodes for selective removal of sulfate by the capacitive deionization process. Environ. Sci. Technol. *52*, 9486–9494. https://doi.org/10.1021/acs.est.8b01868.

48. Chang, J., Li, Y., Duan, F., Su, C., Li, Y., and Cao, H. (2020). Selective removal of chloride ions by bismuth electrode in capacitive deionization. Separ. Purif. Technol. *240*, 116600. https://doi.org/10.1016/j.seppur.2020.116600.

49. Li, Y., Wu, J., Yong, T., Fei, Y., and Qi, J. (2021). Investigation of bromide removal and bromate minimization of membrane capacitive deionization for drinking water treatment. Chemosphere *280*, 130857. https://doi.org/10.1016/j.chemosphere.2021.130857.

50. Liu, Q., Xie, B., and Xiao, D. (2022). High efficient and continuous recovery of iodine in saline wastewater by flow-electrode capacitive deionization. Separ. Purif. Technol. *296*, 121419. https://doi.org/10.1016/j.seppur.2022.121419.

51. Pan, J., Zheng, Y., Ding, J., Gao, C., Van der Bruggen, B., and Shen, J. (2018). Fluoride removal from water by membrane capacitive deionization with a monovalent anion selective membrane. Ind. Eng. Chem. Res. *57*, 7048–7053. https://doi.org/10.1021/acs.iecr.8b00929.

52. Park, G., Hong, S.P., Lee, C., Lee, J., and Yoon, J. (2021). Selective fluoride removal in capacitive deionization by reduced graphene oxide/hydroxyapatite composite electrode. J. Colloid Interface Sci. *581*, 396–402. https://doi.org/10.1016/j.jcis.2020.07.108.

53. Uwayid, R., Guyes, E.N., Shocron, A.N., Gilron, J., Elimelech, M., and Suss, M.E. (2022). Perfect divalent cation selectivity with capacitive deionization. Water Res. *210*, 117959. https://doi.org/10.1016/j.watres.2021.117959.

54. Xiang, S., Mao, H., Geng, W., Xu, Y., and Zhou, H. (2022). Selective removal of Sr(II) from saliferous radioactive wastewater by capacitive deionization. J. Hazard Mater. *431*, 128591. https://doi.org/10.1016/j.jhazmat.2022.128591.

55. Zhang, X., Yang, F., Ma, J., and Liang, P. (2020). Effective removal and selective capture of copper from salty solution in flow electrode capacitive deionization. Environ. Sci, Water Res. Technol. *6*, 341–350. https://doi.org/10.1039/C9EW00467J.

56. Li, H., Zou, J., Yao, Z., Yu, J., Wang, H., and Xu, J. (2010). Using graphene nano-flakes as electrodes to remove ferric ions by capacitive deionization. J. Neuroimmunol. *219*, 8–16. https://doi.org/10.1016/j.seppur.2010.07.003.

57. Wang, C., Li, T., Yu, G., and Deng, S. (2021). Removal of low concentrations of nickel ions in electroplating wastewater using capacitive deionization technology. Chemosphere *284*, 131341. https://doi.org/10.1016/j.chemosphere.2021.131341.

58. Siekierka, A., and Yalcinkaya, F. (2022). Selective cobalt-exchange membranes for electrodialysis dedicated for cobalt recovery from lithium, cobalt and nickel solutions. Separ. Purif. Technol. *299*, 121695. https://doi.org/10.1016/j.seppur.2022.121695.

59. Soysüren, G., Yetgin, A.G., Arar, Ö., and Arda, M. (2022). Removal of manganese (II) from aqueous solution by ionic liquid impregnated polymeric sorbent and electrodeionization (EDI) techniques. Process Saf. Environ. Protect. *158*, 189–198. https://doi.org/10.1016/j.psep.2021.11.053.

60. Tang, W., Wang, X., Zeng, G., Liang, J., Li, X., Xing, W., He, D., Tang, L., and Liu, Z. (2019). Electro-assisted adsorption of Zn(II) on activated carbon cloth in batch-flow mode: experimental and theoretical investigations. Environ. Sci. Technol. *53*, 2670–2678. https://doi.org/10.1021/acs.est.8b05909.

61. Huang, X., Guo, X., Dong, Q., Liu, L., Tallon, R., and Chen, J. (2019). Zero-wastewater capacitive deionization: selective removal of heavy metal ions in tap water assisted by phosphate ions. Environ. Sci.: Nano *6*, 3225–3231. https://doi.org/10.1039/C9EN00730J.

62. Wang, L., Deligniere, L., Husmann, S., Leiner, R., Bahr, C., Zhang, S., Dun, C., Montemore, M.M., Gallei, M., Urban, J.J., et al. (2023). Selective Pb$^{2+}$ removal and electrochemical regeneration of fresh and recycled FeOOH. Nano Res. *16*, 9352–9363. https://doi.org/10.1007/s12274-023-5569-2.

63. Peng, Q., Liu, L., Luo, Y., Zhang, Y., Tan, W., Liu, F., Suib, S.L., and Qiu, G. (2016). Cadmium removal from aqueous solution by a deionization supercapacitor with a birnessite electrode. ACS Appl. Mater. Interfaces *8*, 34405–34413. https://doi.org/10.1021/acsami.6b12224.

64. Bao, S., Duan, J., and Zhang, Y. (2018). Recovery of V(V) from complex vanadium solution using capacitive deionization (CDI) with resin/carbon composite electrode. Chemosphere *208*, 14–20. https://doi.org/10.1016/j.chemosphere.2018.05.149.

65. Su, X., Kushima, A., Halliday, C., Zhou, J., Li, J., and Hatton, T.A. (2018). Electrochemically-mediated selective capture of heavy metal chromium and arsenic oxyanions from water. Nat. Commun. *9*, 4701. https://doi.org/10.1038/s41467-018-07159-0.

66. Li, C., Ramasamy, D.L., Sillanpää, M., and Repo, E. (2021). Separation and concentration of rare earth elements from wastewater using electrodialysis technology. Separ. Purif. Technol. *254*, 117442. https://doi.org/10.1016/j.seppur.2020.117442.

67. Xiang, H.D., Liu, P., Deng, M., and Tong, D.G. (2021). Separation of rare-earth ions from mine wastewater using B$_{12}$S nanoflakes as a capacitive deionization electrode material. J. Nanosci. Nanotechnol. *21*, 5459–5476. https://doi.org/10.1166/jnn.2021.19466.

68. Xiong, Y., Yang, X., Liu, Y., Chen, X., Wang, G., Lu, B., Lin, G., and Huang, B. (2022). Fabrication of phosphorus doping porous carbon derived from bagasse for highly-efficient removal of

La$^{3+}$ ions via capacitive deionization. Electrochim. Acta 404, 139735. https://doi.org/10.1016/j.electacta.2021.139735.

69. Wang, L., Gao, Y., Chai, Y., and Sun, X. (2022). Recovery of rare earth by electro-sorption with sodium diphenylamine sulfonate modified activated carbon electrode. Separ. Purif. Technol. 292, 121005. https://doi.org/10.1016/j.seppur.2022.121005.

70. Chen, L., and Tong, D.G. (2020). Amorphous boron phosphide nanosheets: A highly efficient capacitive deionization electrode for uranium separation from seawater with superior selectivity. Separ. Purif. Technol. 250, 117175. https://doi.org/10.1016/j.seppur.2020.117175.

71. Zhang, Y., Peng, J., Feng, G., and Presser, V. (2021). Hydration shell energy barrier differences of sub-nanometer carbon pores enable ion sieving and selective ion removal. Chem. Eng. J. 419, 129438. https://doi.org/10.1016/j.cej.2021.129438.

72. Hemmatifar, A., Oyarzun, D.I., Palko, J.W., Hawks, S.A., Stadermann, M., and Santiago, J.G. (2017). Equilibria model for pH variations and ion adsorption in capacitive deionization electrodes. Water Res. 122, 387–397. https://doi.org/10.1016/j.watres.2017.05.036.

73. Oyarzun, D.I., Hemmatifar, A., Palko, J.W., Stadermann, M., and Santiago, J.G. (2018). Ion selectivity in capacitive deionization with functionalized electrode: Theory and experimental validation. Water Res. X 1, 100008. https://doi.org/10.1016/j.wroa.2018.100008.

74. Liu, Y., Ma, W., Cheng, Z., Xu, J., Wang, R., and Gang, X. (2013). Preparing CNTs/Ca-Selective zeolite composite electrode to remove calcium ions by capacitive deionization. Desalination 326, 109–114. https://doi.org/10.1016/j.desal.2013.07.022.

75. Yan, J., and Indra, E.M. (2012). Colorimetric Method for Determining Pb2+ Ions in Water Enhanced with Non-Precious-Metal Nanoparticles. Anal. Chem. 84, 6122–6127. https://doi.org/10.1021/ac301018y.

76. Guyes, E.N., Shocron, A.N., Chen, Y., Diesendruck, C.E., and Suss, M.E. (2021). Long-lasting, monovalent-selective capacitive deionization electrodes. npj Clean Water 4, 1–11. https://doi.org/10.1038/s41545-021-00109-2.

77. Bahga, S.S., Bercovici, M., and Santiago, J.G. (2010). Ionic strength effects on electrophoretic focusing and separations. Electrophoresis 31, 910–919. https://doi.org/10.1002/elps.200900560.

78. Kay, R.L. (1960). An application of the fuoss-onsager conductance theory to the alkali halides in several solvents. J. Am. Chem. Soc. 82, 2099–2105.

79. Zhao, R., van Soestbergen, M., Rijnaarts, H.H.M., van der Wal, A., Bazant, M.Z., and Biesheuvel, P.M. (2012). Time-dependent ion selectivity in capacitive charging of porous electrodes. J. Colloid Interface Sci. 384, 38–44. https://doi.org/10.1016/j.jcis.2012.06.022.

80. Dykstra, J.E., Dijkstra, J., van der Wal, A., Hamelers, H.V.M., and Porada, S. (2016). On-line method to study dynamics of ion adsorption from mixtures of salts in capacitive deionization. Desalination 390, 47–52. https://doi.org/10.1016/j.desal.2016.04.001.

81. Santos, C., and La Mantia, F. (2022). Recent advances in reactor design and control for lithium recovery by means of electrochemical ion pumping. Curr. Opin. Electrochem. 35, 101089. https://doi.org/10.1016/j.coelec.2022.101089.

82. Qu, Y., Campbell, P.G., Gu, L., Knipe, J.M., Dzenitis, E., Santiago, J.G., and Stadermann, M. (2016). Energy consumption analysis of constant voltage and constant current operations in capacitive deionization. Desalination 400, 18–24. https://doi.org/10.1016/j.desal.2016.09.014.

83. Halliday, D., Resnick, R., and Walker, J. (2013). Fundamentals of Physics (John Wiley & Sons).

84. Rafik, F., Gualous, H., Gallay, R., Crausaz, A., and Berthon, A. (2007). Frequency, thermal and voltage supercapacitor characterization and modeling. J. Power Sources 165, 928–934.

https://doi.org/10.1016/j.jpowsour.2006.12.021.

85. Haque, M., Li, Q., Smith, A.D., Kuzmenko, V., Rudquist, P., Lundgren, P., and Enoksson, P. (2020). Self-discharge and leakage current mitigation of neutral aqueous-based supercapacitor by means of liquid crystal additive. J. Power Sources 453, 227897. https://doi.org/10.1016/j.jpowsour.2020.227897.

86. Kötz, R., Sauter, J.-C., Ruch, P., Dietrich, P., Büchi, F., Magne, P., and Varenne, P. (2007). Voltage balancing: Long-term experience with the 250 V supercapacitor module of the hybrid fuel cell vehicle HY-LIGHT. J. Power Sources 174, 264–271. https://doi.org/10.1016/j.jpowsour.2007.08.078.

87. Atkins, P., Atkins, P.W., and de Paula, J. (2014). Atkins' Physical Chemistry (Oxford University Press).

88. Castellan, G.W. (1983). Physical Chemistry (Wesley Publishing Company).

89. Dill, K., and Bromberg, S. (2010). Molecular Driving Forces: Statistical Thermodynamics in Biology, Chemistry, Physics, and Nanoscience (Garland Science).

90. Dalal, M. (2018). A Textbook of Physical Chemistry (Dalal Institute).

91. Light, T.S., Kingman, B., and Bevilacqua, A.C. (1995). The conductivity of low concentrations of CO$_2$ dissolved in ultrapure water from 0-100°C. In 209$^{th}$ American Chemical Society National Meeting.

92. Aslan, M., Zeiger, M., Jäckel, N., Grobelsek, I., Weingarth, D., and Presser, V. (2016). Improved capacitive deionization performance of mixed hydrophobic/hydrophilic activated carbon electrodes. J. Phys. Condens. Matter 28, 114003. https://doi.org/10.1088/0953-8984/28/11/114003.

93. Bi, S., Zhang, Y., Cervini, L., Mo, T., Griffin, J.M., Presser, V., and Feng, G. (2020). Permselective ion electrosorption of subnanometer pores at high molar strength enables capacitive deionization of saline water. Sustain. Energy Fuels 4, 1285–1295. https://doi.org/10.1039/C9SE00996E.

# Supplemental information

# Best practice for electrochemical water

# desalination data generation and analysis

**Mohammad Torkamanzadeh, Cansu Kök, Peter Rolf Burger, Panyu Ren, Yuan Zhang, Juhan Lee, Choonsoo Kim, and Volker Presser**
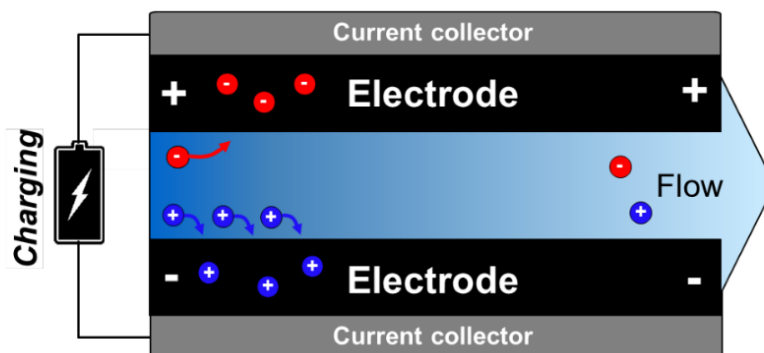
**Supplemental Figures**

**Figure S1.**



**Figure S1. A simple electrochemical desalination cell.** Schematic representation of an electrochemical desalination cell with flow-by configuration, where the water stream passes in between the two electrodes.

**Figure S2.**
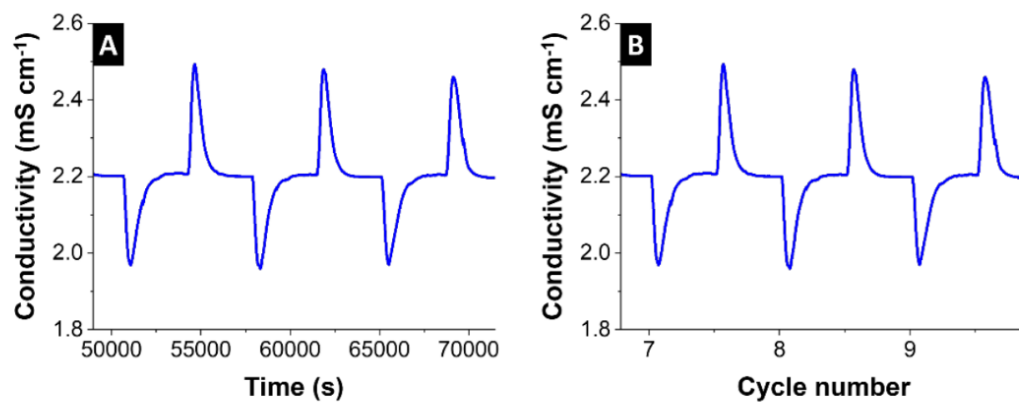


Figure S2. **Changing the time into cycle number.** Conversion of conductivity vs. time data (A) into conductivity vs. cycle number (B).

**Figure S3.**
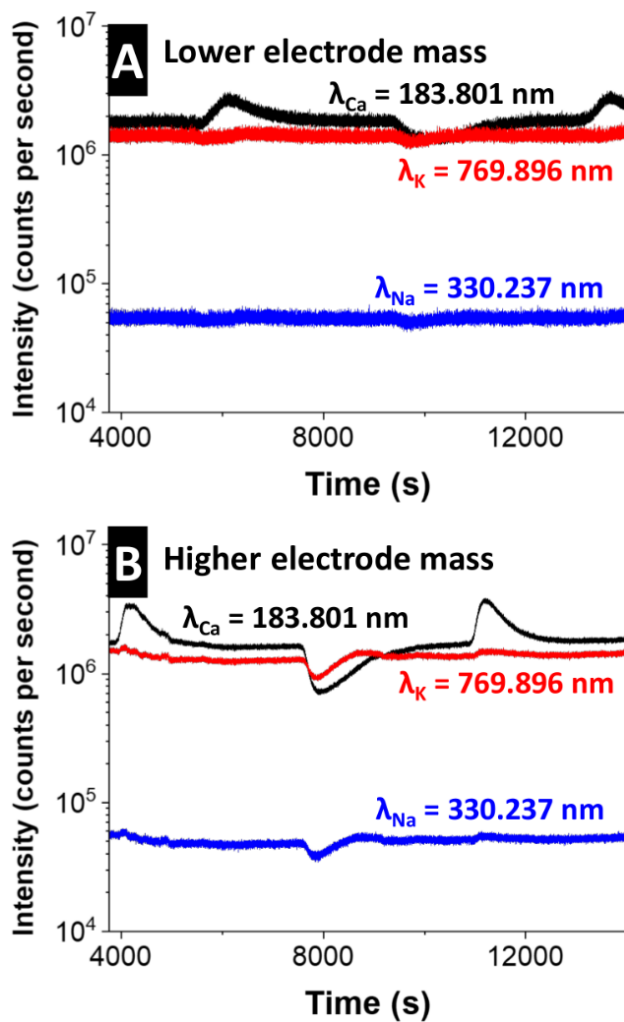


**Figure S3. Raw online elemental monitoring data.** Variation of the intensities individually recorded from calcium, potassium, and sodium ions using online ICP-OES monitoring of effluent water stream of a carbon/carbon electrochemical cell showing (A) rather noisy data with a cell containing 294 mg carbon cloth as negative electrode and 293 mg carbon cloth as positive electrode, and (B) less noisy data with a cell containing 506 mg carbon cloth as negative electrode and 501 mg carbon cloth as positive electrode.

**Figure S4.**
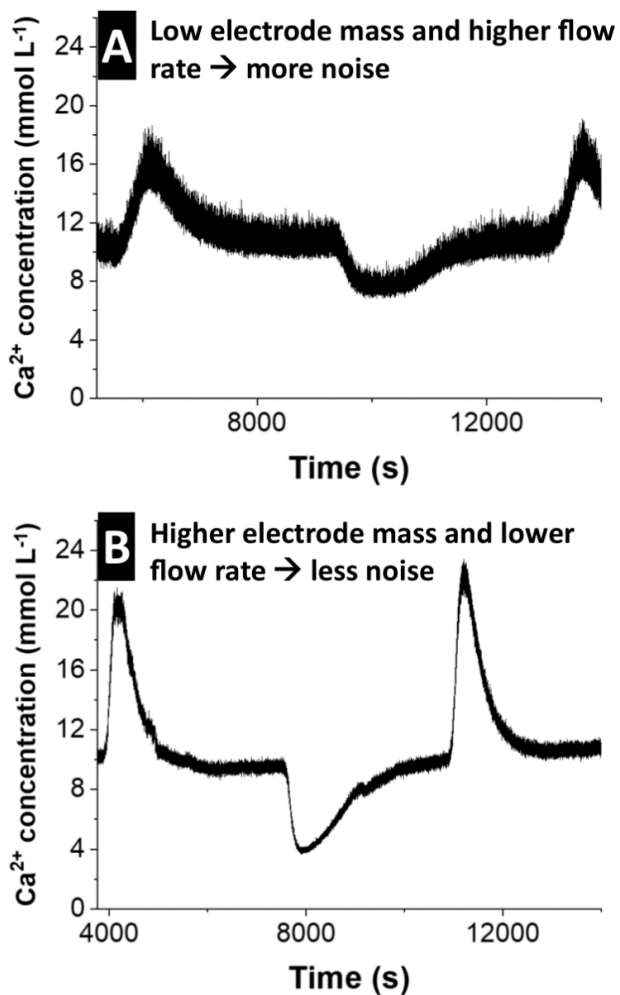


**Figure S4. Improving the signal to noise ratio.** Calcium concentration change derived from raw ICP-OES intensity data (**Figure S7**) using concentration-intensity equations obtained from calibration curves (**Figure S6**): (A) a rather noisy concentration profile with a cell containing 294 mg carbon cloth as negative electrode and 293 mg carbon cloth as positive electrode and (B) less noisy concentration profile with a cell containing 506 mg carbon cloth as negative electrode and 501 mg carbon cloth as positive electrode.

**Figure S5.**
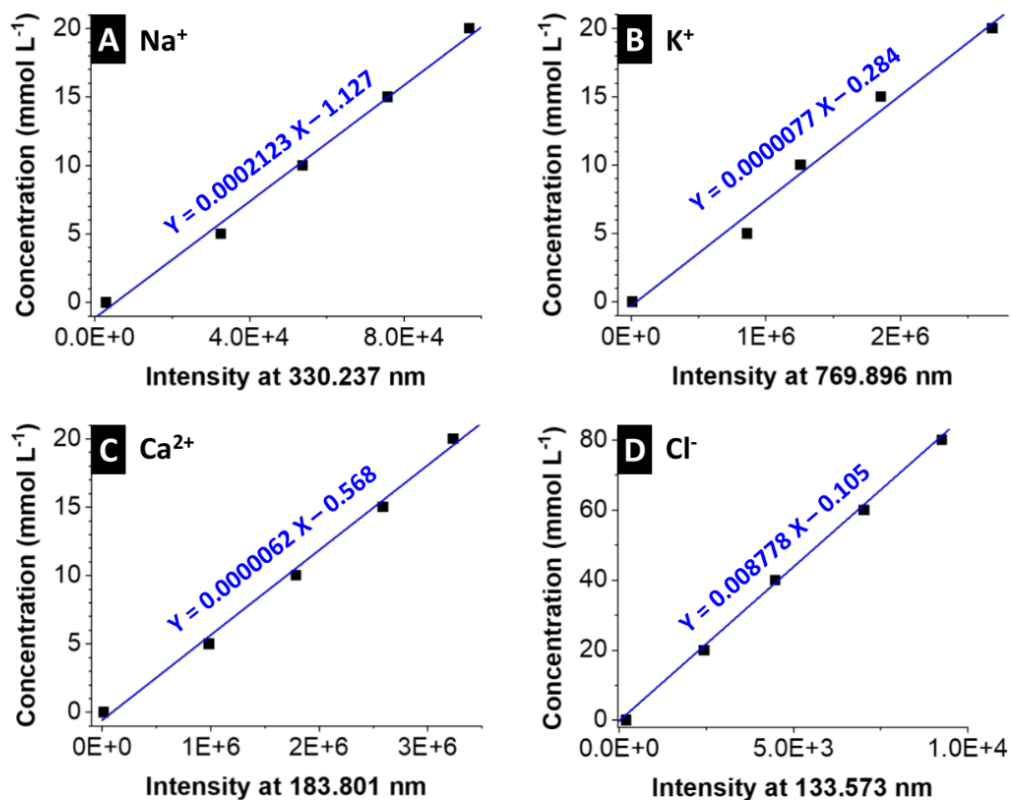


**Figure S5. Construction of the calibration curves relating the ICP-OES intensity to the concentration.** Concentration-intensity curves constructed using the solutions listed in **Table S1** to calibrate the ICP-OES instrument so that the measured optical emission intensity of each element can be individually converted into its concentration for (A) sodium, (B) potassium, (C) calcium, and (D) chloride ions.

**Figure S6.**
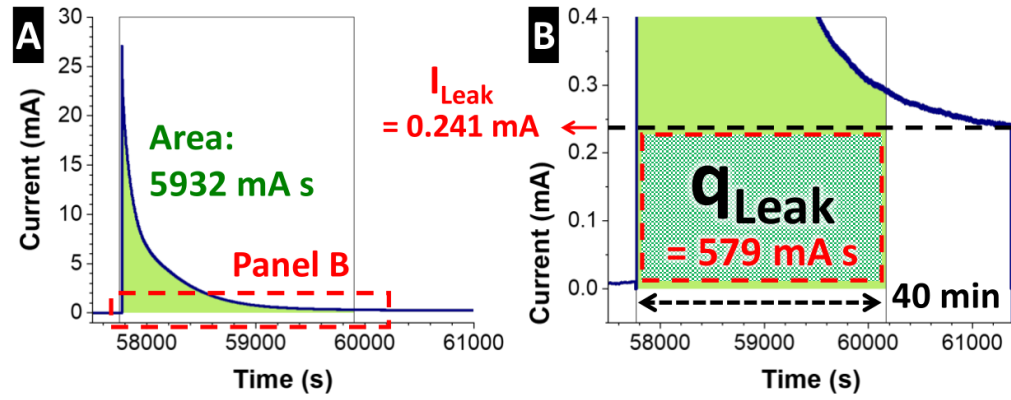


**Figure S6. Calculation of the leakage current of the electrochemical desalination cell in this study.** (A) Current-time profile for the charging half-cycle of an electrochemical desalination cell and (B) the zoomed view of the current-time curve showing the leakage current and leakage charge.
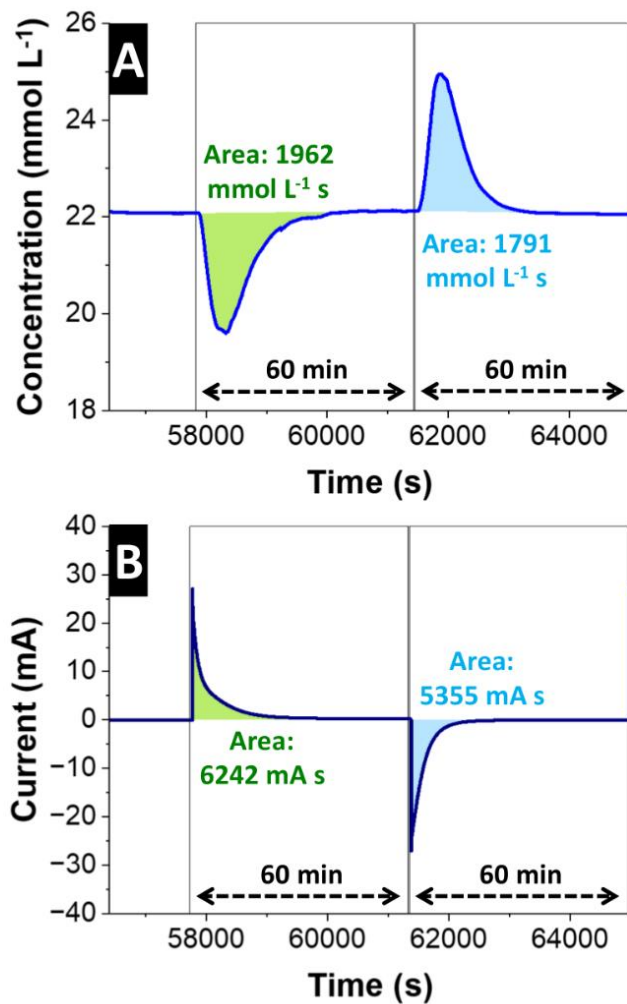
**Figure S7. Integration of the area under the curves of concentration-time and current-time profiles.** Integration of area under curve for charging and discharging half-cycles with 60 min duration each: (A) Concentration-time data and (B) current-time data.
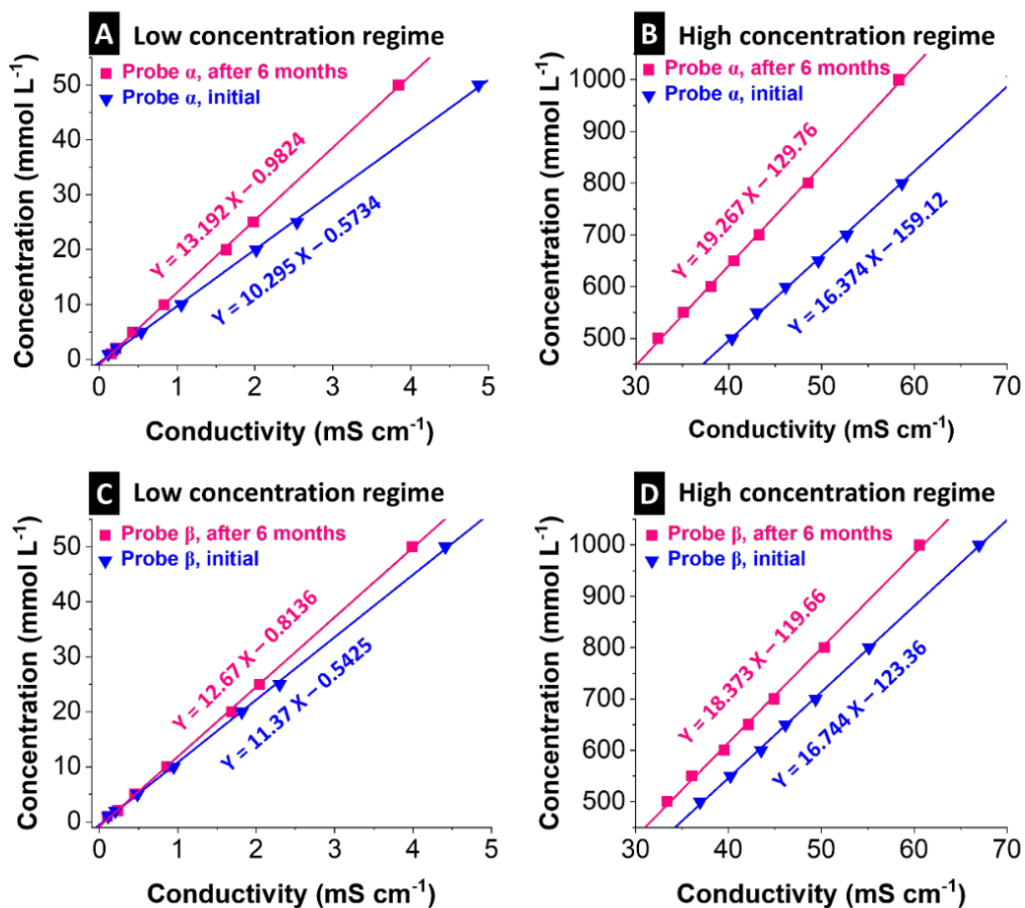
**Figure S8. Effect of aging of the conductivity probes.** Calibration curves of conductivity probe α, performed two times with 6 months interval in between 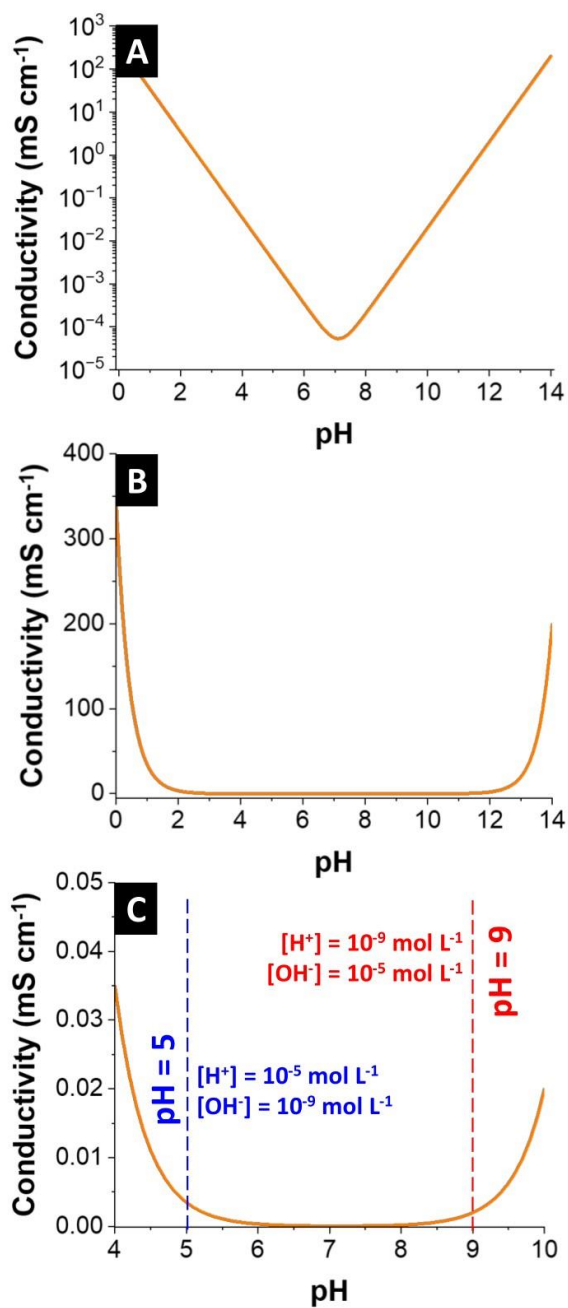for (A) low concentration and (B) high concentration regimes; calibration curves of conductivity probe β, performed two times with 6 months interval in between for (C) low concentration and (D) high concentration regimes.

**Figure S9.**



**Figure S9. How pH can theoretically affect the conductivity.** Theoretical dependence of the conductivity of ideally pure water on its pH is shown via (A) wide conductivity-pH scale, showing a conductivity of 0.055 μS cm$^{-1}$ at pH = 7; (B) narrower, and (C) narrower conductivity-pH scales showing a pH range where conductivity contribution of water is minimal.

**Supplemental Table**

**Table S1.** Composition and concentrations of the solutions used to calibrate ICP-OES instrument prior to ion selectivity measurements.

| Sample number | NaCl concentration (mmol L$^{-1}$) | KCl concentration (mmol L$^{-1}$) | CaCl$_2$ concentration (mmol L$^{-1}$) |
|---|---|---|---|
| 1 (blank) | 0 | 0 | 0 |
| 2 | 5 | 5 | 5 |
| 3 | 10 | 10 | 10 |
| 4 | 15 | 15 | 15 |
| 5 | 20 | 20 | 20 |

**Supplemental Notes**

**Note S1.** The following is a checklist of what to report as the results of an electrochemical desalination experiment.

- Electrolyte parameters:
    - electrolyte concentration (mM, mg/L, or ppm)
    - electrolyte flow rate (mL/min)
    - de-aerated with an inert gas? (e.g., Ar or $N_2$)
- Cell parameters:
    - cell configuration (e.g., flow-by, flow-through, or flow-electrode)
    - for each electrode: type, mass, thickness
    - types of membranes used, if any.
    - electrodes configuration (2-electrode system or 3-electrode system, half-cell or full-cell, with or without reference electrode)
- Other operational parameters:
    - single-pass or batch-mode
    - conductivity probe calibration status: when was it last calibrated? what was the concentration range used for calibration? how was the goodness-of-fit ($R^2$ value)?
    - pH probe calibration status: when was it last calibrated?
    - pH variation: pH-time or pH-cycle curves, showing pH variation upon charge and discharge
- Electrochemical parameters:
    - specific current applied for charging and discharging (e.g., in A/g). it is important to specify here which mass was considered: the mass of both electrodes combined, the average mass of both electrodes, or the mass of a single electrode?
    - charging and discharging voltage, and voltage holding time in each step
    - number of cycles tested
- Performance metrics:
    - concentration-time or concentration-cycle curves
    - electrode potential-time (or cycle), cell voltage-time (or cycle), and current-time (or cycle) curves
    - average desalination capacity for each cycle, as well as the DC for charging half-cycle and for discharging half-cycle
    - the time duration considered for integration of C-t curve
    - charge efficiency, with and without leakage current subtraction
    - is the time duration considered for integration of I-t curve the same as that in C-t curve?
    - energy consumption (kT/ion removed)

**Note S2.** The following is a checklist of necessary items/considerations for an electrochemical desalination experiment.

- Hardware and infrastructure:
    - peristaltic pump: does the flow rate set on the pump match the real flow rate passing through its tubes? One can measure the flow rate manually by using a graduated cylinder and a simple chronometer.
    - conductivity probe: freshly calibrated with stock solutions
    - pH probe
    - temperature-controlled environment
    - inert gas source to bubble the electrolyte, as well as a gas washing bottle to minimize electrolyte evaporation
    - galvanostat/potentiostat that is capable of exporting outputs such as: electric charge stored in the electrodes during charging and the charge retrieved during discharging; energy consumed during charge; potential and current vs. time
- Software and other considerations:
    - reproducibility ensuring: does the software used for integration of area under concentration-time or current-time curves generate the same results when handled at a different time, or by a different user?
    - are the conductivity and pH probes close enough to the cell effluent to capture the characteristics of the outflowing water without long delays from the electrochemical results obtained by the galvanostat/potentiostat?

## 4.2. MXene/activated-carbon hybrid capacitive deionization for permselective ion removal at low and high salinity

Mohammad Torkamanzadeh,[1,2] Lei Wang,[1,2] Yuan Zhang,[1,2]
Öznil Budak,[1,2] Pattarachai Srimuk,[1] Volker Presser,[1,2,*]

[1]    *INM - Leibniz Institute for New Materials, D2 2, 66123, Saarbrücken, Germany*

[2]    *Department of Materials Science & Engineering, Saarland University, Campus D2 2, 66123, Saarbrücken, Germany*

*      Corresponding author.

Own contributions:

Investigation, Methodology, Conceptualization, Data curation, Visualization, Writing - Original Draft, Writing - Review & Editing.

# MXene/Activated-Carbon Hybrid Capacitive Deionization for Permselective Ion Removal at Low and High Salinity

Mohammad Torkamanzadeh, Lei Wang, Yuan Zhang, Öznil Budak, Pattarachai Srimuk, and Volker Presser*

Cite This: *ACS Appl. Mater. Interfaces* 2020, 12, 26013−26025

Read Online

ACCESS | Metrics & More | Article Recommendations | Supporting Information

**ABSTRACT:** Two-dimensional, layered transition metal carbides (MXenes) are an intriguing class of intercalation-type electrodes for electrochemical applications. The ability for preferred counterion uptake qualifies MXenes as an attractive material for electrochemical desalination. Our work explores $Ti_3C_2T_x$-MXene paired with activated carbon in such a way that both electrodes operate in an optimized potential range. This is accomplished by electrode mass balancing and control over the cell voltage. Thereby, we enable effective remediation of saline media with low (brackish) and high (seawater-like) ionic strength by using 20 and 600 mM aqueous NaCl solutions. It is shown that MXene/activated-carbon asymmetric cell design capitalizes on the permselective behavior of MXene in sodium removal, which in turn forces carbon to mirror the same behavior in the removal of chloride ions. This has minimized the notorious co-ion desorption of carbon in highly saline media (600 mM NaCl) and boosted the charge efficiency from 4% in a symmetric activated-carbon/ activated-carbon cell to 85% in a membrane-less asymmetric MXene/activated-carbon cell. Stable electrochemical performance for up to 100 cycles is demonstrated, yielding average desalination capacities of 8 and 12 mg/g, respectively, for membrane-less MXene/activated-carbon cells in NaCl solutions of 600 mM (seawater-level) and 20 mM (brackish-water-level). In the case of the 20 mM NaCl solutions, surprising charge efficiency values of over 100% have been obtained, which is attributed to the role of MXene interlayer surface charges.

**KEYWORDS:** MXene, intercalation, capacitive deionization, desalination, seawater, asymmetric
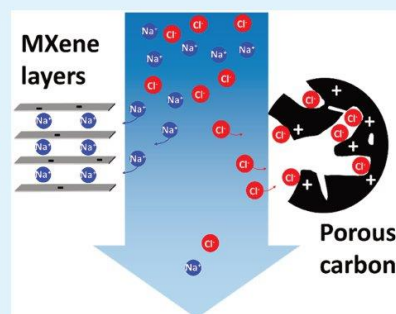
## 1. INTRODUCTION

The development of sustainable water desalination technologies is crucial as clean water shortage has become a global concern.[1] This challenge pertains to enhanced energy efficiency and performance durability at low operational costs. Capacitive deionization (CDI) is a promising water desalination technology that offers certain advantages over other widely employed alternatives such as reverse osmosis, and thermal desalination.[2] CDI devices operate at low pressure and have reduced energy consumption, especially at ultralow to low salinity levels.[3] A CDI cell is conceptually a flow-through electrochemical capacitor.[4] Upon charging the CDI cell, water-dissolved ions are removed from the saline water feed stream via electrosorption: Sodium ions are attracted to the negatively charged electrode, and chloride ions are attracted to the positively charged electrode. Upon discharging, the ions are released back to the stream, and, as a result, the regenerated electrodes can be used in the subsequent cycle. At the same time, the invested electrical charge is (mostly) recovered by which feature added energy efficiency of the CDI technology is afforded. In this context, there are two important, among other performance metrics: the desalination capacity (DC) measures the effective amount of salt removed per mass of the electrode and the charge efficiency (CE) gives the ratio of invested total charge versus the charge corresponding to the removed ionic species.[5]

Until recently, CDI research had focused on carbon-based materials as electrodes.[6] The large surface area of nanoporous carbon provides microporous channels for effective electrostatic immobilization of ions at the carbon/electrolyte interface.[7] In the absence of intrinsic permselectivity, co-ion desorption of microporous carbon prevents bulk ion removal via ion electrosorption at high molar strength, such as that found in saline water or brine.[7] This issue can, partially, be remedied by implementing ion-exchange membranes, giving rise to membrane CDI (MCDI).[8] However, while the implementation of ion-exchange membranes also allows the design of multichannel desalination cells,[9] it adds additional costs and cannot overcome the intrinsic charge-limitation of

carbon material. Alternatively, permselective counterion adsorption via suppressed co-ion presence can be enhanced even at high molar strength when lowering the carbon pore size below 1 nm.[10]

In recent years, electrochemical desalination employing Faradaic (charge-transfer) materials has overcome the limitation to low molar regimes (<100−200 mM) and limited desalination capacity (ca. 20−30 $mg_{NaCl}/g_{electrode}$) of carbon-based CDI.[11] In 2012, Pasta et al. introduced a desalination battery by employing layered sodium manganese oxide to remove sodium ions from seawater without a need for ion-exchange membranes.[12] Lee et al. introduced the combination of a Faradaic and an electrosorption (carbon) electrode to enhance the CDI performance, but without accessing high molar strength regimes.[13] Until now, a large and rapidly growing number of charge-transfer materials have already been explored, including intercalation compounds,[14] conversion materials,[15] electroactive polymers,[16] redox-active electrolytes,[17] and combinations of such materials. Even more advanced approaches utilize high-capacity processes, such as oxidant generation[18] or metal−air processes.[19]

Of interest for any application involving the intercalation of cations and anions are two-dimensional (2D) materials. For example, $Ti_3C_2T_x$ is a member of a large family of 2D materials called MXene.[20] MXene is derived via selective etching of A-site atoms form a $M_{n+1}AX_n$ phase, where M stands for an early transition metal, A stands for group 13 or 14 elements (typically Al), X stands for carbon and/or nitrogen, and $n = 1$, 2, or 3.[21] To carry the meaning of surface functional groups, $T_z$ is added to the chemical formula of MXene, to describe fluorine-, chlorine-, and oxygen-containing functionalities.[22] For instance, $Ti_3C_2T_x$ is commonly obtained by removing Al from $Ti_3AlC_2$ through aqueous HF etching (but nonaqueous processing is also possible).[23] Upon etching, Al is replaced by a mixture of surface terminations (O, OH, and F), rendering a typical MXene hydrophilic with a negative surface charge.[20] The layered structure of MXene allows for ions to be inserted into the material (ion intercalation), a property that in addition to a high conductivity[24] and facile processability[25] makes MXene attractive for electrochemical energy storage and water remediation. MXenes have shown promise in numerous energy storage applications as lithium-ion battery[26] or supercapacitor[27] electrodes, as well as in environmental remediation applications such as ion-sieving membranes[28] or heavy metal ion removal.[29]

Electrochemical desalination is a less widely explored domain of MXene research.[30] As the first, Srimuk et al. introduced $Ti_3C_2T_x$-MXene in a symmetric cell for desalination of low molar (5 mM NaCl) water.[14] Using MXene as an intercalation type material for both electrodes, a desalination capacity of 13 $mg_{NaCl}/g_{electrode}$ was obtained with stable performance for 30 cycles. Subsequent works on MXene electrochemical desalination have focused on postprocessing and modification of $Ti_3C_2T_x$ MXene to enhance its salt removal capacity. The latter works include vacuum freeze-drying and (45 $mg_{NaCl}/g_{electrode}$),[31] substituting HF-etching with LiF/HCl treatment (68 $mg_{NaCl}/g_{electrode}$),[32] and nitrogen-doping (44 $mg_{NaCl}/g_{electrode}$)[33] to prevent restacking of MXene layers and form electrochemically active porous structures. These promising works underline MXene as an aspiring material for water treatment applications.[34]

However, Ti-based MXenes operated in aqueous environments are notoriously affected by aging via hydrolysis-aided oxidation.[35] This issue particularly affects the usefulness of $Ti_3C_2T_x$ as the positively polarized electrode for electrochemical desalination of water. To fully capitalize on the electrochemical performance of Ti-MXene in aqueous media, it is convenient to limit its application to the negatively polarized electrode where no oxidation will occur. Unlike operation as asymmetric supercapacitors,[36] asymmetric desalination cells with MXene as only one of the electrode pair has remained incompletely explored.[34] This includes the important aspect of mass balancing to optimize the operational cell voltage of each of the two electrodes, as recently shown by Dryfe's group for carbon-based CDI.[37] Mechanistically, the interesting aspect of addressing is the degree of permselectivity of the nanoporous carbon electrode when paired with a permselective intercalation-type electrode, such as MXene. We explore if the permselective behavior of the intercalation electrode will "force" the carbon electrode to prefer counterions rather than 1:1 exchange a co-ion with a counterion. This is of high importance for saline media with high salt concentration because using only one intercalation-type electrode paired with activated carbon as the other electrode would lower system cost because of the high abundance of carbon and eliminate the need for expensive ion-exchange membranes.

Our study investigates the desalination of seawater-level saline solutions (600 mM NaCl) and brackish water (20 mM NaCl). We paired $Ti_3C_2T_x$-MXene with activated carbon in an asymmetric cell so that we can capitalize on sodium-ion intercalation on the MXene side and chloride ion electrosorption within carbon nanopores. Our focus is not the optimization toward the highest possible desalination metrics; instead, our work focuses on the mechanistic aspect of the desalination process. Specifically, our work explores the ion permselectivity of the carbon electrode paired with that of MXene by comparing cell performance with and without adding a polymeric ion-exchange membrane in front of the activated carbon. Thereby, we can compare the electrochemical desalination performance of the cell when the carbon electrode is shielded (with an ion-exchange membrane) or directly exposed to the saline medium. Characterization of the MXene-CNT electrodes before and after use for over 100 cycles provides insights into performance stability and degradation mechanisms.

## 2. MATERIALS AND METHODS

**2.1. Electrode Preparation and Electrochemical Measurements.** The following materials were used as-received: activated carbon (type YP-80F, Kuraray), multiwalled carbon nanotubes (CNT, Graphene Supermarket), and $Ti_3C_2T_x$-MXene (Laizhou Kai Kai Ceramic Materials Co.). As seen from Figure S1, activated carbon has a large surface area of 1644 $m^2/g$ and is composed of internal porosity within the activated carbon particles. In contrast, carbon nanotubes have a very small surface area of just 71 $m^2/g$ (Figure S1) which relates to external porosity.[38]

To prepare carbon electrodes, activated carbon and polytetrafluoroethylene binder (PTFE, 60 mass% solution in water from Sigma-Aldrich) in a 95:5 carbon/binder mass-ratio were mixed in ethanol to give a homogeneous carbon paste.[39] Afterward, the carbon paste was rolled (MTI HR01, MIT Corp.) to 600 $\mu$m thick freestanding electrode films, which was then dried in a vacuum oven at +120 °C overnight.

To prepare MXene-CNT electrodes, $Ti_3C_2T_x$-MXene and CNT in a 10:1 MXene/CNT mass ratio were tip-sonicated in ethanol for 30 min.[40] The solution was subsequently vacuum filtered through polyvinylidene fluoride (PVDF) membranes (0.22 $\mu$m, Durapore)
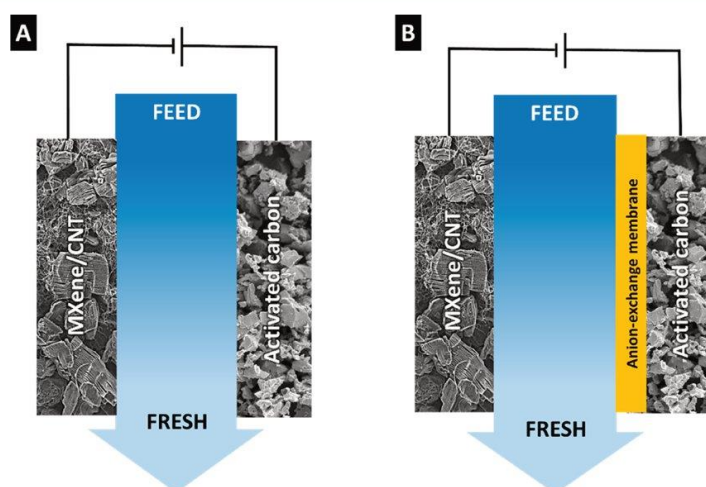
**Figure 1.** Schematic of an asymmetric electrochemical water desalination cell (A) without an ion-exchange membrane and (B) with an anion-exchange membrane.

and dried in an oven at +80 °C overnight. This electrode is labeled MXene-CNT in our work.

In a typical half-cell experiment, circular-shaped 12 mm diameter pieces were punched out of the MXene-CNT electrode and used as the working electrode. An oversized activated carbon electrode was used as counter electrode and glass fiber (GF/A, Whatman) was used as a separator. All components were placed in a custom-built cell between spring-loaded titanium pistons.[41] A reference electrode (Ag/AgCl, 3 M NaCl) was mounted onto the side of the cell in a way that its porous frit was near the working and counter electrodes. The cell was filled with 600 mM NaCl aqueous electrolyte by vacuum backfilling using a syringe. Cyclic voltammetry (CV; scan rate: 1 mV/s) and galvanostatic charge/discharge tests were performed with a VSP300 potentiostat/galvanostat (Bio-Logic).

For full-cell electrochemical water desalination, a 30 mm diameter MXene-CNT electrode was punched out and used as the working electrode. On the basis of the mass of MXene-CNT, an activated carbon electrode with a suitable mass ratio (section 2.2) was cut and used as the counter electrode. The working and counter electrodes were stacked together and separated by glass fiber membranes. Thereby, the middle channel was formed and provided a pathway for 600 mM NaCl electrolyte to flow in between the electrodes (flow-by mode, Figure 1).[42] A nonreinforced 31 ± 2 μm thick anion-exchange membrane (Fumatech, FAS-30) was used on the side of the carbon electrode in certain cells. An Ag/AgCl spectator reference electrode was used to allow recording the electrode potentials of the activated carbon and MXene-CNT electrodes individually.

**2.2. Electrode Mass Balancing.** To determine the suitable mass ratio between MXene-CNT and activated carbon electrodes in a full desalination cell, cyclic voltammetric window-opening experiments[43] were performed at both negative and positive potentials. The results of this method reveal the ideal stable potential window for each of the electrode materials, as well as quantifying the amount of charge storable in each electrode at a certain potential. Using eq 1, one can balance the mass ratio of the electrodes based on cyclic voltammetric window-opening experiments:

$$\frac{m_{\text{MXene-CNT}}}{m_{\text{Activated\_carbon}}} = \frac{Q_{\text{Activated\_carbon}}}{Q_{\text{MXene-CNT}}} \tag{1}$$

where $Q_{\text{MXene-CNT}}$ (C/g) and $Q_{\text{Activated\_carbon}}$ (C/g) are, respectively, the specific electric charge stored in MXene-CNT and activated carbon electrodes at a certain potential. The value of $m_{\text{MXene-CNT}}/m_{\text{Activated\_carbon}}$ then gives the mass ratio between the two electrodes,

based on which a full cell with maximum desalination performance can be fabricated.

**2.3. Desalination Experiments.** All desalination experiments were performed using galvanostatic cycling with potential limitation (GCPL) technique via VSP300 potentiostat/galvanostat (Bio-Logic) electrochemical workstation at +25 °C. Each cycle duration was 2 h and consisted of two half-cycles. In the first half-cycle, the cell was charged to 1.2 V and held at that voltage for 1 h. In the second half-cycle, the cell was discharged to 0.3 V and at that voltage for another 1 h. Both charging and discharging steps were accomplished at 0.1 A/g current density (normalized to the combined mass of both activated carbon and MXene-CNT electrodes). A stream of saline was pumped into the cell at a 2 mL/min rate from a reservoir tank, which contained 10 L of electrolyte and was constantly bubbled with nitrogen prior to and during the experiments to deaerate the fluid. The effluent stream flowed out of the cell into a conductivity meter (Metrohm PT1000) and pH meter (WTW SensoLyt 900P) and flowed back into the tank to complete the loop. The pH and conductivity data were recorded every second online by computer. Calculations regarding the correlation of pH and conductivity data to concentration may be found in our previous work.[44] The desalination capacity ($\text{mg}_{\text{NaCl}}/\text{g}_{\text{electrode}}$) was calculated according to eq 2:

$$\text{desalination capacity (DC)} = \frac{\nu M_{\text{NaCl}}}{m_{\text{total}}} \int \Delta C \, dt \tag{2}$$

where $\nu$ is the flow rate (mL/min), $M_{\text{NaCl}}$ is the molecular weight of NaCl (58.44 g/mol), $m_{\text{total}}$ is the total mass of electrodes (g), $t$ is the time over the adsorption or desorption step (min), and $\Delta C$ is the concentration change of NaCl (mM) in the effluent stream of the cell. The charge efficiency (%) was calculated following

$$\text{charge efficiency (CE)} = \frac{\dfrac{\text{DC}}{M_{\text{NaCl}}}}{\dfrac{Q}{F}} \times 100\% \tag{3}$$

where $F$ is the Faraday constant (26 801 mAh/mol) and $Q$ is the average of total charge stored in the two electrodes normalized to the total electrode mass (mAh/g).

**2.4. Material Characterization.** X-ray diffraction (XRD) analysis was conducted using a D8 Advance diffractometer (Bruker AXS) with a Ni-filtered copper X-ray source (Cu Kα, 40 kV, 40 mA) and a 2D detector (VANTEC-500). A JEOL JSM 7500F field-emission scanning electron microscope (JEOL) was used to record scanning electron microscopy (SEM) images. Energy-dispersive X-ray spec-
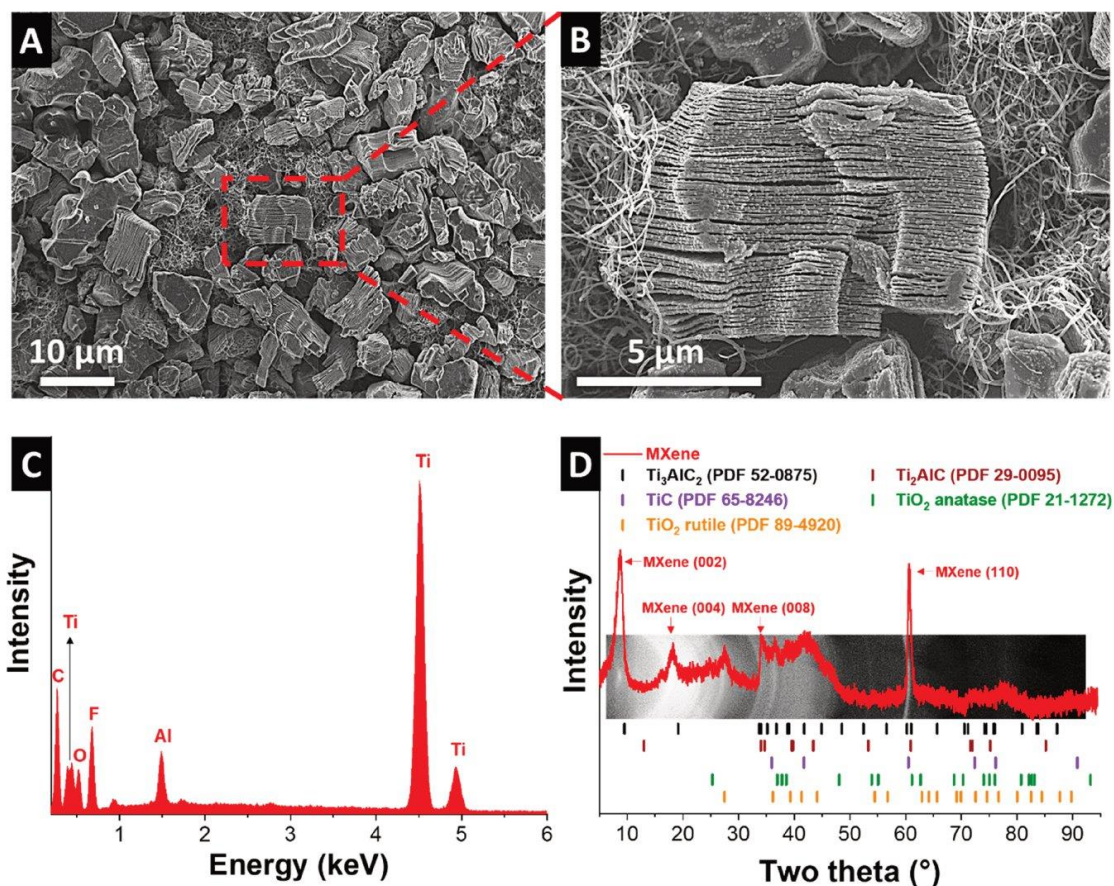
99

**Figure 2.** Characterization of the MXene-CNT electrode. (A, B) Scanning electron micrographs, (C) energy-dispersive X-ray spectrum (EDX), and (D) X-ray diffractogram and overlaid 2D diffraction pattern of $Ti_3C_2T_x$-MXene alongside ideal pattern of different phases [Powder Diffraction File (PDF) nos. 21-1272, 29-0095, 52-0875, 65-8246, and 89-4920 are Joint Committee on Powder Diffraction Standards, 2004].

troscopy (EDX) was carried out at 12 kV with an X-Max Silicon Detector from Oxford Instruments using the AZtec software. Transmission electron microscopy (TEM) was conducted using a JEOL JEM-2100F system at an operating voltage of 200 kV. The samples were dispersed in ethanol and tip-sonicated briefly. The dispersion was then drop casted on a TEM copper grid with a lacy carbon film.

We used an Autosorb iQ system (Quantachrome) for nitrogen sorption at −196 °C. The samples were degassed at 100 Pa and 200 °C for 1 h and then at 300 °C for 20 h. Alongside the isotherm of activated carbon, carbon nanotubes, MXene powder, and MXene-CNT electrodes, the specific surface area (SSA) was obtained via Brunauer−Emmett−Teller (BET) theory and by applying the quenched-solid density functional theory (QSDFT), assuming a slit-shaped pore model as provided in Figure S1.

The streaming potential was measured using a Mütek PCD-T3 instrument with the particle charge detection method. In a typical experiment, 50 mg of MXene or YP-80F carbon was dispersed in 30 mL of water. The mixture was then poured into a cylindrical PTFE container of the instrument with a PTFE piston inside. The automatic titration was conducted by gradual injection of HCl or $NH_3$ solutions into the mixture while the potential recorded online.

## 3. RESULTS AND DISCUSSION

**3.1. Material Characterization.** The SEM images depicted in Figure 2A show the morphology of pristine MXene-CNT electrodes. $Ti_3C_2T_x$-MXene structures are observed with their typical layered accordion-like morphologies, entangled by CNTs. TEM images of the CNTs are provided in Figure S2. The incorporation of CNTs improves the mechanical stability of the electrode, as well as enhancing the electrical conductivity.[40] CNTs themselves have a specific surface area of 71 $m^2/g$, which is predominately on the outer surface. $Ti_3C_2T_x$-MXene exhibits an external surface area of 3 $m^2/g$, and the mechanical mixture of 10 mass % CNTs and 90 mass % of MXene yields a surface area of 12 $m^2/g$. The latter value is very close to the theoretical value of such a mixture (i.e., 10 $m^2/g$), and the same goes for the corresponding pore volume (0.04 $cm^3/g$ measured for the composite electrode; Figure S1). The low values of surface area and pore volume originate from the porous space between the MXene bundles (Figure 2A) and not from within the interlayers of MXenes. There is no detriment to such a low level of porosity since electrochemical desalination via MXene is not based on ion electrosorption but on the ion intercalation between the layers of the electrode material. In addition to providing electronic

100

**Table 1. EDX Elemental Analysis of the Pristine MXene-CNT and Post-Mortem Electrodes of Different Cells after Long-Term Cycling**[a]

| | C | Ti | O | Al | F | Na | Cl |
|---|---|---|---|---|---|---|---|
| pristine | 13 ± 9 | 57 ± 13 | 9 ± 3 | 3 ± 3 | 17 ± 6 | | |
| post-mortem (600 mM + AEM) | 12 ± 2 | 53 ± 5 | 22 ± 3 | 1 ± 0 | 6 ± 1 | 3 ± 0 | 3 ± 1 |
| post-mortem (600 mM) | 15 ± 3 | 58 ± 8 | 16 ± 4 | 0 ± 0 | 8 ± 2 | 2 ± 1 | 1 ± 0 |
| post-mortem (20 mM + AEM) | 10 ± 2 | 67 ± 8 | 15 ± 4 | 0 ± 0 | 5 ± 2 | 2 ± 0 | 1 ± 0 |
| post-mortem (20 mM) | 10 ± 2 | 61 ± 7 | 22 ± 4 | 1 ± 0 | 6 ± 2 | 1 ± 0 | 0 ± 0 |

[a]All values in mass %.

pathways and entangling MXene flakes, the CNTs also likely provide facile ion-transport pathways by preventing too tight packing of MXene particles.

At a higher resolution, we also see from the SEM image in Figure 2B, the presence of cuboid particles spread over the MXene surface. The latter particles are consistent with titanium oxide, and the presence of oxygen is confirmed by the EDX spectrum displayed in Figure 2C (EDX results are listed in Table 1). Ti-based MXene is known to oxidize in air, especially in the presence of humidity.[35] The EDX results also show a low amount (around 3 mass%) of residual aluminum, which stems from nonetched MAX phases or traces of aluminum fluoride from the etching products of the MAX phases.

XRD analysis confirms the presence of $Ti_3C_2T_x$-MXene. The XRD pattern in Figure 2D shows a strong (002) peak at 8.59° $2\theta$ of $Ti_3C_2T_x$, compared to the initial value of (002)-$Ti_3AlC_2$ of the parent MAX phase at 9.52° $2\theta$. This corresponds with an 11% increase in the $d$-spacing along the $c$-axis. In addition to higher-order (00$l$)-type MXene reflections, we also see the characteristic MXene-peak related to (110)-$Ti_3C_2T_x$ at about 61° $2\theta$.[45] No significant amounts of either $Ti_2AlC$ or TiC are found from the diffraction pattern analysis. We also see the presence of minor amounts of titanium oxide (possibly rutile) from the diffraction signal generate at about 27° $2\theta$. Figure S3 provides the XRD pattern of the corresponding phases with their relative intensities.

**3.2. Electrochemical Behavior.** In the first step to determining the stable electrochemical potential window of the MXene-CNT and activated carbon electrodes, half-cell cyclic voltammetric window-opening measurements at a scan rate of 1 mV/s were carried out with 100 mV increments (Figure 3A,B). These experiments were carried out in aqueous 600 mM NaCl to avoid issues of ion starvation and to provide a baseline for later desalination experiments at seawater-like ionic strength.[46]

The cyclic voltammograms of activated carbon are rectangular-shaped, showing a near-ideal capacitive behavior (Figure 3A). As the potential difference is increased, there is a notable increase in the capacitance during positive and negative polarization when comparing identical potential window widths. This effect is linked to the quantum capacitance effect induced by the increased number of charge carriers in carbon, as the latter is not a perfect metallic conductor.[41,47] At very high positive potentials, starting at around +0.6 V vs Ag/AgCl, we also see an irreversible increase in transferred charge linked to water splitting.[38] We note a similar capacitance during positive and negative polarization, which would indicate a similar ability to serve as an electrode for sodium and chloride removal (under the condition of permselectivity).[48,49] These features make activated carbon

electrodes suitable for positive and negative polarization regimes in the context of capacitive deionization.

For MXene-CNT electrodes, an onset of the oxygen evolution peak is seen at positive potentials as early as +0.3 V vs Ag/AgCl (Figure 3B). This makes the chosen MXene-CNT electrodes unsuitable to serve as the positive electrode in our setup. During negative polarization, there is a continued increase in the corresponding capacitance when increasing the voltage bias. This process aligns with the conditioning of the MXene interlayer space and is irreversible. The latter is obvious when comparing the low capacitance found during the initial cycles at low potential bias, seeing the increased area under the cyclic voltammogram as the lower scan limit transitions toward more negative polarization, and the significantly increased capacitance for small voltage windows during repeat measurements (solid line graphs in Figure 3C). Electrochemical dilatometry also shows the increased strain of the MXene-CNT electrode when the polarization bias is increased (Figure 3D). The electrode shrinking follows the same pattern observed during negative polarization in $Na_2SO_4$ reported before and is aligned with the stronger MXene layer attraction in the sodiated state.[50] This process is likely to be accompanied by a change in the number of solvent molecules within the interlayer space.[51] We also note the prominent current-peak at −0.5 V (cathodic scan) and −0.3 V (anodic scan), which may be related to interlayer proton-redox processes and ion arrangement effects.[52] In past works, this peak was mostly reported and analyzed in aqueous $H_2SO_4$ electrolytes.[52]

Half-cell cyclic voltammograms of CNTs are provided in Figure S4. Cyclic voltammograms show a rectangular-shaped profile typical for ion electrosorption. The low surface area of CNTs explains the low capacitance of about 20−30 F/g (depending on the potential range). Given that CNTs account for only 10 mass % of the MXene-CNT electrodes, the electrochemical contribution arising from CNTs to the total capacitance of about 120 F/g of the electrode is negligible. Specifically, at a polarization potential of −0.8 V vs Ag/AgCl, for instance, the charge stored in CNT electrodes is only 6% that of MXene-CNT (Figure 3B).

Galvanostatic charge/discharge cycling was employed to quantify the specific capacitance (Figure 3E) and specific capacity (Figure 3F) of the electrodes. Galvanostatic charge/discharge cycling at 0.1 A/g gave a capacitance of 123 F/g for MXene-CNT at the potential window between −1 and 0 V vs Ag/AgCl and 95 F/g for activated at the potential window from 0 to +0.4 V vs Ag/AgCl. For the two materials, the capacitance originates from different electrochemical processes. While the large surface area of activated carbon (1644 $m^2$/g; Figure S1A) enables ion electrosorption, we see pseudocapacitive ion intercalation of sodium for MXene-CNT considering the low surface area (3 $m^2$/g for MXene and 12 $m^2$/g for
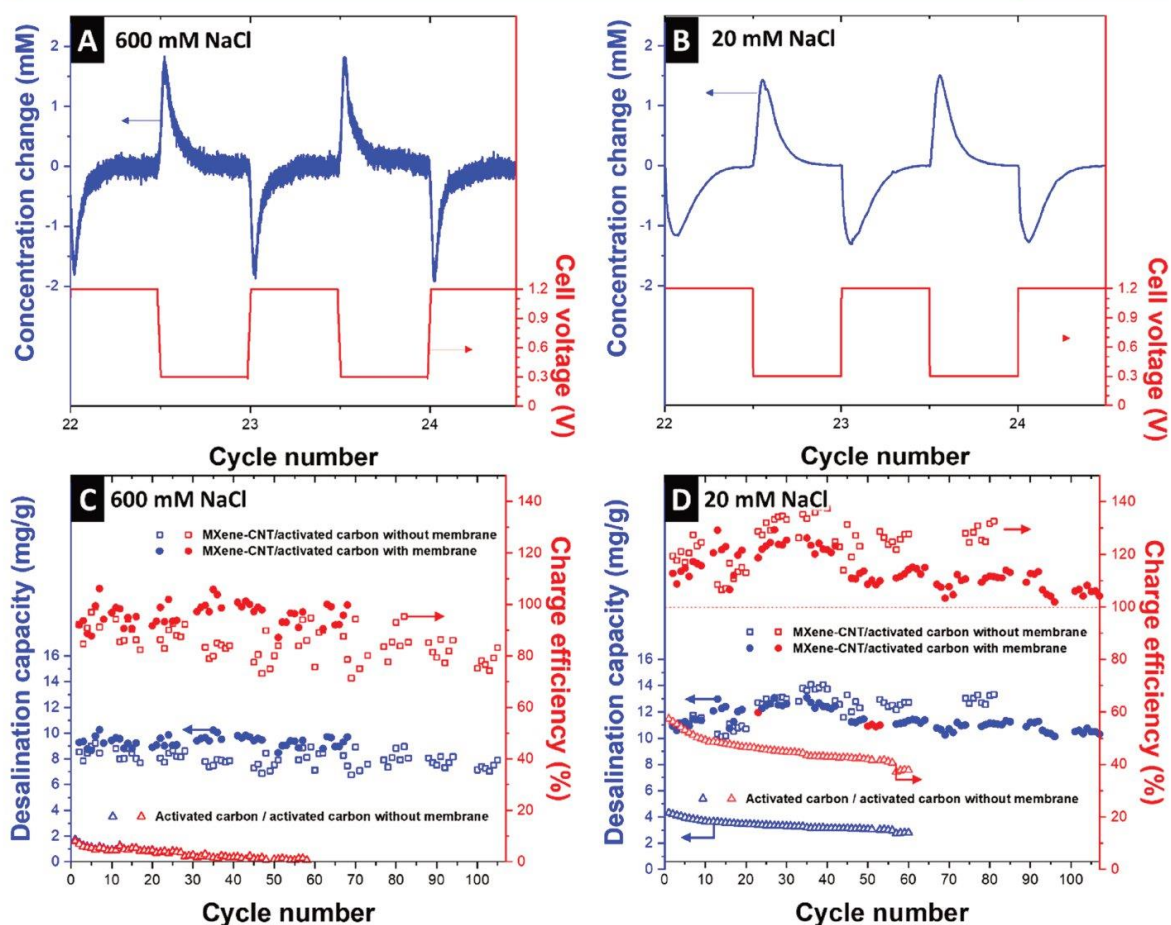
**Figure 4.** Effluent concentration change and cell voltage profiles of MXene/activated-carbon cell for two full cycles in (A) 600 mM NaCl and (B) 20 mM NaCl, both without membrane. Salt removal capacity stability and charge efficiency for cells with and without membrane in (C) 600 mM NaCl and (D) 20 mM NaCl, alongside membrane-less symmetric activated-carbon cells (the latter includes 60 cycles).

V to ensure activated carbon remains within the positive polarization regime (and, in return, MXene-CNT remains negatively polarized). The potential profiles of the individual MXene-CNT and activated carbon electrodes are provided in Figure S5. To ensure stable performance and to avoid first-cycle effects, all cells were initially cycled for around 30 cycles before the desalination experiments. As was seen from the electrochemical characterization data, the low amount of low-surface area carbon nanotubes aligns with a small contribution to the charge capacity of the MXene-CNT electrode, and as a consequence, the contribution of desalination via ion electro-sorption by the CNTs is negligible (based on 2–3 F/g via 10 mass% of pure CNTs, the corresponding desalination capacity is expected to be below 1 $mg_{NaCl}/g_{electrode}$).[53]

Figure 4A,B shows the effluent salt concentrations (alternating peaks and troughs) alongside the voltage profile applied (without the use of an anion-exchange membrane). Upon charging the cell to 1.2 V, ions are attracted to the electrodes, causing a sudden drop in the concentration of the effluent stream. The concentration then levels off to the previous level before discharging, indicating that the system is approaching equilibrium and that the electrodes are saturating

with salt ions. Likewise, a similar process occurs upon discharging the cell to 0.3 V, where electrodes are depleted from ions and are regenerated for the next cycle.

The potential distribution between MXene-CNT and activated-carbon electrodes in different cells are shown in Figure S5. At 600 mM NaCl in the absence of an ion-exchange membrane (Figure S5A), we see the highly linear slope of charge/discharge profiles of each monitored electrode potential. The potential range of activated carbon remains fully in the positive polarization regime and has a lower amplitude compared to the MXene-CNT electrode. This is because of the different charge storage capacities of the two electrode materials and the chosen mass ratio. At low molar strength (20 mM NaCl), we note the presence of short-lived spikes in the potential curves of MXene-CNT at vertex potentials (Figure S5C). This is because of the lowered ion mobility at low molar strength; since we only control the cell voltage and just monitor the individual electrode potentials, we see a quicker charging behavior of the activated carbon electrode because the latter capitalizes on interfacial charge storage via ion electrosorption. In contrast, charge transfer is slightly slower in the case of ion intercalation in MXene-CNT,
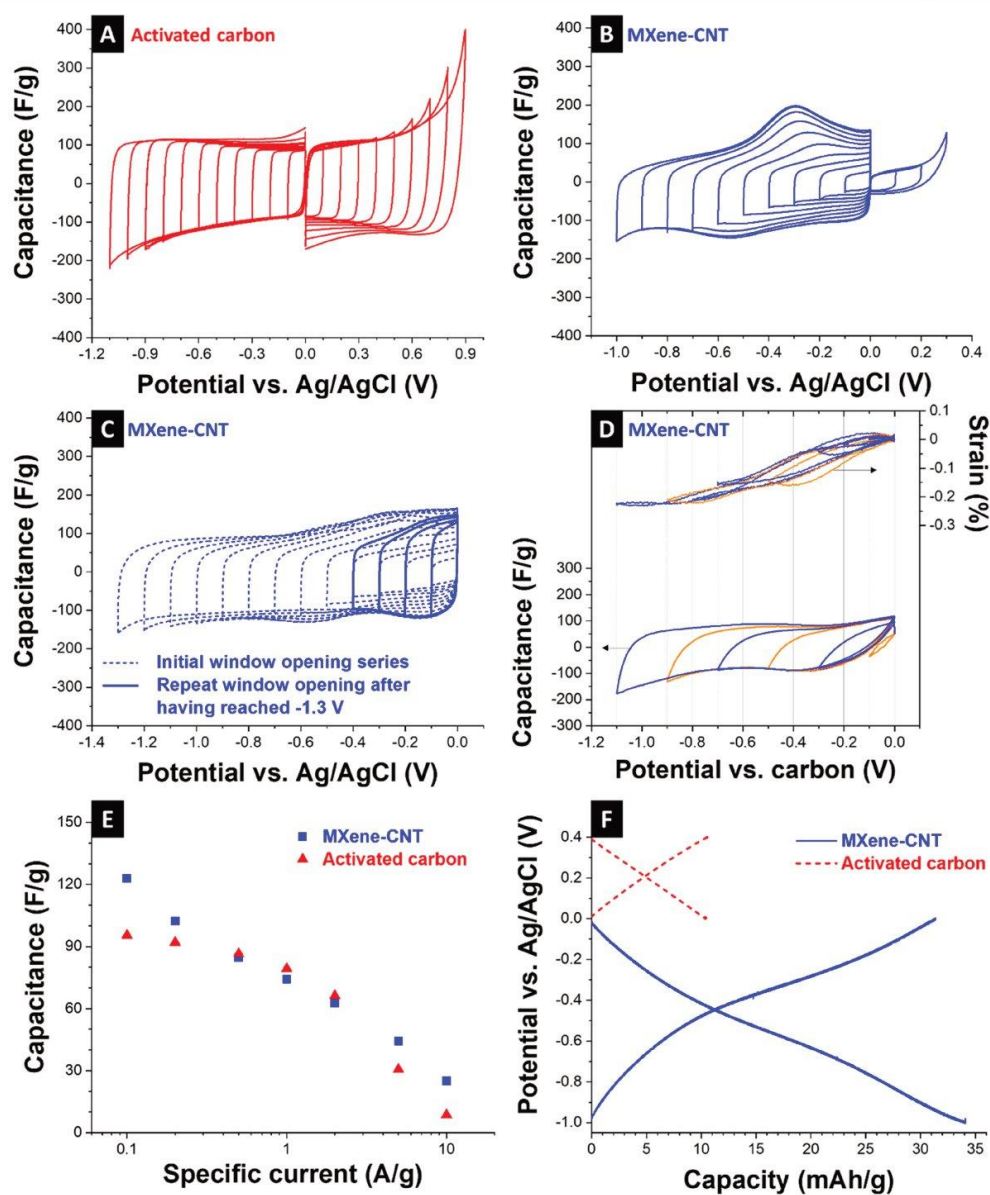
102

**Figure 3.** Half-cell electrochemical characterizations: window-opening cyclic voltammograms of (A) activated carbon and (B) MXene-CNT; (C) initial and repeated cyclic voltammetric window opening. (D) Cyclic voltammograms and corresponding dilatograms (electrode height change/initial height = strain; the different colors help to differentiate between individual scans). (E) Gravimetric capacitance of MXene-CNT (−1 to 0 V vs Ag/AgCl) and activated carbon (0 to +0.4 V vs Ag/AgCl), and (F) corresponding capacities. All measurements were carried out in aqueous 600 mM NaCl.

MXene-CNT; Figure S1C,D). At a rate of 2 A/g, both electrodes yield a comparable capacitance of 63−66 F/g, and we see a lower rate handling ability of the activated carbon electrode compared to MXene-CNT. Characteristic galvanostatic charge/discharge profiles are displayed in Figure 3F, and we chose capacity as the displayed unit to correctly quantify the charge and to compensate for any deviation from a perfectly rectangular cyclic voltammogram found for MXene-CNT. The capacity of about 10 mAh/g for activated carbon

and 34 mAh/g for MXene-CNT informed the mass balancing, which will be used in section 3.3.

**3.3. Desalination Performance.** On the basis of the electrochemical results obtained by half-cell measurements, asymmetric full-cells comprising of MXene-CNT and activated carbon electrodes were fabricated. For the desalination cell, we chose the mass ratio between the two electrodes that was optimized according to the method explained in section 2.2. We also carefully adjusted the potential window to cycle between cell voltages 1.2 and 0.3 V instead of discharging to 0

103

whereby, upon charging and discharging, the slower electrode is briefly forced to higher potentials. Each small spike in the profile of MXene-CNT is accompanied by a small notch in the profile of the activated carbon electrode.

Figure 4C,D shows the desalination capacity and charge efficiency of up to 100 cycles in aqueous 600 mM NaCl and 20 mM NaCl. In the absence of an ion-exchange membrane, we see at 600 mM a desalination capacity of $8 \pm 1$ mg$_{NaCl}$/g$_{electrode}$ at a charge efficiency of $85 \pm 6\%$; at 20 mM, we find a desalination capacity of $12 \pm 1$ mg$_{NaCl}$/g$_{electrode}$ at a charge efficiency of $125 \pm 8\%$ (we comment on exceeding 100% charge efficiency and its importance later in this section).

For comparison: In a membrane-free configuration, activated carbon only affords at 600 mM a desalination capacity of $0.8 \pm 0.3$ mg$_{NaCl}$/g$_{electrode}$ at a charge efficiency of $4 \pm 2\%$; at 20 mM, we find a desalination capacity of $3 \pm 1$ mg$_{NaCl}$/g$_{electrode}$ at a charge efficiency of $41 \pm 9\%$. The data for using only activated carbon for both electrodes is from a previous study where a cell voltage of 1.0 V and discharging to 0 V was employed.[54] Higher desalination capacities for this type of activated carbon are found for membrane-free desalination only at lower molar strength; for example, we found at 5 mM a desalination capacity of about 10 mg$_{NaCl}$/g$_{electrode}$ at a corresponding charge efficiency of 75–79%.[46]

Figure 4C,D displays the desalination capacity and charge efficiency for the cell modified by placing an anion-exchange membrane in front of the activated-carbon electrode. This means that the positively polarized carbon electrode allows (almost exclusively) only the uptake of counterions because of the permselective feature of the ion-exchange membrane.[8,54] For this case, we find at 600 mM a desalination capacity of $9 \pm 0$ mg$_{NaCl}$/g$_{electrode}$ at a charge efficiency of $96 \pm 4\%$; at 20 mM, we find barely statistically differentiable values, namely, a desalination capacity of $11 \pm 1$ mg$_{NaCl}$/g$_{electrode}$ at a charge efficiency of $114 \pm 7\%$. The corresponding electrode potentials are found in Figure S5B,D. While the potential profiles with or without the anion-exchange membrane are highly comparable at aqueous 600 mM NaCl (Figure S5A-B), there is a notable difference at 20 mM. As seen from Figure 4C,D, the spikes in the potential profiles of MXene-CNT in the configuration without the ion-exchange membrane are absent after adapting the anion-exchange membrane in front of the activated-carbon electrode. This caused in return a more sluggish ion transport toward the nanoporous carbon electrode through the ion-exchange membrane, which kinetically resulted in a slower process compared to ion intercalation within the MXene interlayers. Accordingly, there are visible spikes in the potential distribution of the activated-carbon electrode and corresponding notches in the MXene-CNT profiles.

**3.4. Why Is the Asymmetric Cell Accomplishing Desalination Even at High Molar Strength?** As seen from our data (and previous works), it is well-known that activated carbon with pores larger than 1 nm fails to provide any significant permselectivity in the context of counterion electroadsorption during capacitive deionization.[10,55] The activated carbon used in this study has a rather wide pore size of 1.3 nm (Figure S1A), which is much larger than the hydrated sodium or chloride ions (~4 Å).[56,57] Since the pristine activated carbon used in this study is neither oxidized nor reduced, few surface groups must exist on the carbon surface, rendering it nonstereoselective and nonmolecular sieving without discrimination toward cations or anions. In other words, in an uncharged state, both sodium and chloride

ions coexist within carbon micropores, as previously shown in our work, by use of in situ small-angle X-ray scattering[58] and via modeling.[10] Therefore, when two activated-carbon electrodes are paired in a symmetrical desalination cell, carbon micropores will both desorb co-ions (undesired) and attract counterions (desired). At a high molar strength, the co-ion expulsion dominates to such a great extent that effectively no desalination is accomplished (Figure 4C).

When MXene is paired with activated carbon, a charge efficiency of above 80% is maintained in the case of 600 mM without any ion-exchange membrane. This high charge efficiency implies that minimal co-ion expulsion takes place at both MXene and activated-carbon electrodes in an asymmetric configuration. On the side of the MXene-CNT electrode, the negative surface charges repel chloride ions that approach the surface, and as a result, no electric charge is wasted repelling the chloride ions but rather is exclusively invested to intercalating of sodium ions in between the MXene sheets. Given that the bulk solution must be electroneutral, chloride ions are then forced to be electrosorbed onto the otherwise nonpermselective activated carbon. MXene itself has the intrinsic ability to intercalate cations and anions; however, it does so in a nearly perfectly permselective manner, that is, the screened environment within the MXene interlayers allows for counterion intercalation at low and high molar strength of the bulk electrolyte.[14,40]

The permselectivity forced upon the activated carbon by the MXene-CNT electrode can also be aided by the asymmetric electrode potential distribution. In regular CDI with symmetric cells and two electrodes composed of activated carbon, the cell is usually discharged to 0 V. The potential range around 0 V, however, is the regime in which the electroneutrality within the carbon nanopores is re-established by replenishing the initial population of co- and counterions (ideally in the same ratio as that found in bulk).[48,49,59] Keeping the carbon electrode at all times outside that potential regime aids in avoiding the regime of permselectivity failure.[60] For example, Kim et al. demonstrated for a symmetric CDI system based on a similar activated carbon (Kuraray YP-50F) cycled between 0.3 and 1.2 V cell voltage a maximum desalination capacity of about 9 mg$_{NaCl}$/g$_{electrode}$ at a corresponding charge efficiency of 60–90% (depending on the half-cycle time) at a molar strength of 20 mM NaCl.[61] However, it is not realistic to assume that the permselective regime can be accessed by activated carbon within the range of +0.2 V to +0.5 V vs Ag/AgCl at high molar strength, such as studied by us when using 600 mM NaCl. At such a high ion concentration, the entire potential range is dominated by nonpermselective ion-exchange.[58]

When we now compare the performance at low and high molar strength with or without the added ion-exchange membrane to screen ions moving toward the carbon electrode, we see only small effective differences in the desalination performance. At 20 mM NaCl, the desalination capacity is virtually indistinguishable, while at 600 mM, there is a small increase when using the anion-exchange membrane. For the system at 20 mM, it is reasonable to assume that the potential range control of activated carbon and the intrinsic uptake of counterions of MXene-CNT alone allow for permselective ion removal. Adding an ion-exchange membrane has little effect in that case. However, for 600 mM, the carbon electrode is forced by the permselectivity of MXene-CNT to also behave permselectively: This is not a perfect state, and we see an improvement in desalination performance in case of enhancing
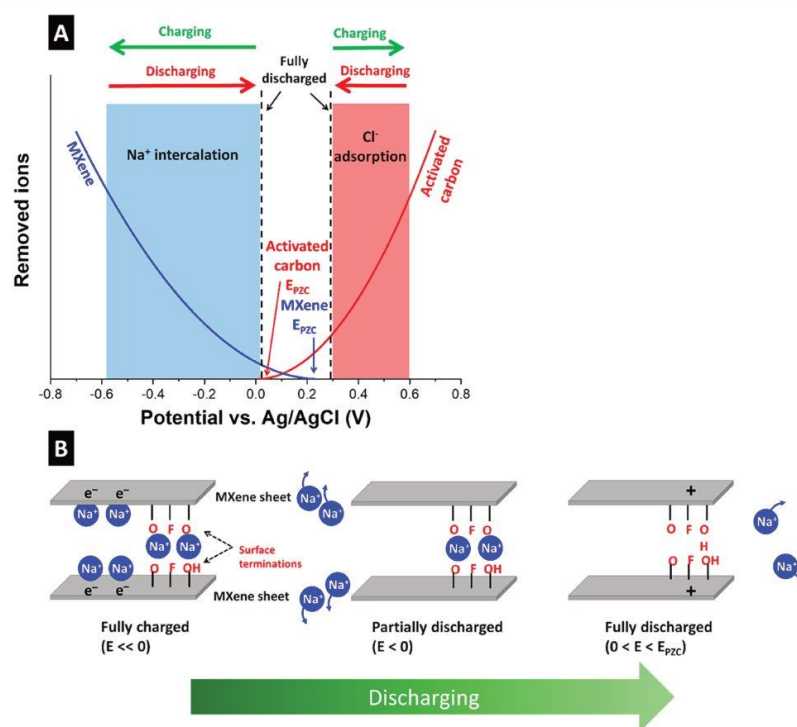
104

**Figure 5.** (A) Illustration of (approximate) location of potential at zero charge and the population of adsorbed ions upon charge/discharge. The $E_{PZC}$ values of MXene and carbon electrodes are meant to schematically show the relative positions of these values with respect to each other. (B) Schematic representation of sodium ions interaction with MXene surface terminations during discharge half-cycle.

the carbon electrode's permselectivity further with an added ion-exchange membrane allowing only the removal of anions.

The enhanced permselectivity of the asymmetric MXene-CNT/activated-carbon system over that of the symmetric activated-carbon/activated-carbon system is seen from the corresponding energy consumptions (Figure S6). In all MXene/activated-carbon cells, the energy consumed per removed salt ion is around 40 kT, and it barely changes across the two concentrations tested. However, activated-carbon/activated-carbon cells show an energy consumption of 82 kT at 20 mM and 670 kT at 600 mM, showing ineffective desalination in case of the latter salt concentration. The energy consumed to accomplish desalination could be an important metric to take into consideration when comparing various CDI systems with each other, as well as comparisons across available desalination technologies.

**3.5. Why Is the Asymmetric System Exceeding a Charge Efficiency of 100% at 20 mM?** In the 20 mM system, the charge efficiency repeatedly exceeds 100% and stays there persistently for the whole duration of measurements. This effect, at low molar strength, is not limited to the presence of an ion-exchange membrane, so we cannot explain the charge efficiency in terms of an addition ion-removal capacity of the (mass-wise not accounted) anion-exchange membrane (as shown, for example, by Zhang et al.[54] and Tang et al.).[62] This effect also enhanced the average desalination capacity at 20 mM system (12 mg/g for the cell without membrane) compared to that in the 600 mM system (8 mg/g for the cell without membrane). In the system operated at aqueous 20 mM NaCl, we do not see much of a statistically

significant difference between operation with or without the anion-exchange membrane regarding the charge efficiency. A charge efficiency above 100% means that per 1 mole of electric charge invested upon charging, more than 1 mole of salt ions is removed (or released upon discharging). This surprising effect might be explained in the context of MXene surface charges and the concept of potential at zero charge ($E_{PZC}$), which follows herein.

$Ti_3C_2T_x$-MXene has negatively charged surface functionalities such as $-O$, $-OH$, or $-F$,[63] and as a result has a strong affinity toward positive ionic species such as metal cations[64,65] in aqueous media even under no applied potential (MXene as an adsorbent powder, not as an electrode). These negative surface charges shift the $E_{PZC}$ toward positive potentials. This is evidenced by the streaming potential measurements (Figure S7) on MXene that show a point of zero charge at a pH of 1.5. This means that MXene is negatively charged all the way down to this highly acidic pH, at which point it exhibits a neutral net electric charge, possibly due to protonation of the hydroxyl terminal groups of MXene.[65] Zeta potential measurements on $Ti_3C_2T_x$-MXene in other studies has also shown a point of zero charge at pH values between 2 and 3.[64,65] For comparison, the activated carbon reaches charge neutrality at a pH value of about 3.5 but with a much steeper streaming potential profile as a function of the pH value (in agreement with previous work).[46]

The applied potential range has an important effect on the charge efficiency of a desalination cell.[42,66,67] Systematic studies on symmetric activated-carbon CDI cells[48,49] have shown that highest charge efficiencies (i.e., low co-ion
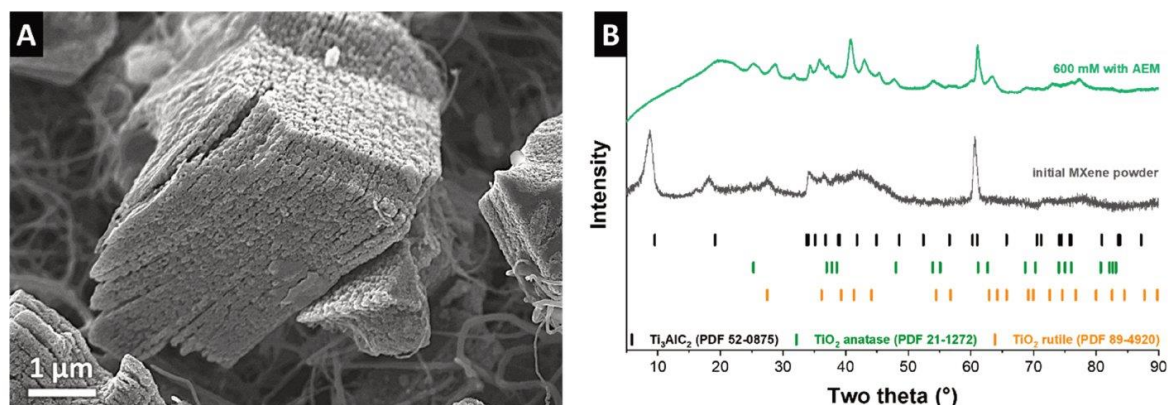
105

**Figure 6.** (A) SEM image of post mortem MXene-CNT electrode after long-term cycling and (B) its corresponding X-ray diffractograms, compared to those of pristine MXene-CNT and a number of different titanium oxide species [Powder Diffraction File (PDF) nos. 21-1272, 52-0875, and 89-4920, Joint Committee on Powder Diffraction Standards, 2004].

expulsion/high counterion uptake) are obtained when the cell is not fully discharged to $E_{PZC}$, but rather to a potential far enough thereof.[61] This condition has apparently been met in our work by cycling within 0.3−1.2 V, as shown schematically in Figure 5A. Discharging to a lower potential limit of 0.3 V prevents MXene and activated carbon to cross their respective $E_{PZC}$ and minimizes parasitic co-ion expulsion phenomenon, resulting in a high charge efficiency. This effect, however, does not explain why the system at low molar strength would be able to exceed charge efficiency values of 100%.

The additional gain in charge efficiency above 100% should then be attributed to the negative surface charges of MXene, which serve as an additional chemical charge.[69] When MXene is negatively polarized, sodium ions intercalate between MXene sheets due to the attraction they feel from both negative applied electric charge and negative surface dipole of functional groups, as schematically illustrated in Figure 5B. Upon discharging the MXene-CNT electrode to 0 V vs Ag/AgCl (Figure S5), all the said applied negative electric charge are retracted, resulting in the release of the corresponding sodium ions adsorbed, while the surface charges still cling to their corresponding sodium ions. Upon further discharging to potentials slightly higher than zero (but still away from $E_{PZC}$), a positive charge is induced in MXene sheets, which helps to overcome the negative charge of surface charges and thereby releasing the remaining sodium ions and regenerating the surface groups. At this point, sodium ions are again in part spontaneously adsorbed to the surface charges in addition to the attraction arising from electric charges. The former is similar to the inverted CDI system at a lower voltage limit, that is, ion adsorption upon discharge due to electrode surface charges.[68] The spontaneous chemisorption of sodium ions onto the negative surface functionalities of MXene could explain the additional gain in charge efficiency. That is, no electric charge is invested for those fractions of ions desalinated via interaction with MXene surface terminations. Consequently, the system capitalizes on MXene surface charges and can remove more than one ion per one electron charge invested; hence, a charge efficiency of above 100% is obtained.

**3.6. Post-Mortem Analysis of MXene-CNT Electrodes after Desalination Operation.** Post-mortem data of the

MXene-CNT electrodes after long-term cycling, including electron microscopy, EDX analysis, and X-ray diffraction, are shown in Figure 6 and Table 1. The data shown in Figure 6 originate from the cell with an anion-exchange membrane at a discharged state cycled in 600 mM solution; SEM images and X-ray diffraction data for post-mortem samples after the operation at 20 mM (with and without ion-exchange membrane) and at 600 mM without the anion-exchange membrane are found in Figures S8 and S9.

As seen in Figure 2, the pristine MXene surface is already slightly oxidized, covered with cuboid-like titanate particles. A comparison of SEM images of pristine MXene-CNT (Figure 2A) and post-mortem electrodes (Figure 6A) reveals a much larger degree of coverage of MXene layers with titanium oxide particles. The increase in oxygen (found for all samples) is mostly accomplished by a decrease in the content of fluorine (Table 1).

The X-ray diffraction pattern of the post-mortem electrode is consistent with previous works on oxidized $Ti_3C_2T_x$;[69] specifically, we note the absence of the characteristic (002)-MXene peak due to oxidation-related disruption in the stacking periodicity and the development of a broad peak at around 20° $2\theta$. The disappearance of the (002) peak can also relate to the insertion/deinsertion of sodium ions between the MXene layers during the electrochemical process and the formation of $TiO_2$ crystals; both effects disrupt the initial MXene-layer stacking order. The low temperature of the oxidation process and the small length-scale of the formed titanium oxide domains are mostly consistent with the formation of nanorutile, but further $TiO_2$ phases (such as anatase) cannot be excluded.

## 4. CONCLUSIONS

Our work explores the electrochemical desalination of asymmetric hybrid CDI using MXene-CNT paired with activated carbon for electrochemical desalination of brackish- and seawater-level NaCl concentrations in aqueous media. Using $Ti_3C_2T_x$-MXene as the negative electrode and nanoporous activated carbon as the positive electrode, stable desalination performance for up to 100 cycles has been accomplished with desalination capacities up to 12 mg/g and charge efficiencies over 80%. It was shown that in the case of

asymmetric configuration permselective behavior is observed without the use of an ion-exchange membrane. While at 20 mM NaCl, the attained permselectivity of the system's response can be rationalized by the selected potential range (avoiding 0 V), it cannot explain the near-100% charge efficiency when using 600 mM NaCl. In addition, we see an excess of the charge efficiency beyond 100% at low molar strength, which can only be explained by the active role played by interlayer surface termination of MXene during the electrochemical desalination cycling. Our data show that at slightly reduced charge efficiency and desalination capacity MXene-CNT paired with activated carbon does not require an ion-exchange membrane for remediation of aqueous 600 mM NaCl. The omission of the ion-exchange membrane from the cell components can thus significantly reduce the overall costs in light of industrial applications.

## ■ ASSOCIATED CONTENT

### ⓈⒾ Supporting Information

The Supporting Information is available free of charge at https://pubs.acs.org/doi/10.1021/acsami.0c05975.

> Nitrogen gas sorption isotherms, transmission electron micrograph images of CNT, cyclic voltammetry of CNT, potential distribution profiles of MXene-CNT/AC cells, energy consumption, streaming potential response of MXene and AC, SEM and XRD of post-mortem MXene-CNT electrodes(PDF)

## ■ AUTHOR INFORMATION

### Corresponding Author

Volker Presser − INM - Leibniz Institute for New Materials, 66123 Saarbrücken, Germany; Department of Materials Science & Engineering, Saarland University, 66123 Saarbrücken, Germany; ⓞ orcid.org/0000-0003-2181-0590; Email: presser@presser-group.com

### Authors

Mohammad Torkamanzadeh − INM - Leibniz Institute for New Materials, 66123 Saarbrücken, Germany; Department of Materials Science & Engineering, Saarland University, 66123 Saarbrücken, Germany

Lei Wang − INM - Leibniz Institute for New Materials, 66123 Saarbrücken, Germany; Department of Materials Science & Engineering, Saarland University, 66123 Saarbrücken, Germany

Yuan Zhang − INM - Leibniz Institute for New Materials, 66123 Saarbrücken, Germany; Department of Materials Science & Engineering, Saarland University, 66123 Saarbrücken, Germany

Öznil Budak − INM - Leibniz Institute for New Materials, 66123 Saarbrücken, Germany; Department of Materials Science & Engineering, Saarland University, 66123 Saarbrücken, Germany

Pattarachai Srimuk − INM - Leibniz Institute for New Materials, 66123 Saarbrücken, Germany

Complete contact information is available at:
https://pubs.acs.org/10.1021/acsami.0c05975

### Notes

The authors declare no competing financial interest.

## ■ ACKNOWLEDGMENTS

## ■ REFERENCES

(1) Elimelech, M.; Phillip, W. A. The Future Of Seawater Desalination: Energy, Technology, And The Environment. *Science* **2011**, *333* (6043), 712−717.

(2) Suss, M. E.; Porada, S.; Sun, X.; Biesheuvel, P. M.; Yoon, J.; Presser, V. Water Desalination Via Capacitive Deionization: What Is It And What Can We Expect From It? *Energy Environ. Sci.* **2015**, *8* (8), 2296−2319.

(3) Porada, S.; Zhao, R.; Van Der Wal, A.; Presser, V.; Biesheuvel, P. Review On The Science And Technology Of Water Desalination By Capacitive Deionization. *Prog. Mater. Sci.* **2013**, *58* (8), 1388−1442.

(4) Andelman, M. D. The Flow Through Capacitor: A New Tool In Wastewater Purification. *Filtr. Sep.* **1998**, *May*, 345−347.

(5) Porada, S.; Weinstein, L.; Dash, R.; Van Der Wal, A; Bryjak, M.; Gogotsi, Y.; Biesheuvel, P. Water Desalination Using Capacitive Deionization With Microporous Carbon Electrodes. *ACS Appl. Mater. Interfaces* **2012**, *4* (3), 1194−1199.

(6) Srimuk, P.; Su, X.; Yoon, J.; Aurbach, D.; Presser, V. Charge-Transfer Materials For Electrochemical Water Desalination, Ion Separation and The Recovery Of Elements. *Nat. Rev. Mater.* **2020**, DOI: 10.1038/s41578-020-0193-1.

(7) Zhao, R.; Biesheuvel, P.; Van der Wal, A. Energy Consumption And Constant Current Operation In Membrane Capacitive Deionization. *Energy Environ. Sci.* **2012**, *5* (11), 9520−9527.

(8) Biesheuvel, P. M.; van der Wal, A. Membrane Capacitive Deionization. *J. Membr. Sci.* **2010**, *346* (2), 256−262.

(9) Kim, N.; Lee, J.; Kim, S.; Hong, P. S.; Lee, C.; Yoon, J.; Kim, C. Short Review Of Multichannel Membrane Capacitive Deionization: Principle, Current Status, And Future Prospect. *Appl. Sci.* **2020**, *10* (2), 683.

(10) Bi, S.; Zhang, Y.; Cervini, L.; Mo, T.; Griffin, J. M.; Presser, V.; Feng, G. Permselective Ion Electrosorption Of Subnanometer Pores At High Molar Strength Enables Capacitive Deionization Of Saline Water. *Sustainable Energy Fuels* **2020**, *4* (3), 1285−1295.

(11) Singh, K.; Porada, S.; de Gier, H. D.; Biesheuvel, P. M.; de Smet, L. C. P. M. Timeline On The Application Of Intercalation Materials In Capacitive Deionization. *Desalination* **2019**, *455*, 115−134.

(12) Pasta, M.; Wessells, C. D.; Cui, Y.; La Mantia, F. A Desalination Battery. *Nano Lett.* **2012**, *12* (2), 839−843.

(13) Lee, J.; Kim, S.; Kim, C.; Yoon, J. Hybrid Capacitive Deionization To Enhance The Desalination Performance Of Capacitive Techniques. *Energy Environ. Sci.* **2014**, *7* (11), 3683−3689.

(14) Srimuk, P.; Kaasik, F.; Krüner, B.; Tolosa, A.; Fleischmann, S.; Jäckel, N.; Tekeli, M. C.; Aslan, M.; Suss, M. E.; Presser, V. MXene As A Novel Intercalation-Type Pseudocapacitive Cathode And Anode For Capacitive Deionization. *J. Mater. Chem. A* **2016**, *4* (47), 18265−18271.

(15) Srimuk, P.; Husmann, S.; Presser, V. Low Voltage Operation Of A Silver/Silver Chloride Battery With High Desalination Capacity In Seawater. *RSC Adv.* **2019**, *9* (26), 14849−14858.

(16) Su, X.; Hatton, T. A. Redox-Electrodes For Selective Electrochemical Separations. *Adv. Colloid Interface Sci.* **2017**, *244*, 6−20.

(17) Lee, J.; Srimuk, P.; Zornitta, R. L.; Aslan, M.; Mehdi, B. L.; Presser, V. High Electrochemical Seawater Desalination Performance Enabled By An Iodide Redox Electrolyte Paired With A Sodium Superionic Conductor. *ACS Sustainable Chem. Eng.* **2019**, *7* (11), 10132−10142.

(18) Kim, S.; Kim, C.; Lee, J.; Kim, S.; Lee, J.; Kim, J.; Yoon, J. Hybrid Electrochemical Desalination System Combined With An Oxidation Process. *ACS Sustainable Chem. Eng.* **2018**, *6* (2), 1620−1626.

(19) Srimuk, P.; Wang, L.; Budak, Ö.; Presser, V. High-Performance Ion Removal Via Zinc-Air Desalination. *Electrochem. Commun.* **2020**, *115*, 106713.

(20) Naguib, M.; Mashtalir, O.; Carle, J.; Presser, V.; Lu, J.; Hultman, L.; Gogotsi, Y.; Barsoum, M. W. Two-Dimensional Transition Metal Carbides. *ACS Nano* **2012**, *6* (2), 1322−1331.

(21) Gogotsi, Y.; Anasori, B. The Rise of MXenes. *ACS Nano* **2019**, *13* (8), 8491−8494.

(22) Anasori, B.; Lukatskaya, M. R.; Gogotsi, Y. 2D Metal Carbides And Nitrides (MXenes) For Energy Storage. *Nat. Rev. Mater.* **2017**, *2*, 16098.

(23) Natu, V.; Pai, R.; Sokol, M.; Carey, M.; Kalra, V.; Barsoum, M. W. 2D $Ti_3C_2T_z$ Mxene Synthesized By Water-Free Etching Of $Ti_3AlC_2$ In Polar Organic Solvents. *Chem.* **2020**, *6* (3), 616−630.

(24) Shahzad, F.; Alhabeb, M.; Hatter, C. B.; Anasori, B.; Man Hong, S.; Koo, C. M.; Gogotsi, Y. Electromagnetic Interference Shielding With 2D Transition Metal Carbides (MXenes). *Science* **2016**, *353* (6304), 1137−1140.

(25) Orangi, J.; Hamade, F.; Davis, V. A.; Beidaghi, M. 3D Printing Of Additive-Free 2D $Ti_3C_2T_x$ (MXene) Ink For Fabrication Of Micro-Supercapacitors With Ultra-High Energy Densities. *ACS Nano* **2020**, *14* (1), 640−650.

(26) Sun, D.; Wang, M.; Li, Z.; Fan, G.; Fan, L.-Z.; Zhou, A. Two-Dimensional $Ti_3C_2$ As Anode Material For Li-Ion Batteries. *Electrochem. Commun.* **2014**, *47*, 80−83.

(27) Lukatskaya, M. R.; Mashtalir, O.; Ren, C. E.; Dall'Agnese, Y.; Rozier, P.; Taberna, P. L.; Naguib, M.; Simon, P.; Barsoum, M. W.; Gogotsi, Y. Cation Intercalation And High Volumetric Capacitance Of Two-Dimensional Titanium Carbide. *Science* **2013**, *341* (6153), 1502−1505.

(28) Ren, C. E.; Hatzell, K. B.; Alhabeb, M.; Ling, Z.; Mahmoud, K. A.; Gogotsi, Y. Charge-And Size-Selective Ion Sieving Through $Ti_3C_2T_x$ MXene Membranes. *J. Phys. Chem. Lett.* **2015**, *6* (20), 4026−4031.

(29) Peng, Q.; Guo, J.; Zhang, Q.; Xiang, J.; Liu, B.; Zhou, A.; Liu, R.; Tian, Y. Unique Lead Adsorption Behavior Of Activated Hydroxyl Group In Two-Dimensional Titanium Carbide. *J. Am. Chem. Soc.* **2014**, *136* (11), 4113−4116.

(30) Rasool, K.; Pandey, R. P.; Rasheed, P. A.; Buczek, S.; Gogotsi, Y.; Mahmoud, K. A. Water Treatment And Environmental Remediation Applications Of Two-Dimensional Metal Carbides (MXenes). *Mater. Today* **2019**, *30*, 80−102.

(31) Bao, W.; Tang, X.; Guo, X.; Choi, S.; Wang, C.; Gogotsi, Y.; Wang, G. Porous Cryo-Dried MXene For Efficient Capacitive Deionization. *Joule* **2018**, *2* (4), 778−787.

(32) Ma, J.; Cheng, Y.; Wang, L.; Dai, X.; Yu, F. Free-Standing $Ti_3C_2T_x$ MXene Film As Binder-Free Electrode In Capacitive Deionization With An Ultrahigh Desalination Capacity. *Chem. Eng. J.* **2020**, *384*, 123329.

(33) Amiri, A.; Chen, Y.; Bee Teng, C.; Naraghi, M. Porous Nitrogen-Doped MXene-Based Electrodes For Capacitive Deionization. *Energy Storage Materials* **2020**, *25*, 731−739.

(34) Chen, B.; Feng, A.; Deng, R.; Liu, K.; Yu, Y.; Song, L. MXene as a Cation-Selective Cathode Material for Asymmetric Capacitive Deionization. *ACS Appl. Mater. Interfaces* **2020**, *12* (12), 13750−13758.

(35) Huang, S.; Mochalin, V. N. Hydrolysis Of 2D Transition-Metal Carbides (MXenes) In Colloidal Solutions. *Inorg. Chem.* **2019**, *58* (3), 1958−1966.

(36) Tian, Y.; Yang, C.; Tang, Y.; Luo, Y.; Lou, X.; Que, W. $Ti_3C_2T_x$//AC Dual-Ions Hybrid Aqueous Supercapacitors With High Volumetric Energy Density. *Chem. Eng. J.* **2020**, *393*, 124790.

(37) Carmona-Orbezo, A.; Le Fevre, L. W.; Dryfe, R. A. W. Performance Optimization Of Carbon Electrodes For Capacitive Deionization By Potentiostatic Analysis. *Electrochim. Acta* **2019**, *325*, 134898.

(38) Zhang, Y.; Srimuk, P.; Husmann, S.; Chen, M.; Feng, G.; Presser, V. Effect Of Pore Size On The Ion Electrosorption And Hydrogen/Deuterium Electrosorption Using Sodium Chloride In $H_2O$ And $D_2O$. *J. Electrochem. Soc.* **2019**, *166* (16), A4158−A4167.

(39) Jäckel, N.; Weingarth, D.; Zeiger, M.; Aslan, M.; Grobelsek, I.; Presser, V. Comparison Of Carbon Onions And Carbon Blacks As Conductive Additives For Carbon Supercapacitors In Organic Electrolytes. *J. Power Sources* **2014**, *272* (1), 1122−1133.

(40) Srimuk, P.; Halim, J.; Lee, J.; Tao, Q.; Rosen, J.; Presser, V. Two-Dimensional Molybdenum Carbide (MXene) With Divacancy Ordering For Brackish And Seawater Desalination Via Cation And Anion Intercalation. *ACS Sustainable Chem. Eng.* **2018**, *6* (3), 3739−3747.

(41) Weingarth, D.; Zeiger, M.; Jäckel, N.; Aslan, M.; Feng, G.; Presser, V. Graphitization As A Universal Tool To Tailor The Potential-Dependent Capacitance Of Carbon Supercapacitors. *Adv. Energy Mater.* **2014**, *4* (13), 1400316.

(42) Zornitta, R. L.; Srimuk, P.; Lee, J.; Krüner, B.; Aslan, M.; Ruotolo, L. A. M.; Presser, V. Charge And Potential Balancing For Optimized Capacitive Deionization Using Lignin-Derived, Low-Cost Activated Carbon Electrodes. *ChemSusChem* **2018**, *11* (13), 2101−2113.

(43) Weingarth, D.; Noh, H.; Foelske-Schmitz, A.; Wokaun, A.; Kötz, R. A Reliable Determination Method Of Stability Limits For Electrochemical Double Layer Capacitors. *Electrochim. Acta* **2013**, *103*, 119−124.

(44) Srimuk, P.; Lee, J.; Fleischmann, S.; Choudhury, S.; Jäckel, N.; Zeiger, M.; Kim, C.; Aslan, M.; Presser, V. Faradaic Deionization Of Brackish And Sea Water Via Pseudocapacitive Cation And Anion Intercalation Into Few-Layered Molybdenum Disulfide. *J. Mater. Chem. A* **2017**, *5* (30), 15640−15649.

(45) Ghidiu, M.; Barsoum, M. W. The {110} Reflection In X-Ray Diffraction Of Mxene Films: Misinterpretation And Measurement Via Non-Standard Orientation. *J. Am. Ceram. Soc.* **2017**, *100* (12), 5395−5399.

(46) Aslan, M.; Zeiger, M.; Jäckel, N.; Grobelsek, I.; Weingarth, D.; Presser, V. Improved Capacitive Deionization Performance Of Mixed Hydrophobic/Hydrophilic Activated Carbon Electrodes. *J. Phys.: Condens. Matter* **2016**, *28* (11), 114003.

(47) Gerischer, H.; McIntyre, R.; Scherson, D.; Storck, W. Density Of The Electronic States Of Graphite: Derivation From Differential Capacitance Measurements. *J. Phys. Chem.* **1987**, *91* (7), 1930−1935.

(48) Avraham, E.; Noked, M.; Bouhadana, Y.; Soffer, A.; Aurbach, D. Limitations Of Charge Efficiency In Capacitive Deionization II. On The Behavior Of CDI Cells Comprising Two Activated Carbon Electrodes. *J. Electrochem. Soc.* **2009**, *156* (10), P157−P162.

(49) Avraham, E.; Noked, M.; Bouhadana, Y.; Soffer, A.; Aurbach, D. Limitations Of Charge Efficiency In Capacitive Deionization Processes III: The Behavior Of Surface Oxidized Activated Carbon Electrodes. *Electrochim. Acta* **2010**, *56* (1), 441−447.

(50) Come, J.; Black, J. M.; Lukatskaya, M. R.; Naguib, M.; Beidaghi, M.; Rondinone, A. J.; Kalinin, S. V.; Wesolowski, D. J.; Gogotsi, Y.; Balke, N. Controlling The Actuation Properties Of MXene Paper Electrodes Upon Cation Intercalation. *Nano Energy* **2015**, *17*, 27−35.

(51) Srimuk, P.; Lee, J.; Budak, Ö.; Choi, J.; Chen, M.; Feng, G.; Prehal, C.; Presser, V. In Situ Tracking Of Partial Sodium Desolvation Of Materials With Capacitive, Pseudocapacitive, And Battery-Like Charge/Discharge Behavior In Aqueous Electrolytes. *Langmuir* **2018**, *34* (44), 13132−13143.

(52) Sun, Y.; Zhan, C.; Kent, P. R. C.; Naguib, M.; Gogotsi, Y.; Jiang, D. E. Proton Redox And Transport In Mxene-Confined Water. *ACS Appl. Mater. Interfaces* **2020**, *12* (1), 763−770.

(53) Porada, S.; Borchardt, L.; Oschatz, M.; Bryjak, M.; Atchison, J. S.; Keesman, K. J.; Kaskel, S.; Biesheuvel, P. M.; Presser, V. Direct Prediction Of The Desalination Performance Of Porous Carbon Electrodes For Capacitive Deionization. *Energy Environ. Sci.* **2013**, *6* (12), 3700−3712.

108

(54) Zhang, Y.; Srimuk, P.; Aslan, M.; Gallei, M.; Presser, V. Polymer Ion-Exchange Membranes For Capacitive Deionization Of Aqueous Media With Low And High Salt Concentration. *Desalination* **2020**, *479*, 114331.

(55) Biesheuvel, P. M.; Porada, S.; Levi, M.; Bazant, M. Z. Attractive Forces In Microporous Carbon Electrodes For Capacitive Deionization. *J. Solid State Electrochem.* **2014**, *18* (5), 1365−1376.

(56) Salitra, G.; Soffer, A.; Eliad, L.; Cohen, Y.; Aurbach, D. Carbon Electrodes For Double-Layer Capacitors I. Relations Between Ion And Pore Dimensions. *J. Electrochem. Soc.* **2000**, *147* (7), 2486.

(57) Avraham, E.; Yaniv, B.; Soffer, A.; Aurbach, D. Developing Ion Electroadsorption Stereoselectivity, By Pore Size Adjustment With Chemical Vapor Deposition Onto Active Carbon Fiber Electrodes. Case of $Ca^{2+}/Na^{+}$ Separation In Water Capacitive Desalination. *J. Phys. Chem. C* **2008**, *112* (19), 7385−7389.

(58) Prehal, C.; Koczwara, C.; Amenitsch, H.; Presser, V.; Paris, O. Salt Concentration And Charging Velocity Determine Ion Charge Storage Mechanism In Nanoporous Supercapacitors. *Nat. Commun.* **2018**, *9* (1), 4145.

(59) Gao, X.; Omosebi, A.; Ma, Z.; Zhu, F.; Landon, J.; Ghorbanian, M.; Kern, N.; Liu, K. Capacitive Deionization Using Symmetric Carbon Electrode Pairs. *Environ. Sci.: Water Res. Technol.* **2019**, *5* (4), 660−671.

(60) Shpigel, N.; Levi, M. D.; Sigalov, S.; Aurbach, D.; Daikhin, L.; Presser, V. Novel In Situ Multiharmonic EQCM-D Approach To Characterize Complex Carbon Pore Architectures For Capacitive Deionization Of Brackish Water. *J. Phys.: Condens. Matter* **2016**, *28* (11), 114001.

(61) Kim, T.; Dykstra, J. E.; Porada, S.; van der Wal, A.; Yoon, J.; Biesheuvel, P. M. Enhanced Charge Efficiency And Reduced Energy Use In Capacitive Deionization By Increasing The Discharge Voltage. *J. Colloid Interface Sci.* **2015**, *446*, 317−326.

(62) Tang, K.; Kim, Y.-h.; Chang, J.; Mayes, R. T.; Gabitto, J.; Yiacoumi, S.; Tsouris, C. Seawater Desalination By Over-Potential Membrane Capacitive Deionization: Opportunities And Hurdles. *Chem. Eng. J.* **2019**, *357* (1), 103−111.

(63) Alhabeb, M.; Maleski, K.; Anasori, B.; Lelyukh, P.; Clark, L.; Sin, S.; Gogotsi, Y. Guidelines For Synthesis And Processing Of Two-Dimensional Titanium Carbide ($Ti_3C_2T_x$ MXene). *Chem. Mater.* **2017**, *29* (18), 7633−7644.

(64) Fard, A. K.; Mckay, G.; Chamoun, R.; Rhadfi, T.; Preud'Homme, H.; Atieh, M. A. Barium Removal From Synthetic Natural And Produced Water Using MXene As Two Dimensional (2-D) Nanosheet Adsorbent. *Chem. Eng. J.* **2017**, *317*, 331−342.

(65) Shahzad, A.; Rasool, K.; Miran, W.; Nawaz, M.; Jang, J.; Mahmoud, K. A.; Lee, D. S. Two-Dimensional $Ti_3C_2T_x$ MXene Nanosheets For Efficient Copper Removal From Water. *ACS Sustainable Chem. Eng.* **2017**, *5* (12), 11481−11488.

(66) Abu Khalla, S.; Suss, M. E. Desalination Via Chemical Energy: An Electrodialysis Cell Driven By Spontaneous Electrode Reactions. *Desalination* **2019**, *467*, 257−262.

(67) Porada, S.; Schipper, F.; Aslan, M.; Antonietti, M.; Presser, V.; Fellinger, T.-P. Capacitive Deionization Using Biomass-Based Microporous Salt-Templated Heteroatom-Doped Carbons. *ChemSusChem* **2015**, *8* (11), 1867−1874.

(68) Gao, X.; Omosebi, A.; Landon, J.; Liu, K. Surface Charge Enhanced Carbon Electrodes For Stable And Efficient Capacitive Deionization Using Inverted Adsorption−Desorption Behavior. *Energy Environ. Sci.* **2015**, *8* (3), 897−909.

(69) Zhang, M.; Chen, X.; Sui, J.; Abraha, B. S.; Li, Y.; Peng, W.; Zhang, G.; Zhang, F.; Fan, X. Improving the Performance of Titanium Carbide MXene in Supercapacitor by Partial Oxidation Treatment. *Inorg. Chem. Front.* **2020**, *7* (5), 1205−1211.

*Supporting Information*

## MXene/activated carbon hybrid capacitive deionization

## for permselective ion removal at low and high salinity

Mohammad Torkamanzadeh,[1,2] Lei Wang,[1,2] Yuan Zhang,[1,2]

Öznil Budak,[1,2] Pattarachai Srimuk,[1] Volker Presser,[1,2,*]

[1]    *INM - Leibniz Institute for New Materials, D2 2, 66123, Saarbrücken, Germany*

[2]    *Department of Materials Science & Engineering, Saarland University, Campus D2 2, 66123, Saarbrücken,*
    *Germany*

\*    Corresponding author's email: presser@presser-group.com
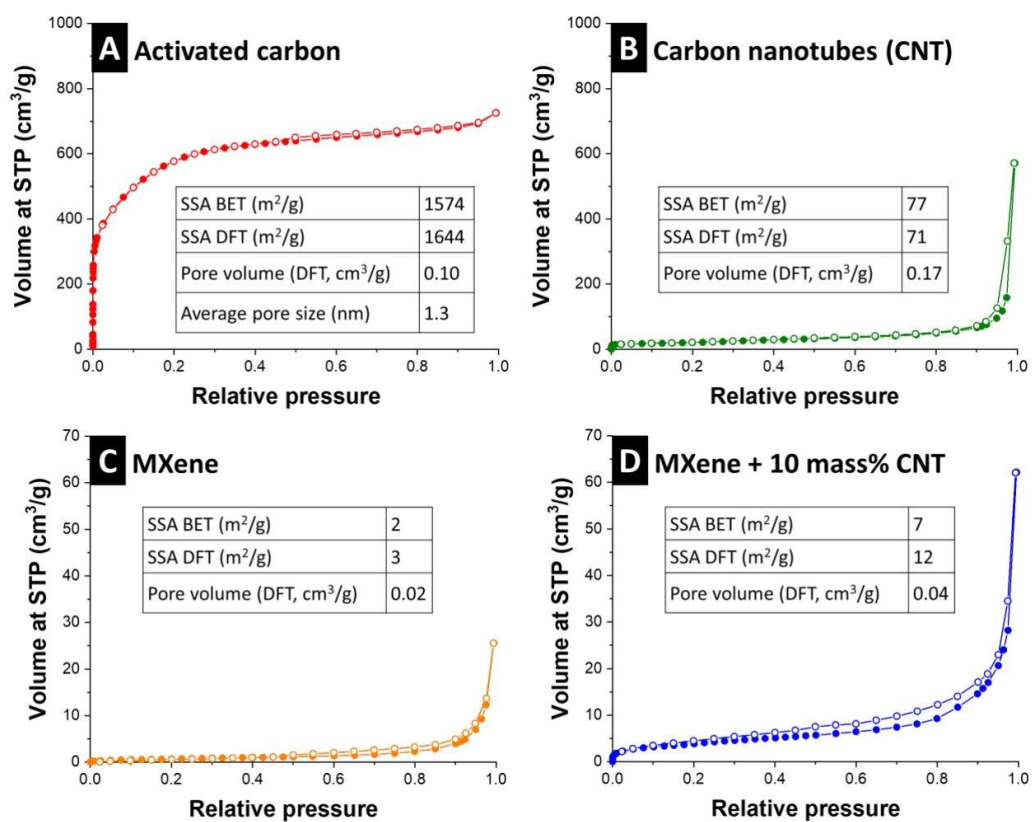
**Figure S1:** Nitrogen gas sorption isotherm of (A) activated carbon, (B) carbon nanotubes, (C) MXene powder, and (D) MXene/carbon nanotube electrodes recorded at a temperature of -196 °C. STP: standard temperature and pressure.
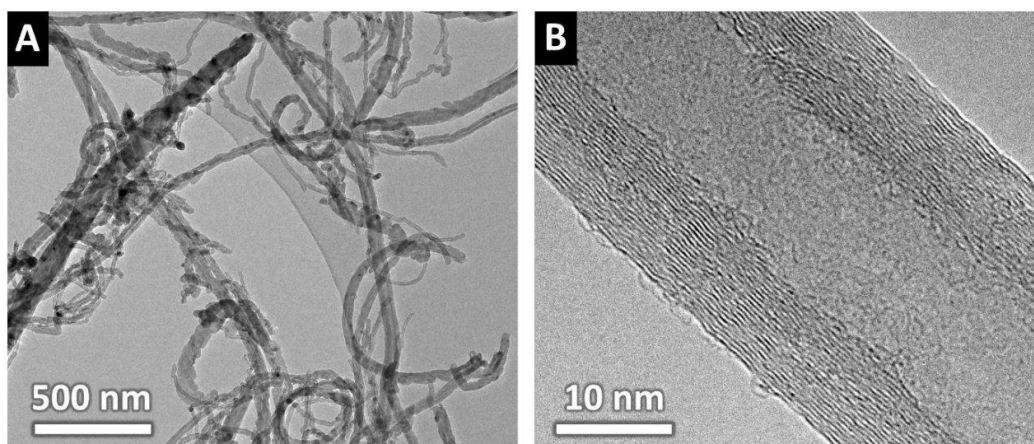


**Figure S2:** Transmission electron micrographs of the carbon nanotubes.
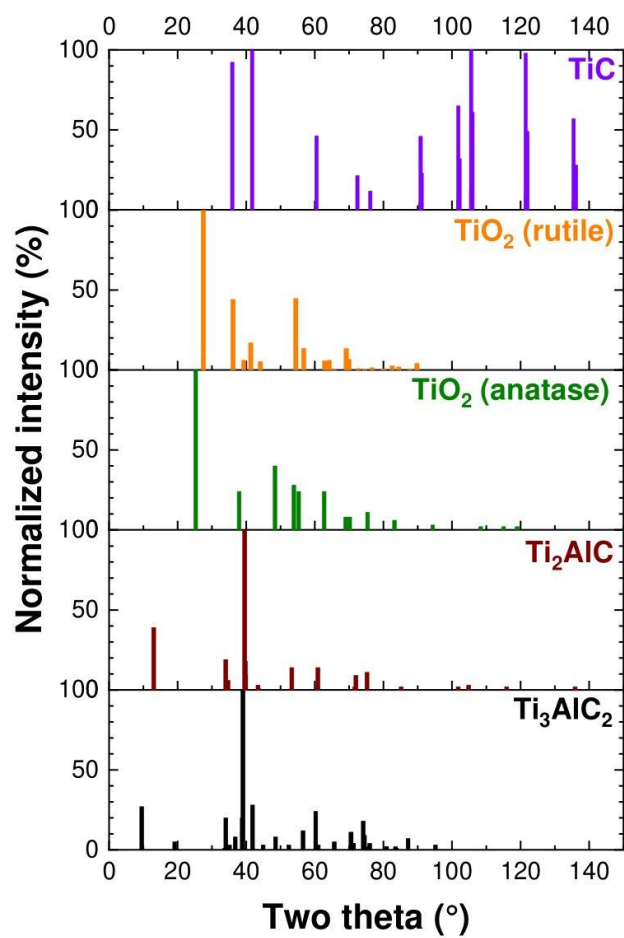
**Figure S3:** Relative intensities of the reference phases provided in Figure 2D.
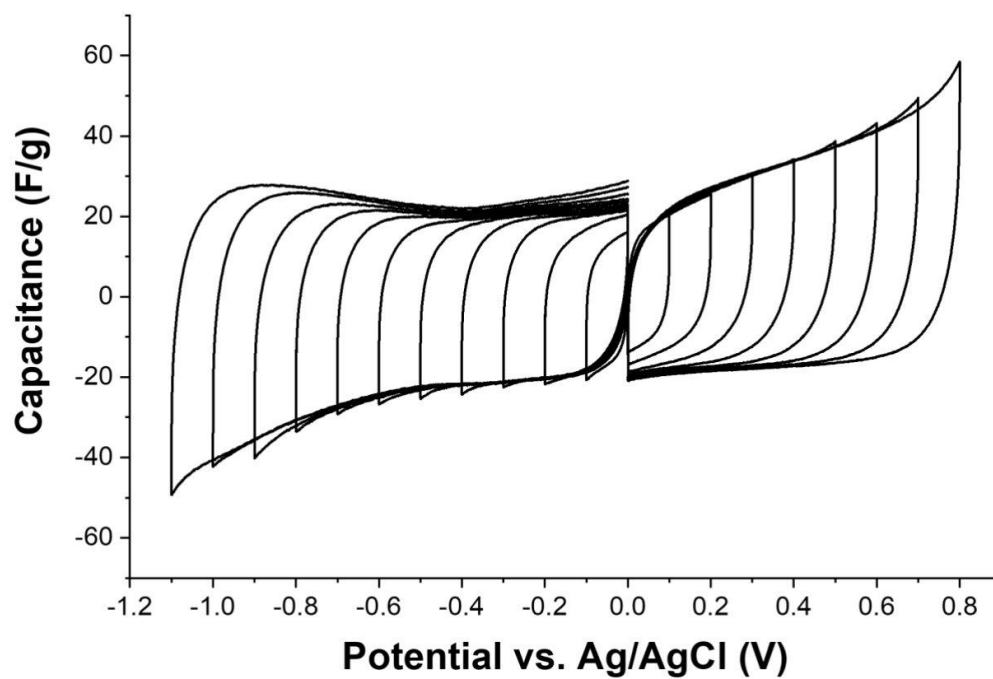
**Figure S4:** Half-cell window opening cyclic voltammograms of electrodes just composed of CNTs in aqueous 1 M NaCl electrolyte.
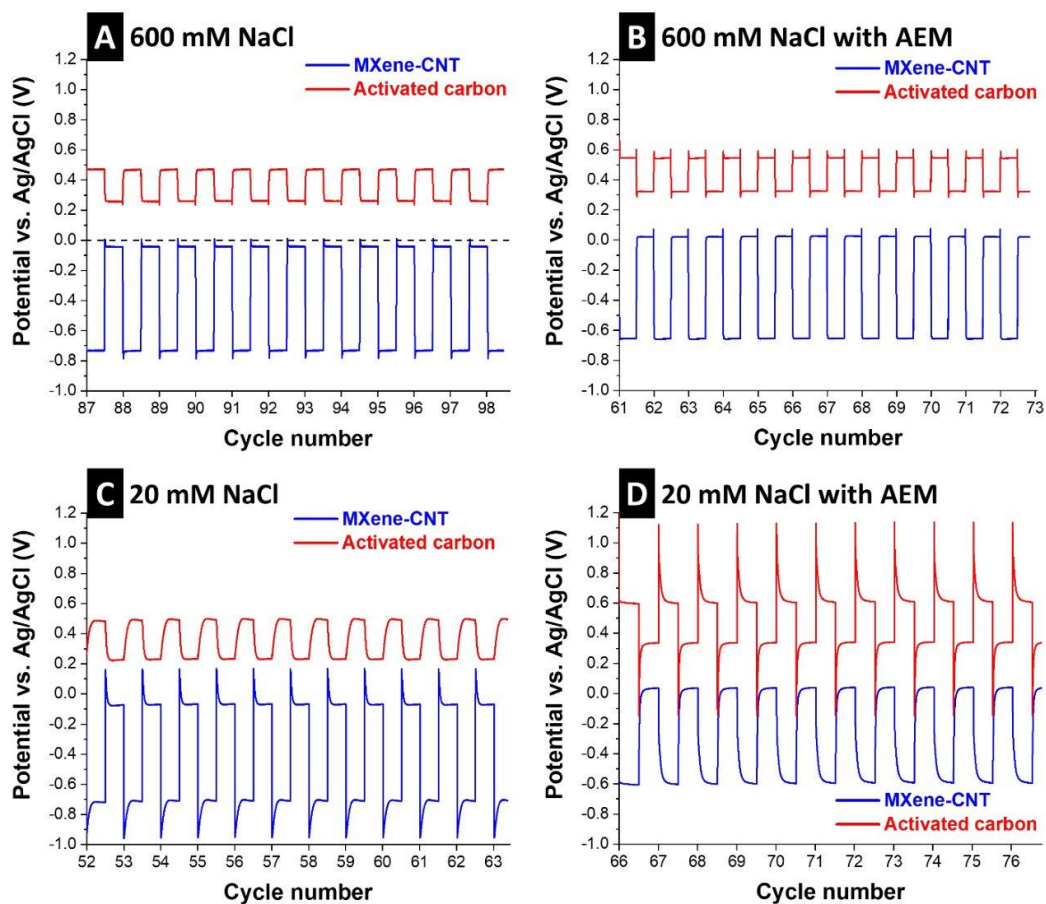
**Figure S5:** Potential development of individual electrodes upon charging the MXene/AC cell to a cell voltage of 1.2 V and discharging to a cell voltage of 0.3 V. (A-B) aqueous 600 mM NaCl; (C-D) aqueous 20 mM NaCl; (A,C) without an anion-exchange membrane (AEM) placed in front of the activated carbon electrode; (B,D) experiments with an AEM at the activated carbon electrode.
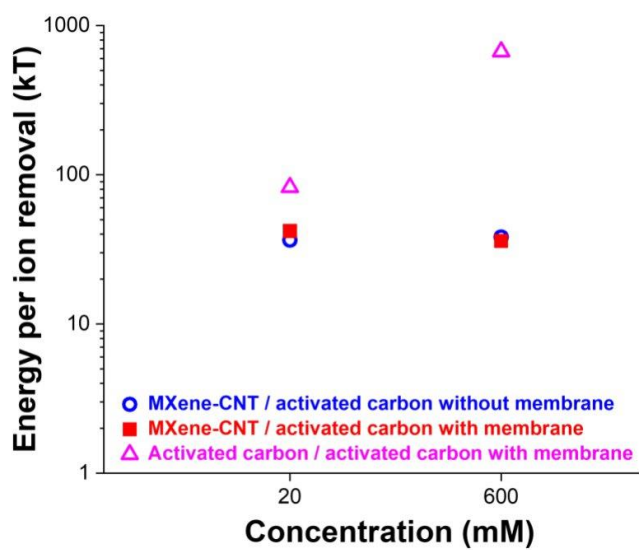
**Figure S6:** Energy consumption per ion removal.
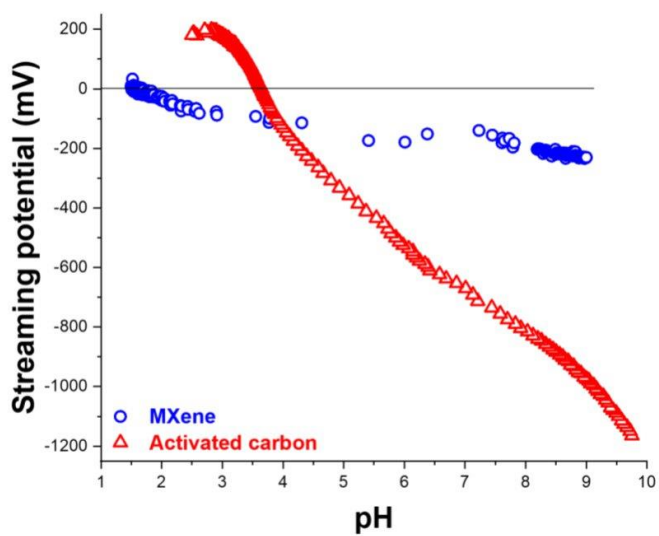


**Figure S7:** Streaming potential response of MXene and activated carbon in water.
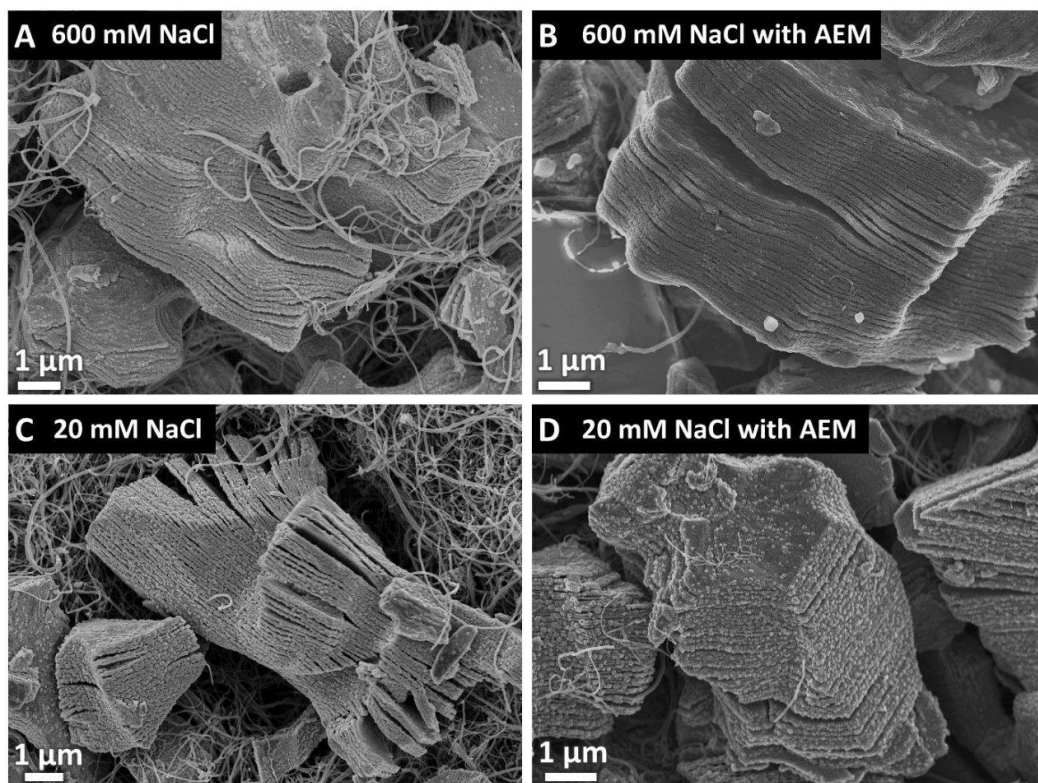
**Figure S8:** Post mortem scanning electron micrographs of MXene-CNT electrodes.
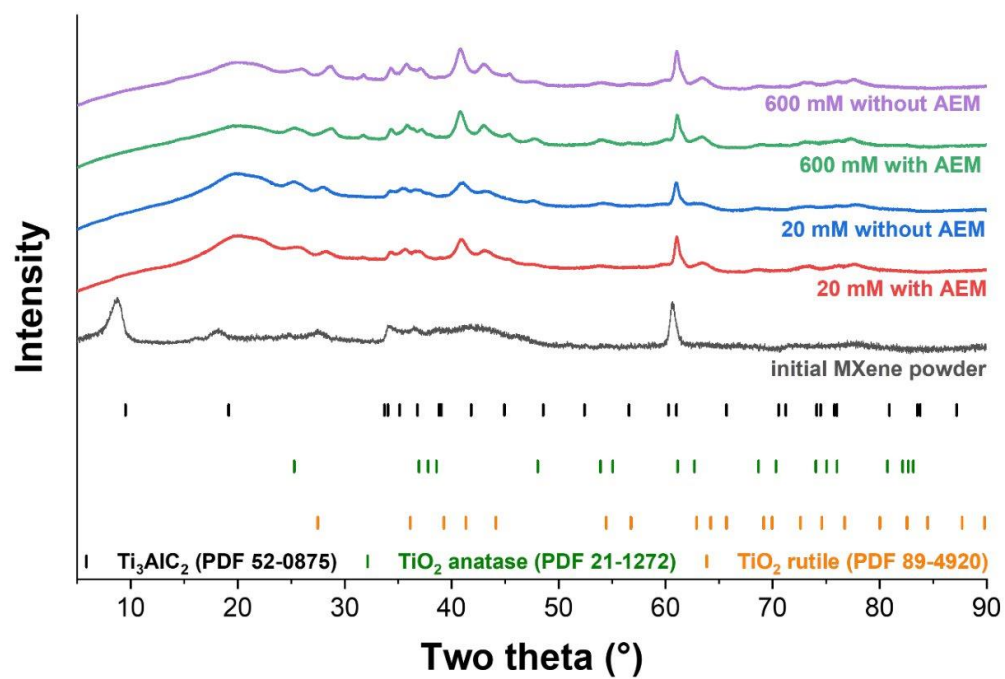
**Figure S9:** X-ray powder diffraction pattern of the initial MXene powder and after electrochemical operation for desalination (post mortem).

## 4.3. Time-Dependent Cation Selectivity of Titanium Carbide MXene in Aqueous Solution

*Lei Wang,[‡] Mohammad Torkamanzadeh,[‡] Ahmad Majed, Yuan Zhang,*

*Qingsong Wang, Ben Breitung, Guang Feng, Michael Naguib, Volker Presser\**


L. Wang, M. Torkamanzadeh, Y. Zhang, Q. Wang, V. Presser

INM - Leibniz Institute for New Materials, D2 2, 66123, Saarbrücken, Germany.


L. Wang, M. Torkamanzadeh, Y. Zhang, V. Presser

Department of Materials Science & Engineering, Saarland University, Campus D2 2, 66123, Saarbrücken, Germany.

A. Majed, M. Naguib

Department of Physics and Engineering Physics, Tulane University, New Orleans, Louisiana 70118, United States of America.

Q. Wang, B. Breitung

Institute of Nanotechnology, Karlsruhe Institute of Technology, Hermann-von-Helmholtz-Platz 1, 76344, Eggenstein-Leopoldshafen, Germany.

G. Feng

State Key Laboratory of Coal Combustion, School of Energy and Power Engineering, Huazhong University of Science and Technology; Nano Interface Centre for Energy, School of Energy and Power Engineering, HUST, Wuhan 430074, Hubei, China.

V. Presser

Saarene, Saarland Center for Energy Materials and Sustainability, Campus C4 2, 66123 Saarbrücken, Germany

[‡] Contributed equally.

Citation:

Own contributions:

Investigation, Methodology, Conceptualization, Data curation, Visualization, Writing - Original Draft, Writing - Review & Editing.

# Time-Dependent Cation Selectivity of Titanium Carbide MXene in Aqueous Solution

*Lei Wang, Mohammad Torkamanzadeh, Ahmad Majed, Yuan Zhang, Qingsong Wang, Ben Breitung, Guang Feng, Michael Naguib, and Volker Presser\**

**Electrochemical ion separation is a promising technology to recover valuable ionic species from water. Pseudocapacitive materials, especially 2D materials, are up-and-coming electrodes for electrochemical ion separation. For implementation, it is essential to understand the interplay of the intrinsic preference of a specific ion (by charge/size), kinetic ion preference (by mobility), and crystal structure changes. $Ti_3C_2T_z$ MXene is chosen here to investigate its selective behavior toward alkali and alkaline earth cations. Utilizing an online inductively coupled plasma system, it is found that $Ti_3C_2T_z$ shows a time-dependent selectivity feature. In the early stage of charging (up to about 50 min), $K^+$ is preferred, while ultimately $Ca^{2+}$ and $Mg^{2+}$ uptake dominate; this unique phenomenon is related to dehydration energy barriers and the ion exchange effect between divalent and monovalent cations. Given the wide variety of MXenes, this work opens the door to a new avenue where selective ion-separation with MXene can be further engineered and optimized.**

## 1. Introduction

Ion separation is an essential process to extract valuable metal from natural water[1] and achieve sustainable development.[2] Most commonly, ion separation is studied through adsorption[3] or membrane-based sieving processes[4] and is extended to organic compounds.[5] In addition to seeking reduced cost and energy consumption approaches, there is also a strong motivation to explore and implement more sustainable ion separation technologies.[6] Recently, electrochemical ion separation

has emerged as a promising alternative to traditional separation processes due to its high selectivity metrics and energy efficiency.[7]

Depending on the nature of electroactive material, the ion immobilization and separation process mechanisms are different. For example, nanoporous carbons immobilize ions via electrosorption. Sub-nanometer pores may cause ion sieving or require ions to (partially) shed their solvation shell; this effect enables further tunability of the ion selectivity.[8] Even more confined sites for ion uptake are found in Faradaic materials.[9] Thereby, processes such as ion intercalation or other redox processes enable selectivity toward certain cations or anions.[9,10] For example, $LiMn_2O_4$ provides facile intercalation into its crystal structure only for specific ions with matched size and valence, aligning with intrinsic ion selectivity.[11] Other materials like $TiS_2$[12] show potential-dependent (tunable) ion selectivity according to the hydration energy of ions. This mechanism is linked with the specific onset potential for ion intercalation (or other redox processes), which gives rise to the unique battery-like feature in electrochemical measurements.[13] Yet, the ion selectivity of pseudocapacitive materials has remained largely unexplored.[14]

MXene is a promising, quickly growing, and novel family of 2D metal carbides or nitrates.[15] The ability to reversibly

L. Wang, M. Torkamanzadeh, Y. Zhang, Q. Wang, V. Presser
INM – Leibniz Institute for New Materials
D2 2, 66123 Saarbrücken, Germany
E-mail: volker.presser@leibniz-inm.de
L. Wang, M. Torkamanzadeh, Y. Zhang, V. Presser
Department of Materials Science and Engineering
Saarland University
Campus D2 2, 66123 Saarbrücken, Germany
A. Majed, M. Naguib
Department of Physics and Engineering Physics
Tulane University
New Orleans, LA 70118, USA

Q. Wang, B. Breitung
Institute of Nanotechnology
Karlsruhe Institute of Technology
Hermann-von-Helmholtz-Platz 1, 76344 Eggenstein-Leopoldshafen, Germany
G. Feng
State Key Laboratory of Coal Combustion
School of Energy and Power Engineering
Huazhong University of Science and Technology
Wuhan, Hubei 430074, China
G. Feng
Nano Interface Centre for Energy
School of Energy and Power Engineering
HUST
Wuhan, Hubei 430074, China
V. Presser
Saarene
Saarland Center for Energy Materials and Sustainability
Campus C4 2, 66123 Saarbrücken, Germany

**ADVANCED
SCIENCE NEWS**
www.advancedsciencenews.com

**ADVANCED
SUSTAINABLE
SYSTEMS**
www.advsustainsys.com

intercalate cations and anions between the MXene-layers[16] yields a pseudocapacitive response, while the carbide/nitride core provides rapid charge transport.[17] Moreover, the surface functional groups such as −F, −OH, and −O on the transition metal atoms formed during the etching process facilitate easier cation intercalation.[18] Thereby, MXenes are widely studied in electrochemical energy storage,[19] water purification,[20] and sensing,[21] among other applications. Regarding aqueous media, Gao et al. used computational simulations to study the positionings of the cations within the MXene slit pores and found that Li+, Na+, and K+ display specific adsorption on the pore surface while Cs+ and Mg2+ are located in the pore center.[22] Recently, Sun et al. reported that titanium carbide-based MXene showed selectivity toward Ca2+ compared with Na+ and Mg2+.[23] The latter work limited its scope to three cations (Ca2+, Mg2+, and Na+) and the influence of the anode on the selectivity performance of the MXene cathode.

Our work investigates the intercalation process of $Ti_3C_2T_z$ in a multi-cation aqueous electrolyte and the competition for intrinsic and time-dependent preferences between different cations. Using online chemical monitoring with inductively coupled plasma optical emission spectroscopy (ICP-OES), we find that the $Ti_3C_2T_z$ exhibits a time-dependent selectivity between Li+, Na+, K+, Ca2+, and Mg2+. At the same time, there is an ion-exchange phenomenon between the divalent cations and monovalent cations (except Li+) during the late ion-intercalation process. The variation of the crystal structure of $Ti_3C_2T_z$ during the electrochemical process is explored by in situ X-ray diffraction (XRD).

## 2. Results and Discussion

The scanning electron images show that $Ti_3C_2T_z$ has common accordion-like multilayers of MXene (Figure S1A,B, Supporting Information), implying a successful exfoliation. The MXene-carbon nanotube ($Ti_3C_2T_z$-CNT) electrode also shows the same morphology as the $Ti_3C_2T_z$ powder except that CNTs are distributed on the surface of $Ti_3C_2T_z$ particle (Figure S2, Supporting Information). CNTs entangle the MXene flakes and enhance the electrode's mechanical stability to avoid MXene loss during the desalination experiments. The removal of aluminum from the parent $Ti_3AlC_2$ MAX phase is confirmed by energy-dispersive X-ray (EDX) spectra of $Ti_3C_2T_z$ (Figure S3, Supporting Information). The XRD patterns (Figure S1C, Supporting Information) also confirm the presence of $Ti_3C_2T_z$-type MXene with repeating (00*l*) diffraction peaks. The (002) reflection of $Ti_3C_2T_z$ splits into two peaks (Figure S1D, Supporting Information), at 6.9° 2$\theta$ (*d*-spacing, 1.28 nm) and 8.2° 2$\theta$ (*d*-spacing, 1.08 nm). After heating at 80 °C under vacuum overnight, only one peak is seen at 8.5° 2$\theta$ (*d*-spacing, 1.04 nm), indicating that the split (002) peak is caused by the residual water in between the layers. Compared with the powder sample, the $Ti_3C_2T_z$ electrode shows almost the same (002) peak, demonstrating that the probe ultrasonication does not affect the inherent characteristics of $Ti_3C_2T_z$.

To investigate the ion selectivity of $Ti_3C_2T_z$ electrodes, we used a low concentration aqueous electrolyte of Li+, Na+, K+, Ca2+, and Mg2+, with a concentration of 10 nM for each cation; and each charging and discharging process of 3 h. As shown in Figure S4 in the Supporting Information, the potential holding

of the $Ti_3C_2T_z$ remains below 0 V versus Ag/AgCl, ensuring that the $Ti_3C_2T_z$ electrode only uptakes cations.[24] **Figure 1** shows the cation concentration changes over time in the 2nd, 6th, 10th, and 17th cycles obtained by subtracting the baseline from the initial concentration curve. The 14th cycle is shown in Figure S5 in the Supporting Information. The baseline of each cycle is established by connecting the start and endpoint of each half-cycle (Figure S6, Supporting Information). During the charging process, in the beginning, the concentration of all the cations decreases over time. Moreover, the concentration changes of these five cations reach the maximum simultaneously, meaning that the intercalation of these cations is synchronous. This phenomenon is different from obvious dynamics-dependent electrosorption (e.g., monovalent cations are up-taken faster than divalent cations) in subnanometer pores of carbon materials.[8] The difference is attributed to the flexible interlayer spacing of $Ti_3C_2T_z$, which will increase (breathe) as the cations intercalate into $Ti_3C_2T_z$.[25] The maximum concentration change during the charging process follows K+ > Na+ > Ca2+ ≈ Mg2+ > Li+, implying that K+ is preferred during this process. After around 50 min, the concentration change of monovalent cations is positive, while that of divalent cations is still negative. This phenomenon can be explained by ion exchange between monovalent and divalent cations, which is because Mg2+ and Ca2+ carry twice the amount of the charge as Li+, Na+, and K+.[26]

Having a certain amount of negative electric charge applied to the MXene electrode, the required number of divalent cations would be less than (half) that of monovalent cations to compensate the same electric charge. Therefore, divalent cations have higher competitiveness for intercalation in a confined space between $Ti_3C_2T_z$ layers. A similar ion exchange between monovalent and divalent cations is also observed in the case of porous carbon electrodes, where ions are stored based on electrical double layers (EDLs). In EDLs, as long as the dilute-theory works, in the beginning, the majority of ions in the solution are preferred while subsequently they will be replaced by ions with higher valence.[27] After the 10th cycle, the cation exchange between divalent and Li+ is very weak, concluded from no net concentration increase in the course of charging.

**Figure 2** shows ion uptake capacities (calculated according to Equation (1)) versus charging time in different cycles. In the 2nd cycle (Figure 2A), before around 64 min, the Li+, Na+, and K+ ion removal capacities steadily increase, representing the continuous uptake of these three cations. The maximum removal capacities are 0.041 mmol g−1 for Li+, 0.083 mmol g−1 for Na+, and 0.095 mmol g−1 for K+. The removal capacities decrease from 64 to 180 min, caused by the ion exchange between monovalent and divalent cations. In contrast to the behavior of monovalent cations, Mg2+ and Ca2+ removal capacities constantly increase before reaching a plateau, with the maximum capacity of 0.12 and 0.086 mmol g−1, respectively. The selectivity factors, $M^{x+}/Li^+$ (M = Na+, K+, Ca2+, and Mg2+), are calculated every 10 min (according to Equation (2)), illustrating the selectivity behavior of $Ti_3C_2T_z$ at different charging times (Figure 2A). From the studied ions, Li+ is least preferred by $Ti_3C_2T_z$. Before 90 min of charging, $Ti_3C_2T_z$ preferably uptakes K+ with a maximum selectivity factor of 2.5 (at 30 min), which will be interpreted by the intercalation process of the cations later herein. After 90 min, Mg2+ dominates and reaches the

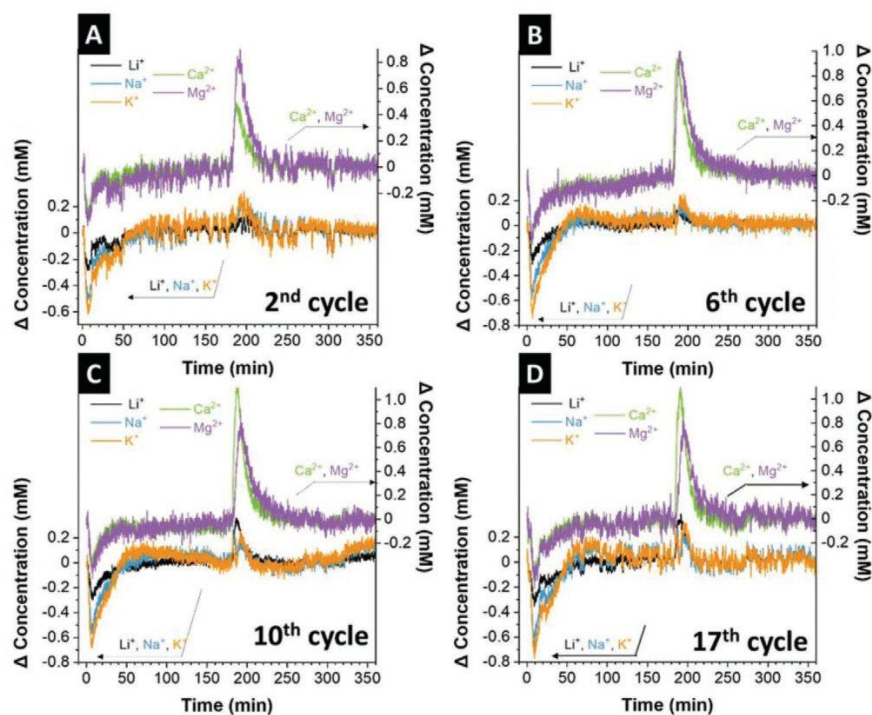**ADVANCED
SCIENCE NEWS**

www.advancedsciencenews.com

**ADVANCED
SUSTAINABLE
SYSTEMS**

www.advsustainsys.com

**Figure 1.** The concentration changes of Li+, Na+, K+, Ca2+, and Mg2+ during the A) 2nd, B) 6th, C) 10th, and D) 17th cycle with a flow rate of 1.1 mL min−1.

highest selectivity factor of 3.9 at 180 min, attributed to the ion exchange between monovalent and divalent cations.

To investigate the material structural changes during the electrochemical process, we conducted in situ XRD measurements. This was done in a coin cell instead of the desalination flow cell while using the same electrolyte and same mass ratio between cathode and anode. The (002) peak shift is illustrated for five X-ray diffractograms for each charging/discharging process (Figure S7, Supporting Information). Without an external circuit, the intercalation distance (the distance between two Ti atoms) is about 0.57 nm (without considering any surface functional groups), calculated by subtracting the theoretical thickness of the MX-layer (Ti-C-Ti-C-Ti)[28] from the $d$-spacing obtained from XRD measurement (Figure S8, Supporting Information). This value is slightly larger than that of the pristine $Ti_3C_2T_z$ electrode (0.51 nm). The intercalation distance of the electrode soaked in deionized water (0.51 nm) suggests that the water and cations cannot spontaneously co-intercalate into the hydrofluoric acid (HF)-etched $Ti_3C_2T_z$, in agreement with the previous study.[29] After charging, the (002) reflection shifts to 5.78° $2\theta$, corresponding to a $d$-spacing of 1.53 nm, that is, 1.05 nm of intercalation distance (Figure 4A). Considering that the initial intercalation distance is less than the smallest hydrated diameters of these five cations in the bulk water (K+, 0.662 nm; Figure S9, Supporting Information), all cations must (partially) dehydrate to intercalate into the $Ti_3C_2T_z$ layers. The dehydration energy (normalized by the charge) of K+ is the lowest while that of Li+ is the highest.[22] As a result, K+ is

most preferred, whereas Li+ is least preferred in the beginning. However, in the late charging stages, Mg2+ is most preferred instead of K+, and Ca2+ becomes the second preferred cation (**Figure 3**A) due to the ion exchange effect.

The other cycles resemble the 2nd cycle and the difference lies only in the slightly different magnitude of removal capacities (Figure 2B–D; Figure S5B, Supporting Information). However, selectivity factors exhibit different trends from the 10th cycle. In the 2nd and 6th cycle, the selectivity factors of K+/Li+ and Na+/Li+ decrease gradually over time (Figure 3A,B), while from the 10th cycle, they drop steeply from 50 min (charging time); and at the end of the charging period, the amount of removed Na+ and K+ ions is less than that of Li+ (Figure 3C,D and Figure S5C, Supporting Information). For example, the selectivity factors of K+/Li+ and Na+/Li+ at 180 min in the 14th cycle are 0.7 and 0.5, respectively. This indicates that Li+ barely participates in the ion exchange after the 10th cycle. Additionally, the maximal selectivity factors of Na+, K+, Ca2+, and Mg2+ all decrease from the 6th cycle to the 17th cycle. This may be due to the growth of amorphous $TiO_2$ on the surface of $Ti_3C_2T_z$ (Figure S10, Supporting Information), which has a lower Li diffusion barrier.[30]

In situ XRD (**Figure 4**) indicates that from the 10th cycle, one more (002) reflection appears at about 6.5° $2\theta$ ($d$-spacing, ≈1.34 nm) apart from that initially at ≈5.8° $2\theta$ (corresponding to a $d$-spacing of 1.53 nm). In the 6th cycle, (002) at 6.5° $2\theta$ already appears with low intensity and broad shape. Among the two latter layer spacings, 1.53 nm is a value similar to the reported
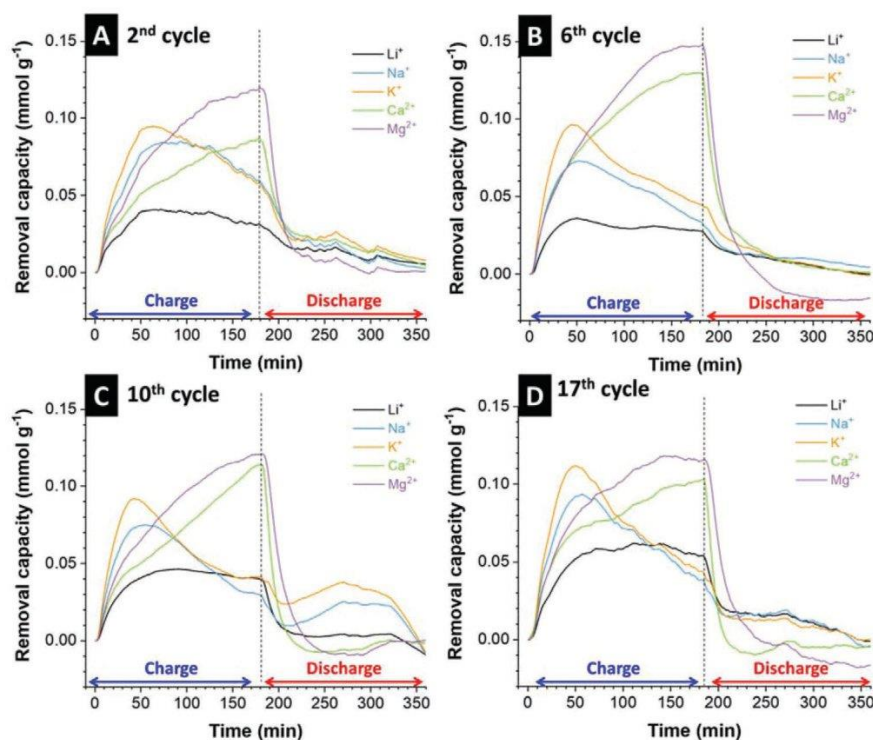
**ADVANCED
SCIENCE NEWS**

www.advancedsciencenews.com

**ADVANCED
SUSTAINABLE
SYSTEMS**

www.advsustainsys.com

**Figure 2.** The ion removal capacity of $Li^+$, $Na^+$, $K^+$, $Ca^{2+}$, and $Mg^{2+}$ during the A) 2nd, B) 6th, C) 10th, and D) 17th cycle with a flow rate of 1.1 mL $min^{-1}$.

results of kosmotropic cations ($Li^+$, $Na^+$, $Mg^{2+}$, and $Ca^{2+}$) intercalated $Ti_3C_2T_z$ at high relative humidity. In comparison, 1.34 nm is a value close to chaotropic cations found for $K^+$-intercalated $Ti_3C_2T_z$ at high relative humidity.[29] This indicates that the kosmotropic cations dictate the $d$-spacing of $Ti_3C_2T_z$ in the 2nd cycle. The second reflection, occurring after the 10th cycle, may result from partially desolvated, kosmotropic cations intercalating $Ti_3C_2T_z$.[31] This may relate to changes in the surface functional groups. In addition, during charging, the reflection shifts toward larger diffraction angles. The associated shrinkage of the $d$-spacing may be related to decreased electrostatic repulsions between negatively charged $Ti_3C_2T_z$ sheets due to cation intercalation.[32] During discharging, the $Ti_3C_2T_z$ sheets expand. While shrinking lasts over the whole charging process (180 min), the expansion is observed only for about an initial 45 min into the discharge process. This can be explained by continued cation intercalation during the whole charging time, caused by the ion exchange. Whereas, there is almost no cation deintercalation after about 45 min during the discharging process (Figure 4B–E).

We additionally studied the selective behavior of $Ti_3C_2T_z$ at a higher flow rate of feed water. In case of a flow rate double as much as before, the ion exchange phenomenon still occurs. However, before the ion exchange occurs, the removal capacities of $Ca^{2+}$ and $Mg^{2+}$ are much higher (Figures S11 and S12, Supporting Information), signaling that the divalent cations are more preferred at a higher flow rate. This is because the higher flow rate reduces the residence time that each cation in the feed

water spends near the electrode surface. As a result, divalent ions, with a higher charge and diffusion rate in the electrolyte,[33] enter the electrodes more readily than monovalent ones.

Development of a selective separation system, such as the one introduced in the present study, is well in alignment with UN's Sustainable Development Goals (SDGs) on a number of different levels. Such a system can specifically remove undesired ions (for example, ions responsible for scaling/fouling such as $Ca^{2+}$) or recover valuable ions like $Li^+$ from industrial wastewater or seawater. Recovery of lithium, particularly, is of great economical interest for the decades to come, as it serves as a key element in construction of Li-ion batteries for electric vehicles and portable electronics. As such, we can envision that the findings presented in this work can contribute to SDGs number 2, 6, 9, and 11–15, encompassing: sustainable management of water and industrialization, sustainable consumption and production patterns, climate change mitigation, sustainable use of the oceans and terrestrial ecosystems, sustainable agriculture, and the development of sustainable cities and human settlements.

## 3. Conclusions

In summary, our work investigates the selectivity of $Ti_3C_2T_z$ toward common alkali and alkaline earth cations. By online monitoring via ICP, we find that the ion-selective behavior of $Ti_3C_2T_z$ depends on the charging time. In the early charging

2100383 (4 of 8)

**ADVANCED
SCIENCE NEWS**

www.advancedsciencenews.com

**ADVANCED
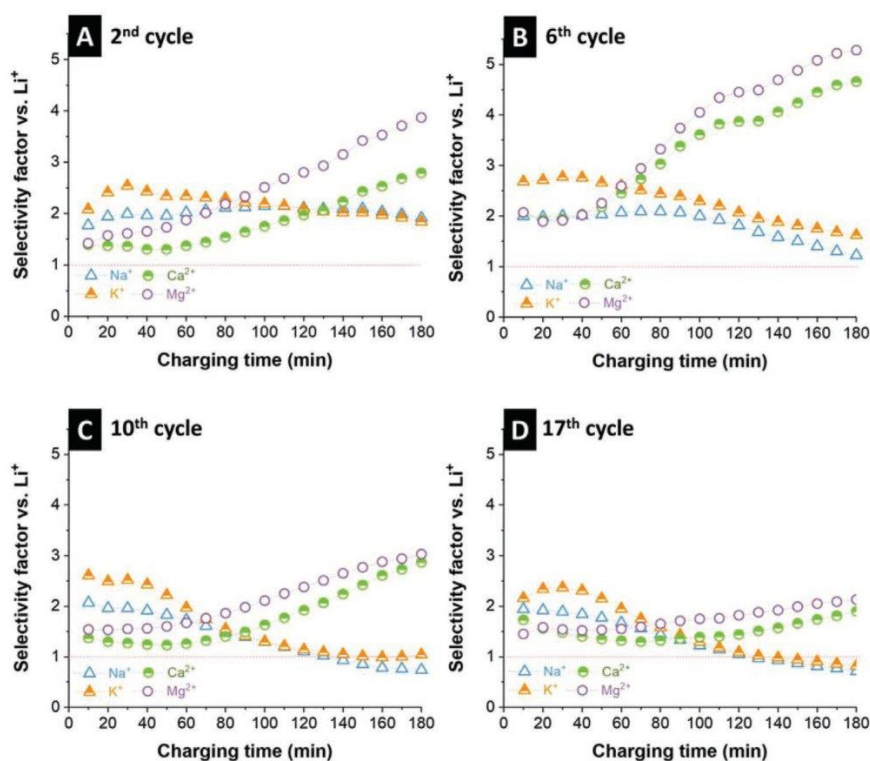SUSTAINABLE
SYSTEMS**

www.advsustainsys.com



**Figure 3.** The selectivity factor versus $Li^+$ of $Na^+$, $K^+$, $Ca^{2+}$, and $Mg^{2+}$ during the A) 2nd, B) 6th, C) 10th, and D) 17th cycle with a flow rate of 1.1 mL min$^{-1}$.

stages (before about 50 min), benefiting from the least dehydration energy, $K^+$ is preferred, with the maximum selectivity factor of $2.5 \pm 0.2$. Subsequently (70–90 min), due to the ion exchange effect between monovalent and divalent cations, the removal capacities of $Ca^{2+}$ and $Mg^{2+}$ (highest value about 0.12 mmol g$^{-1}$) increase and exceed that of $K^+$ at the end of charging time. Meanwhile, fewer $Na^+$ and $K^+$ compared with $Li^+$ are immobilized in $Ti_3C_2T_z$ (from the 10th cycle). In situ XRD data shows a symmetric (002) reflection of $Ti_3C_2T_z$ in the 2nd cycle. In contrast, after the 10th cycle, the asymmetry of the (002) reflection aligns with the emergence of two individual and overlapping peaks associated with the coexistence of cations with a different coordination number of water molecules. This could be an interesting preprocessing step for lithium recovery techniques. Meanwhile, we see potential to extend this approach to other MXene types and other ionic systems such as trivalent cations or metal-organic complexes.

## 4. Experimental Section

*Materials and Material Synthesis*: The parent $Ti_3AlC_2$ MAX phase was synthesized by mixing titanium (Ti, −325 mesh, 99%, Alfa Aesar), aluminum (Al, −325 mesh, 99.5%, Alfa Aesar), and graphite (C, 7–11 μm, 99%, Alfa Aesar) with atomic ratio of Ti:Al:C = 3:1.2:1.88 in a Turbula T2F mixer for 3 h using zirconia balls, followed by sintering inside a Sentro Tech induction furnace (STT-1700C-2.5-12, SN: 1052217) an alumina tube at 1600 °C for 2 h. A heating rate of 10 °C min$^{-1}$ was used to reach the maximum temperature. After the holding time, the sample was left

to cool to room temperature. The sintering process was done under flowing argon.

To prepare $Ti_3C_2T_z$, $Ti_3AlC_2$ was ground to less than 45 μm and slowly added to 10 mass% aqueous HF (Acros Organics, 47–51 mass%). For each 1 g of MAX powder, 10 mL of the acidic solution was used. The mixture was stirred at 27 °C for 24 h. To remove HF and other unwanted products, the mixture was divided equally and distributed to 50 mL centrifuge tubes to have 0.5 g of MAX phase per tube. Deionized (DI) water was added to fill up the tubes to 50 mL. The tubes were centrifuged at 3500 rpm for 5 min to sediment the powders, the supernatant was discarded as hazardous waste. DI water was then added and the sediment was fully redispersed using a vortex machine. The washing step was repeated several times until a pH > 6 was obtained. At that point, the powders were collected and dried using vacuum-assisted filtration at room temperature overnight.

*Electrode Preparation*: Activated carbon (YP-80F, Kuraray) was mixed with polytetrafluoroethylene binder (60 mass% solution in water from Sigma-Aldrich) in 95:5 carbon: binder mass ratio. After adding ethanol, a sticky paste was obtained, which was subsequently cold-rolled (MTI HR01, MTI Corp.) to give 600 μm thick free-standing films and then dried in a vacuum oven at 120 °C overnight. These activated carbon film electrodes are labeled AC herein.

To fabricate MXene electrodes, $Ti_3C_2T_z$ was first mixed with multiwalled CNT (Graphene Supermarket) with a 90:10 MXene:CNT mass ratio. Then the mixture was stirred while being tip-sonicated in ethanol in an ice bath for 30 min using BRANSON Sonifier 450 (maximum power of 400 W) with 30% duty cycle and 30% power. The dispersed MXene-CNT in ethanol mixture was then vacuum filtered through polyvinylidene fluoride (PVDF) membranes (0.22 μm, Durapore), followed by excessive DI water filtration to remove residual salts or acids from the synthesis steps. The electrodes were then dried in a vacuum oven at 80 °C overnight.
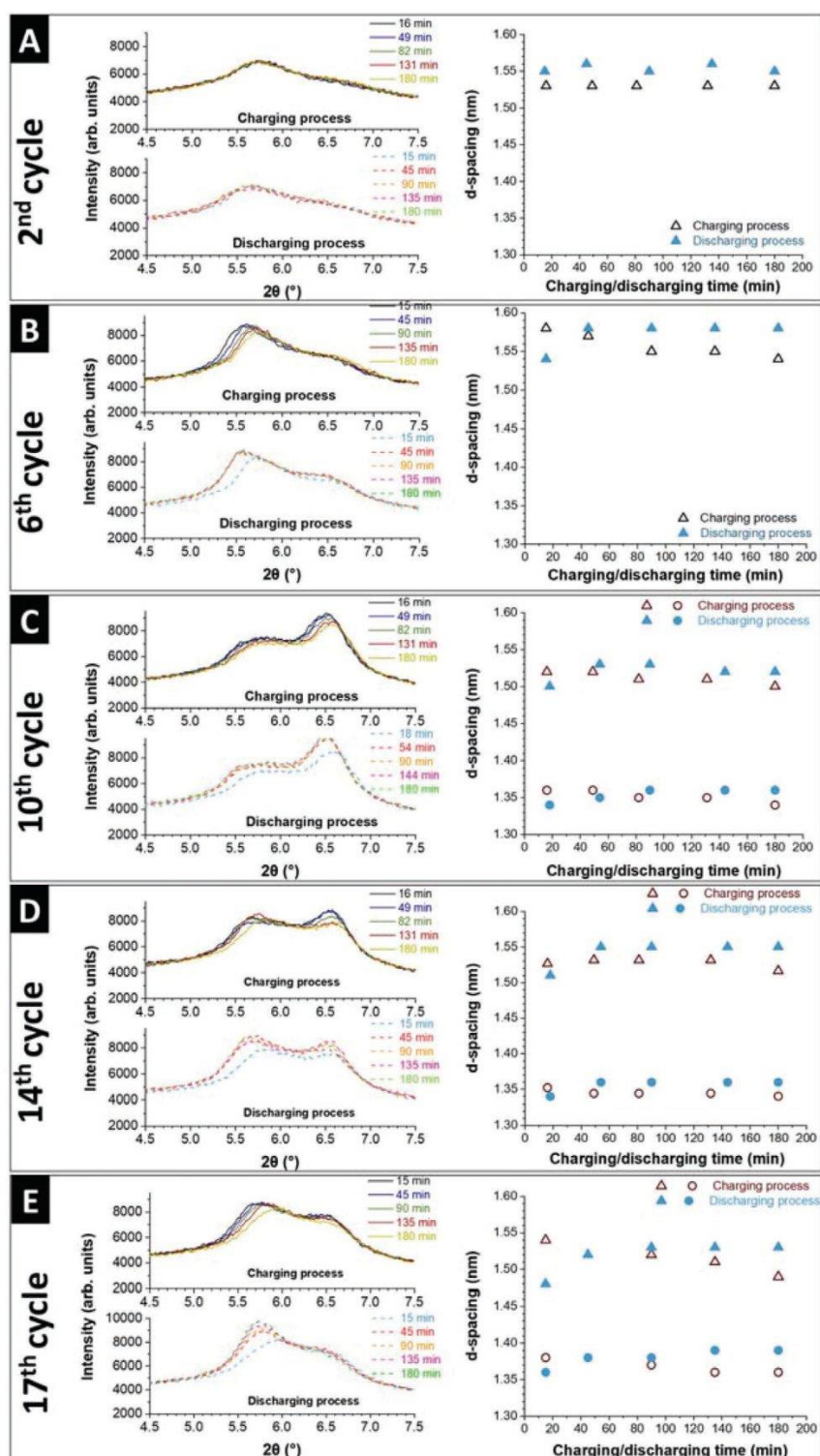
**ADVANCED
SCIENCE NEWS**

www.advancedsciencenews.com

**ADVANCED
SUSTAINABLE
SYSTEMS**

www.advsustainsys.com

**Figure 4.** In situ X-ray diffractograms from 4.5° 2$\theta$ to 7.5° 2$\theta$ of Ti$_3$C$_2$T$_z$ electrode and corresponding $d$-spacing, in different cycles: A) 2nd, B) 6th, C) 10th, D) 14th, and E) 17th cycle. Five X-ray diffractograms are shown for the charging/discharging process of each cycle.

**ADVANCED
SCIENCE NEWS**
www.advancedsciencenews.com

**ADVANCED
SUSTAINABLE
SYSTEMS**
www.advsustainsys.com

*Electrochemical Ion Separation Experiments*: The electrochemical ion separation experiments were performed in a single-pass channel cell. Following the vacuum filtration of $Ti_3C_2T_z$ material (with 10 mass% CNT), a 30 mm diameter electrode (around 120 mg mass loading, 17 mg cm$^{-2}$, on a 30 mm diameter PVDF support) was punched and used as the working electrode. As the counter electrode, free-standing AC films were used, whose mass was adjusted according to the MXene electrode, as described in the previous work.[24] Based on the half-cell cyclic voltammograms of the $Ti_3C_2T_z$ electrode (Figure S13, Supporting Information), $Ti_3C_2T_z$:AC mass ratio of 1:1.7 was maintained for all full-cell experiments throughout this study. The $Ti_3C_2T_z$ and AC electrodes were separated by a central water channel filled with a glass fiber mat (GF/A, Whatman). A Ag/AgCl reference electrode was used as a spectator to measure the potential of the electrodes individually.

To prepare the electrolyte, LiCl, NaCl, KCl, CaCl$_2$, and MgCl$_2$ salts (Sigma-Aldrich) were dissolved in DI water. A 10 L tank containing Li$^+$, Na$^+$, K$^+$, Ca$^{2+}$ and Mg$^{2+}$ with 10 mM concentration for each cation was used as the electrolyte reservoir. The reservoir was constantly flushed with nitrogen gas throughout the experiment to remove the oxygen from the solution to prolong the life of $Ti_3C_2T_z$ electrode, as was done in the previous work.[24,33] Before the cell undergoes charging or discharging, the cell rested overnight to eliminate the influence of adsorption. The cell was charged and discharged with a constant specific current of 0.1 A g$^{-1}$. The upper voltage limit was set to 1.2 V, where the voltage was held for 3 h, and the lower voltage limit was 0.3 V, where the voltage was held for 3 h.

The cell was operated for 20 cycles; each cycle consists out of a charging and discharging process. The outlet of the middle water channel was connected to an ICP-OES (ARCOS FHX22, SPECTRO Analytical Instruments) through a peristaltic pump (at the flow rate of 1.1 mL min$^{-1}$), where the changes of the ions' concentration were recorded online. The extracted solution fed into the ICP-OES system was consumed by the measurement. The measured intensity of the ICP-OES signal was transformed into the concentration according to the calibrated intensity-concentration curves. Finally, the cation removal capacity (mmol g$^{-1}$) was calculated according to Equation (1), and selectivity factors for lithium were calculated following Equation (2).

$$\text{Removal capacity}\left(\text{mmol/g}_{\text{electrode}}\right) = \frac{v}{1000 \cdot m}\int \Delta c \, dt \qquad (1)$$

where $v$ is the flow rate (mL min$^{-1}$), $m$ is the mass of $Ti_3C_2T_z$ electrode, $t$ is the selected time of the cation uptake step (min), and $\Delta c$ is the concentration change of the cations (mM).

$$\text{Selectivity factor} = \frac{\text{Removal capacity of a certain cation}}{\text{Removal capacity of lithium ions}} \qquad (2)$$

*Material Characterization*: XRD analysis was conducted using a D8 Discover diffractometer (Bruker AXS) with a copper X-ray source (40 kV, 40 mA) and a 1D detector. Scanning electron microscopy (SEM) images were obtained using ZEISS (Gemini 500) at acceleration voltages of 1–3 kV. EDX spectroscopy was carried out at 15 kV with X-Max Silicon Detector from Oxford Instruments attached as a column to the SEM instrument. The EDX spectra were recorded and analyzed via AZtec software.

*In Situ X-Ray Diffraction*: In situ XRD measurements were carried out using a customized CR2032 coin cell with Kapton windows on STOE Stadi P diffractometer equipped with a Ga-jet X-ray source (Ga-$K_\beta$ radiation, $\lambda = 1.20793$ Å). The XRD patterns were collected in the transmission mode in the range of $2\theta$ from 3.5° to 10.3°, with a step of 0.04° $2\theta$ and 5 s per step with the equivalent counting time of around 15 min. A 13 mm diameter $Ti_3C_2T_z$ electrode with the mass loading of 8.5 mg cm$^{-2}$ was used for the electrochemical testing to ensure the successful collection of the XRD diffraction signal. The mass ratio between $Ti_3C_2T_z$ electrode (cathode) and AC electrodes (anode) is also 1.7, the same as in the ICP experiments. The same charging and discharging processes as the above-mentioned electrochemical ion separation experiments were performed via potentiostat/galvanostat

(SP-150, BioLogic). The resulted patterns were converted based on the wavelength of Cu-$K_\alpha$ for easier comparison with the literature and ex situ XRD results.

## Supporting Information

Supporting Information is available from the Wiley Online Library or from the author.

## Conflict of Interest

The authors declare no conflict of interest.

## Data Availability Statement

The data that support the findings of this study are available from the corresponding author upon reasonable request.

[1] S. Yang, F. Zhang, H. Ding, P. He, H. Zhou, *Joule* **2018**, *2*, 1648.

[2] H. Yoon, J. Lee, S. Kim, J. Yoon, *Sep. Purif. Technol.* **2019**, *215*, 190.

[3] L. Tian, W. Ma, M. Han, *Chem. Eng. J.* **2010**, *156*, 134.

[4] J. Zhou, Z. Jiao, Q. Zhu, Y. Li, L. Ge, L. Wu, Z. Yang, T. Xu, *J. Membr. Sci.* **2021**, *627*, 119246.

[5] J. Zhou, Y. Zhang, M. Balda, V. Presser, F.-D. Kopinke, A. Georgi, *Chem. Eng. J.*, https://doi.org/10.1016/j.cej.2021.133544.

[6] K.-J. Tan, X. Su, T. A. Hatton, *Adv. Funct. Mater.* **2020**, *30*, 1910363.

[7] F. Yu, L. Wang, Y. Wang, X. Shen, Y. Cheng, J. Ma, *J. Mater. Chem. A* **2019**, *7*, 15999.

[8] Y. Zhang, J. Peng, G. Feng, V. Presser, *Chem. Eng. J.* **2021**, *419*, 129438.

[9] P. Srimuk, X. Su, J. Yoon, D. Aurbach, V. Presser, *Nat. Rev. Mater.* **2020**, *5*, 517.

[10] C. Zhan, F. Aydin, E. Schwegler, A. Noy, T. A. Pham, *ACS Appl. Nano Mater.* **2020**, *3*, 9740.

[11] J. G. Gamaethiralalage, K. Singh, S. Sahin, J. Yoon, M. Elimelech, M. E. Suss, P. Liang, P. M. Biesheuvel, R. L. Zornitta, L. C. P. M. de Smet, *Energy Environ. Sci.* **2021**, *14*, 1095.

[12] P. Srimuk, J. Lee, S. Fleischmann, M. Aslan, C. Kim, V. Presser, *ChemSusChem* **2018**, *11*, 2091.

[13] S. Fleischmann, J. B. Mitchell, R. Wang, C. Zhan, D. E. Jiang, V. Presser, V. Augustyn, *Chem. Rev.* **2020**, *120*, 6738.

[14] C. Choi, D. S. Ashby, D. M. Butts, R. H. DeBlock, Q. Wei, J. Lau, B. Dunn, *Nat. Rev. Mater.* **2019**, *5*, 5.

[15] M. Naguib, V. N. Mochalin, M. W. Barsoum, Y. Gogotsi, *Adv. Mater.* **2014**, *26*, 992.

[16] P. Srimuk, J. Halim, J. Lee, Q. Tao, J. Rosen, V. Presser, *ACS Sustainable Chem. Eng.* **2018**, *6*, 3739.

[17] M. R. Lukatskaya, S. Kota, Z. Lin, M.-Q. Zhao, N. Shpigel, M. D. Levi, J. Halim, P.-L. Taberna, M. W. Barsoum, P. Simon, Y. Gogotsi, *Nat. Energy* **2017**, *2*, 17105.

[18] P. Srimuk, F. Kaasik, B. Krüner, A. Tolosa, S. Fleischmann, N. Jäckel, M. C. Tekeli, M. Aslan, M. E. Suss, V. Presser, *J. Mater. Chem. A* **2016**, *4*, 18265.

[19] X. Zhang, Z. Zhang, Z. Zhou, *J. Energy Chem.* **2018**, *27*, 73.

[20] I. Ihsanullah, *Chem. Eng. J.* **2020**, *388*, 124340.

[21] A. Sinha, Dhanjai, H. Zhao , Y. Huang, X. Lu, J. Chen, R. Jain, *TrAC, Trends Anal. Chem.* **2018**, *105*, 424.

[22] Q. Gao, W. Sun, P. Ilani-Kashkouli, A. Tselev, P. R. C. Kent, N. Kabengi, M. Naguib, M. Alhabeb, W.-Y. Tsai, A. P. Baddorf, J. Huang, S. Jesse, Y. Gogotsi, N. Balke, *Energy Environ. Sci.* **2020**, *13*, 2549.

[23] J. Sun, Q. Mu, T. Wang, J. Qi, C. Hu, *J. Colloid Interface Sci.* **2021**, *590*, 539.

[24] M. Torkamanzadeh, L. Wang, Y. Zhang, Ö. Budak, P. Srimuk, V. Presser, *ACS Appl. Mater. Interfaces* **2020**, *12*, 26013.

[25] J. Li, X. Yuan, C. Lin, Y. Yang, L. Xu, X. Du, J. Xie, J. Lin, J. Sun, *Adv. Energy Mater.* **2017**, *7*, 1602725.

[26] C.-H. Hou, P. Taboada-Serrano, S. Yiacoumi, C. Tsouris, *J. Chem. Phys.* **2008**, *129*, 224703.

[27] R. Zhao, M. van Soestbergen, H. H. M. Rijnaarts, A. van der Wal, M. Z. Bazant, P. M. Biesheuvel, *J. Colloid Interface Sci.* **2012**, *384*, 38.

[28] M. Shekhirev, C. E. Shuck, A. Sarycheva, Y. Gogotsi, *Prog. Mater. Sci.* **2021**, *120*, 100757.

[29] M. Ghidiu, J. Halim, S. Kota, D. Bish, Y. Gogotsi, M. W. Barsoum, *Chem. Mater.* **2016**, *28*, 3507.

[30] C. Liu, Y. Li, D. Lin, P.-C. Hsu, B. Liu, G. Yan, T. Wu, Y. Cui, S. Chu, *Joule* **2020**, *4*, 1459.

[31] E. S. Muckley, M. Naguib, H.-W. Wang, L. Vlcek, N. C. Osti, R. L. Sacci, X. Sang, R. R. Unocic, Y. Xie, M. Tyagi, E. Mamontov, K. L. Page, P. R. C. Kent, J. Nanda, I. N. Ivanov, *ACS Nano* **2017**, *11*, 11118.

[32] J. Come, J. M. Black, M. R. Lukatskaya, M. Naguib, M. Beidaghi, A. J. Rondinone, S. V. Kalinin, D. J. Wesolowski, Y. Gogotsi, N. Balke, *Nano Energy* **2015**, *17*, 27.

[33] L. Wang, K. Frisella, P. Srimuk, O. Janka, G. Kickelbick, V. Presser, *Sustainable Energy Fuels* **2021**, *5*, 3124.

# ADVANCED SUSTAINABLE SYSTEMS

# Supporting Information

## Time-Dependent Cation Selectivity of Titanium Carbide MXene in Aqueous Solution

*Lei Wang, Mohammad Torkamanzadeh, Ahmad Majed, Yuan Zhang, Qingsong Wang, Ben Breitung, Guang Feng, Michael Naguib, and Volker Presser\**

*Supporting Information*

# Time-dependent cation selectivity of
# titanium carbide MXene in aqueous solution

Lei Wang,‡[a,b] Mohammad Torkamanzadeh,‡[a,b] Ahmad Majed,[c] Yuan Zhang,[a,b]
Qingsong Wang,[a,d] Ben Breitung,[d] Guang Feng,[e,f] Michael Naguib,[c] Volker Presser,*[a,b,g]

[a]    *INM - Leibniz Institute for New Materials, D2 2, 66123, Saarbrücken, Germany*

[b]    *Department of Materials Science & Engineering, Saarland University, Campus D2 2, 66123, Saarbrücken,*
      *Germany*

[c]    *Department of Physics and Engineering Physics, Tulane University, New Orleans, Louisiana 70118, United*
      *States of America*

[d]    *Institute of Nanotechnology, Karlsruhe Institute of Technology, Hermann-von-Helmholtz-Platz 1, 76344,*
      *Eggenstein-Leopoldshafen, Germany*

[e]    *State Key Laboratory of Coal Combustion, School of Energy and Power Engineering, Huazhong University*
      *of Science and Technology, Wuhan 430074, Hubei, China*

[f]    *Nano Interface Centre for Energy, School of Energy and Power Engineering, HUST, Hubei, 430074 China*

[g]    *Saarene, Saarland Center for Energy Materials and Sustainability, Campus C4 2, 66123 Saarbrücken,*
      *Germany*

‡     Equal contributions

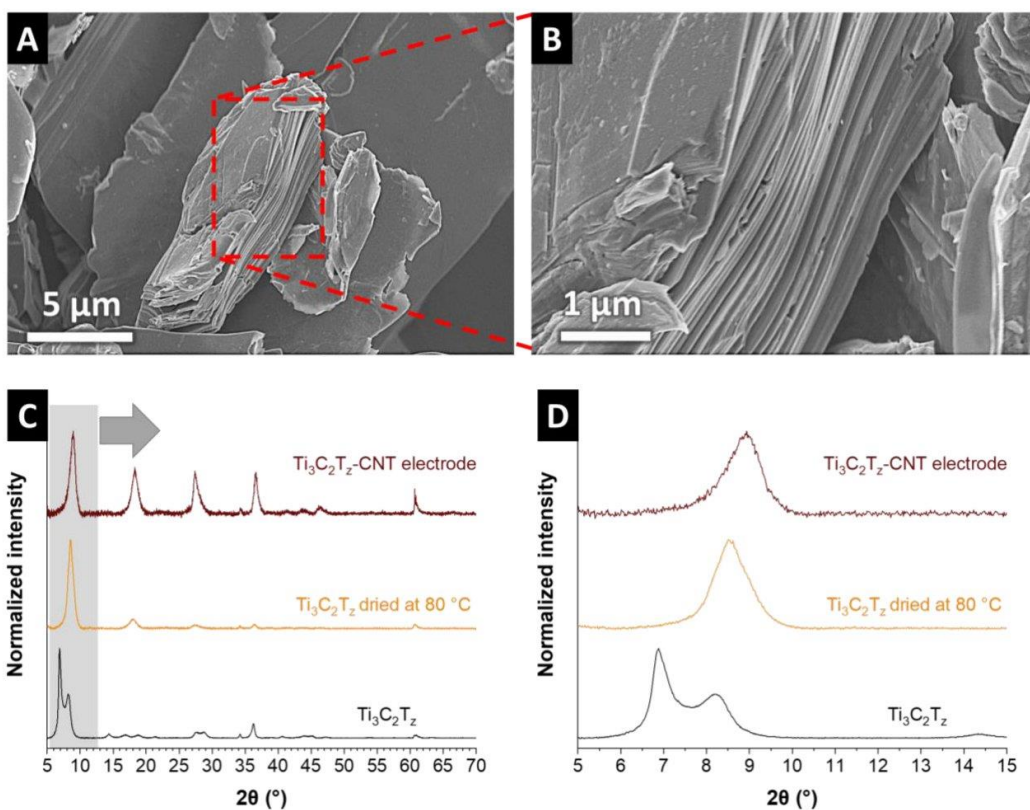*     Corresponding author's email: volker.presser@leibniz-inm.de

**Figure S1:** (A-B) Scanning electron micrographs of $Ti_3C_2T_z$. (C-D) X-ray diffractograms of $Ti_3C_2T_z$, dried $Ti_3C_2T_z$, and the $Ti_3C_2T_z$-CNT electrode.



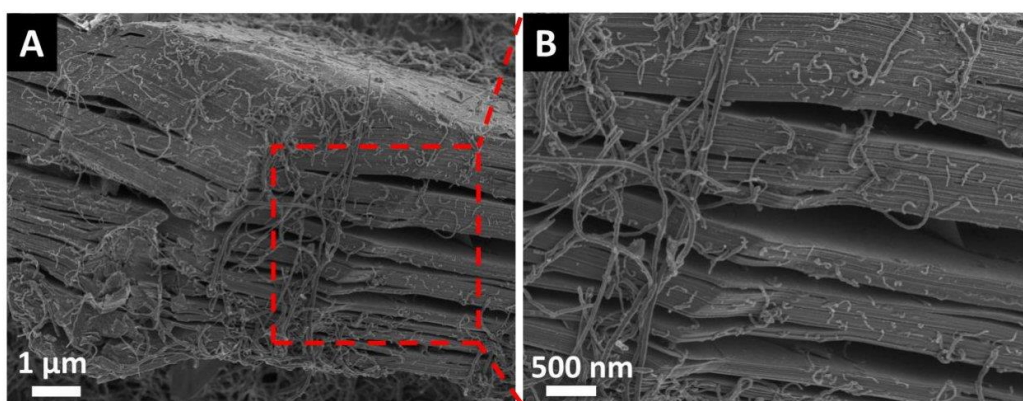**Figure S2:** Scanning electron micrographs of the $Ti_3C_2T_z$ electrode.
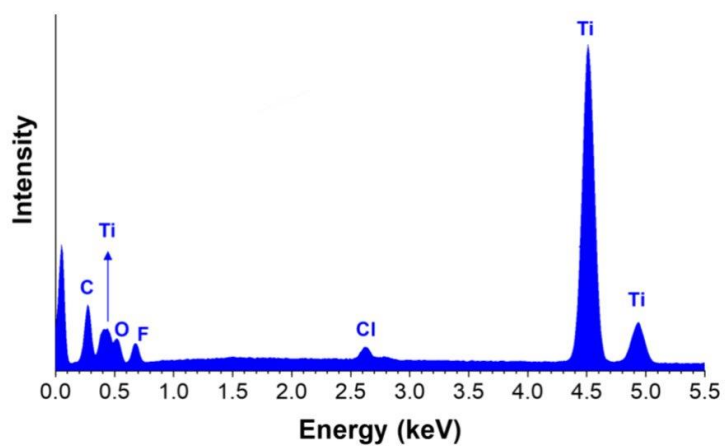
**Figure S3:** Energy-dispersive X-ray (EDX) spectrum of $Ti_3C_2T_z$.



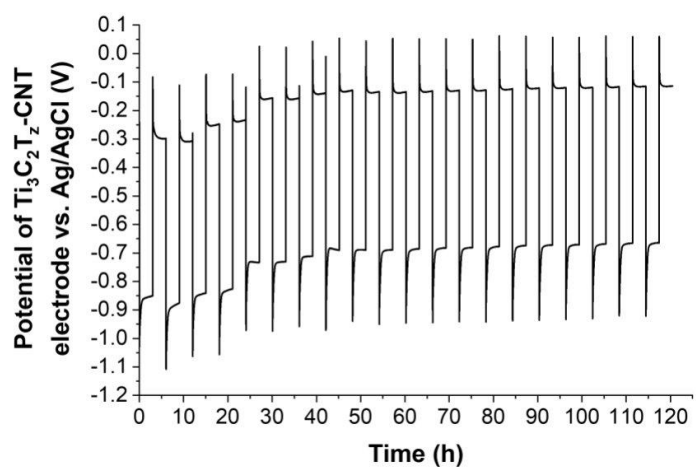**Figure S4:** The potential of the $Ti_3C_2T_z$ electrode in 20 cycles.
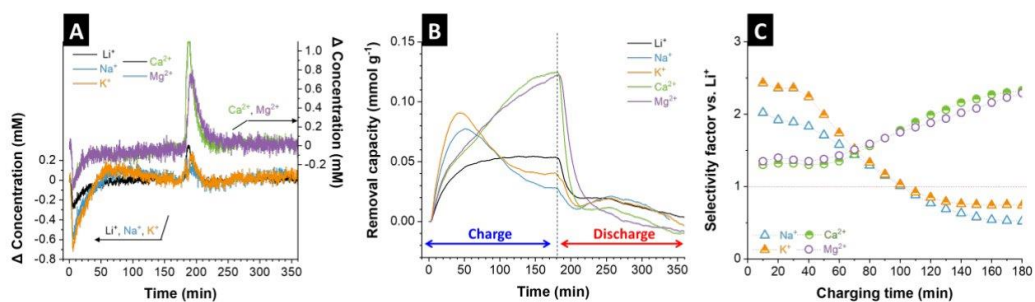
**Figure S5:** The time-dependent concentration change (A), ion removal capacity (B), and selectivity factor vs. Li$^+$ (C) of Li$^+$, Na$^+$, K$^+$, Ca$^{2+}$ and Mg$^{2+}$ during the 14$^{th}$ cycle.
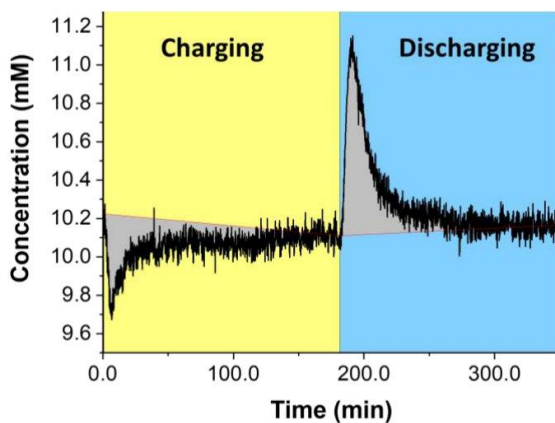


**Fig. S6:** The approach of the baseline establishment, taking Mg$^+$ in the 6$^{th}$ cycle as the example.
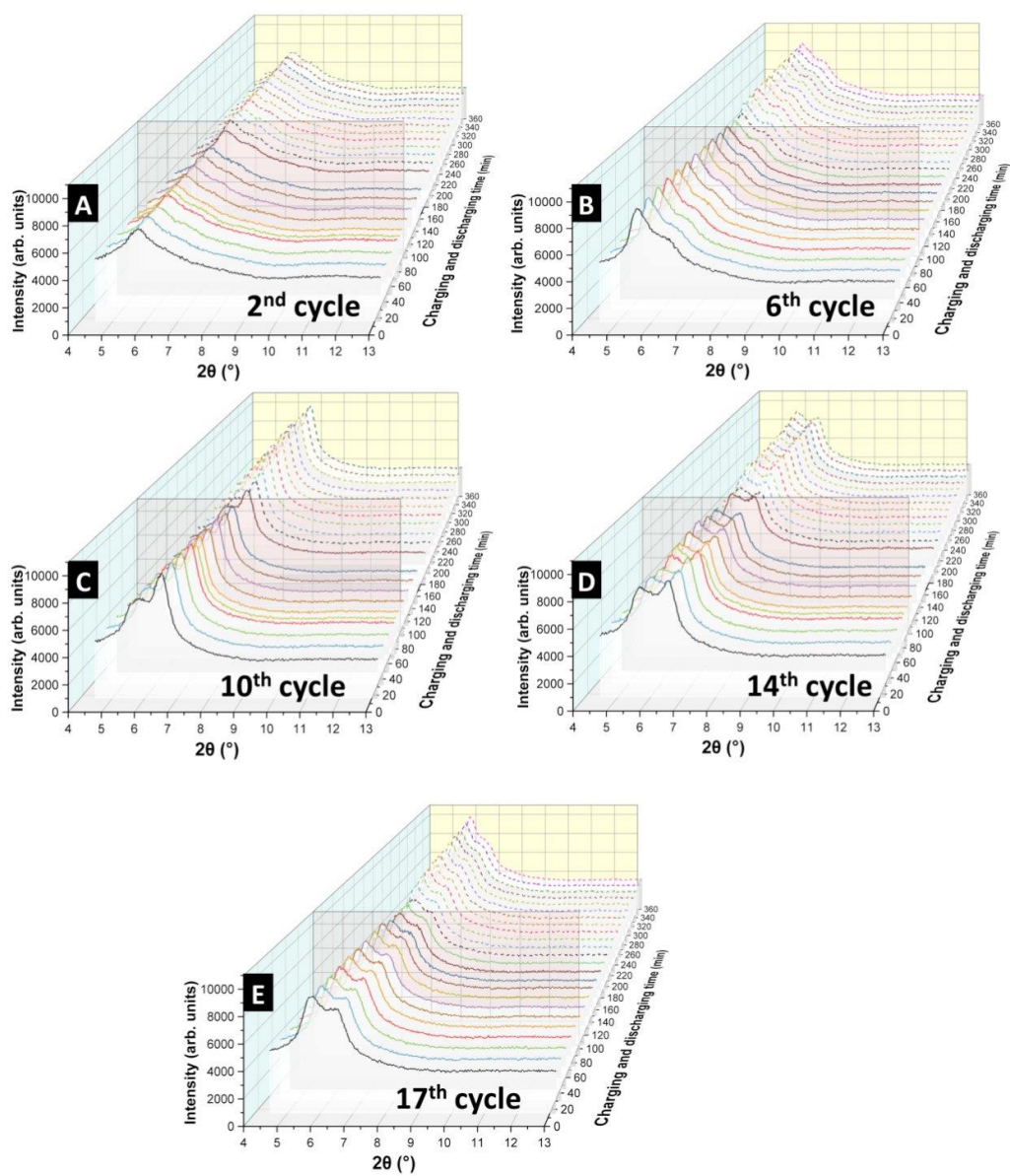
**Fig. S7:** In situ X-ray diffractograms of the $Ti_3C_2T_z$-CNT electrode in different cycles: (A) 2nd, (B) 6th, (C) 10th, (D) 14th, and (E) 17th cycle. The red plane is the dividing plane of the charging and discharging process, and the discharging time is continuously counted after charging time.
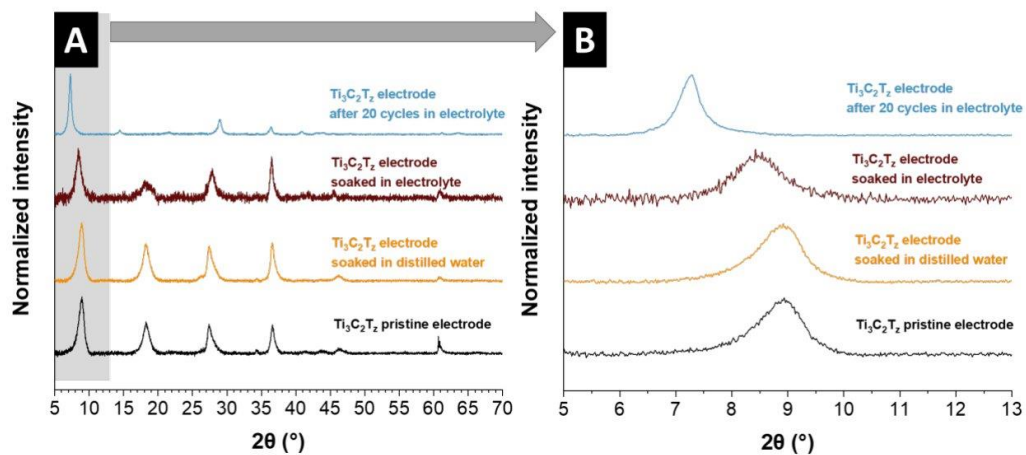
**Fig. S8:** (A-B) X-ray diffractograms (at different angular ranges) of the pristine $Ti_3C_2T_z$ electrode, the electrode soaked in DI water for 3 h, the electrode soaked in electrolyte overnight, and the electrode after ion selectivity experiment.
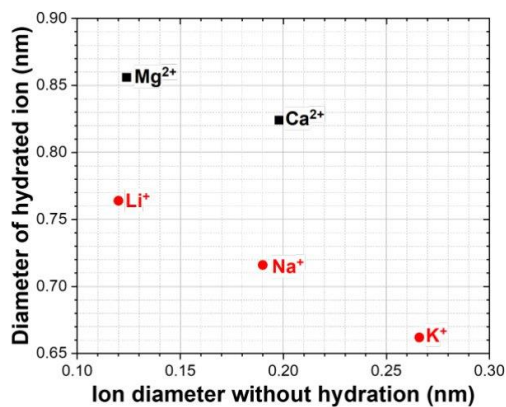


**Fig. S9:** Hydrated and ionic diameters of different cations studied in this work. Data adapted from Ref. [1].
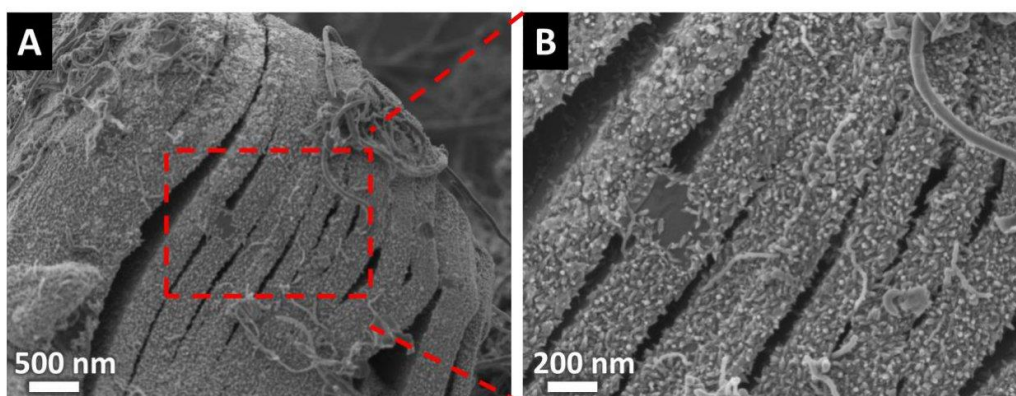
**Fig. S10:**   SEM images of (A, B) postmortem $Ti_3C_2T_z$ electrode of after 20 cycles.
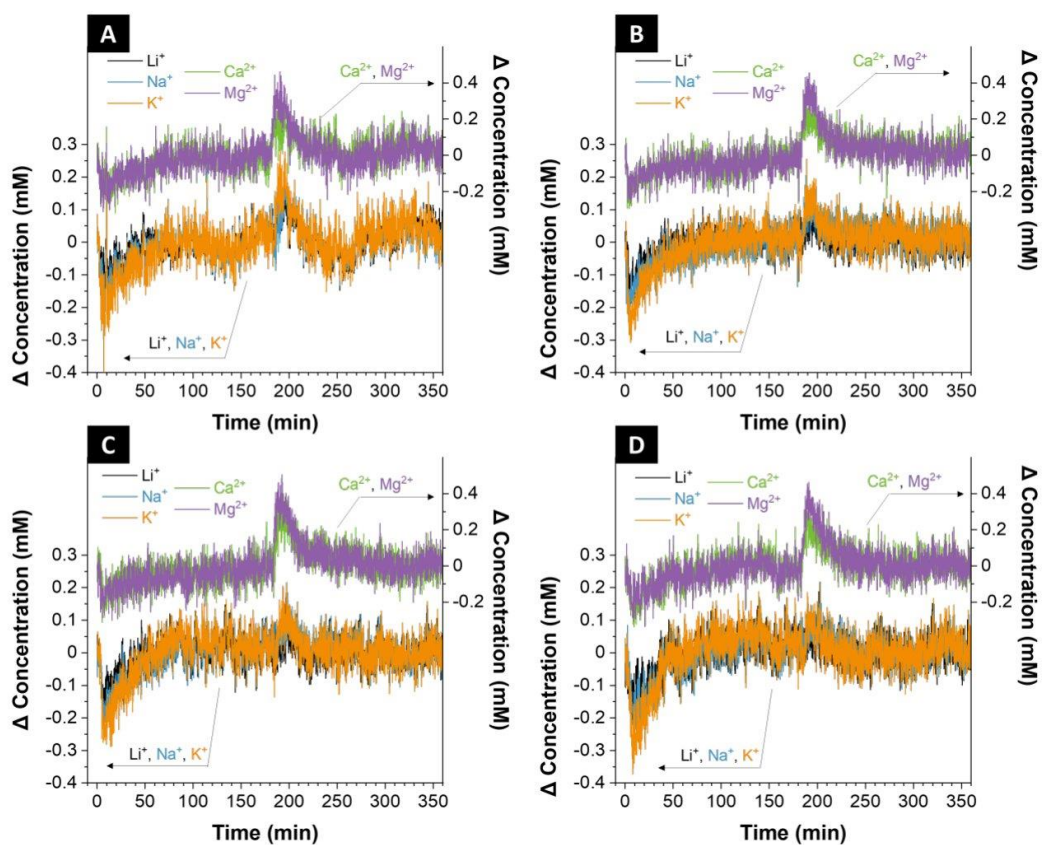


**Fig. S11:**   The concentration change of $Li^+$, $Na^+$, $K^+$, $Ca^{2+}$, and $Mg^{2+}$ during the (A) 2nd, (B) 6th, (C) 10th, and (D) 14th cycle with the flow rate of 2.2 mL/min.
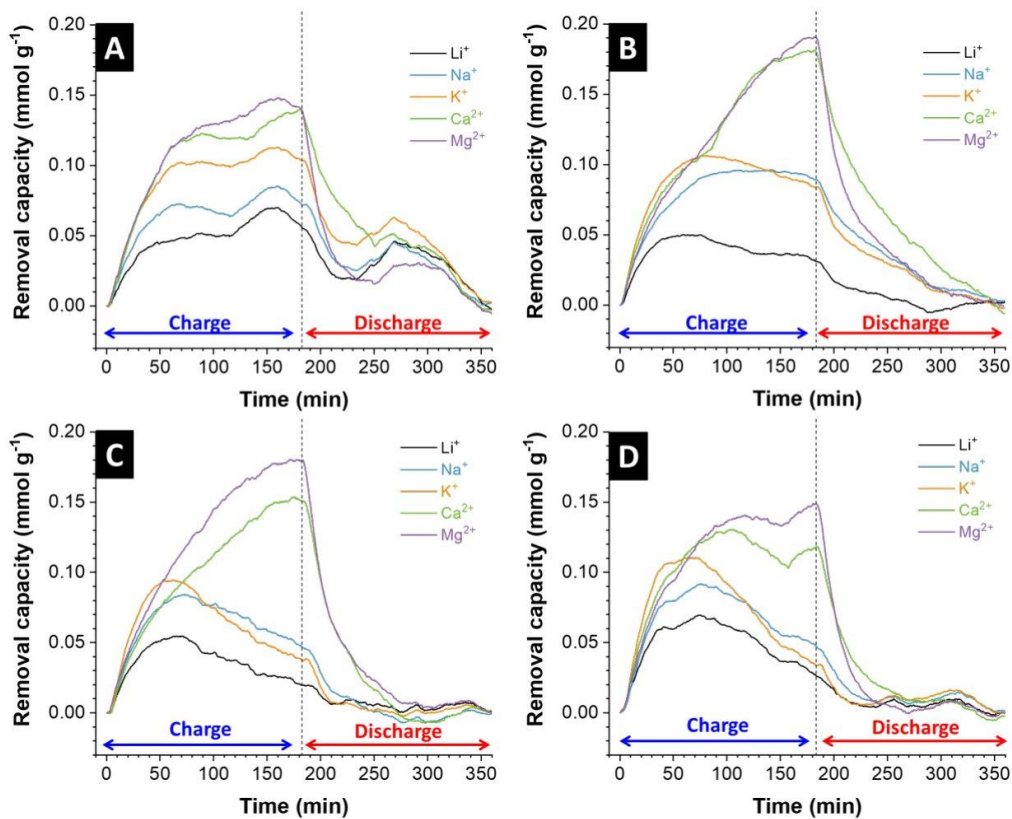
**Fig. S12:** The time-dependent ion removal capacity of $Li^+$, $Na^+$, $K^+$, $Ca^{2+}$ and $Mg^{2+}$ during the (A) 2nd, (B) 6th, (C) 10th, (D) 14th cycle with the flow rate of 2.2 mL/min.
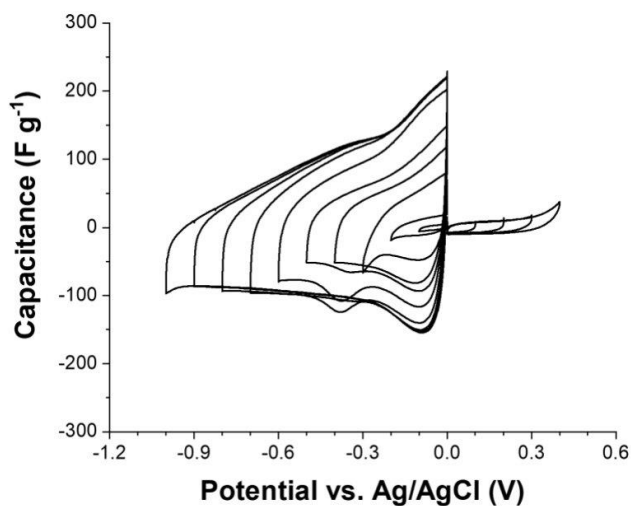


**Fig. S13:** Half-cell window opening cyclic voltammograms of $Ti_3C_2T_z$ in aqueous 1 M NaCl, with the scan rate of 1 mV/s.

## Supporting References

[1]     R. D. Shannon, *Acta Crystallographica A* **1976**, *32*, 751; E. R. Nightingale, *The Journal of Physical Chemistry* **1959**, *63*, 1381.

## 4.4. Layered Nano-Mosaic of Niobium Disulfide Heterostructures by Direct Sulfidation of Niobium Carbide MXenes for Hydrogen Evolution

*Samantha Husmann,[1] Mohammad Torkamanzadeh,[1,2] Kun Liang,[3]*

*Ahmad Majed,[3] Chaochao Dun,[4] Jeffrey J Urban,[4] Michael Naguib[3,*] Volker Presser,[1,2,5,*]*

[1]    *INM - Leibniz Institute for New Materials, D2 2, 66123, Saarbrücken, Germany*

[2]    *Department of Materials Science & Engineering, Saarland University, Campus D2 2, 66123, Saarbrücken, Germany*

[3]    *Department of Physics and Engineering Physics, Tulane University, New Orleans, Louisiana 70118, United States of America*

[4]    *The Molecular Foundry, Lawrence Berkeley National Laboratory, Berkeley, California 94720, United States of America*

[5]    *Saarene, Saarland Center for Energy Materials and Sustainability, Campus C4 2, 66123 Saarbrücken, Germany*

\*    Corresponding authors.

Citation:

Own contributions:

Investigation, Conceptualization, Data curation, Visualization, Writing - Original Draft, Writing - Review & Editing.

Check for upd

# Layered Nano-Mosaic of Niobium Disulfide Heterostructures by Direct Sulfidation of Niobium Carbide MXenes for Hydrogen Evolution

*Samantha Husmann, Mohammad Torkamanzadeh, Kun Liang, Ahmad Majed, Chaochao Dun, Jeffrey J Urban, Michael Naguib,\* and Volker Presser\**

MXene-transition metal dichalcogenide (TMD) heterostructures are synthesized through a one-step heat treatment of $Nb_2C$ and $Nb_4C_3$. These MXenes are used without delamination or any pre-treatment. Heat treatments accomplish the sacrificial transformation of these MXenes into TMD ($NbS_2$) at 700 and 900 °C under $H_2S$. This work investigates, for the first time, the role of starting MXene phase in the derivative morphology. It is shown that while treatment of $Nb_2C$ at 700 °C leads to the formation of pillar-like structures on the parent MXene, $Nb_4C_3$ produces nano-mosaic layered $NbS_2$. At 900 °C, both MXene phases, of the same transition metal, fully convert into nano-mosaic layered $NbS_2$ preserving the parent MXene's layered morphology. When tested as electrodes for hydrogen evolution reaction, $Nb_4C_3$-derived hybrids show better performance than $Nb_2C$ derivatives. The $Nb_4C_3$-derived heterostructure exhibits a low overpotential of 198 mV at 10 mA cm$^{-2}$ and a Tafel slope of 122 mV dec$^{-1}$, with good cycling stability in an acidic electrolyte.

S. Husmann, M. Torkamanzadeh, V. Presser
INM–Leibniz Institute for New Materials
D2 2, 66123 Saarbrücken, Germany
E-mail: volker.presser@leibniz-inm.de
M. Torkamanzadeh, V. Presser
Department of Materials Science & Engineering
Saarland University
Campus D2 2, 66123 Saarbrücken, Germany
K. Liang, A. Majed, M. Naguib
Department of Physics and Engineering Physics
Tulane University
New Orleans, LA 70118, USA
E-mail: naguib@tulane.edu
C. Dun, J. J. Urban
The Molecular Foundry
Lawrence Berkeley National Laboratory
Berkeley, CA 94720, USA
V. Presser
Saarene
Saarland Center for Energy Materials and Sustainability
Campus C4 2, 66123 Saarbrücken, Germany

© 2022 The Authors. Advanced Materials Interfaces published by Wiley-VCH GmbH. This is an open access article under the terms of the Creative Commons Attribution License, which permits use, distribution and reproduction in any medium, provided the original work is properly cited.

## 1. Introduction

MAX phases, such as $Ti_3AlC_2$, are nano-lamellar structures generally comprising an early transition metal element (M), a group 13–15 element (A), and carbon and/or nitrogen (X) with a composition of $M_{n+1}AX_n$ where $n$ can be 1–4.[1] As the metallic bond between M-A is weaker than the mixed ionic-metallic-covalent bond between M-X, elements at the A-site (e.g., Al) can be selectively removed to result in layered MX structures (e.g., $Ti_3C_2$),[2] named MXenes.[3] The typical HF acid etching in an aqueous environment converts MAX into MXene while rendering MXene surfaces terminated with -O, -OH, and -F functionalities.[4] Since their discovery in 2011,[2] MXene has so far found a plethora of wide-ranging applications such as in energy storage devices,[5] electrocatalysis,[6,7] sensing,[8] and environmental remediation.[9] Each of these applications capitalizes on a specific combination of unique properties offered by MXenes: a layered 2D structure that can accommodate ions,[10] an excellent electrical conductivity (a conductivity up to 24 10$^3$ S cm$^{-1}$ was measured for $Ti_3C_2$),[11] a hydrophilic nature (depending on the surface terminations),[3] and rich electrochemically active sites,[7] among others.

Shortly after their discovery, research efforts have been made to modify MXenes further to improve their performances.[12] For instance, alternative etching methods,[13] such as HCl/LiF mixtures,[14] $NH_4HF_2$,[15] molten salt etching,[16] and alkali etching[17] have been proposed to favorably alter the surface terminations,[14] interlayer spacings,[18] electronic,[19] and electrochemical[20] properties of MXene. In contrast to techniques such as layer-by-layer self-assembly[21] or pillaring[20,22] of the MXene sheets where organic molecules need to be present during synthesis, one-step modification methods often offer simplicity and more significant potential for industrial-scale applications. The first report on the latter approach was the one-step conversion of $Ti_3C_2$ into $TiO_2$-C hybrids by oxidation of the MXene precursors in air, $CO_2$, or hydrothermally.[23] The oxidation conditions in $CO_2$ can be adjusted so that MXene is only partially converted to achieve ternary heterostructures such as $Nb_2C$-C-$Nb_2O_5$, resulting in significantly enhanced electrochemical[24] and photocatalytic[25] performances compared to the parent $Nb_2C$. These hierarchical heterostructures benefit from synergistic effects

**ADVANCED**
SCIENCE NEWS
www.advancedsciencenews.com

**ADVANCED
MATERIALS**
INTERFACES
www.advmatinterfaces.de

of a conductive carbon/MXene network, a layered 2D MXene structure, and a transition metal oxide semiconductor, that is, making them electrochemically and/or catalytically active.

Recently, hybrids of MXene-transition metal sulfides have gained growing attention.[26] Examples include $Ti_3C_2$-$MoS_2$ hybrids fabricated either by chemical synthesis of $MoS_2$ in the presence of $Ti_3C_2$ MXene[27,28] or by physical admixing of the two.[29] $MoS_2$ is one of the transition metal dichalcogenides (TMDs) class of 2D materials.[30] TMDs find extensive application in energy storage,[31] electrochemical desalination,[32] and electrocatalysis.[33] However, most TMDs suffer from low electrical conductivity and unfavorable strains during charge/discharge.[34] This translates to limited electron mobility to active sites and low stability upon cycling in electrocatalysis. Furthermore, a general problem of 2D structures is the reduced catalytic activity of the basal plane. Heterostructure engineering can significantly boost the catalytic properties of TMDs by improving conductivity, increasing edge terminations, activating the basal plane, or creating defects.[35] Therefore, heterostructures obtained by integrating TMDs and MXenes benefit from the latter's metallic conductivity, resulting in a more efficient charge transfer. This is shown by a six-fold enhancement of the hydrogen evolution reaction (HER) activity of $Ti_3C_2$-$MoS_2$ hybrid compared with sole $MoS_2$ and a much larger enhancement than that of sole $Ti_3C_2$.[28] Nevertheless, the enhancement of the TMD-heterostructure properties is directly related to the interface quality of the heterojunction and minimization of Fermi level pinning.[26] A high hybridization degree can be achieved by converting or templating one of the heterostructure components into the other through atomic-scale transformation. MXene templating is still mostly limited to metal oxides.[36]

The direct conversion of MXene into TMD via in situ thermal sulfidation was so far explored to produce MXene-TMD heterostructures of $Mo_2TiC_2$-$MoS_2$,[37] $Mo_2C$-$MoS_2$,[38] and $Ti_3C_2$-$TiS_2$,[39] out of their parent delaminated MXenes. These MXene-derived TMDs are distributed in a unique sandwich-like fashion in the matrix of parent MXene. This morphology is accessible to electrolytes allowing for fast charge transfer. The intimate contact between the two phases provides strong adhesion and a nanohybrid interface[38] that is otherwise not achieved through TMD precursors' growth on MXene via other routes exemplified earlier. A variety of (mixed metal) MXenes remain unexplored as the precursor for TMD fabrication. Furthermore, no study has been done comparing the effect of different MXene phases (e.g., with different $n$, such as comparing MXene with $n = 1$ to that of $n = 3$), of the same transition metal, on the resulting derivative of any kind.

The present study thus investigates the one-step thermal sulfidation technique for fabricating two niobium MXene-TMD heterostructures, namely $Nb_2C$-$NbS_2$ and $Nb_4C_3$-$NbS_2$. Unlike other previous reports on MXene sulfidation, no delamination, pre-treatment with sulfur,[37,38] or modification with carbon[39] were employed. The degree of the MXene-to-TMD conversion is shown to depend on the sulfidation temperature and duration, whereby hybrids of MXene-$NbS_2$ or only $NbS_2$ structures could be conveniently obtained. The side-by-side comparison of structures derived from $Nb_2C$ and $Nb_4C_3$ MXenes reveals that each MXene undergoes unique conversion mechanisms, resulting in $NbS_2$ with different nano-morphologies, such as

pillars or mosaics. These heterostructures are further examined as electrocatalysts for HER.

## 2. Results and Discussion

The most common method of performing thermal sulfidation of different materials is by i) mixing the precursor with sulfur powder/sulfur salt,[40] which will likely react at higher temperatures or ii) placing sulfur powder upstream of the furnace, which in the form of vapor, upon heating, is carried to the main part of the furnace, where the precursor is located. $H_2$ gas is often combined to form $H_2S$ and facilitate the transfer.[41] These methods are limited by the amount of sulfur initially placed in the system and its evaporation rate. Above about 450 °C, sulfur quickly reacts with $H_2$, leading to a large amount of released $H_2S$ in the first few minutes of the treatment, which quickly decreases due to sulfur depletion, leading to a nonuniform feed rate of $H_2S$ during treatment.[42] Direct use of $H_2S$ gas, on the other hand, allows a constant flow and sulfur-source feed rate, providing more control over the sulfidation process, especially for longer treatment times (Figures S1 and S2, Supporting Information). $Nb_4C_3$ was treated by two different methods to verify this effect: directly using $H_2S$ gas or reacting sulfur powder with $H_2$ upstream of the tube furnace. **Figure 1**A and Figure S3, Supporting Information, show the X-ray diffractograms of $Nb_4C_3$ thermally treated with $H_2S$ and $H_2/S$ methods, respectively.

At 600 °C, no significant sulfidation is observed in either system, with only a broadening of MXene peaks. At 700 °C, a clear difference appears between the two methods. The sample treated with $H_2S$ still shows the main features of MXene even at prolonged times ($Nb_4C_3$-$H_2S700$-$60'$) with a pronounced broadening of the peaks. The (00$2$) peak from MXene also shifts toward higher $2\theta$ degree (**Table 1**), from 5.93° $2\theta$ ($Nb_4C_3$) to 7.10° $2\theta$ ($Nb_4C_3$-$H_2S600$-$10'$), and 7.18° $2\theta$ ($Nb_4C_3$-$H_2S700$-$10'$), indicating a decrease in the interlayer spacing between the MXene sheets. This change was already detected even when sulfidation did not occur (Figure S3, Supporting Information) at 500 and 600 °C, which can be explained by the removal of interlayer water and other etching products.[43] In the $H_2/S$ setup, the sample clearly shows conversion to $NbS_2$ matching the trigonal structure (PDF 89–3041), with no remaining peaks of the parent MXene when treated at 700 °C. The sharp differences between the two systems can be attributed to the amount of $H_2S$ (and ultimately S) provided by each setup in the same time range (as qualitatively represented in Figure S2B, Supporting Information). This becomes obvious when the temperature increases to 900 °C, where the sample in $H_2/S$ shows mainly $NbS_2$ features within 10 min, while in $H_2S$, evidence of remaining $Nb_4C_3$ is seen even after 60 min treatment.

The faster conversion rate in the $H_2/S$ system can also be verified by the sulfur content obtained by energy-dispersive X-ray (EDX) analysis (Table S1, Supporting Information). The chemical composition obtained by EDX analysis corroborates the X-ray diffraction (XRD) data. The sulfur contents obtained by EDX analysis are cross-examined with CHNS elemental analysis, and the values are in close agreement with each other. No sulfur is detected below 600 °C while it reaches 31 at% when
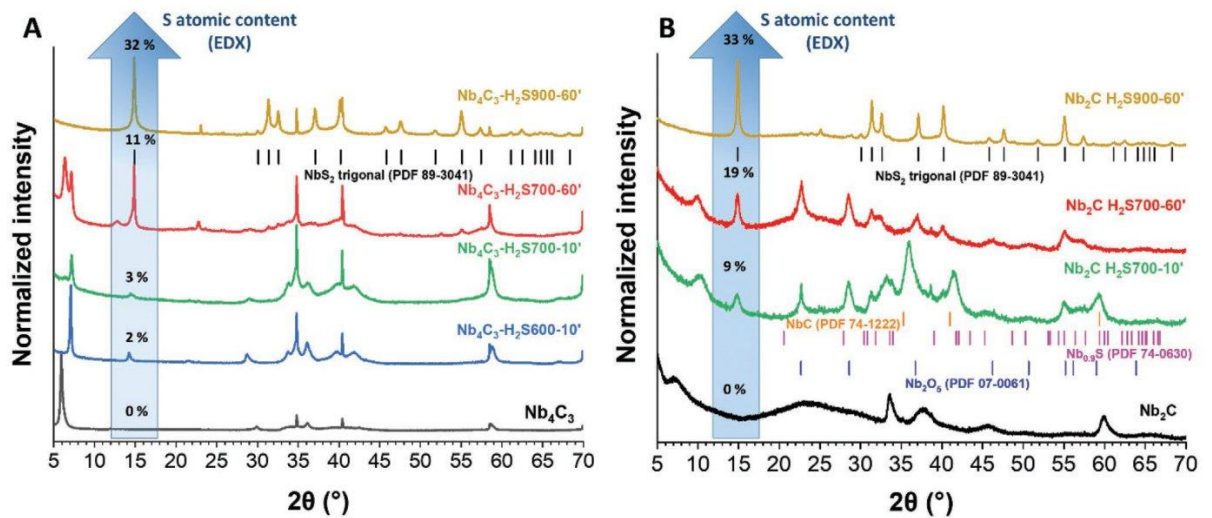
**Figure 1.** X-ray diffraction (XRD) patterns for the treatment in $H_2S$ with A) $Nb_4C_3$ and B) $Nb_2C$. The elemental values of sulfur were derived from energy-dispersive X-ray spectroscopy (EDX).

treated at 900 °C for 60 min. These changes are accompanied by decreased oxygen content and complete fluorine removal (probed via EDX) with increasing treatment temperature and time, confirming the (partial) removal of terminal functional groups from the MXene surface. The similar composition of $Nb_4C_3$-S900-10′ and $Nb_4C_3$-S900-60′ indicates that in this setup, complete conversion is already achieved in 10 min.

The $H_2/S$ setup leads to faster conversion of the material. Hence, the partial conversion of the MXene becomes challenging. Partial conversion is highly desirable since a combination of the properties of the derived material and the parent MXene can be achieved, for example, the redox activity of metal oxides with the conductivity of MXene.[44] Besides, the fast conversion with the $H_2/S$ method leads to heterogeneous reactions and the formation of coarsened particles spread within the original layered structure, as observed in scanning electron micrographs (Figure S4, Supporting Information). That considered, the $Nb_2C$ phase was only treated with the $H_2S$ system.

**Table 1.** MXene (002) peak position and ratio of (003)-$NbS_2$/(002)-MXene peak area.

| Sample | (002)-MXene [° $2\theta$] | $A_{sulfide}/A_{MXene}$ |
|---|---|---|
| $Nb_2C$ | 7.27 | 0 |
| $Nb_2C$-$H_2S700$-10′ | 10.47 | 0.49 |
| $Nb_2C$-$H_2S700$-60′ | 10.02 | 1.18 |
| $Nb_2C$-$H_2S900$-60′ | — | — |
| $Nb_4C_3$ | 5.93 | 0 |
| $Nb_4C_3$-$H_2S600$-10′ | 7.10 | 0.16 |
| $Nb_4C_3$-$H_2S700$-10′ | 7.18 | 0.20 |
| $Nb_4C_3$-$H_2S700$-60′ | 6.39/7.16 | 0.62 |
| $Nb_4C_3$-$H_2S900$-60′ | — | — |
| $Nb_4C_3$-$S700$-10′ | — | — |

For $Nb_2C$, a similar change in composition occurs, ultimately leading to tetragonal $NbS_2$ at 900 °C in 60 min (Figure 1B). In this case, the transition seems to occur faster than in $Nb_4C_3$, as observed by comparing the percentage of sulfide incorporated (Table S2, Supporting Information) and the $A_{sulfide}/A_{MXene}$ ratio (Table 1) in the different treatment conditions between the two MXene phases. This could be explained by the slightly larger surface area of the $Nb_2C$-MXene than $Nb_4C_3$-MXene (Figure S5, Supporting Information), which enhances the exposure to the $H_2S$, facilitating the conversion process. Similar to $Nb_4C_3$, $Nb_2C$ patterns also presented a shift of (002) peaks to higher angles after the heat treatments (Table 1).

Furthermore, the samples treated at 700 °C show reflections corresponding to $Nb_2O_5$ in addition to $Nb_2C$ and $NbS_2$. The $Nb_2O_5$ formation in the case of $Nb_2C$ precursor can be explained by the higher atomic O/Nb ratio in $Nb_2C$ compared to $Nb_4C_3$ (1.47 compared to 0.60, respectively; Tables S1 and S2, Supporting Information). During heat treatment, the large amount of oxygen promotes Nb oxidation in $Nb_2C$, as not all functionalities are lost at 700 °C.[45]

The $Nb_2O_5$ reflections remain even when the treatment is extended to 60 min at 700 °C (Figure 1B), indicating that the oxide neither decomposes nor is further converted during the treatment with $H_2S$. Once $Nb_2O_5$ is formed, its sulfidation is thermodynamically unfavored at 700 °C, requiring higher temperatures than $Nb_2C$ to form $NbS_2$.[46] This can explain the absent $Nb_2O_5$ signal in the $Nb_2C$-$H_2S900$-60′ sample: the higher temperature efficiently removes surface functionalities. Besides, $H_2S$ decomposition is favored above 900 °C, leading to a more significant amount of $H_2$ that helps to reduce oxygenated groups.[42]

In the case of the sample $Nb_2C$-$H_2S700$-10′, in addition to the formation of $NbS_2$ and $Nb_2O_5$, a pronounced reflection also appears at $2\theta = 41.5°$ (Figure 1B). Although the latter reflection could not be assigned to a certain phase, it may originate from cubic NbC and other niobium sulfide

2102185 (3 of 10)

ADVANCED
SCIENCE NEWS
www.advancedsciencenews.com

ADVANCED
MATERIALS
INTERFACES
www.advmatinterfaces.de

species such as $Nb_{0.9}S$. The rather short exposure time to $H_2S$ (10 min) can explain the formation of the latter sulfur-deficient niobium sulfide stoichiometry.

The scanning electron microscopy (SEM) images presented in **Figure 2** and Figure S6, Supporting Information, show the morphology of the materials before and after different sulfidation conditions. The original layered MXene structure is still observed for all samples, and the flake particles remain essentially of the same size. For treatments at 900 °C, such layers are mainly composed of hexagonal and trigonal nano-mosaics, characteristic of $NbS_2$ morphology. The gradual development of morphologies seen at 700 °C further leads to the morphologies seen at 900 °C (Figure 2B–D). At certain particles (Figure 2B), hexagons appear at the edge plane, with a higher surface and exposure to $H_2S$ gas. The same features are also seen at places where the layer-opening is more pronounced. Such morphologies are very different from the samples treated in the $H_2/S$ setup (Figure S4, Supporting Information). Large rhombohedral
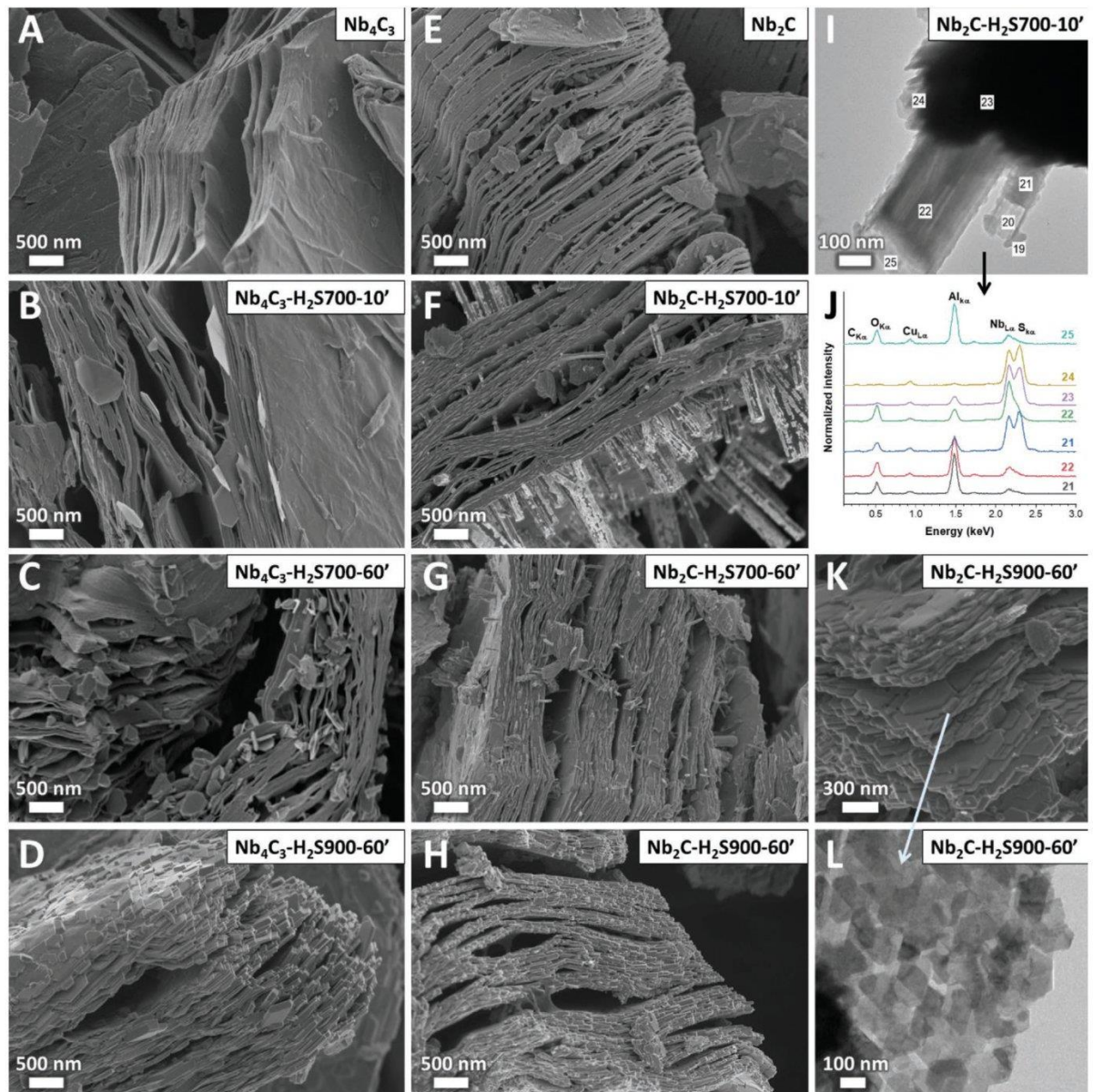


**Figure 2.** Scanning electron micrographs of A) $Nb_4C_3$, B) $Nb_4C_3$-$H_2S700$-10', C) $Nb_4C_3$-$H_2S700$-60', D) $Nb_4C_3$-$H_2S900$-60', E) $Nb_2C$, F) $Nb_2C$-$H_2S700$-10', G) $Nb_2C$-$H_2S700$-60', and H,K) $Nb_2C$-$H_2S900$-60'. Transmission electron micrographs of I) $Nb_2C$-$H_2S700$-10' and L) $Nb_2C$-$H_2S900$-60'. J) Elemental composition via energy-dispersive X-ray spectroscopy of the assigned points in image (I).

particles appear on top and grow from the layers, resulting in a much more heterogeneous material.

A strikingly different feature occurs in the $Nb_2C$ treated at 700 °C (Figure 2F; Figure S6D–F, Supporting Information). Several pillars growing mainly from the basal plane are observed throughout the whole material. Such pillars occur between smaller layers and grow considerably at the external surface, up to 1 µm. When the reaction time is increased from 10 min ($Nb_2C$-$H_2S700$-10′) to 60 min ($Nb_2C$-$H_2S700$-60′), the pillars seem to increase in quantity. At 900 °C ($Nb_2C$-$H_2S900$-60′), however, there are no signs of such morphology, indicating that such structures are decomposed at higher temperatures.

To further investigate these morphologies, transmission electron microscopy (TEM) images were acquired (Figure 2I,L; Figure S7, Supporting Information). In $Nb_2C$-$H_2S900$-60′, the layers composed of prismatic $NbS_2$ nano-mosaics are nicely seen. The lattice spacing of 0.285 nm matches the (101) plane of $NbS_2$ also observed in XRD. The same structures occur for the $Nb_4C_3$ sample treated under the same conditions. For $Nb_2C$-$H_2S700$-10′, the pillars previously seen in SEM appear together with the layered material. The pillars seem to grow parallel to the basal plane in many regions, protruding from in-between the layers. The lattice spacing of the pillars is ≈0.388, 0.314, and 0.250 nm, which matches the (001), (100), and (101) reflections of $Nb_2O_5$, respectively. The base from where the pillars grow also shows organized spacing with ≈0.62 and 0.285 nm, matching the (003) and (101) reflections of $NbS_2$, respectively. While other characterizations indicate the presence of residual MXene in this sample, it was not possible to identify characteristic spacings of $Nb_2C$ in this sample. Possibly the remaining MXene occurs at the inner layers of the material, which cannot be identified in TEM as only the edges and partially delaminated layers can be analyzed. Nevertheless, in the $Nb_4C_3$-$H_2S700$-10′ sample, spacing corresponding to the (002) plane of $Nb_4C_3$ can be more easily found (Figure S7A, Supporting Information), confirming the partial conversion already observed in XRD.

EDX spectra also confirmed the composition (Figure 2J): While the layered particles are mainly composed of Nb and S, the pillars show the presence of Nb and O. Al appears at the far end/top of most of these structures, which could be part of the pillar growing mechanism acting as a catalyst. The evidence that the pillars observed in the $Nb_2C$ samples treated at 700 °C are composed of $Nb_2O_5$ also aligns with XRD data (Figure 1B), since neither the pillars nor $Nb_2O_5$ peaks are seen in $Nb_2C$-$H_2S900$-60′. To understand the decomposition mechanism of such pillars, $Nb_2C$ was heat-treated only in an inert atmosphere (Argon) up to 900 °C. In this condition, $NbO_2$ is observed (Figure S8, Supporting Information). This indicates that the oxide pillars were reduced upon temperature increase and only further reduced/converted during the sulfidation process with the introduction of $H_2S$, leading to the absence of pillars or oxide in the $Nb_2C$-$H_2S900$-60′ sample.

Raman spectra of $Nb_4C_3$ and $Nb_2C$ treated with $H_2S$ are presented in Figure S9, Supporting Information. Before the treatment, Nb-C modes appear below 300 cm$^{-1}$, corresponding to $A_{1g}$ out-of-plane vibration ($\omega_4$ ≈260 cm$^{-1}$) and $E_g$ in-plane oscillations ($\omega_2$ ≈180 cm$^{-1}$).[47] The functional terminations (Nb-F, Nb-O, Nb-OH) appear at 450–800 cm$^{-1}$.[48] Compared

to $Nb_4C_3$, $Nb_2C$ bands present a shift toward higher frequencies as $M_{n+1}X_n$-O tend to be stronger with the decrease of $n$.[49] The difference in the Nb-O bond strength could be one of the factors that lead to the growth of $Nb_2O_5$ pillars in $Nb_2C$ and their absence in $Nb_4C_3$. These modes gradually disappear with increasing temperature and time as this bonding is broken to form $NbS_2$. This transition is more abrupt in $Nb_2C$ as previously discussed that this phase has a faster conversion. With the treatment, typical modes of 2H-$NbS_2$ emerge at 386 cm$^{-1}$ ($A_1$), 322 cm$^{-1}$ ($E_2$), and 153 cm$^{-1}$ (defects).[50] Carbon modes are also present between 1200 cm$^{-1}$ and 1700 cm$^{-1}$. The band at lower wavenumber (≈1350 cm$^{-1}$) is defined as the D-band. It is associated with disordered amorphous sp$^3$ carbon, while the G-band at ≈1600 cm$^{-1}$ is characteristic of graphitic sp$^2$ carbon mode.[51] For $Nb_4C_3$, C modes initially increase with treatment, as free C is formed while niobium is sulfidized.[52] The broadness of the D-band is further decreased when the temperature rises to 900 °C, with a D-mode and G-mode typical of defective graphitic carbon formed at higher temperatures. Even at high temperatures, the presence of carbon modes suggests a hybrid structure between $NbS_2$, carbon, and possibly residual MXene. Conversely, carbon modes disappear upon treatment of $Nb_2C$. The less shielding of niobium layers and the single carbon layer possessed by the 211 MAX-phase leads to less protection of the carbon atoms and further decomposition.

To understand the surface chemistry of $Nb_4C_3$ before and after sulfidation and the nature of Nb at the surface, X-Ray photoelectron spectroscopy (XPS) was studied for both $Nb_4C_3$ (**Figure 3**A,C; Figure S10A,C, Supporting information) and $Nb_4C_3$-S900-60′ (Figure 3B,D; Figure S10B,D, Supporting information). The data of both samples were calibrated using
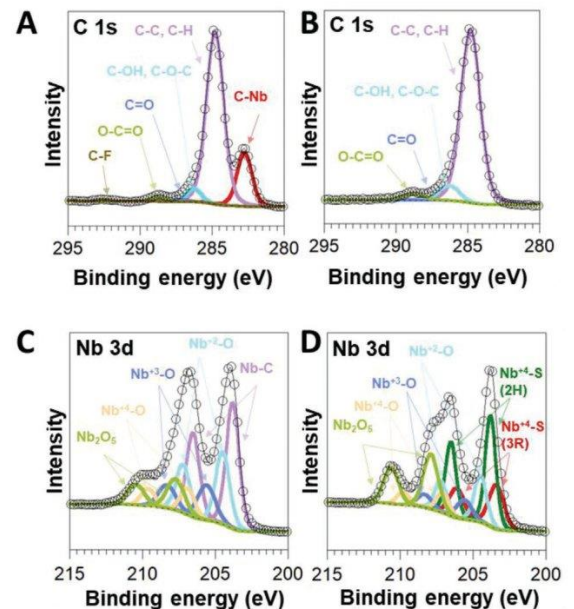
**Figure 3.** X-ray photoelectron spectra of C 1s for A) $Nb_4C_3$, and B) $Nb_4C_3$-S900-60′, and Nb 3d for C) $Nb_4C_3$ and D) $Nb_4C_3$-S900-60′.

142

adventitious carbon (C-C/C-H at 284.8 eV). For the $Nb_4C_3$ sample, Figure 3A shows the C 1s spectrum where the peak at 282.7 eV can be assigned to C-Nb in MXene.[53] Figure 3C shows the Nb 3d spectrum of $Nb_4C_3$ where the doublet peaks at 203.8 and 206.6 eV are assigned to Nb-C in $Nb_4C_3$ MXene. The doublets found at higher binding energies are assigned to Nb-O of different oxidation states.[53] For $Nb_4C_3$-S900-60′ sample, Figure 3B shows the C 1s spectrum where the C-Nb was not observed, which could be attributed to the $NbS_2$ nanomosaic layer formation upon sulfidation. For the Nb 3d spectrum of $Nb_4C_3$-S900-60′ in Figure 3D, it is impossible to differentiate between $Nb_4C_3$ and $NbS_2$ as the Nb-S and Nb-C doublet peaks binding energies are too close to be distinguished from each other. Previous literature of Nb-S doublets were found at (203.4 ± 0.2 eV and 206.1 ± 0.2 eV) for $3R$-$NbS_2$ and (204.0 ± 0.2 eV and 206.7 ± 0.2 eV) for 2H (or 1H) $NbS_2$.[54] Since the C-Nb peak was not observed in the C 1s spectrum of the $Nb_4C_3$-S900-60′ surface, it is reasonable to assume that the Nb 3d spectrum does not include the Nb-C doublet. Therefore, we were able to assign (203.4 and 206.1 eV) to $Nb^{+4}$-S in $3R$-$NbS_2$ and (203.8 and 206.5 eV) to $Nb^{+4}$-S in 2H-$NbS_2$.[54]

We also studied the C 1s and Nb 3d spectra (Figure S10A,B, Supporting information) for both samples after sputtering to study the sub-surface chemistry. The C-Nb peak in C 1s spectrum relatively increased in $Nb_4C_3$ (Figure S10A, Supporting Information), but more importantly, it showed up in $Nb_4C_3$-S900-60′ (Figure S10B, Supporting Information). This reveals the existence of $Nb_4C_3$ under the nanomosaic $NbS_2$ layer. The presence of Nb-C signal in $Nb_4C_3$-S900-60′ sample after sputtering demonstrates that the conversion of the MXene into the sulfide takes place from outer to inner layers. Furthermore, this indicates that the samples treated at milder conversion conditions (700 °C) are indeed partially converted and composed of MXene-$NbS_2$ hybrid. The Nb 3d spectra of both samples after sputtering (Figure S10C,D, Supporting Information) reveal no $Nb_2O_5$ peak at high binding energy.

To investigate the electrocatalytic behaviors of the as-prepared samples, linear sweep voltammetry (LSV) was carried out in an $H_2$-bubbled 0.5 M $H_2SO_4$ aqueous electrolyte. As shown in **Figure 4**A, $Nb_4C_3$ pristine, $Nb_4C_3$-$H_2$S600-10′, $Nb_4C_3$-$H_2$S700-10′, and $Nb_4C_3$-$H_2$S900-60′ exhibit similar electrocatalytic activities with almost the same onset-overpotentials. It can be seen that all samples show similar overpotentials of around 200 mV at 10 mA cm$^{-2}$. A similar trend can be found for $Nb_2C$-$H_2$S700-10′ and $Nb_2C$-$H_2$S900-60′, in which the respective overpotentials of 250 and 252 mV are needed to deliver a current density of 10 mA cm$^{-2}$. Given the lower overpotential for $Nb_4C_3$ and $Nb_4C_3$-derived samples compared to $Nb_2C$ and its derived samples, we focus herein on the electrocatalytic behavior of the formers.

Generally, the following three possible pathways can be used to describe the HER mechanism in the acidic electrolyte (Equations (1)–(3)):[55]

$$\text{Volmer step: } H^+ + e^- \rightarrow H_{ads} \tag{1}$$
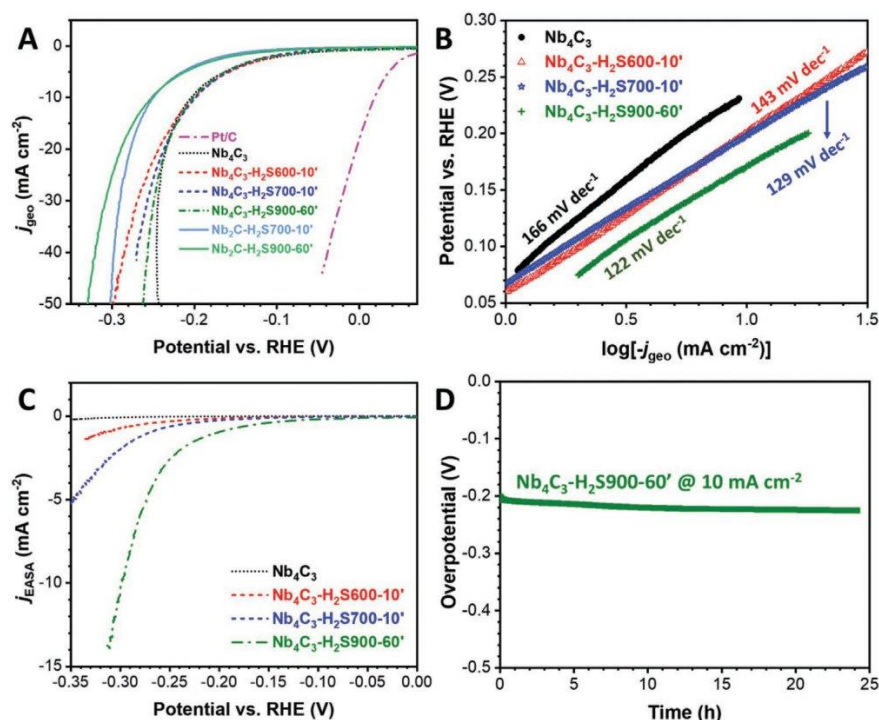


**Figure 4.** Electrocatalytic HER performance. A) iR-corrected LSV curves for HER measured at 5 mV s$^{-1}$ and B) the corresponding Tafel slopes for $Nb_4C_3$ pristine, $Nb_4C_3$-$H_2$S600-10′, $Nb_4C_3$-$H_2$S700-10′, and $Nb_4C_3$-$H_2$S900-60′. C) iR-corrected LSV curves normalized to the electrochemically active surface area (EASA). D) The long-term electrochemical stability of $Nb_4C_3$-$H_2$S900-60′ with a constant current density of 10 mA cm$^{-2}$.

Heyrovsky step: $H_{ads} + H^+ + e^- \rightarrow H_2$     (2)

Tafel step: $2H_{ads} \rightarrow H_2$     (3)
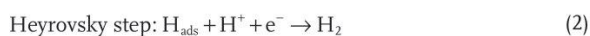
where $H_{ads}$ stands for the adsorbed H on the catalyst surface. Therefore, two possible mechanisms can be predicted, viz. Volmer–Heyrovsky or Volmer–Tafel.

The Tafel slopes of $Nb_4C_3$ pristine, $Nb_4C_3$-$H_2$S600-10', $Nb_4C_3$-$H_2$S700-10', and $Nb_4C_3$-$H_2$S900-60' are calculated to be 166, 143, 129, and 122 mV dec$^{-1}$, respectively (Figure 4B). The lower Tafel slope of $Nb_4C_3$-$H_2$S900-60' indicates faster electron transfer than the others. The large Tafel slopes suggest that a Volmer–Heyrovsky step generated the hydrogen, and H (Volmer step) adsorption is the limiting step.[55]

To further study the HER activity, each sample's electrochemically active surface area (EASA) was calculated by performing cyclic voltammetry (CV) at different scan rates (Figure S11, Supporting Information). In this work, a non-Faradaic potential region with the center of open circuit potential is used. The open-circuit potential varies from one sample to the other, so a different potential range is employed in this work to avoid any Faradic contribution from any of the samples for accurate estimation of the EASA. The EASA differs from the Brunauer–Emmett–Teller (BET)-specific surface area as the first determines the electrochemically available surface while the latter probes the area accessible for nitrogen physisorption.

The EASA values for $Nb_4C_3$ pristine, $Nb_4C_3$-$H_2$S600-10', $Nb_4C_3$-$H_2$S700-10', and $Nb_4C_3$-$H_2$S900-60' were obtained as 35.1, 5.1, 2.6, and 0.7 cm$^2$, respectively. The EASA decreases significantly after treatments, and the higher temperatures result in smaller EASA values. The very high EASA of $Nb_4C_3$ is attributed to the large $d$-spacing that renders the interlayer spacing accessible for ions and available for electrochemical processes. The reduction in EASA upon treatment can be explained by collapsing MXene's interlayer spacing during the heating cycle. Unlike normalizing the current by geometric area of the electrode, normalizing by the specific surface area or EASA reflects the intrinsic catalytic activity of the material rather than size dependence.[56] When LSV curves are normalized to EASA (Figure 4C), the $Nb_4C_3$-$H_2$S900-60' sample shows the highest HER activity. This suggests that even though this sample has lower EASA, it is intrinsically much more catalytically active than untreated MXene. Therefore, further enhancement in the kinetics of the HER is expected for $Nb_4C_3$-$H_2$S900-60' in the future by approaches to increase its EASA, such as milling.

Table S3, Supporting Information, lists the electrocatalytic performance of various $NbS_2$ morphologies employed as HER catalysts in recent literature. The $Nb_4C_3$-$H_2$S900-60' in the present work shows a relatively low overpotential (198 mV at 10 mA cm$^{-2}$) and Tafel slope (122 mV dec$^{-1}$), revealing higher electrocatalytic activity than most of the reported $NbS_2$ and MXenes as HER catalysts. The improved performance of the latter sample can be attributed to the nano mosaic morphology achieved where more edges are exposed. The long-term electrocatalytic stability was conducted in a 0.5 M $H_2SO_4$ electrolyte with a current density of 10 mA cm$^{-2}$ for 24 h. As shown in Figure 4D, $Nb_4C_3$-$H_2$S900-60' exhibits promising electrochemical stability.

## 3. Conclusions

In summary, heterostructures of MXene-TMD were obtained by a one-step thermal sulfidation of niobium MXenes. Our work for the first time demonstrated that by a facile manipulation of the treatment temperature and duration, different degrees of MXene-to-TMD conversion are obtained. Our results showed that the parent MXene slab thickness plays a crucial role in the derived TMD nanostructure. $Nb_2C$ MXene is more susceptible to conversion into $NbS_2$ than $Nb_4C_3$ MXene when treated at 700 °C for 10 min due to higher $H_2S$ exposure of Nb-C-Nb layers in $Nb_2C$ rather than Nb-C-Nb-C-Nb-C-Nb layers in $Nb_4C_3$. Tuning treatment conditions yielded various nanostructures depending on the MXene type, such as pillars in $Nb_2C$ and mosaics in the case of $Nb_4C_3$ MXene. The treatment at 700 °C resulted in MXene-$NbS_2$ hybrids, whereas treatment at 900 °C for 60 min resulted in the conversion of MXene into $NbS_2$ nano-mosaic heterostructures with C/MXene core. Overall, the $H_2S$ gas method has better control over the conversion degree than the $H_2$ gas + S powder method.

When used as electrodes for HER, the $Nb_4C_3$ MXene treated in $H_2S$ gas at 900 °C for 60 min exhibited the highest HER activity among all samples tested, and promising cycling stability. Our study encourages the possibility of constructing a plethora of MXene-based TMD heterostructures for use as electrode materials for energy storage and conversion, among other applications. Further fine-tuning the derivatization parameters to optimize the electrochemical performance of the produced heterostructures in future work may provide the path toward applications in more complex electrocatalytic applications and improved performances.

## 4. Experimental Section

*Synthesis of $Nb_2AlC$ and $Nb_4AlC_3$ MAX Phases*: $Nb_2C$ and $Nb_4C_3$ were synthesized by selective etching of the Al from their parent MAX phases, $Nb_2AlC$ and $Nb_4AlC_3$, respectively. $Nb_2AlC$ and $Nb_4AlC_3$ were prepared via solid-state synthesis processes by mixing niobium (Nb, Alfa Aesar, < 45 µm, 99.8%), aluminum (Al, Alfa Aesar, 7–15 µm, 99.5%), and carbon (C, Alfa Aesar, 7–11 µm, 99%) with atomic ratios of 2:1.3:0.95 and 4:1.5:2.7, respectively. Each mixture was added to yttria-stabilized zirconia balls in a high-density polyethylene jar and was mixed using a Turbula mixer for 3 h at 56 rpm. The samples were then pressed at room temperature into pellets. $Nb_2AlC$ pellets were heated from room temperature to 1600 °C. The samples were held at the peak temperature for 4 h, then left to cool naturally to room temperature. $Nb_4AlC_3$ pellets were heated through a three-temperature-step program: first at 750 °C for 30 min, second at 1450 °C for 30 min, and third at 1700 °C for 1 h. The heating rate used for both samples was 300 °C h$^{-1}$. All the heating and cooling steps were in an alumina tube furnace under a continuous flow of argon (Ar) at a flow rate of 100 sccm.

*Synthesis of $Nb_2C$ and $Nb_4C_3$ MXenes*: Both $Nb_2AlC$ and $Nb_4AlC_3$ were etched using hydrofluoric acid (48–51% by mass HF, Acros Organics, 10 mL for each 1 g of MAX phase powder). The mixtures were heated to 40 °C in an oil bath, mechanically agitated using Teflon coated magnetic stirrer, and held for 90 h. Afterward, the products were washed with de-ionized (DI) water to remove the acid and etching side-products. The washing procedure starts with dividing the mixture into several centrifuging tubes (one tube for each 0.5 g of starting MAX phase), centrifuging at 3500 rpm for 5 min, discarding the supernatant, refilling the tube with DI water, and finally redispersing the sediment using vortex machine. This washing step was repeated several times until the pH level exceeded a value of 6. Finally, the as-prepared product was dried using vacuum-assisted filtration overnight.

**ADVANCED
SCIENCE NEWS**

www.advancedsciencenews.com

**ADVANCED
MATERIALS
INTERFACES**

www.advmatinterfaces.de

*MXene Sulfidation*: $Nb_4C_3$ was placed in a quartz crucible inside a quartz tube positioned in a one-zone furnace. Two different methods were used to perform the sulfidation, named $H_2/S$ and $H_2S$ (Figure S1, Supporting Information).

Method $H_2/S$: To produce $H_2S$ gas, a second crucible containing sulfur (S) powder was placed upstream in the tube outside the furnace, with a heating jacket fixed around it. The system was purged with Ar at 100 sccm for 2 h, heated at a rate of 300 °C $h^{-1}$ to the target temperature (500, 600, 700, or 900 °C) with holding times of 10 or 60 min. The Ar flow was kept at 50 sccm during heating, holding, and cooling steps. 20 min before reaching the holding temperature, $H_2$ gas flow was started at 10 sccm and turned off after holding time. Throughout the $H_2$ flow period, the heating jacket was kept at 550 °C (Figure S2A, Supporting Information).

Method $H_2S$: Like method $H_2/S$, initial purging, Ar flow, heating rates, and temperatures were kept the same. $H_2S$ gas was directly used instead of the combination of $H_2$ + S powder. $H_2S$ gas was initiated when the target temperature was reached and kept flowing during holding time at 50 sccm. The samples were named according to the target temperature and holding time, "S" for method $H_2/S$, and "$H_2S$" for method $H_2S$. For example, $Nb_4C_3$-S700-10′ stands for $Nb_4C_3$ sulfidized at 700 °C for 10 min in the $H_2/S$ system. $Nb_4C_3$-$H_2S$900-60′ stands for $Nb_4C_3$ sulfidized at 900 °C for 60 min with $H_2S$ gas. For the sulfidation of $Nb_2C$, only method $H_2S$ was applied, and the nomenclature follows the same pattern.

*Material Characterization*: SEM was carried out using a ZEISS-Gemini SEM500 system coupled to an EDX detector (Oxford Instruments for EDX analysis). Acceleration voltages of 1–3 kV were used for imaging and 15 kV for spectroscopy. The samples were analyzed without any conductive sputtering.

TEM (JEOL 2100F) was performed at an acceleration voltage of 200 kV. The samples were dispersed in ethanol by tip sonication for 30 s, drop-cast onto a copper grid coated with a lacey carbon film, and dried at room temperature overnight.

XRD was conducted with a D8 Advance diffractometer (Bruker AXS) with a copper source (Cu-K$\alpha$, 40 kV, 40 mA). Signal was collected using a 1D Lynxeye detector at 0.02 $2\theta$ step with a rate of 1 s/step.

XPS measurements were performed using the Thermo-Fisher K-Alpha Plus XPS. An air-free holder is used during the whole process to protect the samples from oxidation. The photon source was a monochromatized Al K $\alpha$ line (h$\nu$ = 1486.6 eV). The spectra were acquired using a spot size of 400 µm. A flood gun with combined electrons and low-energy Ar ions was used during the measurements. A dual monoatomic and gas cluster Argon ion source was used for depth profiling and sample cleaning.

Raman spectra (Renishaw inVia Raman microscope) were acquired with an Nd-YAG laser (532 nm) at 0.5 mW power with 10 s acquisition time for 10 accumulations using an objective lens with a numeric aperture of 0.75. At least 12 points were collected for each sample. The data show a representative spectrum of each sample.

Nitrogen gas sorption measurements were performed with an Autosorb iQ system (Quantachrome, Anton Paar) at −196 °C. The $Nb_2C$ and $Nb_4C_3$ samples were first degassed at 200 °C at $10^2$ Pa for one day. The specific surface areas were calculated by applying the BET model[57] within the linear pressure range (up to 0.3 relative pressure).[58]

Elemental analysis (CHNS) was performed with Vario Micro Cube System using sulfanilamide for calibration and a reduction temperature of 850 °C. An OXY cube oxygen analyzer at 1450 °C was employed for the quantitative analysis of elemental oxygen.

*Electrochemical Measurements*: The electrochemical performance was conducted by a Bio-Logic SP200 portable electrochemical workstation with an RRDE-3A rotating ring disk electrode system. A standard SVC-2 three-electrode system with a working electrode of as-prepared samples, a $Hg/Hg_2SO_4$ electrode with saturated KCl supporting solution as a reference electrode, and a graphite rod as a counter electrode were used to investigate the hydrogen evolution activity in 0.5 M $H_2SO_4$ aqueous electrolyte. The working electrode was prepared by dispersing the as-prepared materials (10 mg) in a mixture of 750 µL water, 250 µL ethanol, and 10 µL Nafion 117 solution (≈5% in a mixture of lower aliphatic alcohols and water, Sigma Aldrich), followed by 1 h sonication. After that, 7 µL dispersion was drop-cast on the glassy carbon electrode

and dried at room temperature. The mass loading of active materials was ≈1 mg $cm^{-2}$. LSV was measured at 5 mV $s^{-1}$ by rotating the working electrode at 1600 rpm with flowing $H_2$ in the electrolyte. All LSV curves were *iR*-corrected, and the potentials were converted in reference to a reversible hydrogen electrode.

The CV polarization curves were used to calculate EASA. EASA values were obtained from the hydrogen adsorption/desorption region, so only the double-layer charging current is used. In this work, a non-Faradaic potential region with the center of open circuit potential was used. EASA was estimated from the electrical double-layer capacitance ($C_{dl}$) of the as-prepared materials. The $C_{dl}$ was analyzed via CV at scan rates of 20–100 mV $s^{-1}$.

The EASA was calculated using Equation (4):[59]

$$EASA = (C_{dl} \times A)/C_s \tag{4}$$

where A is the geometric area of the electrode, and $C_s$ is the capacitance from a smooth planar surface per unit area. An average value of $C_s = 40$ µF $cm^{-2}$ is used in this work.[59]

## Supporting Information

Supporting Information is available from the Wiley Online Library or from the author.

## Acknowledgements

## Conflict of Interest

The authors declare no conflict of interest.

## Data Availability Statement

The data that support the findings of this study are available from the corresponding author upon request.

## Keywords

[1] M. W. Barsoum, *MAX Phases: Properties of Machinable Ternary Carbides and Nitrides*, Wiley, New York **2013**.

[2] M. Naguib, M. Kurtoglu, V. Presser, J. Lu, J. Niu, M. Heon, L. Hultman, Y. Gogotsi, M. W. Barsoum, *Adv. Mater.* **2011**, *23*, 4248.

[3] M. Naguib, O. Mashtalir, J. Carle, V. Presser, J. Lu, L. Hultman, Y. Gogotsi, M. W. Barsoum, *ACS Nano* **2012**, *6*, 1322.

[4] M. Naguib, V. N. Mochalin, M. W. Barsoum, Y. Gogotsi, *Adv. Mater.* **2014**, *26*, 992.

[5] a) M. Naguib, J. Halim, J. Lu, K. M. Cook, L. Hultman, Y. Gogotsi, M. W. Barsoum, *J. Am. Chem. Soc.* **2013**, *135*, 15966; b) M. R. Lukatskaya, O. Mashtalir, C. E. Ren, Y. Dall'Agnese, P. Rozier, P. L. Taberna, M. Naguib, P. Simon, M. W. Barsoum, Y. Gogotsi, *Science* **2013**, *341*, 1502; c) M. Naguib, J. Come, B. Dyatkin, V. Presser, P. L. Taberna, P. Simon, M. W. Barsoum, Y. Gogotsi, *Electrochem. Commun.* **2012**, *16*, 61.

[6] A. D. Handoko, K. D. Fredrickson, B. Anasori, K. W. Convey, L. R. Johnson, Y. Gogotsi, A. Vojvodic, Z. W. Seh, *ACS Appl. Energy Mater.* **2017**, *1*, 173.

[7] Z. W. Seh, K. D. Fredrickson, B. Anasori, J. Kibsgaard, A. L. Strickler, M. R. Lukatskaya, Y. Gogotsi, T. F. Jaramillo, A. Vojvodic, *ACS Energy Lett.* **2016**, *1*, 589.

[8] a) E. Muckley, M. Naguib, I. N. Ivanov, *Nanoscale* **2018**, *10*, 21689; b) P. A. Rasheed, R. P. Pandey, T. Gomez, M. Naguib, K. A. Mahmoud, *RSC Adv.* **2020**, *10*, 24697; c) X. Zhu, B. Liu, H. Hou, Z. Huang, K. M. Zeinu, L. Huang, X. Yuan, D. Guo, J. Hu, J. Yang, *Electrochim. Acta* **2017**, *248*, 46.

[9] a) K. Rasool, R. P. Pandey, P. A. Rasheed, S. Buczek, Y. Gogotsi, K. A. Mahmoud, *Mater. Today* **2019**, *30*, 80; b) M. Torkamanzadeh, L. Wang, Y. Zhang, O. Budak, P. Srimuk, V. Presser, *ACS Appl. Mater. Interfaces* **2020**, *12*, 26013.

[10] O. Mashtalir, M. Naguib, V. N. Mochalin, Y. Dall'Agnese, M. Heon, M. W. Barsoum, Y. Gogotsi, *Nat. Commun.* **2013**, *4*, 1716.

[11] A. S. Zeraati, S. A. Mirkhani, P. Sun, M. Naguib, P. V. Braun, U. Sundararaj, *Nanoscale* **2021**, *13*, 3572.

[12] H. Wang, J. -M. Lee, *J. Mater. Chem. A* **2020**, *8*, 10604.

[13] a) S. Husmann, O. Budak, H. Shim, K. Liang, M. Aslan, A. Kruth, A. Quade, M. Naguib, V. Presser, *Chem. Commun.* **2020**, *56*, 11082; b) V. Natu, R. Pai, M. Sokol, M. Carey, V. Kalra, M. W. Barsoum, *Chem* **2020**, *6*, 616; c) A. Jawaid, A. Hassan, G. Neher, D. Nepal, R. Pachter, W. J. Kennedy, S. Ramakrishnan, R. A. Vaia, *ACS Nano* **2021**, *15*, 2771; d) W. Sun, S. Shah, Y. Chen, Z. Tan, H. Gao, T. Habib, M. Radovic, M. Green, *J. Mater. Chem. A* **2017**, *5*, 21663; e) M. Ghidiu, M. R. Lukatskaya, M. Q. Zhao, Y. Gogotsi, M. W. Barsoum, *Nature* **2014**, *516*, 78; f) Y. Li, H. Shao, Z. Lin, J. Lu, L. Liu, B. Duployer, P. O. Å. Persson, P. Eklund, L. Hultman, M. Li, K. Chen, X. -H. Zha, S. Du, P. Rozier, Z. Chai, E. Raymundo-Piñero, P. -L. Taberna, P. Simon, Q. Huang, *Nat. Mater.* **2020**, *19*, 894.

[14] M. A. Hope, A. C. Forse, K. J. Griffith, M. R. Lukatskaya, M. Ghidiu, Y. Gogotsi, C. P. Grey, *Phys. Chem. Chem. Phys.* **2016**, *18*, 5099.

[15] A. Feng, Y. Yu, F. Jiang, Y. Wang, L. Mi, Y. Yu, L. Song, *Ceram. Int.* **2017**, *43*, 6322.

[16] M. Li, J. Lu, K. Luo, Y. Li, K. Chang, K. Chen, J. Zhou, J. Rosen, L. Hultman, P. Eklund, P. O. Å. Persson, S. Du, Z. Chai, Z. Huang, Q. Huang, *J. Am. Chem. Soc.* **2019**, *141*, 4730.

[17] T. Li, L. Yao, Q. Liu, J. Gu, R. Luo, J. Li, X. Yan, W. Wang, P. Liu, B. Chen, W. Zhang, W. Abbas, R. Naz, D. Zhang, *Angew. Chem., Int. Ed.* **2018**, *57*, 6115.

[18] L. Verger, V. Natu, M. Ghidiu, M. W. Barsoum, *J. Phys. Chem. C* **2019**, *123*, 20044.

[19] A. Al-Temimy, K. Prenger, R. Golnak, M. Lounasvuori, M. Naguib, T. Petit, *ACS Appl. Mater. Interfaces* **2020**, *12*, 15087.

[20] J. Luo, W. Zhang, H. Yuan, C. Jin, L. Zhang, H. Huang, C. Liang, Y. Xia, J. Zhang, Y. Gan, X. Tao, *ACS Nano* **2017**, *11*, 2459.

[21] W. Tian, A. VahidMohammadi, Z. Wang, L. Ouyang, M. Beidaghi, M. M. Hamedi, *Nat. Commun.* **2019**, *10*, 2558.

[22] a) P. A. Maughan, V. R. Seymour, R. Bernardo-Gavito, D. J. Kelly, S. Shao, S. Tantisriyanurak, R. Dawson, S. J. Haigh, R. J. Young, N. Tapia-Ruiz, N. Bimbo, *Langmuir* **2020**, *36*, 4370; b) K. Liang,

R. A. Matsumoto, W. Zhao, N. C. Osti, I. Popov, B. P. Thapaliya, S. Fleischmann, S. Misra, K. Prenger, M. Tyagi, E. Mamontov, V. Augustyn, R. R. Unocic, A. P. Sokolov, S. Dai, P. T. Cummings, M. Naguib, *Adv. Funct. Mater.* **2021**, *31*, 2104007.

[23] M. Naguib, O. Mashtalir, M. R. Lukatskaya, B. Dyatkin, C. Zhang, V. Presser, Y. Gogotsi, M. W. Barsoum, *Chem. Commun.* **2014**, *50*, 7420.

[24] C. F. Zhang, M. Beidaghi, M. Naguib, M. R. Lukatskaya, M. Q. Zhao, B. Dyatkin, K. M. Cook, S. J. Kim, B. Eng, X. Xiao, D. H. Long, W. M. Qiao, B. Dunn, Y. Gogotsi, *Chem. Mater.* **2016**, *28*, 3937.

[25] T. Su, R. Peng, Z. D. Hood, M. Naguib, I. N. Ivanov, J. K. Keum, Z. Qin, Z. Guo, Z. Wu, *ChemSusChem* **2018**, *11*, 688.

[26] N. R. Hemanth, T. Kim, B. Kim, A. H. Jadhav, K. Lee, N. K. Chaudhari, *Mater. Chem. Front.* **2021**, *5*, 3298.

[27] a) M. Xu, N. Bai, H. -X. Li, C. Hu, J. Qi, X. -B. Yan, *Chin. Chem. Lett.* **2018**, *29*, 1313; b) X. Wu, Z. Wang, M. Yu, L. Xiu, J. Qiu, *Adv. Mater.* **2017**, *29*, 1607017.

[28] L. Huang, L. Ai, M. Wang, J. Jiang, S. Wang, *Int. J. Hydrogen Energy* **2019**, *44*, 965.

[29] a) C. Wang, X. -D. Zhu, K. -X. Wang, L. -L. Gu, S. -Y. Qiu, X. -T. Gao, P. -J. Zuo, N. -Q. Zhang, *Sustain. Energy Fuels* **2019**, *3*, 2577; b) Y. Wu, P. Nie, L. Wu, H. Dou, X. Zhang, *Chem. Eng. J.* **2018**, *334*, 932.

[30] H. Wang, X. Xiao, S. Liu, C. -L. Chiang, X. Kuai, C. -K. Peng, Y. -C. Lin, X. Meng, J. Zhao, J. Choi, Y. -G. Lin, J. -M. Lee, L. Gao, *J. Am. Chem. Soc.* **2019**, *141*, 18578.

[31] L. Lin, S. Zhang, D. A. Allwood, in *Two Dimensional Transition Metal Dichalcogenides: Synthesis, Properties, and Applications* (Eds: N. S. Arul, V. D. Nithya), Springer Singapore, Singapore **2019**, 173.

[32] P. Srimuk, J. Lee, S. Fleischmann, S. Choudhury, N. Jäckel, M. Zeiger, C. Kim, M. Aslan, V. Presser, *J. Mater. Chem. A* **2017**, *5*, 15640.

[33] Q. Fu, J. Han, X. Wang, P. Xu, T. Yao, J. Zhong, W. Zhong, S. Liu, T. Gao, Z. Zhang, L. Xu, B. Song, *Adv. Mater.* **2021**, *33*, 1907818.

[34] C. Zhu, X. Mu, P. A. van Aken, Y. Yu, J. Maier, *Angew. Chem., Int. Ed.* **2014**, *126*, 2184.

[35] a) P. Prabhu, V. Jose, J. -M. Lee, *Matter* **2020**, *2*, 526; b) Q. Yu, Y. Luo, A. Mahmood, B. Liu, H. -M. Cheng, *Electrochem. Energy Rev.* **2019**, *2*, 373.

[36] L. Yu, B. Liu, Y. Wang, F. Yu, J. Ma, *J. Power Sources* **2021**, *490*, 229250.

[37] C. Chen, X. Xie, B. Anasori, A. Sarycheva, T. Makaryan, M. Zhao, P. Urbankowski, L. Miao, J. Jiang, Y. Gogotsi, *Angew. Chem., Int. Ed.* **2018**, *57*, 1846.

[38] K. R. G. Lim, A. D. Handoko, L. R. Johnson, X. Meng, M. Lin, G. S. Subramanian, B. Anasori, Y. Gogotsi, A. Vojvodic, Z. W. Seh, *ACS Nano* **2020**, *14*, 16140.

[39] a) X. Huang, J. Tang, B. Luo, R. Knibbe, T. Lin, H. Hu, M. Rana, Y. Hu, X. Zhu, Q. Gu, D. Wang, L. Wang, *Adv. Energy Mater.* **2019**, *9*, 1901872; b) J. Tang, X. Huang, T. Lin, T. Qiu, H. Huang, X. Zhu, Q. Gu, B. Luo, L. Wang, *Energy Storage Mater.* **2020**, *26*, 550.

[40] a) R. Tan, J. Yang, J. Hu, K. Wang, Y. Zhao, F. Pan, *Chem. Commun.* **2016**, *52*, 986; b) L. Fei, Y. Jiang, Y. Xu, G. Chen, Y. Li, X. Xu, S. Deng, H. Luo, *J. Power Sources* **2014**, *265*, 1; c) X. Yang, F. Xiao, S. Wang, J. Liu, M. K. H. Leung, D. Y. W. Yu, A. L. Rogach, *J. Mater. Chem. A* **2019**, *7*, 11877.

[41] a) C. -F. Du, Q. Liang, Y. Zheng, Y. Luo, H. Mao, Q. Yan, *ACS Appl. Mater. Interfaces* **2018**, *10*, 33779; b) A. Frank, T. Gänsler, S. Hieke, S. Fleischmann, S. Husmann, V. Presser, C. Scheu, *Nanoscale Adv.* **2021**, *3*, 1067; c) S. Husmann, Ö. Budak, A. Quade, A. Frank, A. Kruth, C. Scheu, A. Tolosa, V. Presser, *J. Power Sources* **2020**, *450*, 227674; d) S. Fleischmann, T. S. Dörr, A. Frank, S. W. Hieke, D. Doblas-Jimenez, C. Scheu, P. W. de Oliveira, T. Kraus, V. Presser, *Batter. Supercaps* **2019**, *2*, 668; e) S. Choudhury, M. Zeiger, P. Massuti-Ballester, S. Fleischmann, P. Formanek, L. Borchardt, V. Presser, *Sustain. Energy Fuels* **2017**, *1*, 84.

[42] N. I. Dowling, P. D. Clark, *Ind. Eng. Chem. Res.* **1999**, *38*, 1369.

[43] a) J. L. Hart, K. Hantanasirisakul, A. C. Lang, B. Anasori, D. Pinto, Y. Pivak, J. T. van Omme, S. J. May, Y. Gogotsi, M. L. Taheri, *Nat. Commun.* **2019**, *10*, 522; b) I. Persson, L. -Å. Näslund, J. Halim, M. W. Barsoum, V. Darakchieva, J. Palisaitis, J. Rosen, P. O. Å. Persson, *2D Mater.* **2017**, *5*, 015002.

[44] a) C. Zhang, S. J. Kim, M. Ghidiu, M. -Q. Zhao, M. W. Barsoum, V. Nicolosi, Y. Gogotsi, *Adv. Funct. Mater.* **2016**, *26*, 4143; b) M. Zhang, X. Chen, J. Sui, B. S. Abraha, Y. Li, W. Peng, G. Zhang, F. Zhang, X. Fan, *Inorg. Chem. Front.* **2020**, *7*, 1205.

[45] M. Seredych, C. E. Shuck, D. Pinto, M. Alhabeb, E. Precetti, G. Deysher, B. Anasori, N. Kurra, Y. Gogotsi, *Chem. Mater.* **2019**, *31*, 3324.

[46] A. Mansouri, N. Semagina, *ACS Catal.* **2018**, *8*, 7621.

[47] a) H. Lin, S. Gao, C. Dai, Y. Chen, J. Shi, *J. Am. Chem. Soc.* **2017**, *139*, 16235; b) N. J. Lane, M. Naguib, V. Presser, G. Hug, L. Hultman, M. W. Barsoum, *J. Raman Spectrosc.* **2012**, *43*, 954.

[48] a) E. Capelli, R. Konings, *J. Fluorine Chem.* **2018**, *208*, 55; b) T. Hu, J. Wang, H. Zhang, Z. Li, M. Hu, X. Wang, *Phys. Chem. Chem. Phys.* **2015**, *17*, 9997.

[49] a) M. Magnuson, J. Halim, L. -Å. Näslund, *J. Electron Spectrosc. Relat. Phenom.* **2018**, *224*, 27; b) F. D. Hardcastle, I. E. Wachs, *Solid State Ion.* **1991**, *45*, 201.

[50] W. G. McMullan, J. C. Irwin, *Solid State Commun.* **1983**, *45*, 557.

[51] M. S. Dresselhaus, A. Jorio, R. Saito, *Annu. Rev. Condens. Matter Phys.* **2010**, *1*, 89.

[52] A. J. Owen, K. W. Sykes, D. J. D. Thomas, P. White, *Trans. Faraday Soc.* **1953**, *49*, 1198.

[53] J. Halim, K. M. Cook, M. Naguib, P. Eklund, Y. Gogotsi, J. Rosen, M. W. Barsoum, *Appl. Surf. Sci.* **2016**, *362*, 406.

[54] L. Najafi, S. Bellani, R. Oropesa-Nuñez, B. Martín-García, M. Prato, V. Mazánek, D. Debellis, S. Lauciello, R. Brescia, Z. Sofer, F. Bonaccorso, *J. Mater. Chem. A* **2019**, *7*, 25593.

[55] K. Liang, S. Pakhira, Z. Yang, A. Nijamudheen, L. Ju, M. Wang, C. I. Aguirre-Velez, G. E. Sterbinsky, Y. Du, Z. Feng, J. L. Mendoza-Cortes, Y. Yang, *ACS Catal.* **2018**, *9*, 651.

[56] S. Sun, H. Li, Z. J. Xu, *Joule* **2018**, *2*, 1024.

[57] S. Brunauer, P. H. Emmett, E. Teller, *J. Am. Chem. Soc.* **1938**, *60*, 309.

[58] J. Rouquerol, D. Avnir, C. W. Fairbridge, D. H. Everett, J. M. Haynes, N. Pernicone, J. D. F. Ramsay, K. S. W. Sing, K. K. Unger, *Pure Appl. Chem.* **1994**, *66*, 1739.

[59] K. Liang, L. Guo, K. Marcus, S. Zhang, Z. Yang, D. E. Perea, L. Zhou, Y. Du, Y. Yang, *ACS Catal.* **2017**, *7*, 8406.

147

Layered Nano-Mosaic of Niobium Disulfide
Heterostructures by Direct Sulfidation of Niobium
Carbide MXenes for Hydrogen Evolution

*Samantha Husmann, Mohammad Torkamanzadeh, Kun
Liang, Ahmad Majed, Chaochao Dun, Jeffrey J Urban,
Michael Naguib,\* and Volker Presser\**

# Layered nano-mosaic of niobium disulfide heterostructures

# by direct sulfidation of niobium carbides MXenes

# for hydrogen evolution

*Samantha Husmann,[1] Mohammad Torkamanzadeh,[1,2] Kun Liang,[3]*

*Ahmad Majed,[3] Chaochao Dun,[4] Jeffrey J Urban,[4] Michael Naguib[3,*] Volker Presser,[1,2,5,*]*

[1]   *INM - Leibniz Institute for New Materials, D2 2, 66123, Saarbrücken, Germany*

[2]   *Department of Materials Science & Engineering, Saarland University, Campus D2 2, 66123, Saarbrücken, Germany*

[3]   *Department of Physics and Engineering Physics, Tulane University, New Orleans, Louisiana 70118, United States of America*

[4]   *The Molecular Foundry, Lawrence Berkeley National Laboratory, Berkeley, California 94720, United States of America*

[5]   *Saarene, Saarland Center for Energy Materials and Sustainability, Campus C4 2, 66123 Saarbrücken, Germany*

*   Corresponding authors' email: naguib@tulane.edu (MN), volker.presser@leibniz-inm.de (VP)

**Supporting Figures**
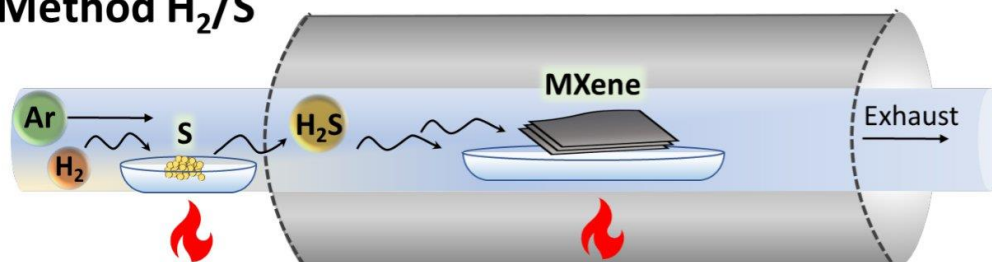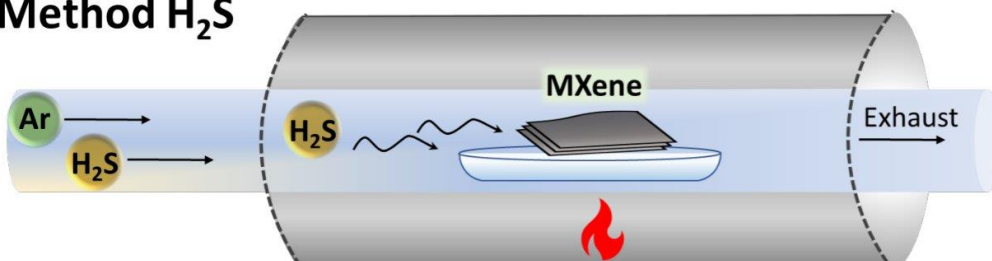


**Figure S1:** Schematic illustration of the experimental setup for MXene sulfidation with $H_2$+S and $H_2$S methods.
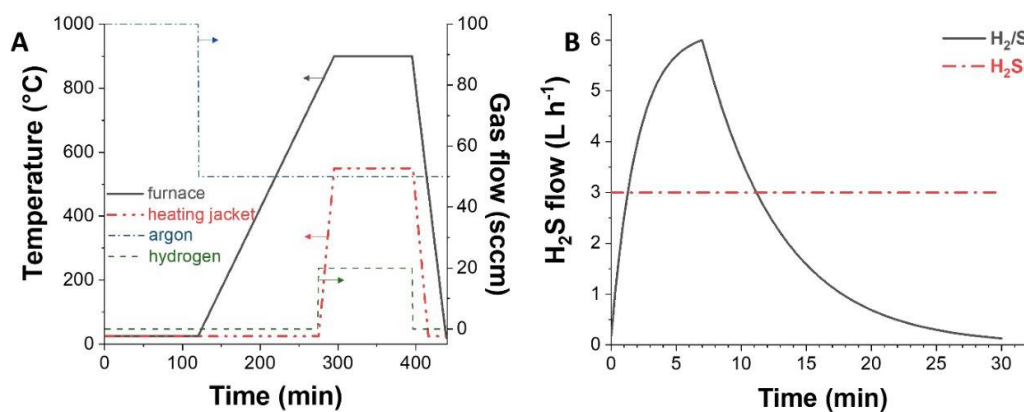


**Figure S2:** (A) Temperature and gas program during sulfidation with $H_2$/S method. (B) Qualitative flow of $H_2$S gas over time in the different furnace setups.
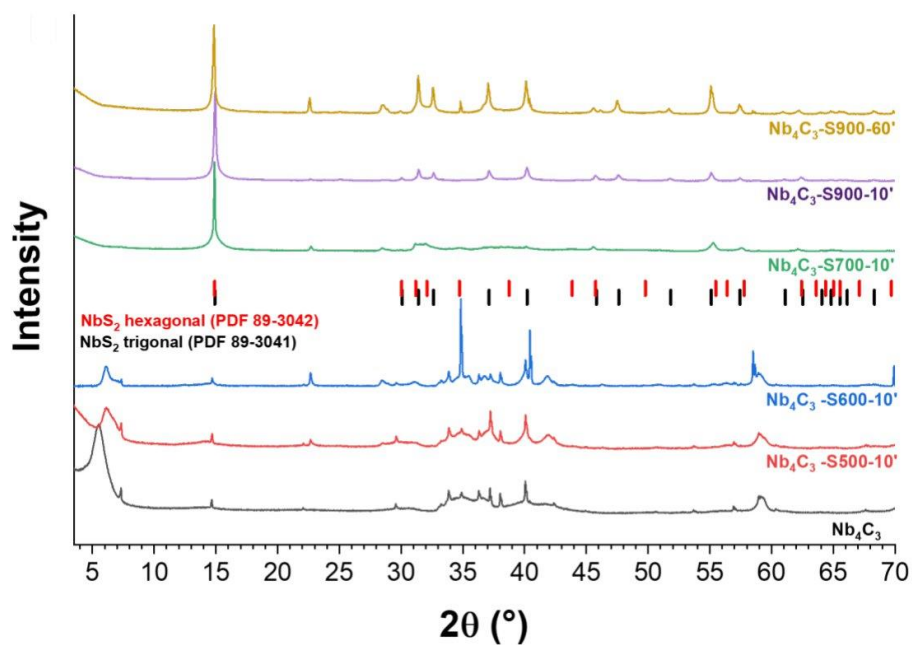
**Figure S3:** X-ray diffractograms of $Nb_4C_3$ treated in different conditions by method $H_2/S$.
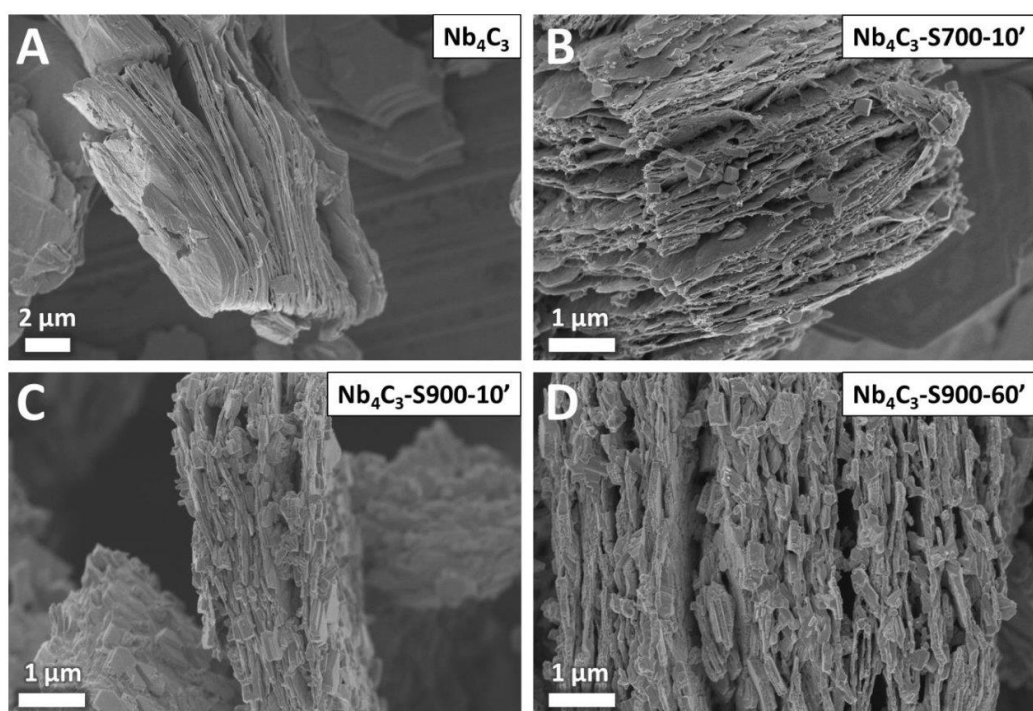


**Figure S4:** Scanning electron micrographs of (A) $Nb_4C_3$, (B) $Nb_4C_3$-S700-10', (C) $Nb_4C_3$-S900-10', and (D) $Nb_4C_3$-S900-60'.
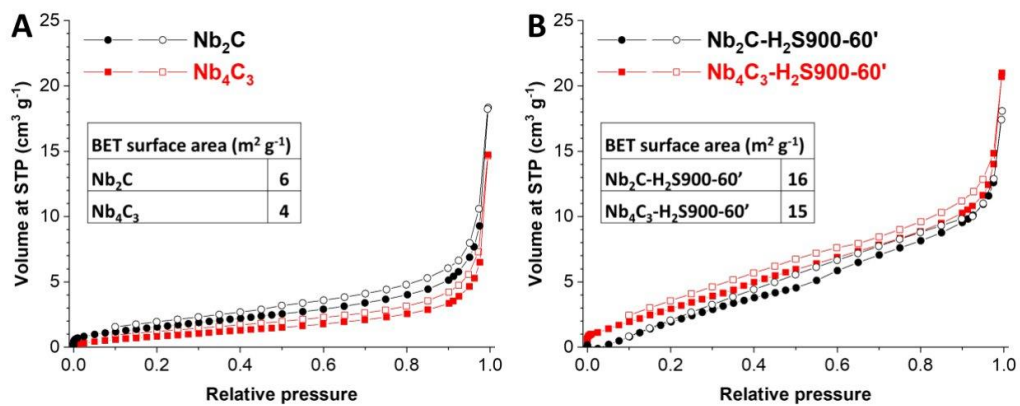
**Figure S5:** Nitrogen gas sorption isotherms of (A) $Nb_2C$ and $Nb_4C_3$ MXenes and (B) the corresponding sulfidized samples recorded at -196 °C. STP: standard temperature and pressure.
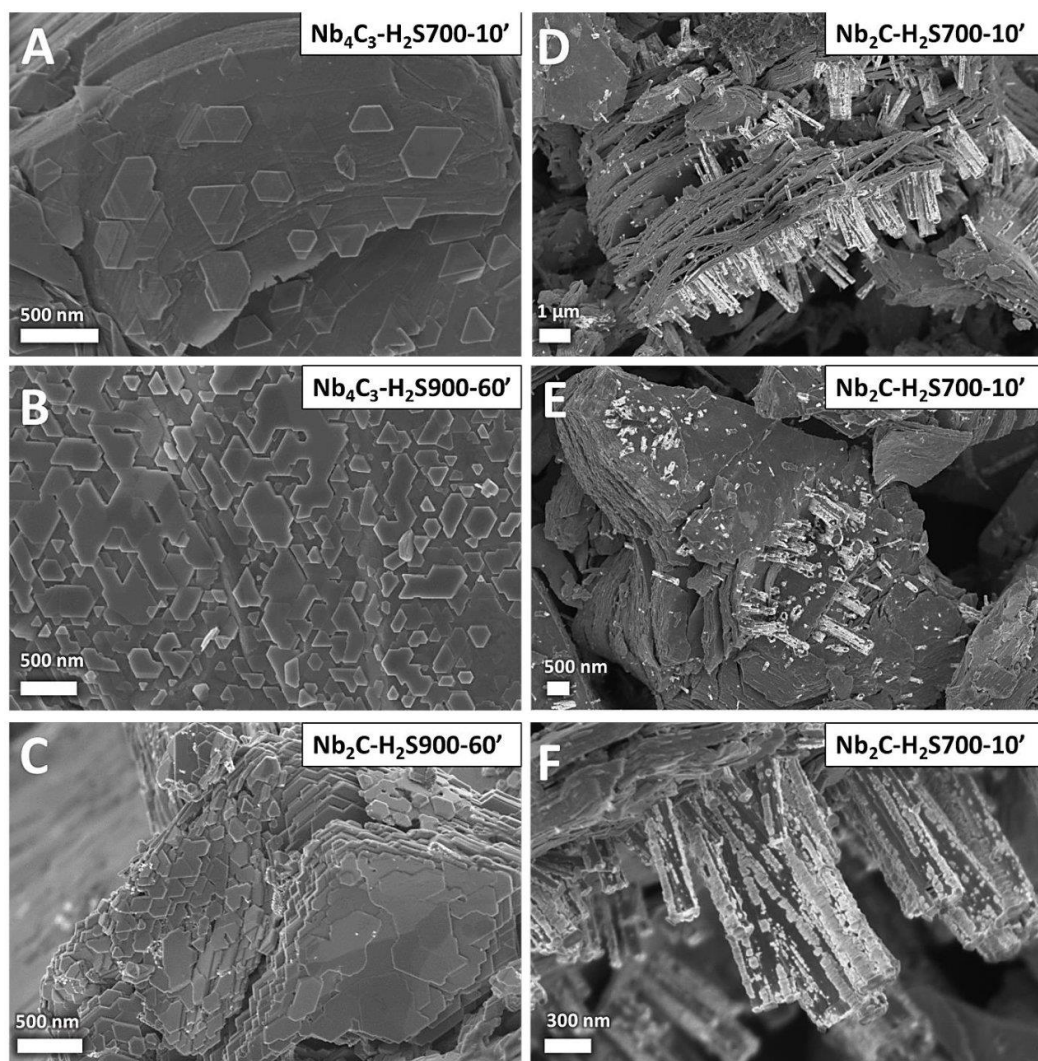
**Figure S6:** Scanning electron micrographs of (A) $Nb_4C_3$-$H_2S700$-10', (B) $Nb_4C_3$-$H_2S900$-60', (C) $Nb_2C$-$H_2S900$-60', and (D-F) $Nb_2C$-$H_2S700$-10'.
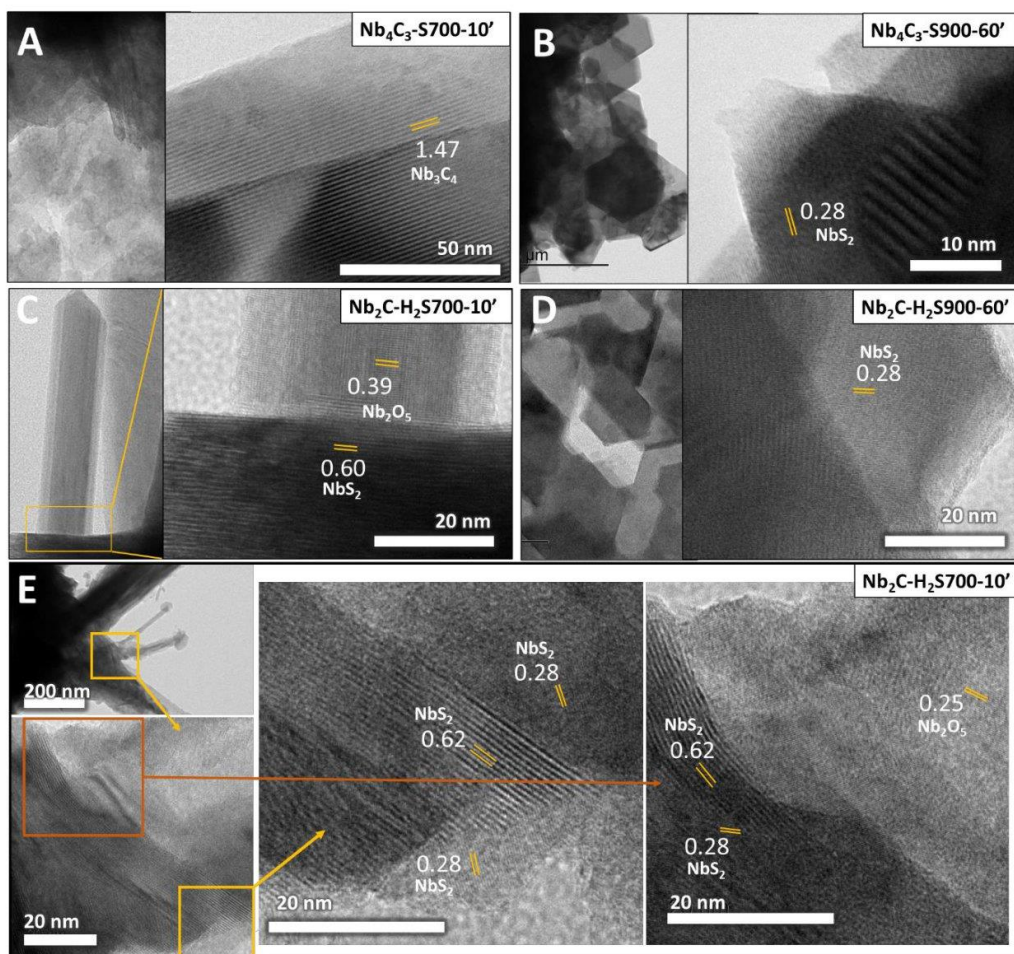
**Figure S7:** Transmission electron micrographs of (A) $Nb_4C_3$-S700-10', (B) $Nb_4C_3$-S900-60', (C-E) $Nb_2C$-$H_2$S700-10', and (D) $Nb_2C$-$H_2$S900-60'.
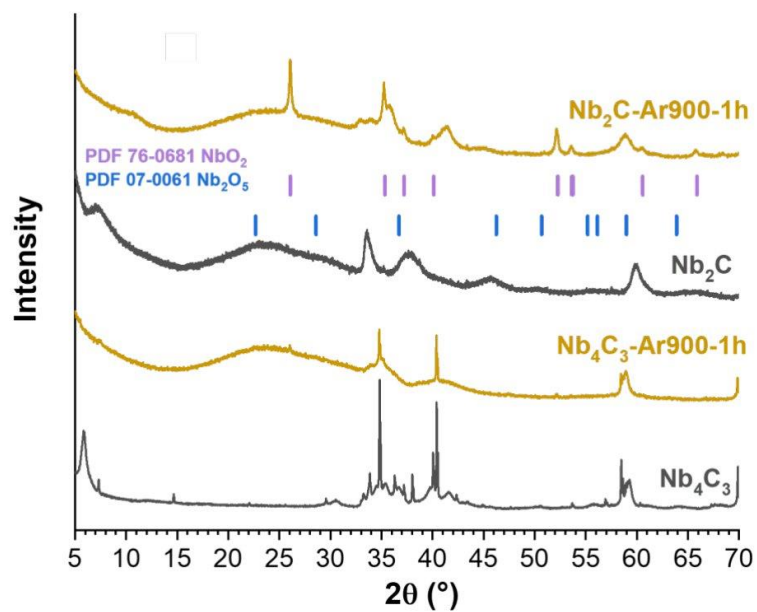
**Figure S8:** X-ray diffractograms of $Nb_4C_3$ and $Nb_2C$ before and after treatment at 900 °C in Ar.
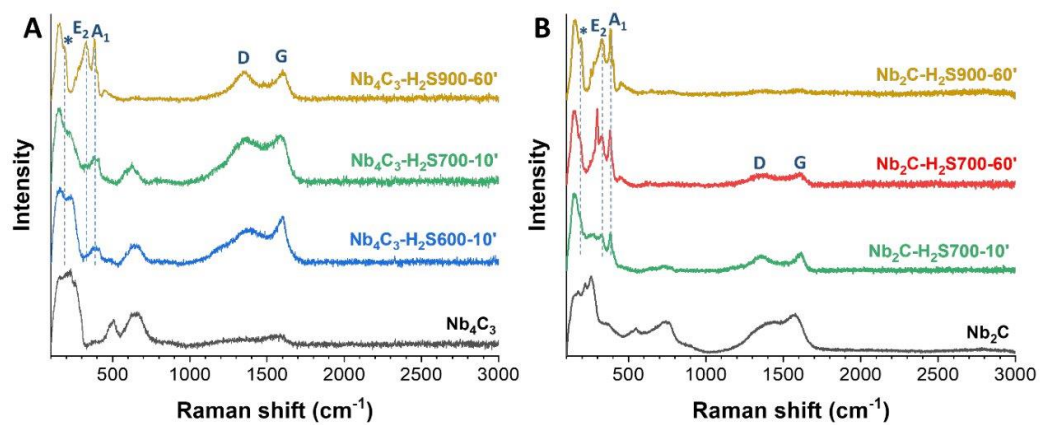


**Figure S9:** Raman spectra of (A) $Nb_4C_3$ and (B) $Nb_2C$ treated with $H_2S$.
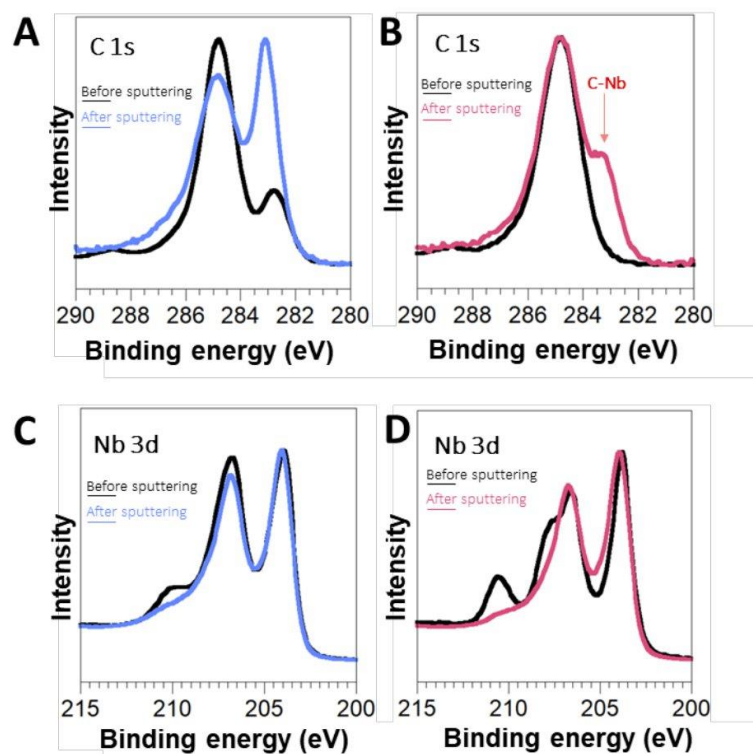
**Figure S10**. Comparison of the X-ray photoelectron spectra of C 1s before and after sputtering for (a) $Nb_4C_3$, and (b) $Nb_4C_3$-S900-60', and Nb 3d for (c) $Nb_4C_3$, and (d) $Nb_4C_3$-S900-60'.
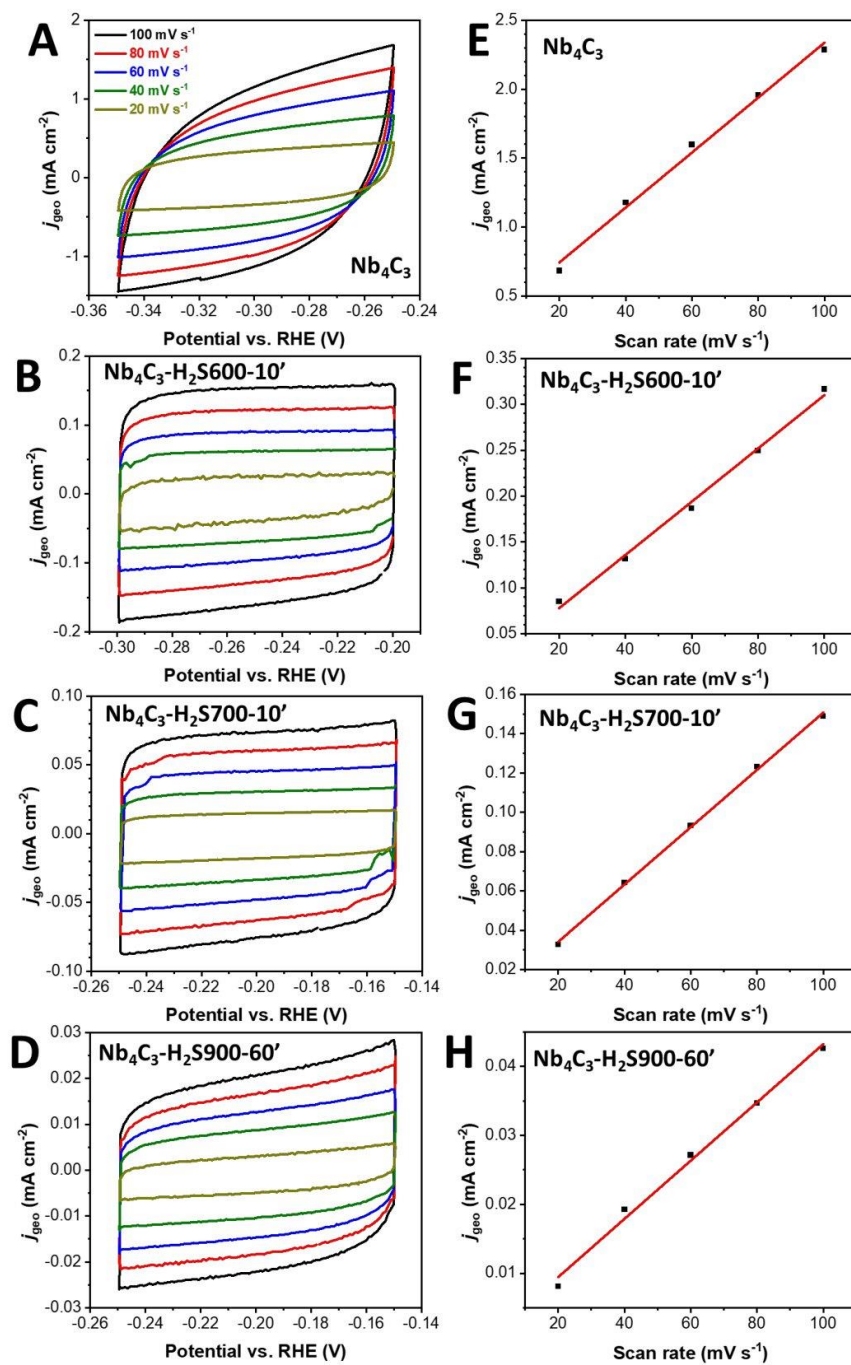
**Figure S11.** EASA of (A,E) $Nb_4C_3$ pristine, (B,F) $Nb_4C_3$-$H_2$S600-10', (C,G) $Nb_4C_3$-$H_2$S700-10', and (D,H) $Nb_4C_3$-$H_2$S900-60'.

## Supporting Tables

**Table S1:** Elemental composition of $Nb_4C_3$ samples after treatment with $H_2/S$ and $H_2S$. Data obtained by energy-dispersive X-ray spectroscopy (EDX) and elemental analysis (CNHSO).

| EDX (at%) | Nb | C | O | F | Al | S |
|---|---|---|---|---|---|---|
| $Nb_4C_3$ | 26±5 | 50±4 | 17±1 | 7±2 | <1 | - |
| $Nb_4C_3$-$H_2$S600-10' | 34±5 | 47±4 | 14±2 | 4±1 | <1 | 2±0 |
| $Nb_4C_3$-$H_2$S700-10' | 27±7 | 53±6 | 13±2 | 3±1 | <1 | 3±2 |
| $Nb_4C_3$-$H_2$S700-60' | 22±5 | 53±8 | 9±3 | <1 | <1 | 13±5 |
| $Nb_4C_3$-$H_2$S900-60' | 19±3 | 48±8 | 3±2 | - | <1 | 32±5 |
| $Nb_4C_3$-S500-10' | 30±5 | 45±4 | 21±8 | 2±1 | 2±3 | - |
| $Nb_4C_3$-S600-10' | 26±8 | 40±11 | 27±10 | - | 3±6 | 4±3 |
| $Nb_4C_3$-S700-10' | 214 | 29±8 | 10±8 | - | 2±3 | 38±8 |
| $Nb_4C_3$-S900-10' | 23±4 | 30±11 | 15±18 | - | 1±1 | 31±14 |
| $Nb_4C_3$-S900-60' | 21±3 | 36±8 | 12±6 | - | 1±1 | 31±6 |
| **EDX (mass%)** | Nb | C | O | F | Al | S |
| $Nb_4C_3$ | 70±6 | 18±3 | 8±1 | 4±1 | <1 | - |
| $Nb_4C_3$-$H_2$S600-10' | 77±4 | 15±3 | 5±1 | 2±1 | <1 | 1±0 |
| $Nb_4C_3$-$H_2$S700-10' | 71±7 | 19±4 | 6±2 | 1±1 | <1 | 3±1 |
| $Nb_4C_3$-$H_2$S700-60' | 60±5 | 19±5 | 4±2 | < 1 | <1 | 12±3 |
| $Nb_4C_3$-$H_2$S900-60' | 52±3 | 17±4 | 1±1 | - | <1 | 30±2 |
| $Nb_4C_3$-S500-10' | 74±4 | 14±2 | 9±4 | 1±0 | 2±2 | - |
| $Nb_4C_3$-S600-10' | 62±19 | 13±6 | 15±13 | 1±1 | 5±14 | 3±2 |
| $Nb_4C_3$-S700-10' | 52±5 | 10±3 | 5±5 | - | 2±3 | 32±4 |
| $Nb_4C_3$-S900-10' | 57±5 | 10±4 | 7±8 | - | 1±1 | 26±11 |
| $Nb_4C_3$-S900-60' | 54±3 | 12±3 | 5±3 | - | 1±0 | 28±3 |
| **CHNS (mass%)** | | C | | | | S |
| $Nb_4C_3$ | | 9.1±0.1 | | | | - |
| $Nb_4C_3$-$H_2$S600-10' | | 8.8±0.1 | | | | 1.0±0.2 |
| $Nb_4C_3$-$H_2$S700-10' | | 8.8±0.1 | | | | 3.3±0.1 |
| $Nb_4C_3$-$H_2$S900-60' | | 4.5±0.1 | | | | 34.7±0.4 |

S10

**Table S2:** Elemental composition of $Nb_2C$ samples after treatment with $H_2S$. Data obtained by energy-dispersive X-ray spectroscopy (EDX) and elemental analysis (CNHSO).

| EDX (at%) | Nb | C | O | F | Al | S |
|---|---|---|---|---|---|---|
| $Nb_2C$ | 26±4 | 30±3 | 38±2 | 5±1 | 2±0 | - |
| $Nb_2C$-$H_2S$700-10' | 26±4 | 39±5 | 23±4 | 2±1 | 2±0 | 9±3 |
| $Nb_2C$-$H_2S$700-60' | 24±5 | 40±6 | 15±6 | <1 | 2±0 | 19±4 |
| $Nb_2C$-$H_2S$900-60' | 22±5 | 36±9 | 7±3 | - | 2±0 | 33±7 |
| **EDX (mass%)** | Nb | C | O | F | Al | S |
| $Nb_2C$ | 68±5 | 10±2 | 18±2 | 3±1 | 1±0 | - |
| $Nb_2C$-$H_2S$700-10' | 67±4 | 13±3 | 10±2 | 2±1 | 1±0 | 8±3 |
| $Nb_2C$-$H_2S$700-60' | 61±4 | 14±3 | 7±3 | <1 | 1±0 | 17±3 |
| $Nb_2C$-$H_2S$900-60' | 55±4 | 12±4 | 3±2 | - | 2±0 | 28±3 |
| **CHNSO (mass%)** | | C | O | | | S |
| $Nb_2C$ | | 4.6±0.2 | 18.2±5.4 | | | - |
| $Nb_2C$-$H_2S$700-10' | | 4.3±0.0 | 10.8±1.7 | | | 8.2±0.2 |
| $Nb_2C$-$H_2S$700-60' | | 3.9±0.0 | | | | 17.4±0.4 |
| $Nb_2C$-$H_2S$900-60' | | 1.9±0.1 | 3.9±0.8 | | | 31.6±0.3 |

**Table S3:** Electrocatalytic performance of various $NbS_2$ morphologies and different MXene types as HER catalysts in aqueous 0.5 M $H_2SO_4$ electrolyte.

| Electrocatalyst | $\eta_{10}$ (mV) | Tafel slope (mV dec$^{-1}$) | Reference |
|---|---|---|---|
| *$Nb_4C_3$-$H_2S900$-60'* | *198* | *122* | *This work* |
| $NbS_2$ nanoflakes | 550 | 103 | [1] |
| $NbS_2$ flake | 420 | - | [2] |
| $NbS_2$ nanoflakes | 221 | 162 | [3] |
| $NbS_2$ | 368 | 119 | [4] |
| $NbS_2$ flake | 453 | 125 | [5] |
| $NbS_2$ nanosheets | 280 | 67 | [6] |
| Few-layer $NbS_2$ nanosheets | 236 | 125 | [7] |
| H-$NbS_2$ crystal platelets | 50 | 30 | [8] |
| 3R-$NbS_2$ | 182 | 97 | [9] |
| $NbS_2$ nanowires | 439 | 95 | [10] |
| 2H-$NbS_2$ | 150 | 140 | [11] |
| 3R-$NbS_2$ | - | 168 | [11] |
| $Mo_2CT_x$ | 189 | - | [12] |
| $Ti_2CT_x$ | 609 | 88 | [12] |
| $Ti_3C_2O_x$ | 190 | 61 | [13] |
| $W_{1.33}C$ (annealed) | 320 | - | [14] |
| $Mo_2C$ nanosheets | 189 | 82 | [15] |
| F-$Ti_2CT_x$ nanosheets | 170 | 100 | [16] |
| $V_4C_3T_x$ | 600 | 168 | [17] |
| $Ti_3C_2T_x$ | 337 | 162 | [18] |
| $Ti_3C_2$ nanofibers | 169 | 97 | [19] |
| $Ti_3C_2T_x$ | 600 | 217 | [20] |
| $V_2CT_x$ | - | 149 | [21] |
| $Ti_3C_2T_x$ | - | 268 | [22] |
| Porous $Ti_3AlC_2$ | 260 | 148 | [23] |
| Porous $Ti_3C_2T_x$ | 220 | 292 | [23] |
| $Nb_2C$ | - | 95 | [24] |
| $Nb_4C_3$ (annealed) | 568 | 114 | [25] |
| $Mo_2TiC_2T_x$ | 280 | 58 | [26] |

## Supporting References

[1]     D. Gopalakrishnan, A. Lee, N. K. Thangavel, L. M. Reddy Arava, *Sustainable Energy Fuels* **2018**, 2, 96.

[2]     L. Najafi, S. Bellani, R. Oropesa-Nuñez, B. Martín-García, M. Prato, V. Mazánek, D. Debellis, S. Lauciello, R. Brescia, Z. Sofer, F. Bonaccorso, *J. Mater. Chem. A* **2019**, 7, 25593.

[3]     X. Zhou, S.-H. Lin, X. Yang, H. Li, M. N. Hedhili, L.-J. Li, W. Zhang, Y. Shi, *Nanoscale* **2018**, 10, 3444.

[4]     C. Huang, X. Wang, D. Wang, W. Zhao, K. Bu, J. Xu, X. Huang, Q. Bi, J. Huang, F. Huang, *Chem. Mater.* **2019**, 31, 4726.

[5]     H. Kumar, K. Wang, F. Tang, X. Zeng, L. Gan, Y. Su, *Int. J. Energy Res.* **2020**, 44, 10551.

[6]     P. Gnanasekar, K. S. Ranjith, P. Manivel, Y.-K. Han, J. Kulandaivel, *ACS Appl. Energy Mater.* **2020**, 3, 6717.

[7]     J. Si, Q. Zheng, H. Chen, C. Lei, Y. Suo, B. Yang, Z. Zhang, Z. Li, L. Lei, Y. Hou, K. Ostrikov, *ACS Appl. Mater. Interfaces* **2019**, 11, 13205.

[8]     Y. Liu, J. Wu, K. P. Hackenberg, J. Zhang, Y. M. Wang, Y. Yang, K. Keyshar, J. Gu, T. Ogitsu, R. Vajtai, J. Lou, P. M. Ajayan, Brandon C. Wood, B. I. Yakobson, *Nat. Energy* **2017**, 2, 17127.

[9]     J. Zhang, J. Wu, X. Zou, K. Hackenberg, W. Zhou, W. Chen, J. Yuan, K. Keyshar, G. Gupta, A. Mohite, P. M. Ajayan, J. Lou, *Mater. Today* **2019**, 25, 28.

[10]     X. Gong, D. Kong, M. E. Pam, L. Guo, S. Fan, S. Huang, Y. Wang, Y. Gao, Y. Shi, H. Y. Yang, *Nanotechnol.* **2019**, 30, 405601.

[11]     J. Yang, A. R. Mohmad, Y. Wang, R. Fullon, X. Song, F. Zhao, I. Bozkurt, M. Augustin, E. J. G. Santos, H. S. Shin, W. Zhang, D. Voiry, H. Y. Jeong, M. Chhowalla, *Nat. Mater.* **2019**, 18, 1309.

[12]     Z. W. Seh, K. D. Fredrickson, B. Anasori, J. Kibsgaard, A. L. Strickler, M. R. Lukatskaya, Y. Gogotsi, T. F. Jaramillo, A. Vojvodic, *ACS Energy Letters* **2016**, 1, 589.

[13]     Y. Jiang, T. Sun, X. Xie, W. Jiang, J. Li, B. Tian, C. Su, *ChemSusChem* **2019**, 12, 1368.

[14]     R. Meshkian, M. Dahlqvist, J. Lu, B. Wickman, J. Halim, J. Thörnberg, Q. Tao, S. Li, S. Intikhab, J. Snyder, M. W. Barsoum, M. Yildizhan, J. Palisaitis, L. Hultman, P. O. Å. Persson, J. Rosen, *Adv. Mater.* **2018**, 30, 1706409.

[15]     A. D. Handoko, K. D. Fredrickson, B. Anasori, K. W. Convey, L. R. Johnson, Y. Gogotsi, A. Vojvodic, Z. W. Seh, *ACS Appl. Energy Mater.* **2018**, 1, 173.

[16]     S. Li, P. Tuo, J. Xie, X. Zhang, J. Xu, J. Bao, B. Pan, Y. Xie, *Nano Energy* **2018**, 47, 512.

[17]     M. H. Tran, T. Schäfer, A. Shahraei, M. Dürrschnabel, L. Molina-Luna, U. I. Kramm, C. S. Birkel, *ACS Appl. Energy Mater.* **2018**, 1, 3908.

[18]     J. Liu, Y. Liu, D. Xu, Y. Zhu, W. Peng, Y. Li, F. Zhang, X. Fan, *Appl. Catal., B* **2019**, 241, 89.

[19]     W. Yuan, L. Cheng, Y. An, H. Wu, N. Yao, X. Fan, X. Guo, *ACS Sustainable Chem. Eng.* **2018**, 6, 8976.

[20]     V. Ramalingam, P. Varadhan, H.-C. Fu, H. Kim, D. Zhang, S. Chen, L. Song, D. Ma, Y. Wang, H. N. Alshareef, J.-H. He, *Adv. Mater.* **2019**, 31, 1903841.

[21]     P. Kuang, M. He, B. Zhu, J. Yu, K. Fan, M. Jaroniec, *J. Catal.* **2019**, 375, 8.

[22]     T. A. Le, Q. V. Bui, N. Q. Tran, Y. Cho, Y. Hong, Y. Kawazoe, H. Lee, *ACS Sustainable Chem. Eng.* **2019**, 7, 16879.

[23]     C. Cui, R. Cheng, C. Zhang, X. Wang, *Chin. Chem. Lett.* **2020**, 31, 988.

[24]     S. Zhang, H. Zhuo, S. Li, Z. Bao, S. Deng, G. Zhuang, X. Zhong, Z. Wei, Z. Yao, J.-g. Wang, *Catal. Today* **2021**, 368, 187.

[25]     Y. Tan, Z. Zhu, X. Zhang, J. Zhang, Y. Zhou, H. Li, H. Qin, Y. Bo, Z. Pan, *International Journal of Hydrogen Energy* **2021**, 46, 1955.

[26]     J. Zhang, Y. Zhao, X. Guo, C. Chen, C.-L. Dong, R.-S. Liu, C.-P. Han, Y. Li, Y. Gogotsi, G. Wang, *Nat. Catal.* **2018**, 1, 985.

## 4.5. Toward MBenes Battery Electrode Materials: Layered Molybdenum Borides for Li-Ion Batteries

Ahmad Majed,[1] Mohammad Torkamanzadeh,[2,3] Chukwudi F. Nwaokorie,[4]

Karamullah Eisawi,[1] Chaochao Dun,[5] Audrey Buck,[1] Jeffrey J. Urban,[5]

Matthew M. Montemore,[4] Volker Presser,[2,3,6] Michael Naguib[1,*]

1    Department of Physics and Engineering Physics, Tulane University, New Orleans, Louisiana 70118, United States of America

2    INM - Leibniz Institute for New Materials, D2 2, 66123, Saarbrücken, Germany

3    Department of Materials Science & Engineering, Saarland University, Campus D2 2, 66123, Saarbrücken, Germany

4    Department of Chemical and Biomolecular Engineering, Tulane University, New Orleans, Louisiana 70118, United States of America

5    The Molecular Foundry, Lawrence Berkeley National Laboratory, Berkeley, California 94720, United States of America

6    saarene - Saarland Center for Energy Materials and Sustainability, Campus C4 2, 66123 Saarbrücken, Germany

*    Corresponding author.

Own contributions:

Investigation, Data curation, Visualization, Writing - Original Draft, Writing - Review & Editing.

# Toward MBenes Battery Electrode Materials: Layered Molybdenum Borides for Li-Ion Batteries

*Ahmad Majed, Mohammad Torkamanzadeh, Chukwudi F. Nwaokorie, Karamullah Eisawi, Chaochao Dun, Audrey Buck, Jeffrey J. Urban, Matthew M. Montemore, Volker Presser, and Michael Naguib\**

Lithium-ion and sodium-ion batteries (LIBs and SIBs) are crucial in our shift toward sustainable technologies. In this work, the potential of layered boride materials (MoAlB and $Mo_2AlB_2$) as novel, high-performance electrode materials for LIBs and SIBs, is explored. It is discovered that $Mo_2AlB_2$ shows a higher specific capacity than MoAlB when used as an electrode material for LIBs, with a specific capacity of 593 mAh g$^{-1}$ achieved after 500 cycles at 200 mA g$^{-1}$. It is also found that surface redox reactions are responsible for Li storage in $Mo_2AlB_2$, instead of intercalation or conversion. Moreover, the sodium hydroxide treatment of MoAlB leads to a porous morphology and higher specific capacities exceeding that of pristine MoAlB. When tested in SIBs, $Mo_2AlB_2$ exhibits a specific capacity of 150 mAh g$^{-1}$ at 20 mA g$^{-1}$. These findings suggest that layered borides have potential as electrode materials for both LIBs and SIBs, and highlight the importance of surface redox reactions in Li storage mechanisms.

## 1. Introduction

Lithium-ion batteries (LIBs), owing to their relatively high energy and power density, are commonly used within portable applications such as mobile phones and laptops. Since Sony started using LIBs in the 1990s,[1] exponential growth in manufacturing batteries reached a current market size of $34.2 billion (USD), which is expected to grow at a compound annual growth rate of 13.0% from 2020 to 2027.[2] Lithium, among other alkali metals, has been studied the most due to its relatively small atomic size, mass, and higher ion mobility, giving batteries with higher energy storage capacity.[3]

2D nanosheets are potentially suitable active materials for hosting ions generally due to their higher surface areas, favorable diffusion kinetics, and higher ion capacities owing to their unique morphology.[4] Transition metal borides (TMBs), such as $MoB_2$, $TiB_2$, $NbB_2$, $ReB_2$, and $OsB_2$, are considered refractory materials because of their high chemical, mechanical, and thermal stability.[5] This family has unique mechanical, electronic, and thermal properties, broadening the range of applications to include tribology,[6] electrochemical energy storage,[7] catalysis,[8] and high-temperature structures in the aerospace industry.[9] Ternary transition metal borides, such as MoAlB, $Cr_2AlB_2$, $Mn_2AlB_2$, and $Fe_2AlB_2$, are considered layered materials with an orthorhombic crystal structure that can be described as blocks of TMB (e.g., MoB and FeB) interleaved by aluminum atoms (double layers of Al in the case of MoAlB, mono layers for the rest).[10]

A. Majed, K. Eisawi, A. Buck, M. Naguib
Department of Physics and Engineering Physics
Tulane University
New Orleans, LA 70118, USA
E-mail: naguib@tulane.edu

M. Torkamanzadeh, V. Presser
INM − Leibniz Institute for New Materials
66123 Saarbrücken, Germany

M. Torkamanzadeh, V. Presser
Department of Materials Science and Engineering
Saarland University
66123 Saarbrücken, Germany

C. F. Nwaokorie, M. M. Montemore
Department of Chemical and Biomolecular Engineering
Tulane University
New Orleans, LA 70118, USA

C. Dun, J. J. Urban
The Molecular Foundry
Lawrence Berkeley National Laboratory
Berkeley, CA 94720, USA

V. Presser
saarene − Saarland Center for Energy Materials and Sustainability
66123 Saarbrücken, Germany

**ADVANCED
SCIENCE NEWS**

www.advancedsciencenews.com

**small
methods**

www.small-methods.com

MBene is a term derived from MXene (M: early transition metal, X: C and/or N), given their similarities to graphene from morphological and high electrical conductivity aspects,[11,12] with one change where X is boron.[13] Combining first-principles density functional method and crystal structure prediction techniques, Bo et al. reported a group of hexagonal 2D MBenes, transition metal borides such as $Sc_2B_2$, $Ti_2B_2$, $Y_2B_2$, $Zr_2B_2$, and $Mo_2B_2$, that are predicted to have good stability and excellent electronic conductivity.[14] It was also predicted that MBenes like $V_2B_2$, $Cr_2B_2$, $Mn_2B_2$, $Mo_2B_2$, and $Fe_2B_2$ have promising performance as electrode materials in LIBs and/or sodium-ion batteries.[12,15] $Mo_2B_2$ and $Fe_2B_2$ were predicted to have low omnidirectional diffusion energy barriers and high specific capacity for Li atoms.[12]

In the Mo–B binary phase diagram, Mo borides have many possible compositions, such as $Mo_2B$, $MoB$, $MoB_2$, $Mo_2B_5$, and $MoB_4$.[16] For $MoB$, there are two possible phases: tetragonal $\alpha$-MoB ($I4_1/amd$, $Z = 8$) and orthorhombic $\beta$-MoB (Cmcm, $Z = 4$). However, $\beta$-MoB was found to be slightly less stable than $\alpha$-MoB, which explains why $\beta$-MoB can only be synthesized at low temperatures.[16] Similar to the synthesis of MXenes from MAX phases using selective etching of the A element layer,[17] in principle, 2D $\beta$-MoB nanosheets can be realized by the selective etching of Al from MoAlB at relatively low temperatures to maintain the structure of the MoB building blocks. Using ab initio calculations, Guo et al. reported that 2D $Mo_2B_2$ with van der Waals bonding between the atomic layers could be achieved through selective etching of the single Al layer from $Mo_2AlB_2$, which could be a potential MBene precursor.[12] However, since $Mo_2AlB_2$ is metastable, one has to start with MoAlB (despite having double Al layers) as it is the only stable phase that can be obtained by a solid-state synthesis in the Mo–Al–B ternary phase diagram.[18]

Partial etching of MoAlB was first reported in 2017, where the powdery sample was stirred in NaOH solutions of different concentrations (10% and 30%), etching times (24 and 72 h), and temperatures (room temperature and 70 °C).[19] The best results were achieved by stirring MoAlB in 10% NaOH at room temperature for 24 h. The effects of concentration and etching time were not significant, while raising the etching temperature to 70 °C or replacing the etchant with 48% HF caused significant corrosion.[19] After the NaOH treatment, it was observed that Al was etched out of the surface of the particles only, as the formed $MoAl_{1-x}B$ hinders further etching. To obtain crystalline $Mo_2AlB_2$,[20] the already NaOH-treated MoAlB powders were pressed, vacuum-sealed into quartz ampules, and then heated to 600 °C for 4.5 h; the heating cycle was ended by quenching since $Mo_2AlB_2$ is metastable.[20] Alameda et al. also reported that using 2 M LiF and 6 M HCl at room temperature results in similar outcomes to using 10% NaOH.[21] Through optimization of the synthetic parameters, Kim et al. reported a phase-pure $Mo_2AlB_2$ by etching MoAlB in 3 M LiF and 10 M HCl at 40 °C for 48 h, though they did not further explore the conversion of $Mo_2AlB_2$ into 2D MBene.[22]

As outlined above, the etching and exfoliating MAB phases into 2D MBenes have been shown to be synthetically elusive,[21,23] hence the scarce experimental reports on their applications.[24] While general aspects of $Mo_2AlB_2$ synthesis and the resulting partially-etched species were investigated in past works, their actual use for Li-ion batteries has remained unexplored. In this study, we report synthesizing single-phase $Mo_2AlB_2$ and its electrochemical performance as electrode materials for Li-ion and Na-ion batteries for the first time. At a specific current of 20 mA $g^{-1}$, a specific capacity of 380 mAh $g^{-1}$ (corresponding to 2.7 Li per 1 $Mo_2AlB_2$) was achieved. The lithiation and delithiation mechanisms were studied through X-ray photoelectron spectroscopy (XPS) to confirm the intrinsic electrochemical properties of the structure in our study.

## 2. Results and Discussion

The MoAlB structure can be viewed as $Mo_2B_2$-2Al-$Mo_2B_2$, where each $Mo_2B_2$ atomic layer is interleaved with double zigzag Al layers while $Mo_2AlB_2$ has only one Al layer, as shown in the schematic view in **Figure 1**a. The solid-state synthesis of MoAlB was confirmed by comparing the X-ray diffractogram in Figure 1b to the reflections predicted for MoAlB (PDF#01-072-1277). The as-synthesized MoAlB pellet was pulverized into powders, poured into HF acid, stirred at 45 °C for 48 h, washed with de-ionized water, and dried using vacuum-assisted filtration to obtain $Mo_2AlB_2$. Energy dispersive X-ray spectroscopy (EDS) of the treated sample showed Mo:Al to be 2:1 (atomic ratio) after etching, indicating 50% Al reduction. To confirm the topochemical transformation of MoAlB into $Mo_2AlB_2$, XRD patterns of the two samples were collected. As shown in Figure 1b, a significant change in the structure is noticed. The inset of Figure 1b shows the (020) reflection shift due to etching from 12.6° ($2\theta$) to 13.8° ($2\theta$), indicating a reduction in $d$-spacing from ≈7.0 to 6.4 Å and removal of an Al layer, which was also reported in the previous literature.[19–22,25] Alameda et al.[20] utilized annular dark-field in the scanning transmission electron microscope to investigate the structural transformation from MoAlB to $Mo_2AlB_2$. Their findings indicated that the double Al layers are reduced to a singular layer upon etching, and that the layered structure is made of $[Al-(Mo_2B_2)]_n$ blocks. The researchers also observed that the nanolaminate sheets have varying thicknesses ranging from 1 to 3 unit cells of $Mo_2AlB_2$, with the majority of the sheets having a thickness of 1 unit cell (≈1.3 nm). Figure 1c shows a scanning electron micrograph of $Mo_2AlB_2$, revealing accordion-like flakes with a layered morphology similar to MXenes.[17]

From previous literature, particle size selection was reported to affect etching quality.[20,26] Therefore, we separated the precursor MoAlB sample sizes into two ranges, namely, small (≤10 μm) and large (10 to 45 μm) particles. Results after applying HF treatment to both samples can be found in Figure S1 and Table S1, Supporting Information. The larger particle size range showed a larger shift in the (020) peak in Figure S1a, Supporting Information, less Al% content in the EDS results, higher mass loss of 30% for (10 to 45 μm) and 15% for (≤10 μm), and an accordion-like morphology, Figure S1c, Supporting Information. Therefore, larger particles (10 to 45 μm) are expected to have a better etching response from the HF treatment etching compared to smaller (≤10 μm) particles. This could be due to the easier passivation of smaller particles,[27] or due to the higher reactivity of smaller particles with larger surface area raising the possibility that they are etched then dissolved completely in HF, which can be observed during the washing step when a dark purple colored solution appears, indicating the existence of $Mo^{3+}$ in the solution. The lower mass loss of particles ≤10 μm suggests a combined mechanism
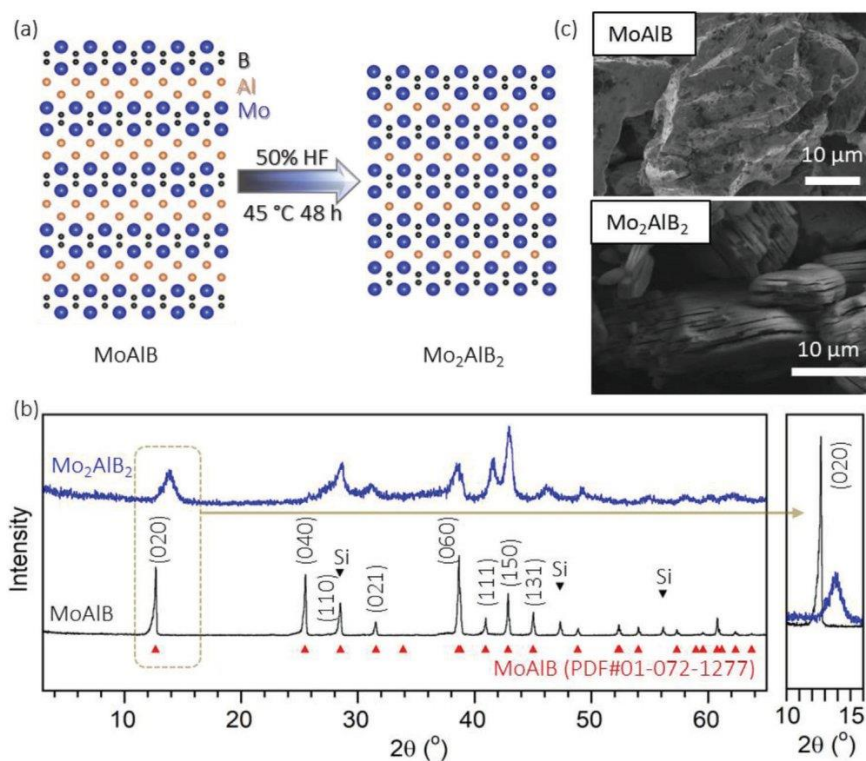
**ADVANCED
SCIENCE NEWS**

www.advancedsciencenews.com

**small
methods**

www.small-methods.com

**Figure 1.** From MoAlB to $Mo_2AlB_2$: a) Schematic for the structural evolution of $Mo_2AlB_2$ from MoAlB. b) X-ray diffractograms of MoAlB before and after HF treatment. Si was added as an internal reference for the peak position. c) Scanning electron micrograph of MoAlB before and after etching.

where small particles become passivated or fully etched. From these results, we can recommend using size selection to target larger particles before etching to narrow the particle size distribution and increase the etching efficiency. For further tests in this study, we focused on the (10 to 45 μm) sample. After etching, we milled the $Mo_2AlB_2$ powder (scanning electron micrographs are shown in Figure S2, Supporting Information) to explore the milling effect on the electrochemical performance.

The electrochemical behavior of $Mo_2AlB_2$ as an electrode material for LIBs is shown in **Figure 2** and Figures S3–S7, Supporting Information, and for Na-ion batteries (SIBs) the electrochemical behavior is shown in Figure S8, Supporting Information. The cyclic voltammograms of MoAlB and $Mo_2AlB_2$ at 0.2 mV s$^{-1}$ scan rate in Figure 2a show a significant difference. Specifically, there are two redox pairs at (0.39 and 0.45 V) versus Li/Li$^+$ and (1.25 and 1.52 V) versus Li/Li$^+$ appearing after HF etching, indicating that more electroactive species existed. The redox peaks of the electrodes before etching were at potentials below 0.1 V versus Li/Li$^+$, which are related to the activated carbon suggesting that MoAlB is not electrochemically active.[28] The redox peak positions in the cyclic voltammograms after milling remained unchanged. Figure S3, Supporting Information, shows the first four cycles in milled $Mo_2AlB_2$. The first discharge had relatively more peaks due to irreversible reactions and likely the formation of solid electrolyte interphase (SEI). Potentiostatic electrochemical impedance spectroscopy (PEIS) of MoAlB, $Mo_2AlB_2$,

and milled $Mo_2AlB_2$ are shown in Figure S4a, Supporting Information, along with their fits. The circuit used in fitting the PEIS data is shown in Figure S4c, Supporting Information. Etching appeared to reduce the charge transfer resistance $R_{ct}$ from 3.9 to 3.2 mΩ cm$^2$ without significantly affecting the system resistance $R_s$ from 0.64 (MoAlB) to 0.7 mΩ cm$^2$ ($Mo_2AlB_2$). Etching also reduced the slope of the straight line at the lower frequency region, indicating a more diffusion-limited regime is accessed, which agrees with the results from the $b$-value. Milling $Mo_2AlB_2$ showed more deviation toward the diffusion regime with a slight increase in the resistances $R_s = 1.1$ mΩ cm$^2$ and $R_{ct} = 3.9$ mΩ cm$^2$.

A range of scan rates (namely, 0.1, 0.2, 0.5, 1.0, and 2.0 mV s$^{-1}$), was tested for the electrodes before etching, after etching, and after milling of the etched material (Figure S3a–c, Supporting Information). Higher current values are usually observed for faster scan rates due to the decrease in the size of the diffusion layer.[29] In $Mo_2AlB_2$, the minimum peak-to-peak separation was 0.13 V for 0.1 mV s$^{-1}$ while the maximum value was 0.55 V for 2 mV s$^{-1}$, which may indicate a decrease in reversibility for faster scan rates.[29] The general relationship between peak current and scan rate is given by $i_p = av^b$ where $a$ and $b$ are adjustable parameters.[30] The $b$-value can range from ($b = 0.5$) if the electrochemical reaction is limited by semi-infinite diffusion to ($b = 1$) if the current is interface-controlled (typical for capacitive and pseudocapacitive systems).[31–33] Recording the upper peak

**ADVANCED
SCIENCE NEWS**

www.advancedsciencenews.com

**small
methods**

www.small-methods.com
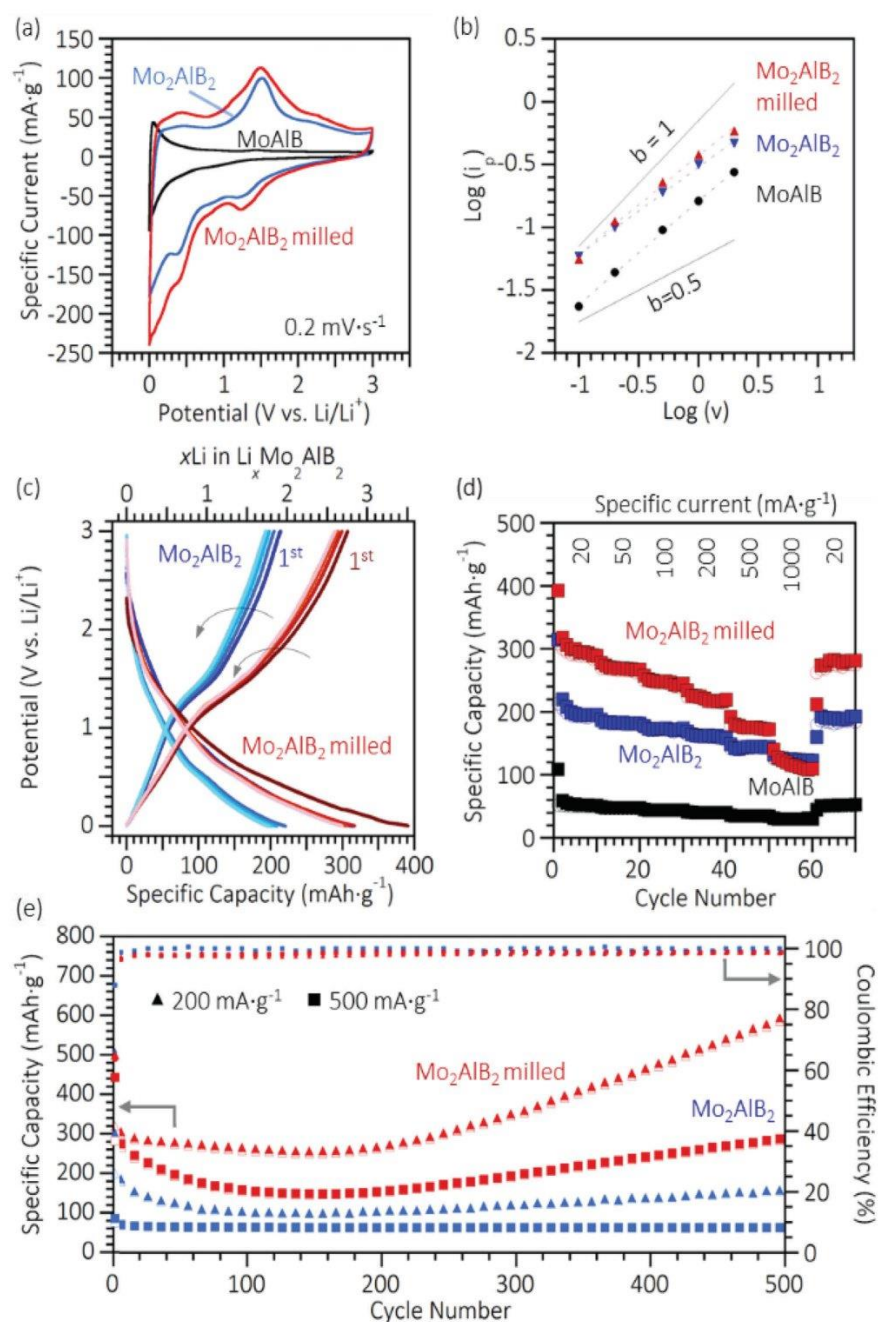
**Figure 2.** Electrochemical analysis. a) Cyclic voltammetry of MoAlB, $Mo_2AlB_2$ before and after milling at 0.2 mV s$^{-1}$ scan rate. b) $b$-value $\log(i_p)$–$\log(v)$ plot of voltammograms of MoAlB, $Mo_2AlB_2$, and milled $Mo_2AlB_2$ tested at scan rates 0.1–2.0 mV s$^{-1}$. c) Voltage profile of milled versus non-milled $Mo_2AlB_2$ for the first five cycles at specific current 20 mA g$^{-1}$. d) Rate handling capability of MoAlB, $Mo_2AlB_2$, and $Mo_2AlB_2$ milled at specific currents of 20–1000 mA g$^{-1}$. e) Cycling stability of non-milled and milled $Mo_2AlB_2$ at specific currents of 200 and 500 mA g$^{-1}$.

**ADVANCED
SCIENCE NEWS**
www.advancedsciencenews.com

**small
methods**
www.small-methods.com

current values from each profile, we plotted log ($i_p$) versus log ($v$), as shown in Figure 2b. After linear fitting, the $b$ value for MoAlB, $Mo_2AlB_2$, and milled $Mo_2AlB_2$ was 0.82, 0.70, and 0.78, respectively.

The voltage profile before and after milling is shown in Figure 2c, where the coin cell was cycled at 20 mA g$^{-1}$ and the first five cycles of each $Mo_2AlB_2$ (blue profile) and $Mo_2AlB_2$ milled (red profile). Both samples plateaued at ≈1.2 (discharge) and ≈1.5 V (charge) versus Li/Li$^+$, which agrees with results obtained from cyclic voltammograms in Figure 2a. A specific capacity of 380 mAh g$^{-1}$ (3.5 Li per $Mo_2AlB_2$) was obtained in the first cycle of milled $Mo_2AlB_2$, which is 19% higher than the unmilled ones storing 320 mAh g$^{-1}$ (2.8 Li per $Mo_2AlB_2$). By the fifth cycle, milled $Mo_2AlB_2$ had a 55% higher capacity of about 310 mAh g$^{-1}$ (2.7 Li) compared to the unmilled sample with a capacity of 200 mAh g$^{-1}$ (1.7 Li). Although the specific capacity of $Mo_2AlB_2$ has not been reported before, the $Mo_2B_2$ structure has been theoretically predicted to have a specific capacity of 444 mAh g$^{-1}$, corresponding to 4 Li per $Mo_2B_2$. The difference between our reported values and the theoretical values of $Mo_2B_2$ could be attributed to the incomplete removal of Al as singular Al layers exist in the $Mo_2AlB_2$ structure.[12]

The rate handling was carried out at specific currents of 20–1000 mA g$^{-1}$ for MoAlB, $Mo_2AlB_2$, and $Mo_2AlB_2$ milled in Figure 2d. In the first cycle, milled $Mo_2AlB_2$ had a specific capacity about four times higher than MoAlB. The specific capacity for MoAlB was generally low (40–50 mAh g$^{-1}$) in all tested specific currents. On the other hand, the capacity increased 230% and 300% for $Mo_2AlB_2$, and milled $Mo_2AlB_2$, respectively. At 20 mA g$^{-1}$, milling the sample before testing increased the capacity 50%. The milling effect appeared to fade for higher specific currents until it vanished at a rate of 1000 mA g$^{-1}$.

Exploring the cycling stability of $Mo_2AlB_2$ in Figure 2e, we tested $Mo_2AlB_2$ before and after milling at specific currents of 200 and 500 mA g$^{-1}$. The first discharge specific capacity of the non-milled sample was 302 and 83 mAh g$^{-1}$ for specific currents 200 and 500 mA g$^{-1}$, respectively. At 200 mA g$^{-1}$, a minimum specific capacity was reached after 100 cycles; however, the capacity increased gradually with cycling reaching a specific capacity of 156 mAh g$^{-1}$ after 500 cycles. Milling $Mo_2AlB_2$ had a beneficial effect on the specific capacity. For 200 and 500 mA g$^{-1}$ cells, the first discharge specific capacities of milled $Mo_2AlB_2$ were 496 and 441 mAh g$^{-1}$, respectively, which are 1.6- and 5.0-times higher than their respective non-milled. Coulombic efficiency for the first cycle was 68%, and after 20 cycles, it was maintained at >99%. After 500 cycles, the difference in capacity between milled and non-milled $Mo_2AlB_2$ was significant and noticeable. The specific capacities of the milled ones were 594 and 283 mAh g$^{-1}$ at 200 and 500 mA g$^{-1}$, respectively, which are 281% and 342% higher than the non-milled ones. The increase in specific capacity due to milling can be attributed to the decrease in average particle size, thereby increasing the accessible surface area and enabling more electrochemically active sites to store Li. The specific capacity values of milled $Mo_2AlB_2$ are close to that of MXenes and commercial graphite in LIBs (372 mAh g$^{-1}$). However, further studies to completely etch out the aluminum layer, will potentially increase the capacity.[3] The cycling-induced capacity enhancement was reported in previous literature.[34–39] Several reasons have been proposed to explain the anomalous ca-

pacity increase with cycling, including improved electrolyte wettability and creation of more accessible paths for shorter Li$^+$ ion migration,[34,35] the formation/decomposition of an electrolyte-derived surface layer, the possibility of additional charge storage at sharp interfaces between electronic and ionic sinks, redox reactions of Li-containing species, unconventional activity of structural defects, and metallic-cluster like Li storage.[38] Experimental evidence suggest that the reversible formation/decomposition of lithium oxide plays a major in the enhanced capacity upon long cycling.[39] However, further studies are needed to fully understand the reason behind this capacity increase in $Mo_2AlB_2$ system. To shed light on the Li storage mechanism within $Mo_2AlB_2$, we used ex situ XRD before and after lithiation. The electrode was galvanostatically lithiated by discharging from open circuit potential to 1 mV versus Li/Li$^+$ at a specific current of 10 mA g$^{-1}$, then maintained at 1 mV until disassembly; the voltage profile of the half cycle is shown in **Figure 3**a. The X-ray diffractogram after lithiation, in Figure 3b, shows no significant change in the (0l0) peak compared to the one before lithiation, suggesting that the storage mechanism is not likely to be intercalation. Furthermore, the absence of new reflections eliminates the possibility of a conversion reaction. The particles within the lithiated sample appeared to maintain their morphology without swelling, as shown in the scanning electron micrograph (inset, Figure 3a).

To investigate whether the higher performance of $Mo_2AlB_2$ compared to MoAlB was related intrinsically to $Mo_2AlB_2$, not just due to oxides that might evolve during etching, we oxidized our material using rapid thermal annealing (RTA) by heating at 900 °C for 30 s in air. Figure S9a, Supporting Information, shows post-RTA XRD where $MoO_2$ (PDF#00-032-0671) and $MoO_3$ (PDF#00-067-0476) were observed, in addition to the significant unoxidized $Mo_2AlB_2$. If the performance were related to the oxides, it would be intuitive to assume that having more oxides would enhance the electrochemical performance and amplify the redox peaks. However, post-RTA cyclic voltammetry (CV) (Figure S9b, Supporting Information) revealed a cyclic voltammogram profile that can be distinguished from $Mo_2AlB_2$ where three redox pairs were observed at (0.20 and 0.42 V), (1.25 and 1.42 V), and (1.54 and 1.72 V) versus Li/Li$^+$ which are related to both $MoO_2$ and $MoO_3$.[40,41] The specific capacity decreased after oxidation; this suggests that plausible surface oxides are not responsible for the capacity we measured for $Mo_2AlB_2$.

We utilized XPS to explore the material's bonding and surface chemistry and probe changes, if any, in the oxidation state of Mo due to electrochemical cycling. The results are shown in Figure 3c and Table S2, Supporting Information. Four samples were used for the XPS study, namely, i) MoAlB before etching, ii) $Mo_2AlB_2$ electrode before lithiation (MoAlB after HF etching), iii) $Mo_2AlB_2$ electrode after lithiation, and iv) $Mo_2AlB_2$ electrode after delithiation. In the Mo 3d spectra, a low binding energy peak at 228.0 eV that was observed in i) MoAlB can be assigned the $3d_{5/2}$ of Mo–Al–B.[42] Other Mo $3d_{5/2}$ peaks were observed at 229.5, 232.0, and 233.4 eV can be attributed to Mo(IV), Mo(V), and Mo(VI), respectively.[43] HF etching appeared to shift the Mo–Al–B $3d_{5/2}$ peak to a higher binding energy of 228.4 eV, which could be attributed to the higher oxidation state of molybdenum after etching, similar to what was observed for MXenes.[44,45] The Mo–Al–B $3d_{5/2}$ peak was observed at 227.8 eV for iii) fully lithiated (half cycle), and 228.2 eV for iv) fully lithiated and
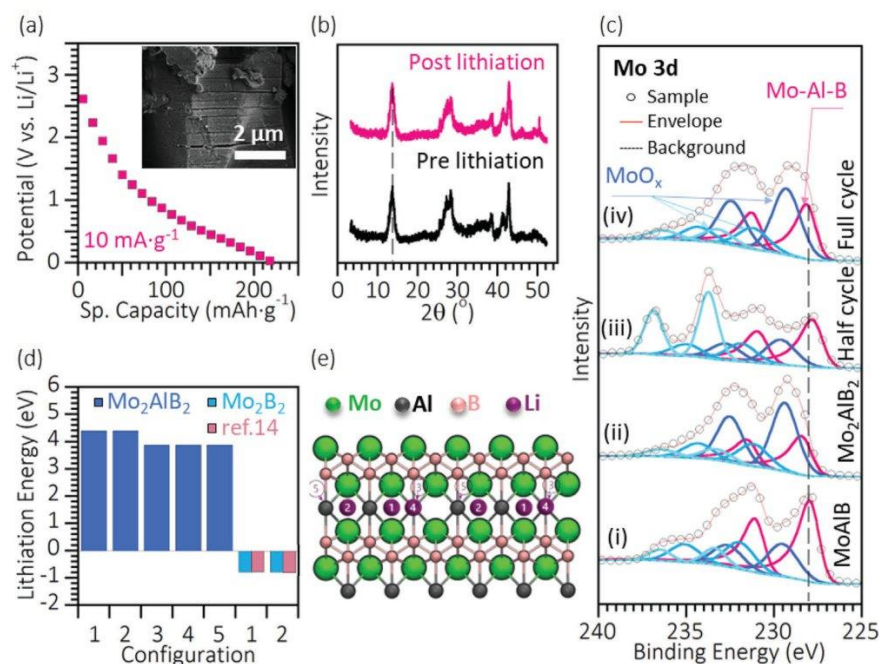
**ADVANCED
SCIENCE NEWS**
www.advancedsciencenews.com

**small
methods**
www.small-methods.com

**Figure 3.** $Mo_2AlB_2$ lithiation. a) Voltage profile of $Mo_2AlB_2$ wafer during discharge at 10 mA g$^{-1}$ with inset scanning electron micrograph of $Mo_2AlB_2$ after lithiation. b) X-ray diffractograms before and after lithiation. c) XPS analysis of molybdenum spectrum for i) MoAlB, $Mo_2AlB_2$ electrode ii) before cycling, iii) half cycle, and iv) full cycle. d) DFT-calculated lithiation energies for varying Li configurations for $Mo_2AlB_2$ and $Mo_2B_2$ shown in (e) where the atomic structure of $Mo_2AlB_2$ is shown with the different configurations where Mo = Green, Al = Black, B = Pink, and Li = Purple. More details about the atomic structure and Li configurations of $Mo_2AlB_2$ and $Mo_2B_2$ are shown in Figure S11, Supporting Information.

delithiated (full cycle). The lower binding energy of Mo-Al-B $3d_{5/2}$ in the half cycle (after fully lithiated) suggests that $Mo_2AlB_2$ is reduced by Li. This is direct evidence that $Mo_2AlB_2$ is contributing to Li storage. The Mo–Al–B $3d_{5/2}$ peak for the full-cycle sample partially recovered as it was shifted to a relatively higher binding energy (viz., higher oxidation state) compared to the half-cycle one, where 33% of the shift in binding energy was irreversible. This agrees with our electrochemical results of $Mo_2AlB_2$ in Figure 2d, showing irreversibility in the first cycle from 300 to 200 mAh g$^{-1}$. This irreversibility could be due to Li reaction with surface terminations or etching products. A summary of the XPS findings for Mo 3d can be found in Table S2, Supporting Information, in addition to C 1s, B 1s, Al 2p, O 1s, F 1s, and Li 1s high-resolution spectra shown in Figure S10, Supporting Information. From these results, we can conclude that the electrochemical performance observed in this study is intrinsic and related to the reversible redox reaction of Li with $Mo_2AlB_2$ surface according to the following reaction: $Mo_2AlB_2 + yLi^+ + ye^- \longleftrightarrow Li_yMo_2AlB_2$. Associating the higher Li storage with the milled sample suggests that Li was stored only at the surface of the particles. With milling, the particle size decreased, and relatively more surfaces were available to interact with lithium. To observe the effect of etching and milling treatments on the specific surface area (SSA) of MoAlB via nitrogen gas sorption analysis, as provided in Figure S12 and Table S3, Supporting Information. Although the SSA values are low for all samples (1–13 m$^2$ g$^{-1}$), HF-etching raised the SSA values from 1 to 7 m$^2$ g$^{-1}$. Further-

more, milling $Mo_2AlB_2$ resulted in an increase of the SSA from 7 to 13 m$^2$ g$^{-1}$.

To gain more insights into why Li does not intercalate in $Mo_2AlB_2$ and is rather stored through surface redox, we carried out ab initio calculations. In the selection and use of MAB phases as electrode materials, the lithiation energy $\Delta E_{Li}$ is a vital criterion for estimating the performance and the charge storage mechanism.[46] Therefore, we used DFT to calculate the lithiation energy into the bulk of $Mo_2AlB_2$. The structures in Figure 3e show the lowest energy configurations of both the pristine $Mo_2AlB_2$ and lithiated $Mo_2AlB_2$. Our calculated lattice parameters were $a = 3.06$ Å, $b = 11.5$ Å, and $c = 3.18$ Å, which match well with previous experimental work.[20] We tested five different intercalation configurations to find the most stable, as shown in Figure 3d. Our results indicate that Li is the most stable in the Al layer. In all these sites, the Li intercalation energy is positive (>3.8 eV), indicating that the Li atom is quite unstable. As a comparison, we also performed calculations for Li intercalation into $Mo_2B_2$, which has been studied previously. For $Mo_2B_2$, we calculate an intercalation energy of −0.77 eV, in agreement with previous work.[14,47] Therefore, intercalation into bulk $Mo_2AlB_2$ is more than 4 eV less favorable than $Mo_2B_2$. This suggests that intercalation into the bulk is unlikely to occur, in agreement with the XRD findings on the lithiated material.

Since Li storage is mostly due to the redox process at the surface of the layered borides and increasing the surface area by milling of $Mo_2AlB_2$ results in higher specific capacity, it is

**ADVANCED
SCIENCE NEWS**

www.advancedsciencenews.com
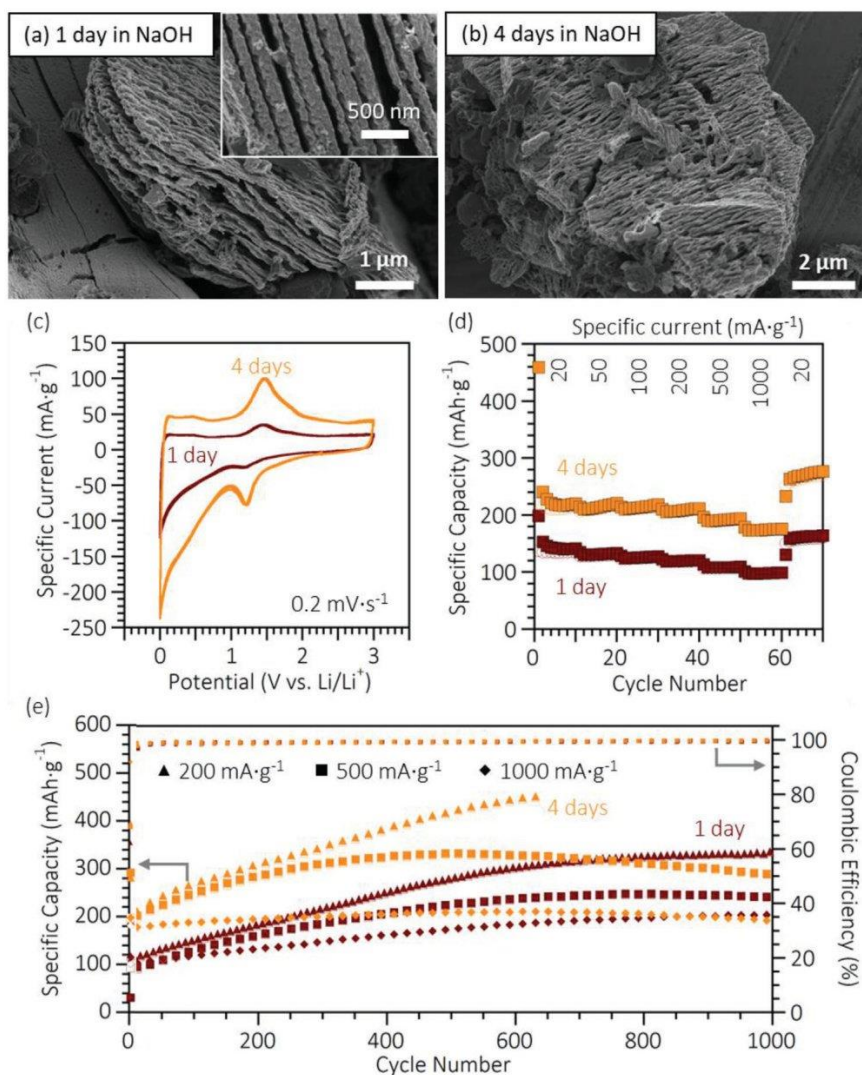
**small
methods**

www.small-methods.com

**Figure 4.** MoAlB + NaOH Scanning electron micrographs of MoAlB treated with NaOH for a) 1 and b) 4 days. Effect of NaOH treatment on the electrochemical behavior of MoAlB showing c) cyclic voltammograms of samples etched for 1 (brown color) and 4 days (orange color) at a 0.2 mV s$^{-1}$ scan rate. d) Rate capability at specific currents of 20–1000 mA g$^{-1}$. e) Cycling stability at 200, 500, and 1000 mA g$^{-1}$.

reasonable to hypothesize that increasing the Li-accessible surface in MoAlB will have a similar effect to the etching and milling process in Mo$_2$AlB$_2$. Previous studies reported the effect of NaOH on MoAlB.[19–21] NaOH treatment was observed to etch the surface of MoAlB particles by removing the aluminum and forming Mo$_2$AlB$_2$ on the surface with a MoAlB core.[20] Hence, we utilized NaOH to form Mo$_2$AlB$_2$ surfaces and increase the SSA of MoAlB, as provided in Figure S12 and Table S3, Supporting Information. After treating MoAlB with NaOH for 1 and 4 days, the EDS analysis in Table S4, Supporting Information, showed a decrease in the Al content as the Mo:Al ratio changed from ≈1.0:1.0 to 1.0:0.8 after 1 day, and 1.0:0.7 after 4 days. A significant increase was noticed upon etching of the parent MoAlB

that has only 1 m$^2$ g$^{-1}$ SSA to 4 m$^2$ g$^{-1}$ for the 1 day-etched and to 11 m$^2$ g$^{-1}$ for the 4 days-etched samples.

The X-ray diffractograms, shown in Figure S13, Supporting Information, revealed no peak shift. However, a significant asymmetric broadening to higher $2\theta$ was observed, particularly in the early (020) peak, which could be attributed to double peaks (MoAlB and Mo$_2$AlB$_2$) or anisotropic strain. The emergence of shoulders and peak broadenings, which are observed in most of the peaks, are more pronounced upon longer NaOH treatment compared to that of parent MoAlB, in agreement with previous reports.[20] After NaOH treatment, scanning electron micrographs (**Figure 4**) show layered porous morphology. Since the formation of Mo$_2$AlB$_2$ on the surface of MoAlB is a self-limiting

process, little visible difference can be observed from scanning electron micrographs of 1 day or 4 days treated samples. However, the distinction manifests itself in EDS (reduction of Al content) and XRD analyses outlined above. The particles were observed to be corrugated due to NaOH treatment. The layers were spaced out, and the surface roughness increased. We believe that both effects have a positive contribution to electrochemical activity.

Figure 4 shows the CVs of MoAlB treated in NaOH for 1 day and 4 days. Both voltammograms show redox peaks at (1.2 and 1.5 V); comparable to redox peaks for HF-etched $Mo_2AlB_2$ in Figure 2. PEIS of 1 day versus 4 days NaOH-treated MoAlB are shown in Figure S4b, Supporting Information, where the circuit used for fitting is shown in Figure S4c, Supporting Information. We observed that for 1 and 4 days, $R_s$ was 0.11 and 0.06 mΩ cm$^2$, respectively. For the charge transfer resistance, $R_{ct}$, was 4.5 and 4.1 mΩ cm$^2$ for 1 day and 4 days, respectively. The longer treatment appeared to reduce the system and charge transfer resistance. Recording the upper peak current values from each profile, we plotted log ($i_p$) versus log ($v$), as shown in Figure S4d, Supporting Information. After linear fitting, the $b$-values for MoAlB before and after NaOH treated for 1 day and 4 days were 0.82, 0.82, and 0.85, respectively. The rate handling capability in Figure 4d shows a significant increase in specific capacity after treating for 4 days, compared to 1 day. A specific capacity of 460 mAh g$^{-1}$ was achieved in the first discharge cycle of the 4 days sample, which is more than double the capacity of the 1 day sample. At 20 mA g$^{-1}$, HF-treated samples appeared to have a higher specific capacity. However, at a higher specific current of 1000 mA g$^{-1}$, the 4 days NaOH-treated sample exceeded both the milled and non-milled HF-treated samples. NaOH-treated samples showed a slight loss in the specific capacity by doubling the specific current from 500 to 1000 mA g$^{-1}$. In addition, the specific capacity appeared to increase with the ten cycles under constant specific current, especially when comparing the samples when cycled at 20 mA g$^{-1}$ at the beginning and the end of the test.

The cycling stability of NaOH-treated samples, shown in Figure 4e, confirms the significantly enhanced specific capacity. The electrodes were cycled at specific currents of 200, 500, and 1000 mA g$^{-1}$. After 500 cycles, the specific capacity of the 4 days NaOH treated sample was 420, 332, and 209 mAh g$^{-1}$ for cells tested under specific currents of 200, 500, and 1000 mA g$^{-1}$, respectively. The 1 day NaOH treated sample showed 280, 225, and 174 mAh g$^{-1}$ for the same respective specific currents. At 500 mA g$^{-1}$, both NaOH-treated samples have higher specific capacity than the non-milled HF-treated samples; however, not as high as the milled HF-treated samples.

Due to the abundance and low cost of sodium, SIBs are explored as a more sustainable alternative to LIBs. Hence, we incorporated our material into SIBs to test their performance, as shown in Figure S8, Supporting Information. The cyclic voltammogram (Figure S8a, Supporting Information) from cycling at 0.1 mV s$^{-1}$ for 20 cycles shows that the redox peaks shifted significantly to lower values <1 V versus Na/Na$^+$. However, the capacity gradually decreased with more cycling. Rate capability was also tested at the same specific currents as before (Figure S8b, Supporting Information). The maximum capacity was 150 mAh g$^{-1}$ at 20 mA g$^{-1}$, gradually decreasing with higher specific currents. The electrode showed good capacity retention when tested

at 20 mA g$^{-1}$ again after cycling at higher rates. Figure S8c, Supporting Information, shows the voltage profile of the first five cycles of Figure S8b, Supporting Information, where the capacity started low then gradually increased with more cycling. The measured specific capacity corresponds to 1 Na per $Mo_2AlB_2$ formula unit. Although the capacity values reported for the SIB are not as high as that for the LIB, the results confirm the feasibility of storing both Li and Na in layered molybdenum borides.

Based on the experimental work we presented, it was found that the as-furnaced MoAlB has low SSA (Figure S12 and Table S3, Supporting Information) and low specific capacity (Figure 2). Etching MoAlB either by HF or NaOH increased the SSA (Figure S12 and Table S3, Supporting Information) and electrochemical performance, Figures 2 and 4). Although increasing the electroactive surface area may facilitate side reactions like SEI formation, studies show it can improve battery performance.[48] Among the etched samples, NaOH-treated MoAlB (4 days) and HF-etched-milled MoAlB exhibited high SSAs, $b$-values, capacitive contribution percentages, and, consequently, high energy storage capacities.

Structurally, HF-etching fully transformed MoAlB to $Mo_2AlB_2$, as shown in Figure 1. NaOH treatment was less aggressive than HF acid. It was enough to etch only the surface of MoAlB particles and form $Mo_2AlB_2$ surfaces; however, the core is still MoAlB (Figure S13, Supporting Information) which agrees with previous results.[20] From a surface area point of view, HF-etching resulted in a higher SSA than MoAlB, and milling further increased the SSA significantly by reducing the particle size. 1 day NaOH treatment increased surface area of MoAlB, and extending the NaOH treatment to 4 days significantly increased the surface area even more (Figure S12 and Table S3, Supporting Information).

To confirm that the electrochemical redox reactions are surface-controlled, we analyzed the voltammograms at different scan rates. HF-etched MoAlB had the lowest $b$-value of 0.7 (Figure 2 and Figure S4, Supporting Information), indicating a stronger limitation by diffusion of the species entering and leaving the electrode surface. Milling $Mo_2AlB_2$ increased the $b$-value due to exposing more surfaces via particle size reduction. 4 days NaOH-treated MoAlB had the highest $b$-value of 0.85 (Figure 2 and Figure S4, Supporting Information). The capacitive contribution at scan rates 0.2 and 2.0 mV s$^{-1}$ are shown in Figures S5–S7, Supporting Information. The surface-controlled contribution appeared to increase due to milling the HF-etched MoAlB and extending NaOH treatment from 1 to 4 days.

## 3. Conclusions

In conclusion, we succesfully synthesized the $Mo_2AlB_2$ structure, which is one step closer to the $Mo_2B_2$ MBene than MoAlB. We used solid-state synthesis to produce the $Mo_2AlB_2$ precursor (i.e., MoAlB), which was then partially etched to remove 50% of Al using HF acid at 45 °C for 2 days. The etching process caused significant changes in XRD, morphology, and EDS. When we tested the materials as electrodes for Li-ion battery, we found that the specific capacity of the first discharge was quadrupled when milled $Mo_2AlB_2$ was used instead of MoAlB. After 500 cycles, specific capacities 594 and 302 mAh g$^{-1}$ were obtained for milled $Mo_2AlB_2$ and non-milled $Mo_2AlB_2$, respectively, when tested at 200 mA g$^{-1}$. Ex situ XRD and XPS studies for electrochemically

**ADVANCED
SCIENCE NEWS**

www.advancedsciencenews.com

**small
methods**

www.small-methods.com

lithiated and delithiated samples were performed to understand the underlying charge storage mechanism. XRD showed no shift in (0l0) peaks even for Li discharge capacity of >200 mAh g$^{-1}$, suggesting that the charge storage is not by ion intercalation. This aligns with DFT calculations, showing unfavorable Li intercalation in $Mo_2AlB_2$. XPS was used to understand the bonding nature after etching, lithiation, and delithiation. The binding energy of the Mo–Al–B peak in the Mo 3d spectra was found to be shifted to higher values due to etching, lower due to lithiation, and higher again due to delithiation. NaOH treatment of MoAlB resulted in a corrugated porous morphology with layers of high surface roughness. NaOH-treated MoAlB has a significantly higher specific capacity compared to $Mo_2AlB_2$. Specific capacities of 420, 332, and 200 mAh g$^{-1}$ were achieved for 4 days NaOH-treated samples tested under specific currents of 200, 500, and 1000 mA g$^{-1}$, respectively. When $Mo_2AlB_2$ was tested in Na-ion batteries, a specific capacity of 150 mAh g$^{-1}$ was obtained at 20 mA g$^{-1}$ suggesting potential applications in electrochemical energy storage beyond Li-ion batteries. The present work highlights the viability of transition metal borides as electrode materials for ion batteries. It suggests further studies to realize borides and explore other layered transition metal boride systems for energy storage.

## 4. Experimental and Methods Section

*Synthesis of MoAlB Powder*: The MoAlB powder was synthesized by mixing and heating molybdenum boride (MoB, <45 μm, 99%, Alfa Aesar) and aluminum (Al, <45 μm, 99.5%, Alfa Aesar) with atomic ratio Mo:B:Al of 1:1.2. For mixing, zirconia balls were added with the powders into a high-density polyethylene (HDPE) bottle that was then loaded to a Turbula T2F mixer and rotated at 56 rpm for 3 h. Afterward, the mixture was cold-pressed into a 1 in. diameter pellet and put into an alumina crucible in the center of an alumina tube furnace. The pellet was heated from room temperature to 750 °C, held for 2 h, then heated to 1550 °C for 2 h, and finally cooled naturally to room temperature. A heating rate of 10 °C min$^{-1}$ was used throughout the heating steps, and the whole thermal cycle was performed under constant argon (Ar) gas flow.

*Synthesis of $Mo_2AlB_2$*: $Mo_2AlB_2$ phase was synthesized by partial selective etching of Al from the MoAlB phase. The MoAlB pellet was ground into powders (<45 μm) and then added to a bottle containing hydrofluoric acid (HF, 48–51 mass%, Acros Organics, CAS: 7664-39-3) at a MoAlB:HF ratio of (1 g:10 mL). The latter was done by carefully following the strict safety protocols for handling HF.[49] During the initial step of adding powders to the solution, the bottle was submerged in an ice bath. The mixture was then heated to 45 °C inside a bath of mineral oil and held at this temperature for 48 h with continuous stirring using a polytetrafluoroethylene-coated magnetic bar at ≈500 rpm. Afterward, the powders were washed using de-ionized (DI) water through centrifuging at 3500 rpm for 5 min, decanting the supernatant, and refilling with DI water. The washing steps were repeated until a near-neutral pH level (>6) was achieved, and finally, the powders were dried using vacuum-assisted filtration. To reduce the particle size, zirconia balls were added to the $Mo_2AlB_2$ powders into a 15 mL HDPE bottle filled with absolute ethanol (200 Proof, meets USP/EP/ACS, Fisher Chemical). The bottle was sealed and inserted into a high-energy ball milling (8000 M Mixer/Mill High-Energy Ball Mill, SPEX SamplePrep) for six cycles (5 min each). After 5 min of milling, the HDPE bottle was cooled in an ice bath. Afterward, the milled powders were collected and dried through vacuum-assisted filtration.

*MoAlB Particle Size Selection before Etching*: To narrow the particle size distribution of MoAlB before etching, we followed a procedure similar to that reported by Zhang et al.,[26] where the ground MoAlB powder with particle size <45 μm was put into a bath sonication with DI water for 20 min to deagglomerate particles and then the mixture was stirred to maintain

uniform distribution. Once stirring was stopped, powders in DI water were allowed to settle for 154 s to sediment particles in the range of 10–45 μm, and the particles <10 μm were filtered from the supernatant.

*NaOH Treatment of MoAlB*: The NaOH treatment of MoAlB powders was performed following a procedure reported elsewhere.[21] Typically, 250 mg of MoAlB was treated with 250 mL of 10 mass% NaOH solution (Sigma-Aldrich) at RT for 1 day (24 h) or 4 days (96 h) under stirring. Afterward, the mixture was vacuum-filtered through polyvinylidene fluoride (PVDF) membranes (0.22 μm, Merck Durapore), followed by filtration of an excessive amount of DI water to wash away residual NaOH. The wet PVDF membrane with the powder cake on its top was then placed in a vacuum oven at room temperature overnight. The dried powder was then gently removed from the membrane and stored to be used as electrode material.

*Material Characterization*: The crystal structure of the samples was investigated using a Cu K$_\alpha$ Rigaku D/Max-2200 X-ray diffractometer. X-ray diffraction patterns were collected at a 2θ step size of 0.02° and scan rate of 1° min$^{-1}$. Scanning electron microscopy (SEM) images were captured using either an INCA-Hitachi S-4800 at an acceleration voltage of 3 kV, or a ZEISS-Gemini SEM500 system with acceleration voltages between 1–3 kV. The chemical composition within each sample was obtained through EDS via the INCA-Hitachi S-3400 at an accelerating voltage of 30 kV. The XPS measurements were performed using the K-Alpha XPS System from Thermo Scientific. The photon source was a monochromatized Al X-Ray source (1.486 keV). The spectra were acquired using a spot size of 300 μm and constant pass energy (150 eV for a survey and 20 eV for high-resolution spectra). A combined low-energy electron/ion flood source was used for charge neutralization. A dual monoatomic and gas cluster Ar ion source was adopted for depth profiling and sample cleaning. A vacuum transfer vessel was used to protect the sample from oxidation. To clean the sample surface from contamination, Ar sputtering was applied onto MoAlB powder, $Mo_2AlB_2$, lithiated $Mo_2AlB_2$, and delithiated $Mo_2AlB_2$ for 30, 360, 600, and 360 s, respectively. More sputtering time was required for the lithiated $Mo_2AlB_2$ to remove the SEI layer. The X-ray photoelectron spectra were calibrated using adventitious carbon at 284.8 eV.[50] Linear and Shirley backgrounds were used for C 1s and Mo 3d, respectively. Most peaks were fitted using a Gaussian Lorentzian curve GL(30), except for Mo–Al–B which was fit using A(0.38,0.6,10)GL(10), assuming peak asymmetry. The Mo 3d high-resolution spectrum was fitted using doublets $3d_{5/2}$ and $3d_{3/2}$ with an area ratio 3:2 and separated by 3.13 eV.

*Electrochemical Testing*: LIBs with $Mo_2AlB_2$ as an active material were assembled to study their electrochemical performance. The slurry was prepared using the active material, carbon black (CB, Alfa Aesar, >99.9%), and PVDF (molecular weight ≈534 000, Sigma-Aldrich) in a mass ratio of 8:1:1, respectively. 1-Methyl-2-pyrrolidone (99.5%, Acros Organics, extra dry over molecular sieve) was added to the mixture and ground together using mortar and pestle until a homogeneous slurry was formed. The slurry was drop cast using a pipette on copper foil discs (10 μm thick, 12 mm diameter) and allowed to dry overnight in an oven at 60 °C. In the standard two-electrode CR2032 coin cells used in this study, the active material acted as a working electrode, and lithium/sodium metal acted as a counter and reference electrode. For LIBs, 1 M lithium hexafluorophosphate (LiPF$_6$) dissolved in ethylene carbonate (EC) and ethyl methyl carbonate (EMC) EC:EMC (3:7 by volume) was used on the glass fiber separator, while for SIBs, 1 M sodium hexafluorophosphate (NaPF$_6$) dissolved in ethylene carbonate (EC) and diethyl carbonate (DEC) EC:DEC (1:1 by volume) was used. Coin cells assembly was carried out in an Ar-filled glovebox (O$_2$ and H$_2$O <0.1 ppm)

CV and PEIS tests in this study were performed at room temperature using an electrochemical workstation (VMP3, BioLogic), and EC-Lab software was utilized for data collection and analysis. CV was measured at scan rates of 0.1, 0.2, 0.5, 1.0, and 2.0 mV s$^{-1}$ between 1 mV and 3 V versus Li/Li$^+$ (for SIB, the voltages are measured versus Na/Na$^+$). 200 kHz to 10 mHz was the frequency range for PEIS test. Galvanostatic cycling for rate handling capability and stability tests were performed by battery cycler (CT2001A, LANDHE, Wuhan, China). The rate handling capability was quantified using specific currents of 20, 50, 100, 200, 500, 1000, and

back to 20 mA g$^{-1}$. Cycling stability was studied at specific currents of 100, 200, 500, and 1000 mA g$^{-1}$.

*Gas Sorption Analysis*: Nitrogen gas sorption analysis was performed using an Autosorb iQ system (Quantachrome; now Anton-Paar) at liquid nitrogen temperature (−196 °C). Before each measurement, the samples in test tubes were outgassed by heating mantles that heated the samples at a ramping rate of 20 °C min$^{-1}$ to reach the target temperature of 300 °C and held for 3 h. The SSA was calculated by the ASiQwin-software using the Brunauer–Emmett–Teller equation[51] and quenched-solid DFT.[52]

*Theoretical Calculations*: Density functional theory (DFT) calculations were carried out using the Vienna ab initio simulation package.[53,54] The generalized gradient approximation of Perdew, Burke, and Ernzerhof, was utilized for the exchange–correlation functional.[55] The projector-augmented wave method was used to treat the electron–ion interaction, and the cut-off energy of the plane-wave basis set was 550 eV. A $3 \times 3 \times 1$ cell of $Mo_2AlB_2$ was employed to model the intercalation of Li using a $4 \times 4 \times 1$ k-point grid.[56,57]

We performed a full geometry optimization for the Li-incorporated $Mo_2AlB_2$, placing the Li in multiple sites to find the most favorable configuration. The energy for Li intercalation was calculated as

$$\Delta E_{Li} = E_{Mo_2AlB_2+Li_n} - E_{Mo_2AlB_2} - nE_{Li} \tag{1}$$

Here, $E_{Mo_2AlB_2+Li_n}$ is the total energy of the lithiated $Mo_2AlB_2$ with $n$ Li atoms, $E_{Mo_2AlB_2}$ represents the total energy of the pristine $Mo_2AlB_2$, and $E_{Li}$ denotes the total energy per atom of bulk Li metal. A negative value of the intercalation energy indicates that the Li atom prefers to intercalate into the $Mo_2AlB_2$ rather than Li cluster formation.[12] In this work, our calculated lattice parameters were $a = 3.06$ Å, $b = 11.5$ Å, and $c = 3.18$ Å, which match well with previous experimental work.[20]

## Supporting Information

Supporting Information is available from the Wiley Online Library or from the author.

## Conflict of Interest

The authors declare no conflict of interest.

## Data Availability Statement

The data that support the findings of this study are available from the corresponding author upon reasonable request.

## Keywords

layered materials, lithium-Ion batteries, molybdenum boride

[1] Y. Nishi, *J. Power Sources* **2001**, *100*, 101.
[2] Y. S. Zhang, N. E. Courtier, Z. Zhang, K. Liu, J. J. Bailey, A. M. Boyce, G. Richardson, P. R. Shearing, E. Kendrick, D. J. L. Brett, *Adv. Energy Mater.* **2021**, *12*, 2.
[3] D. Er, J. Li, M. Naguib, Y. Gogotsi, V. B. Shenoy, *ACS Appl. Mater. Interfaces* **2014**, *6*, 11173.
[4] J. Liu, X. W. Liu, *Adv. Mater.* **2012**, *24*, 4097.
[5] Q. Gu, G. Krauss, W. Steurer, *Adv. Mater.* **2008**, *20*, 3620.
[6] C. Martini, G. Palombarini, G. Poli, D. Prandstraller, *Wear* **2004**, *256*, 608.
[7] X. Yu, S. Licht, *J. Power Sources* **2008**, *179*, 407.
[8] H. Vrubel, X. Hu, *Angew. Chem., Int. Ed. Engl.* **2012**, *51*, 12703.
[9] W. G. Fahrenholtz, G. E. Hilmas, *Int. Mater. Rev.* **2013**, *57*, 61.
[10] L. Verger, S. Kota, H. Roussel, T. Ouisse, M. W. Barsoum, *J. Appl. Phys.* **2018**, *124*, 205108.
[11] M. Naguib, M. W. Barsoum, Y. Gogotsi, *Adv. Mater.* **2021**, *33*, 2103393.
[12] Z. Guo, J. Zhou, Z. Sun, *J. Mater. Chem.* **2017**, *5*, 23530.
[13] V. G. Nair, M. Birowska, D. Bury, M. Jakubczak, A. Rosenkranz, A. M. Jastrzębska, *Adv. Mater.* **2022**, *34*, 2108840.
[14] T. Bo, P. F. Liu, J. Zhang, F. Wang, B. T. Wang, *Phys. Chem. Chem. Phys.* **2019**, *21*, 5178.
[15] J. Jia, B. Li, S. Duan, Z. Cui, H. Gao, *Nanoscale* **2019**, *11*, 20307.
[16] M. Zhang, H. Wang, H. Wang, T. Cui, Y. Ma, *Phys. Chem. Chem. Phys.* **2010**, *144*, 6722.
[17] M. Naguib, V. N. Mochalin, M. W. Barsoum, Y. Gogotsi, *Adv. Mater.* **2014**, *26*, 992.
[18] W. Jeitschko, *Monatsh. Chem.* **1966**, *97*, 1472.
[19] L. T. Alameda, C. F. Holder, J. L. Fenton, R. E. Schaak, *Chem. Mater.* **2017**, *29*, 8953.
[20] L. T. Alameda, R. W. Lord, J. A. Barr, P. Moradifar, Z. P. Metzger, B. C. Steimle, C. F. Holder, N. Alem, S. B. Sinnott, R. E. Schaak, *J. Am. Chem. Soc.* **2019**, *141*, 10852.
[21] L. T. Alameda, P. Moradifar, Z. P. Metzger, N. Alem, R. E. Schaak, *J. Am. Chem. Soc.* **2018**, *140*, 8833.
[22] K. Kim, C. Chen, D. Nishio-Hamane, M. Okubo, A. Yamada, *Chem. Commun.* **2019**, *55*, 9295.
[23] J. Zhou, J. Palisaitis, J. Halim, M. Dahlqvist, Q. Tao, I. Persson, L. Hultman, P. O. Å. Persson, J. Rosen, *Science* **2021**, *373*, 801.
[24] N. F. Rosli, M. Z. M. Nasir, N. Antonatos, Z. Sofer, A. Dash, J. Gonzalez-Julian, A. C. Fisher, R. D. Webster, M. Pumera, *ACS Appl. Nano Mater.* **2019**, *2*, 6010.
[25] Y. Zhou, H. Xiang, H. Zhang, F.-Z. Dai, *J. Mater. Sci. Technol.* **2019**, *35*, 2926.
[26] J. Zhang, N. Kong, S. Uzun, A. Levitt, S. Seyedin, P. A. Lynch, S. Qin, M. Han, W. Yang, J. Liu, X. Wang, Y. Gogotsi, J. M. Razal, *Adv. Mater.* **2020**, *32*, 2001093.
[27] S. Kota, E. Zapata-Solvas, A. Ly, J. Lu, O. Elkassabany, A. Huon, W. E. Lee, L. Hultman, S. J. May, M. W. Barsoum, *Sci. Rep.* **2016**, *6*, 26475.
[28] K. Yu, J. Li, H. Qi, C. Liang, *Diamond Relat. Mater.* **2018**, *86*, 139.
[29] N. Elgrishi, K. J. Rountree, B. D. McCarthy, E. S. Rountree, T. T. Eisenhart, J. L. Dempsey, *J. Chem. Educ.* **2017**, *95*, 197.
[30] H. Lindström, S. Södergren, A. Solbrand, H. Rensmo, J. Hjelm, A. Hagfeldt, S. E. Lindquist, *J. Phys. Chem. B* **1997**, *101*, 7717.
[31] V. Augustyn, E. R. White, J. Ko, G. Grüner, B. C. Regan, B. Dunn, *Mater. Horiz.* **2014**, *1*, 219.
[32] S. Fleischmann, J. B. Mitchell, R. Wang, C. Zhan, D. E. Jiang, V. Presser, V. Augustyn, *Chem. Rev.* **2020**, *120*, 6738.
[33] M. Opitz, J. Yue, J. Wallauer, B. Smarsly, B. Roling, *Electrochim. Acta* **2015**, *168*, 125.
[34] Y. Xie, H. Zou, H. Xiang, R. Xia, D. Liang, P. Shi, S. Dai, H. Wang, *J. Membr. Sci.* **2016**, *503*, 25.

[35] C. Gao, Z. Jiang, S. Qi, P. Wang, L. R. Jensen, M. Johansen, C. K. Christensen, Y. Zhang, D. B. Ravnsbaek, Y. Yue, *Adv. Mater.* **2022**, *34*, 2110048.

[36] T. B. Schon, S. Y. An, A. J. Tilley, D. S. Seferos, *ACS Appl. Mater. Interfaces* **2019**, *11*, 1739.

[37] J. Guo, Y. Li, J. Meng, K. Pedersen, L. Gurevich, D.-I. Stroe, *J. Energy Chem.* **2022**, *74*, 34.

[38] H. Kim, W. Choi, J. Yoon, J. H. Um, W. Lee, J. Kim, J. Cabana, W.-S. Yoon, *Chem. Rev.* **2020**, *120*, 6934.

[39] Y. Huang, Z. Xu, J. Mai, T.-K. Lau, X. Lu, Y.-J. Hsu, Y. Chen, A. C. Lee, Y. Hou, Y. S. Meng, *Nano Energy* **2017**, *41*, 426.

[40] W. Wang, J. Qin, Z. Yin, M. Cao, *ACS Nano* **2016**, *10*, 10106.

[41] L. C. Yang, Q. S. Gao, Y. Tang, Y. P. Wu, R. Holze, *J. Power Sources* **2008**, *179*, 357.

[42] V. Natu, S. S. Kota, M. W. Barsoum, *J. Eur. Ceram. Soc.* **2020**, *40*, 305.

[43] T. Zhang, C.-Y. Lee, B. Gong, B. Hoex, *AIP Conf. Proc.* **2018**, *1999*, 040027.

[44] J. Halim, K. M. Cook, M. Naguib, P. Eklund, Y. Gogotsi, J. Rosen, M. W. Barsoum, *Appl. Surf. Sci.* **2016**, *362*, 406.

[45] L.-Å. Näslund, P. O. Å. Persson, J. Rosen, *J. Phys. Chem.* **2020**, *124*, 27732.

[46] P. Xiao, N. Jin, Z. Lin, *Mater. Res. Lett.* **2021**, *9*, 516.

[47] Y. Xiao, Y. Li, Z. Guo, C. Tang, B. Sa, N. Miao, J. Zhou, Z. Sun, *Appl. Surf. Sci.* **2021**, *566*, 150634.

[48] X. Han, L. Lu, Y. Zheng, X. Feng, Z. Li, J. Li, M. Ouyang, *eTransportation* **2019**, *1*, 100005.

[49] C. E. Shuck, K. Ventura-Martinez, A. Goad, S. Uzun, M. Shekhirev, Y. Gogotsi, *ACS Chem. Health Saf.* **2021**, *28*, 326.

[50] G. Schön, *J. Electron Spectrosc. Relat. Phenom.* **1972**, *1*, 377.

[51] S. Brunauer, P. H. Emmett, E. Teller, *J. Am. Chem. Soc.* **1938**, *60*, 309.

[52] G. Y. Gor, M. Thommes, K. A. Cychosz, A. V. Neimark, *Carbon* **2012**, *50*, 1583.

[53] G. Kresser, J. Furthmüller, *Comput. Mater. Sci.* **1996**, *6*, 15.

[54] G. Kresse, J. Hafner, *Phys. Rev. B: Condens. Matter Mater. Phys.* **1993**, *47*, 558.

[55] J. P. Perdew, K. Burke, M. Ernzerhof, *Phys. Rev. Lett.* **1996**, *77*, 3865.

[56] G. Kresse, D. Joubert, *Phys. Rev. B* **1999**, *59*, 1758.

[57] P. E. Blöchl, *Phys. Rev. B* **1994**, *50*, 17953.

# small
## methods

## Supporting Information

Toward MBenes Battery Electrode Materials: Layered Molybdenum Borides for Li-Ion Batteries

*Ahmad Majed, Mohammad Torkamanzadeh, Chukwudi F. Nwaokorie, Karamullah Eisawi, Chaochao Dun, Audrey Buck, Jeffrey J. Urban, Matthew M. Montemore, Volker Presser and Michael Naguib\**

Supplementary Information


## Toward MBenes Battery Electrode Materials:

## Layered Molybdenum Borides for Li-ion Batteries

Ahmad Majed,[1] Mohammad Torkamanzadeh,[2,3] Chukwudi F. Nwaokorie,[4]
Karamullah Eisawi,[1] Chaochao Dun,[5] Audrey Buck,[1] Jeffrey J. Urban,[5]
Matthew M. Montemore,[4] Volker Presser,[2,3,6] Michael Naguib[1,*]


[1]      Department of Physics and Engineering Physics, Tulane University, New Orleans, Louisiana 70118, United States of America

[2]      INM - Leibniz Institute for New Materials, D2 2, 66123, Saarbrücken, Germany

[3]      Department of Materials Science & Engineering, Saarland University, Campus D2 2, 66123, Saarbrücken, Germany

[4]      Department of Chemical and Biomolecular Engineering, Tulane University, New Orleans, Louisiana 70118, United States of America

[5]      The Molecular Foundry, Lawrence Berkeley National Laboratory, Berkeley, California 94720, United States of America

[6]      saarene - Saarland Center for Energy Materials and Sustainability, Campus C4 2, 66123 Saarbrücken, Germany

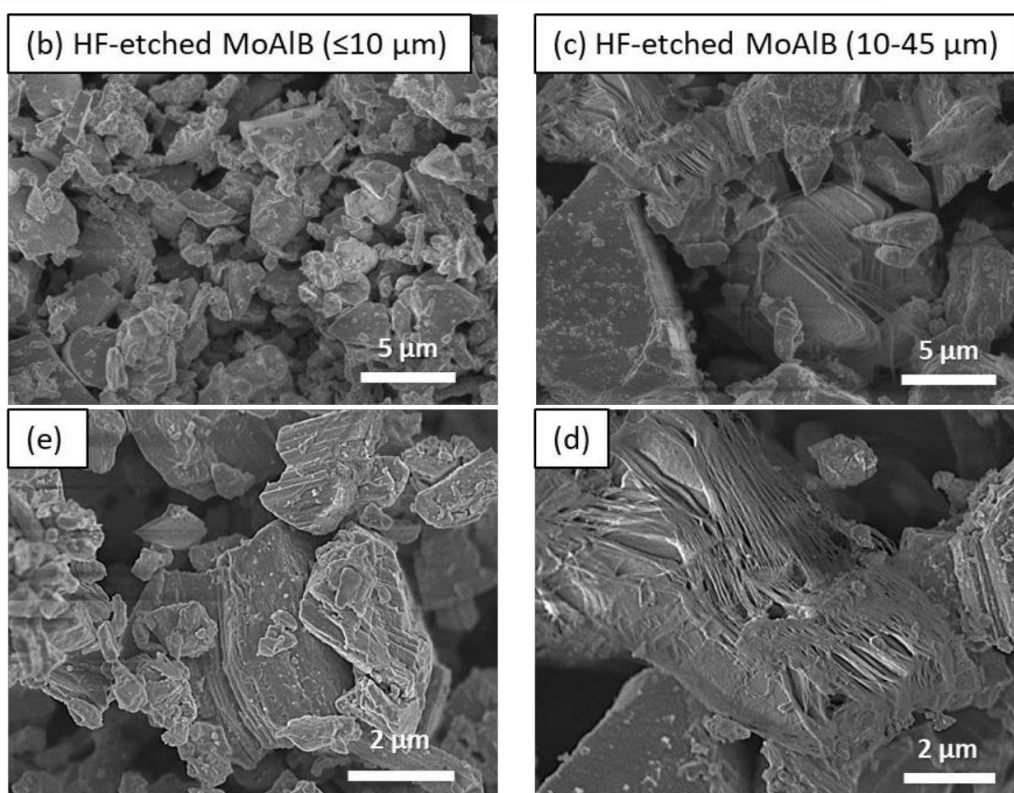*      Corresponding author's email: naguib@tulane.edu

S1

**Figure S1**. Effect of particle size: (a) X-ray diffractograms of HF-etched samples at 45 °C for 24 h using different particle sizes of MoAlB ≤ 10 μm versus 10-45 μm, both compared to untreated MoAlB sample. Scanning electron micrographs of HF-etched (b, d) ≤ 10 μm and (c, e) 10-45 μm particles.
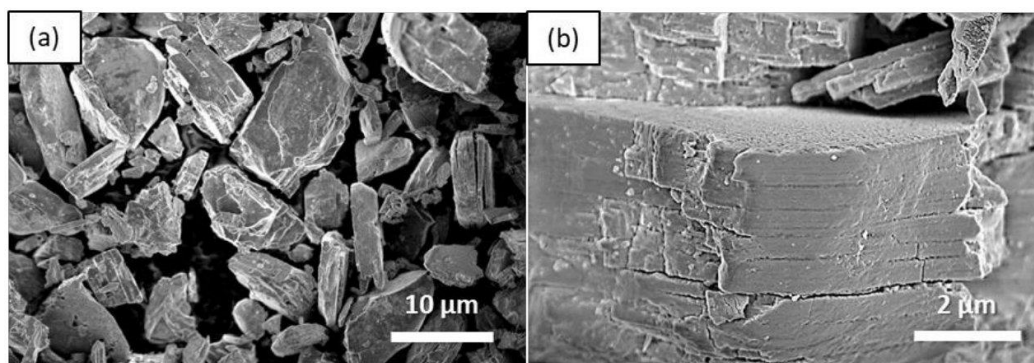
**Figure S2.** Scanning electron micrographs of $Mo_2AlB_2$ after milling at two different magnifications.
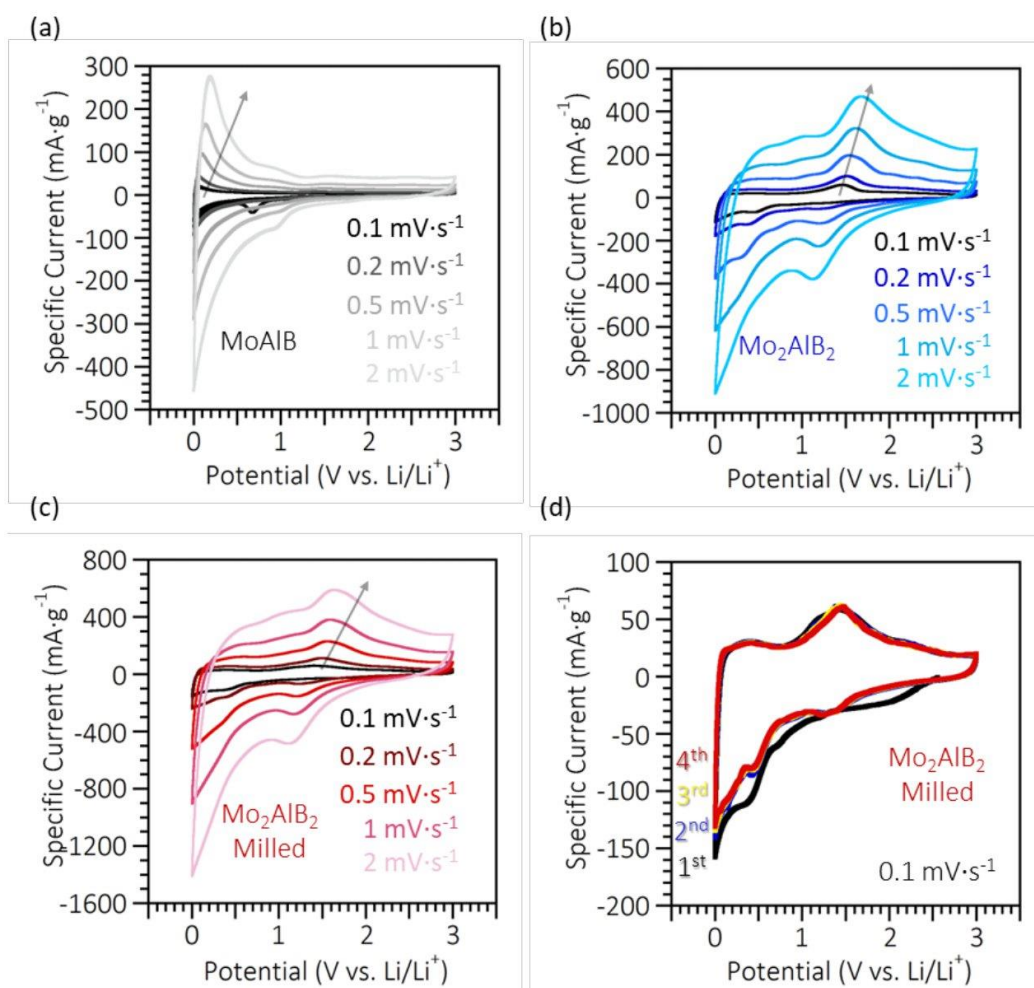


**Figure S3**. LIB performance. Cyclic voltammograms at scan rates of 0.1-2.0 mV·s$^{-1}$ for (a) MoAlB, and $Mo_2AlB_2$ (c) before and (d) after milling. (d) first four cycles of milled $Mo_2AlB_2$ at 0.1 mV·s$^{-1}$.
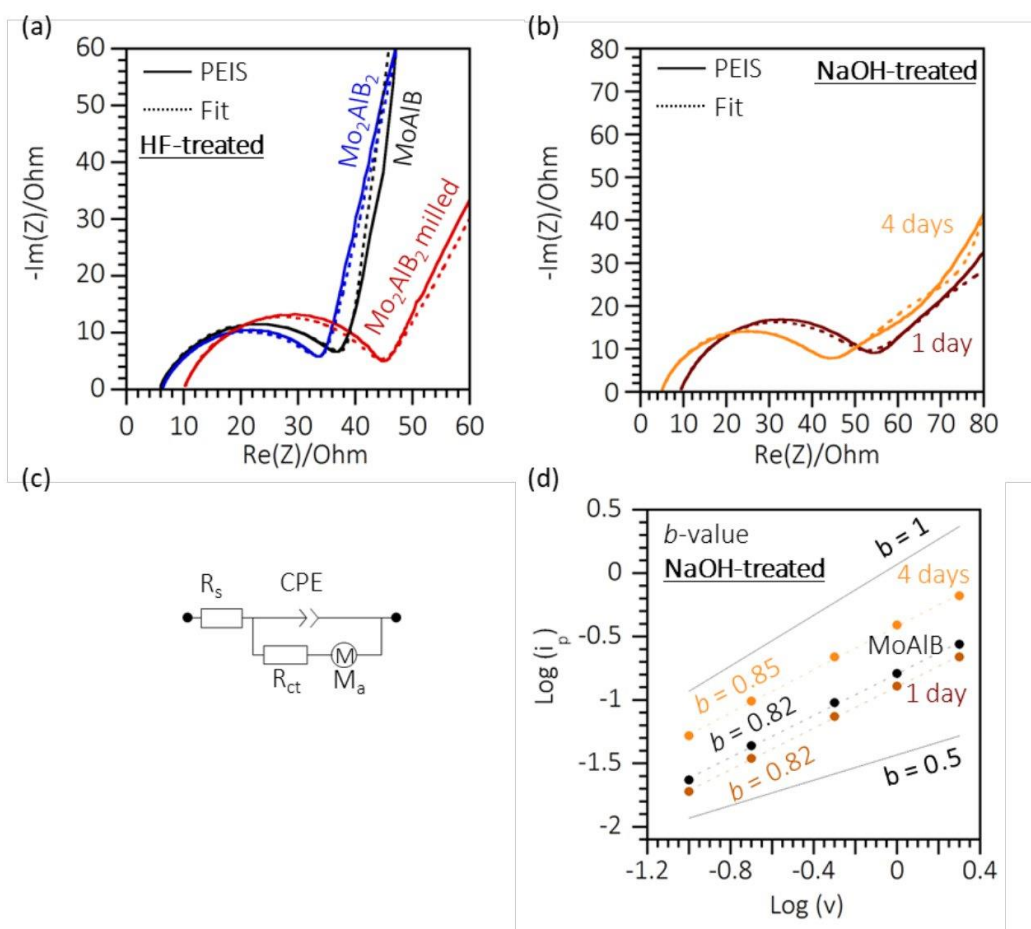
**Figure S4.** LIB performance. Potentiostatic electrochemical impedance spectroscopy (PEIS) of **(a)** MoAlB and HF-treated MoAlB before milling (Mo₂AlB₂) and after milling (Mo₂AlB₂ milled) **(b)** NaOH-treated MoAlB for 1 day and 4 days. **(c)** Circuit used in fitting the PEIS data where $R_s$ is system resistance, $R_{ct}$ is charge transfer resistance, $CPE$ is a constant phase element, and $M_a$ is a modified, restricted diffusion. **(d)** $b$-values of NaOH treated samples.

S4
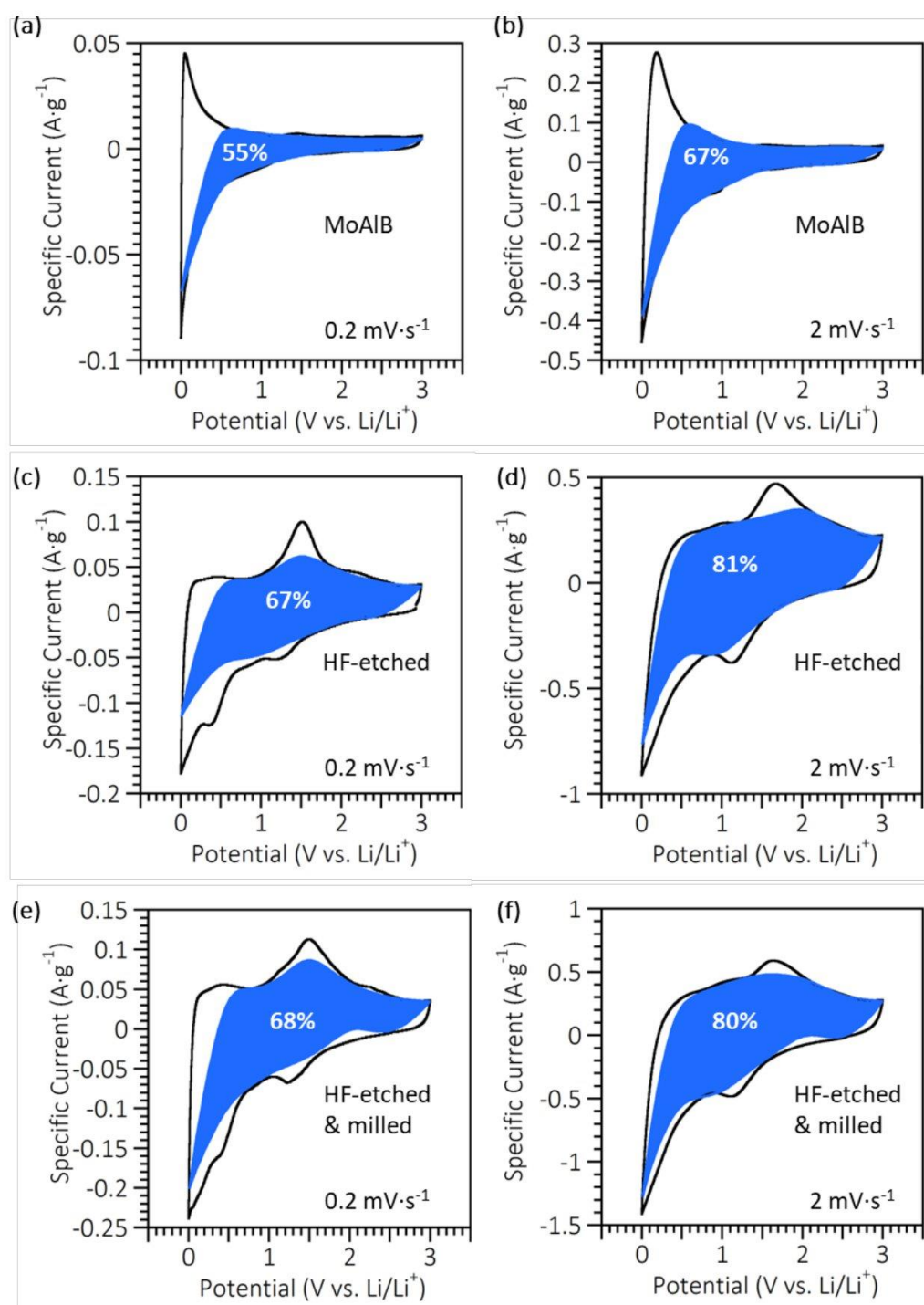
**Figure S5.** LIB performance. Cyclic voltammograms at scan rates **(a, c, e)** 0.2 mV·s$^{-1}$, and **(b, d, f)** 2 mV·s$^{-1}$ with the estimated surface-controlled current contribution shown in blue region. Samples include **(a,b)** MoAlB, and HF-treated MoAlB **(c,d)** before milling (Mo$_2$AlB$_2$) and **(e,f)** after milling (Mo$_2$AlB$_2$ milled).
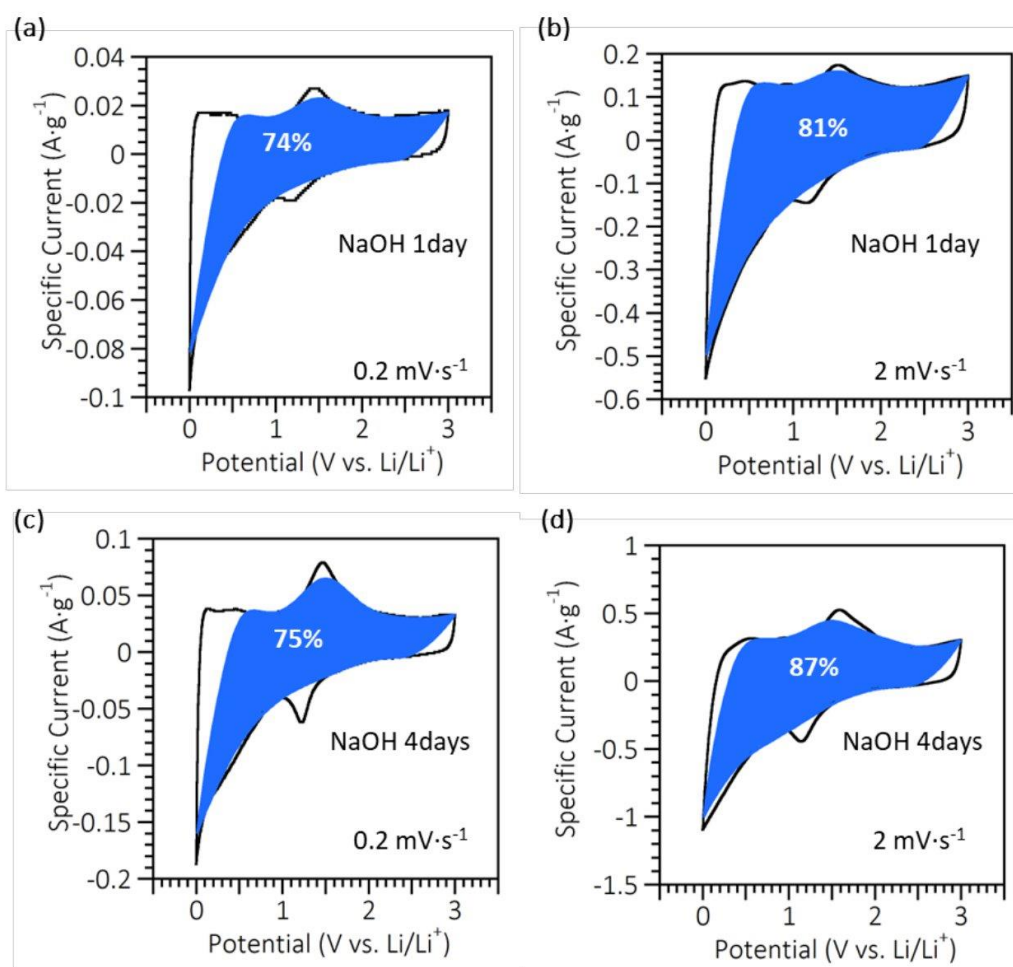
**Figure S6.** LIB performance. Cyclic voltammograms of NaOH treated MoAlB at scan rates **(a, c)** 0.2 mV·s⁻¹, and **(b, d)** 2 mV·s⁻¹ with the estimated surface-controlled current contribution shown in blue region. Samples include NaOH treated for **(a,b)** 1 day, and **(c,d)** 4 days.
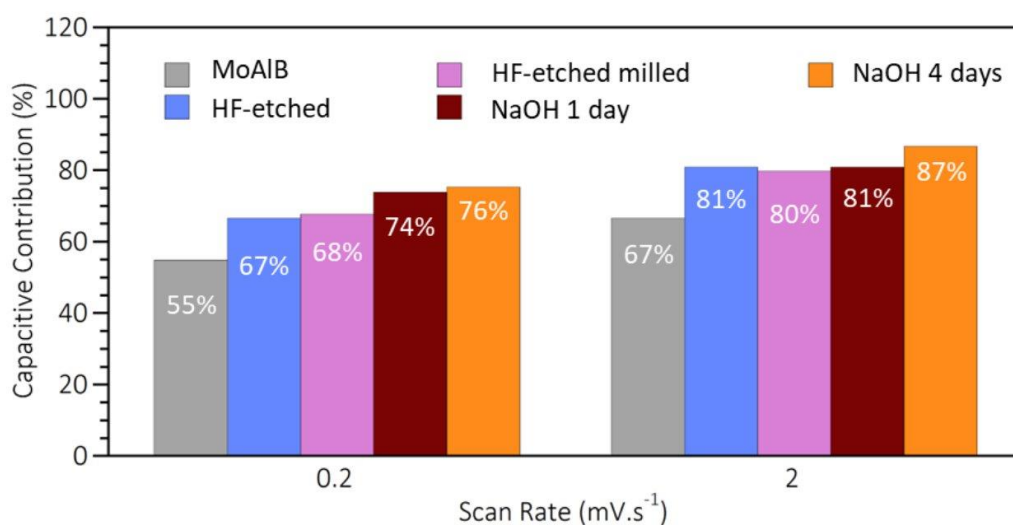
**Figure S7.** Summary of surface-controlled current contribution percentages for MoAlB, HF-etched MoAlB ($Mo_2AlB_2$), HF-etched milled sample ($Mo_2AlB_2$ milled), and NaOH-treated MoAlB at 1 and 4 days at scan rates 0.2 mV·s⁻¹, and 2 mV·s⁻¹.
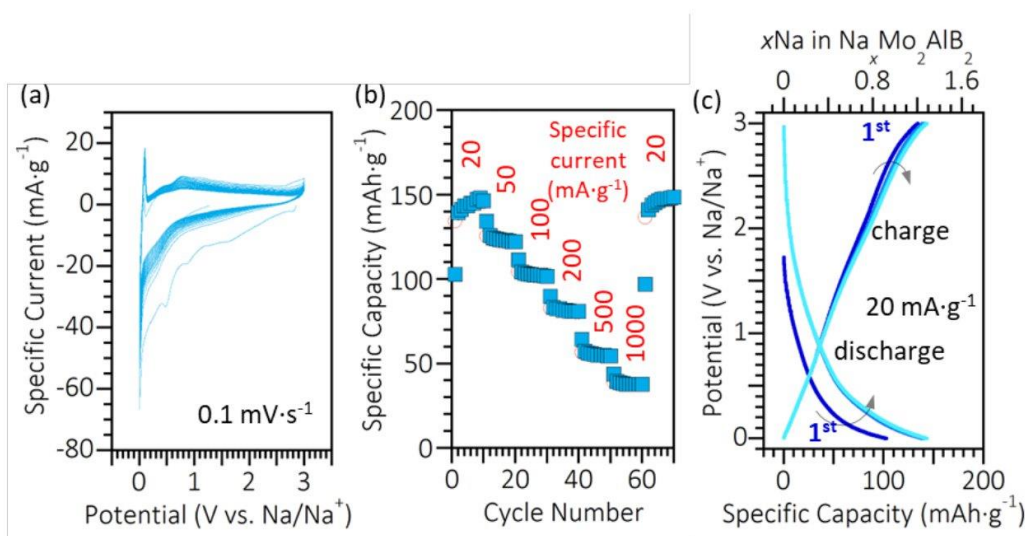


**Figure S8.** SIB performance of as-synthesized $Mo_2AlB_2$ (a) Cyclic voltammograms of the first 10 cycles at 0.1 mV.s⁻¹. (b) Rate handling capability specific currents of 20 mA·g⁻¹, 50 mA·g⁻¹, 100 mA·g⁻¹, 200 mA·g⁻¹, 500 mA·g⁻¹, and 1000 mA·g⁻¹ (c) Voltage profile of $Mo_2AlB_2$ for cycles 1-5 at a specific current 20 mA·g⁻¹.
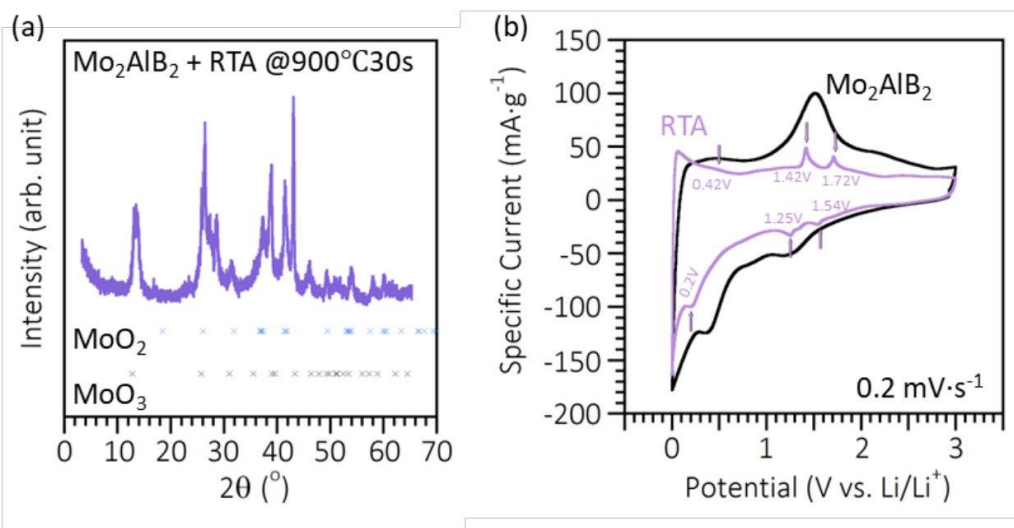
**Figure S9.** Structure and electrochemical behavior of $Mo_2AlB_2$ after rapid thermal annealing (RTA) at 900 °C for 30 s. (a) X-ray diffractogam after RTA. (b) LIB performance. Cyclic voltammogram before and after RTA tested at 0.2 mV·s$^{-1}$.
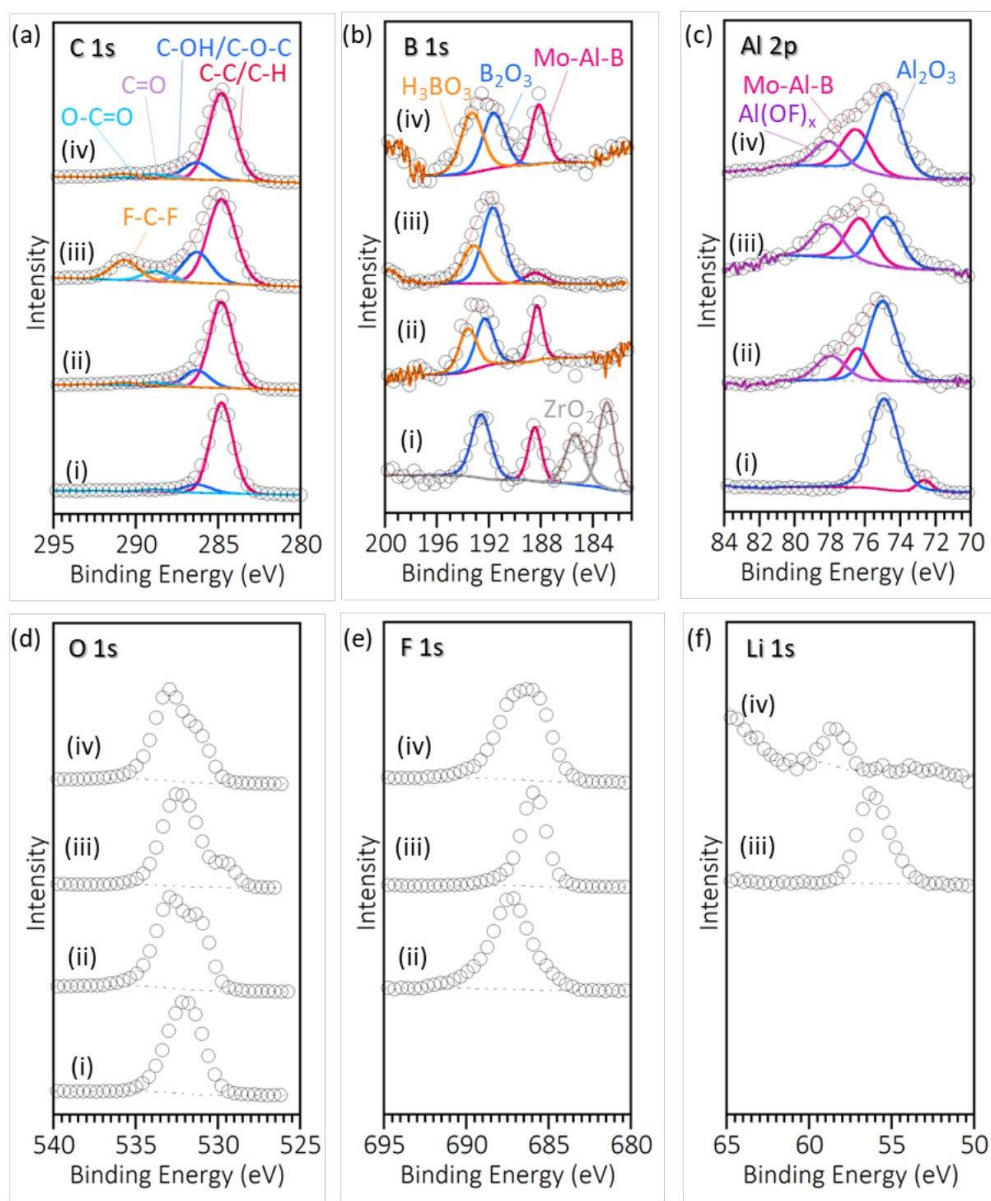
**Figure S10.** High resolution XPS spectra of of **(a)** C 1s, **(b)** B 1s, **(c)** Al 2p, **(d)** O 1s, **(e)** F 1s, **(f)** Li 1s studying (i) MoAlB, $Mo_2AlB_2$ electrode (ii) before cycling, (iii) half cycled, and (iv) fully cycled (LIB).
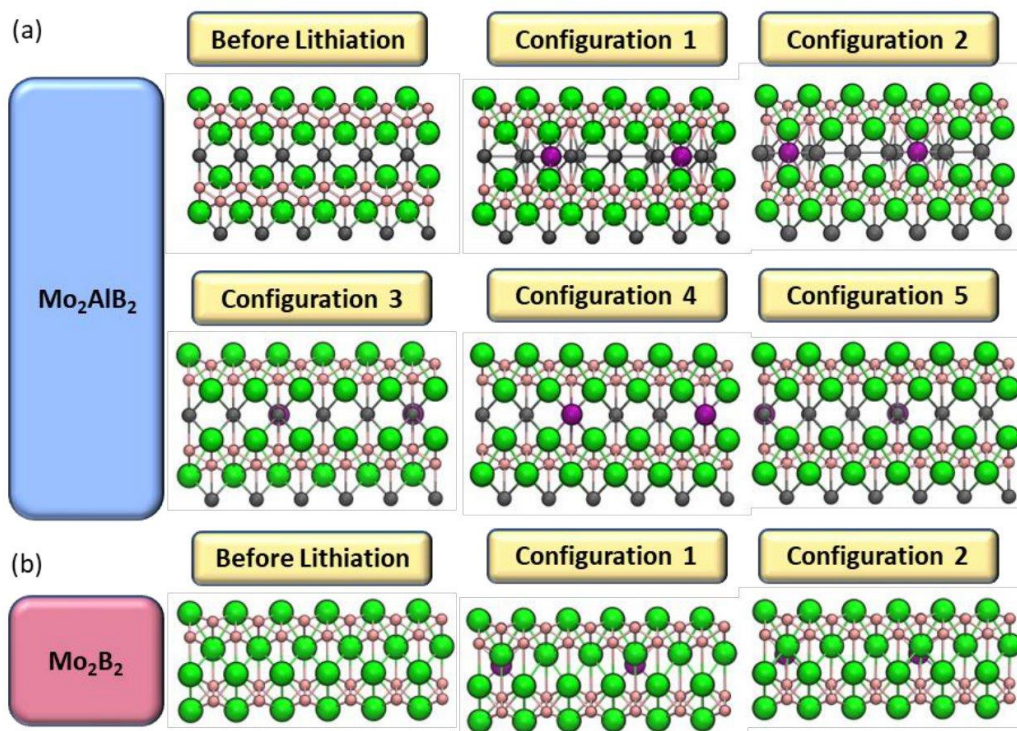
**Figure S11.** Different atomic configurations used in DFT before and after Li intercalation for (a) Mo$_2$AlB$_2$ and (b) Mo$_2$B$_2$.
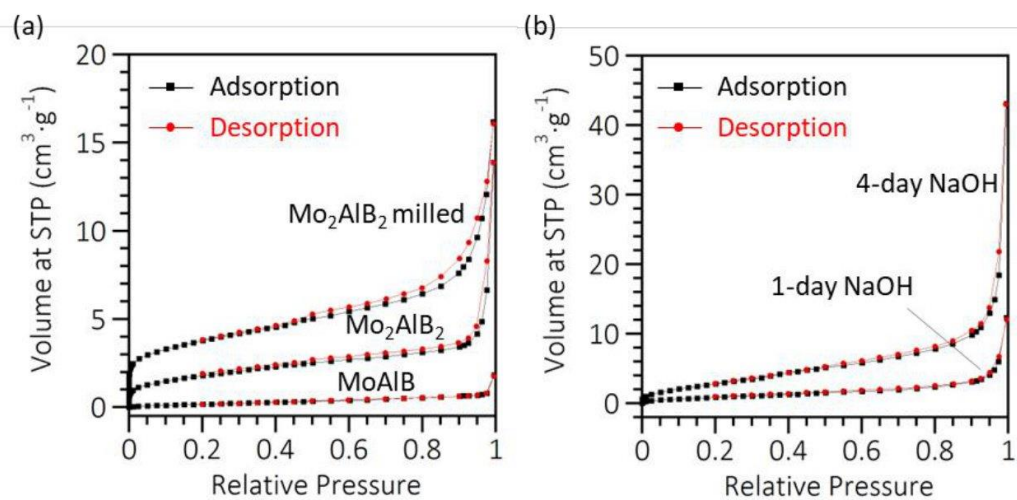


**Figure S12. Gas sorption analysis.** Nitrogen gas sorption isotherm of (a) HF-MoAlB and (b) NaOH-MoAlB. Measurements were performed at a temperature of -196 °C. STP: standard temperature and pressure.

S10
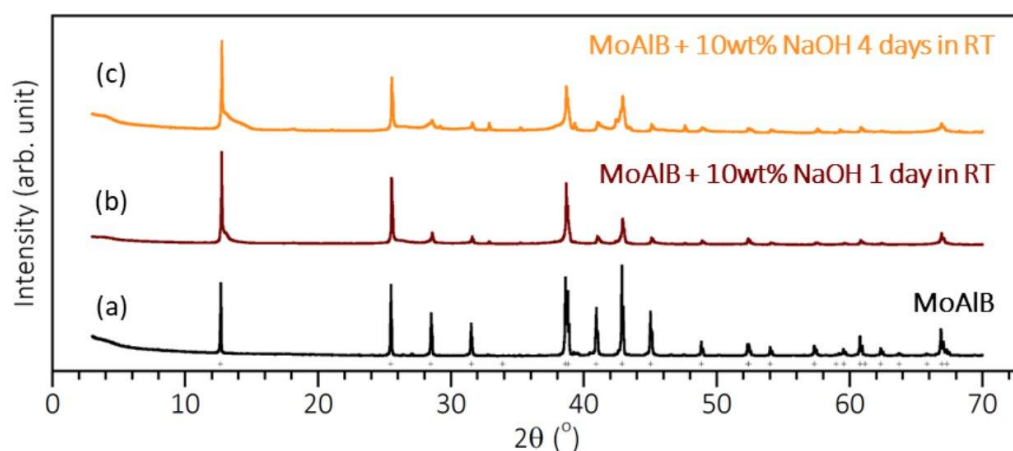
**Figure S13.** X-ray diffractograms of MoAlB before (a) and after NaOH treatment at room temperature for (b) 1 day, and (c) 4 days. "+" marks are assigned to MoAlB orthorhombic (PDF 72-1277)

**Table S1.** Effect of particle size on the etching outcomes of MoAlB (detecting B using EDS is challenging).

| Particle size range (μm) | Mass loss (mass%) | (020) peak position | Mo:Al (atomic%) |
|---|---|---|---|
| < 10 | 15 | 12.8° 2θ | 1.00:0.67 |
| 10 to 45 | 30 | 13.8° 2θ | 1.00:0.50 |

**Table S2.** XPS peak fitting results of Mo 3d for MoAlB, $Mo_2AlB_2$ electrode before cycling, half cycled and fully cycled.

| Element | Binding energy (eV) | FWHM (eV) | Fraction | Assigned to | Literature binding energy (eV) / Ref. |
|---|---|---|---|---|---|
| MoAlB | 228.0 (231.1) | 1.2 (1.2) | 34.5% | Mo-Al-B | 228.1 / [1] |
| | 229.5 (232.7) | 2.0 (2.0) | 22.9% | Mo(IV) | 229.7 / [1, 2] |
| | 232.0 (235.1) | 2.0 (2.0) | 18.7% | Mo(V) | 231.9 / [2] |
| | 233.4 (236.5) | 1.5 (1.5) | 8.8% | Mo(VI) | 233.1 / [2] |
| $Mo_2AlB_2$ | 228.4 (231.6) | 1.3 (1.3) | 19.3% | Mo-Al-B | |
| | 229.4 (232.5) | 1.7 (1.7) | 45.9% | Mo(IV) | 229.7 / [1, 2] |
| | 231.2 (234.3) | 2.0 (2.0) | 17.3% | Mo(V) | 231.9 / [2] |
| | 233.3 (236.4) | 2.0 (2.0) | 8.4% | Mo(VI) | 233.1 / [2] |
| $Mo_2AlB_2$ Lithiated | 227.8 (231.0) | 1.3 (1.3) | 24.1% | Mo-Al-B | |
| | 229.6 (232.8) | 2.0 (2.0) | 19.3% | Mo(IV) | 229.7 / [1, 2] |
| | 231.9 (235.0) | 2.0 (2.0) | 13.8% | Mo(V) | 231.9 / [2] |
| | 233.8 (236.9) | 1.2 (1.2) | 31.8% | Mo(VI) | 233.1 / [2] |
| $Mo_2AlB_2$ Delithiated | 228.2 (231.3) | 1.2 (1.2) | 22.8% | Mo-Al-B | |
| | 229.3 (232.4) | 1.9 (1.9) | 42.9% | Mo(IV) | 229.7 / [1, 2] |
| | 231.2 (234.3) | 2.0 (2.0) | 14.6% | Mo(V) | 231.9 / [2] |
| | 233.2 (236.3) | 2.0 (2.0) | 9.3% | Mo(VI) | 233.1 / [2] |

S11

**Table S3.** Gas sorption analysis with nitrogen gas at -196 °C using the quenched solid density functional theory (QSDFT) and the Brunauer-Emmett-Teller theory (BET).

| | SSA BET $(m^2 \cdot g^{-1})$ | SSA DFT $(m^2 \cdot g^{-1})$ | DFT total pore volume $(cm^3 \cdot g^{-1})$ |
|---|---|---|---|
| MoAlB | 1 | 0.5 | 0.00 |
| MoAlB-1 day in NaOH | 4 | 2 | 0.01 |
| MoAlB-4 days in NaOH | 11 | 8 | 0.02 |
| $Mo_2AlB_2$ | 7 | 5 | 0.01 |
| $Mo_2AlB_2$ milled | 13 | 13 | 0.02 |

**Table S4.** EDS analysis (atomic%) of MoAlB before and after NaOH treatment for 1 day and 4 days.

| Duration | Mo | Al | O |
|---|---|---|---|
| Before | 23 | 23 | 4 |
| 1 day | 28 | 22 | 20 |
| 4 days | 27 | 19 | 15 |

**Supporting references:**

1.  Natu, V.; Kota, S. S.; Barsoum, M. W., X-ray photoelectron spectroscopy of the MAB phases, MoAlB, $M_2AlB_2$ (M = Cr, Fe), $Cr_3AlB_4$ and their binary monoborides. *Journal of the European Ceramic Society* **2020,** *40* (2), 305-314.
2.  Zhang, T.; Lee, C.-Y.; Gong, B.; Hoex, B., Thermal stability analysis of $WO_x$ and $MoO_x$ as hole-selective contacts for Si solar cells using in situ XPS. 2018.

S12

## 4.6. Functional two-dimensional high-entropy materials

Srinivasa Kartik Nemani[1#], Mohammad Torkamanzadeh[2,3#],

Brian C. Wyatt[1#], Volker Presser[2,3,4*], Babak Anasori[1,5*]

1. Department of Mechanical and Energy Engineering, and Integrated Nanosystems Development Institute (INDI), Indiana University, Purdue University, IN 46202, United States of America

2. INM – Leibniz Institute for New Materials, Campus D2 2, 66123 Saarbrücken, Germany

3. Department of Materials Science & Engineering, Saarland University Campus D2 2, 66123 Saarbrücken, Germany

4. Saarene – Saarland Center for Energy Materials and Sustainability, Campus C4 2, 66123 Saarbrücken

5. School of Materials Engineering, Purdue University, West Lafayette, IN 47907, United States of America

\#   Contributed equally

\*   Corresponding authors

Own contributions:

Investigation, Visualization, Writing - Original Draft, Writing - Review & Editing.

PERSPECTIVE

# Functional two-dimensional high-entropy materials

Srinivasa Kartik Nemani [1,6], Mohammad Torkamanzadeh[2,3,6],
Brian C. Wyatt[1,6], Volker Presser [2,3,4 ✉] & Babak Anasori[1,5 ✉]

Multiple principal element or high-entropy materials have recently been studied in the two-dimensional (2D) materials phase space. These promising classes of materials combine the unique behavior of solid-solution and entropy-stabilized systems with high aspect ratios and atomically thin characteristics of 2D materials. The current experimental space of these materials includes 2D transition metal oxides, carbides/carbonitrides/nitrides (MXenes), dichalcogenides, and hydrotalcites. However, high-entropy 2D materials have the potential to expand into other types, such as 2D metal-organic frameworks, 2D transition metal carbo-chalcogenides, and 2D transition metal borides (MBenes). Here, we discuss the entropy stabilization from bulk to 2D systems, the effects of disordered multi-valent elements on lattice distortion and local electronic structures and elucidate how these local changes influence the catalytic and electrochemical behavior of these 2D high-entropy materials. We also provide a perspective on 2D high-entropy materials research and its challenges and discuss the importance of this emerging field of nanomaterials in designing tunable compositions with unique electronic structures for energy, catalytic, electronic, and structural applications.

istorically, alloying has been a popular method in metallurgy to derive unique and superior properties in metals[1,2]. Efforts toward the exploration of alloys with multiple principal metals at equimolar or near equimolar ratios have led to the realization of multicomponent systems with unique structure–property synergies[3,4]. These materials are stabilized by the increased effect of configurational entropy, as demonstrated in the high-entropy alloys phase space at the bulk scale since the 2000s[5–9].

Furthermore, the inclusion of non-metallic species, such as carbon, hydrogen, nitrogen, and oxygen, has been studied either at a few at.% in high-entropy alloys or to occupy the interstitial sites of the metal lattice to form new compounds to accentuate the properties of these materials. For example, the addition of 2 at.% oxygen increases the mechanical strength and ductility[10], <0.5 at.% carbon enhances phase stability and wear resistance[11,12], <0.6 at.% boron improves hardness, while the inclusion of hydrogen at ~50 mass% ppm reduces the stacking fault energies leading to localized strain hardening in alloys[13]. Consequently, the high-entropy materials space has expanded further into non-metallic compounds with bulk nitride films[14,15], crystalline[16–18] and amorphous[19] oxides, carbides[20,21], borides[22], silicides[23,24], and chalcogenides[25] mostly since 2015. This expansion has been driven by their potential for attractive properties in applications ranging from mechanical[20], catalysis[26,27], thermal[28,29], electrical, energy storage, and harvesting[30]. Some of the compounds reported to date have a low or medium entropic

[1]Department of Mechanical and Energy Engineering, and Integrated Nanosystems Development Institute (INDI), Indiana University, Purdue University, 723W. Michigan Street, West Lafayette, IN 46202, USA. [2]INM—Leibniz Institute for New Materials, Campus D2 2, 66123 Saarbrücken, Germany. [3]Department of Materials Science & Engineering, Saarland University, Campus D2 2, 66123 Saarbrücken, Germany. [4]Saarene—Saarland Center for Energy Materials and Sustainability, Campus C4 2, 66123 Saarbrücken, Germany. [5]School of Materials Engineering, Purdue University, Neil Armstrong Hall of Engineering, 701W Stadium Ave, West Lafayette, IN 47907, USA. [6]These authors contributed equally: Srinivasa Kartik Nemani, Mohammad Torkamanzadeh, Brian C. Wyatt. ✉email: volker.presser@leibniz-inm.de; banasori@iupui.edu

contribution (non-equimolar compositions and less than four principal elements), also referred to as compositionally complex ceramics[31].

The concept of high entropy at the nanoscale was introduced in 2017[32], and further expanded to layered two-dimensional (2D) materials in 2020–2022 with entropy-stabilized multiple principal elements in oxide, chalcogenide, carbide/carbonitride (MXenes), hydroxide forms with promising practical applications[27,33–42]. Furthermore, van der Waals heterostructures of entropy-stabilized 2D chalcogenides and halides have exhibited super-conductivity, unique magnetic behavior, and heterogeneous cat-alytic activity[43]. Figure 1a shows the timeline from the realization of entropy stabilization in bulk phases, alloys in 2004 and cera-mics in 2015, to layered 2D materials in 2020–2021. While high-entropy 2D materials are still in their infancy, the combination of their high surface area and functionalities of 2D materials with entropy stabilization brings the promise to accelerate materials discovery for applications such as energy conversion or storage.

In this perspective, we discuss entropy stabilization from bulk to 2D systems, the effects of disordered multi-valent elements on lattice distortion and local electronic structures, and elucidate these changes on the catalytic and electrochemical behavior of 2D high-entropy materials. While in bulk form, these materials have been explored for their stability and mechanical behavior,

since no studies have reported the mechanical properties of high-entropy 2D materials, we focus more on applications such as energy conversion and storage, which are current areas of interest for 2D materials.

## High entropy structures

The formation and stabilization of high-entropy materials come with various degrees of mixing in the metallic sublattices. Figure 1b shows an array of entropy-stabilized systems where order–disorder transitions are possible with substitutional inter-faces (non-equimolar systems)[44], short-range ordering (localized clustering)[45], and complete randomized solid solutions (with an increase in the number of constituents) in a system comprising multiple elements. Increasing the number of species increases the contribution of the entropy term in Gibbs' free energy equation, making configurational entropy the main contributor to system stability, as shown in Fig. 1c. Unlike in high-entropy alloys, in high-entropy compounds, the presence of non-metals (as we will refer to them as X) in the metal interstitial sites (referred to as M) can lead to complex M–X coordination bonding states[17,46]. Further, the presence of non-metallic sublattices enables a larger selectivity and diversity in the M species with room for elements of larger ionic radii and M–X bond lengths with little effect on
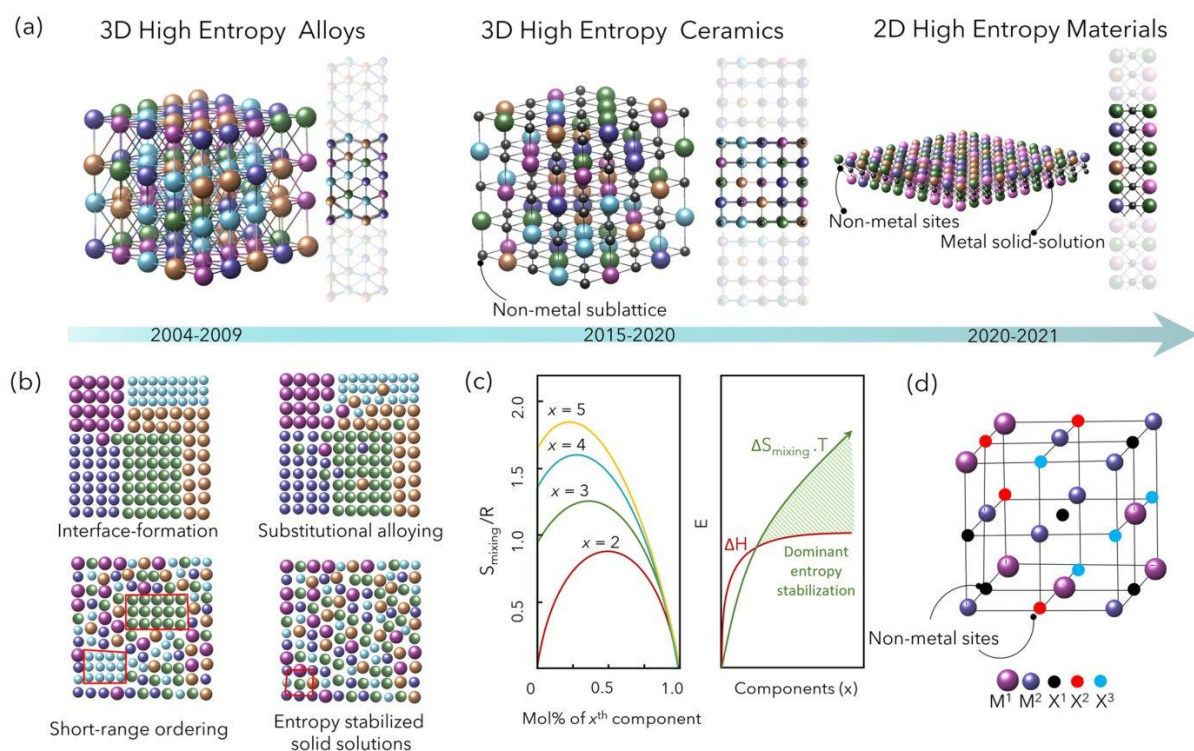


**Fig. 1 Progress in high-entropy materials research. a** Timeline and progress in entropy-stabilized systems over the past decade with the transition toward high-entropy 2D materials in 2021. **b** Four degrees of order and disorder between the phase-segregated structures and the ideal entropy-stabilized solid solutions. **b** reproduced with permission from ref. [75] (copyright AAAS, 2021); **c** Configurational entropy change as a function of the number of species (N) and the mole fraction of the Xth component system varying from $N = 2$ to $N = 5$. **c** Reproduced with permission from ref. [17] (copyright Springer Nature, 2015). The maximum entropy is attained at equimolar compositions. Depending on S/R, one distinguishes between low, medium, and high-entropy materials. The panel on the right shows the energy (E) region for dominant entropy effects (shaded area) in a system. Reproduced with permission from ref. [88] (copyright Wiley, 2017). The red line indicates the enthalpic contribution ($\Delta H$), and the line in green shows the entropic contribution ($\Delta S$). **d** A multiple principal element system with 2 metallic and 3 non-metallic species in the crystal lattice as an example of entropy stabilization by both metal and non-metal sites. Entropic contribution from both the sublattices is given by: $\Delta S_{\text{mix}} = -R\left[\left(\sum_{i=1}^{N} x_i \ln x_i\right)_{\text{cation-site}} + \left(\sum_{j=1}^{N} x_j \ln x_j\right)_{\text{anion-site}}\right]$. **d** Reproduced with permission from ref. [49] (copyright, Elsevier, 2020).
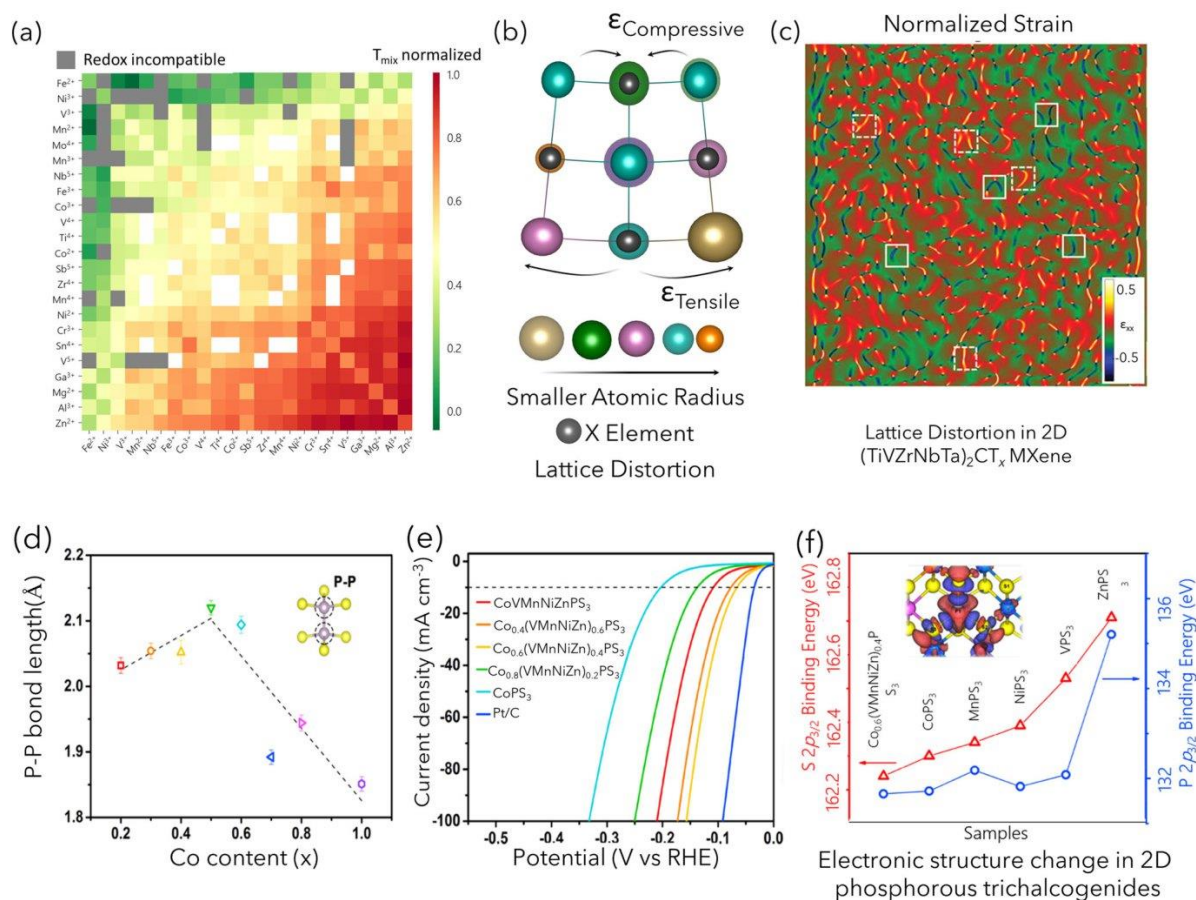
**Fig. 2 Compatibility and effect of coordination states in multiple M elements. a** Normalized temperature at which two paired cations are stable in a cation-disordered rock-salt structure. **a** reproduced with permission from ref. [56] (copyright Springer Nature, 2021). **b** Mechanical straining of multiple different-sized cations on the distortion of a rock-salt ceramic structure. **c** Mechanical distortion of the lattice of a $(TiVZrNbTa)_2CT_x$ MXene as-measured via scanning transmission electron microscopy (STEM). **c** Reproduced with permission from ref. [38] (copyright Wiley, 2021). **d** Local changes in P–P bond length in a high-entropy $Co_x(VMnNiZn)_{1-x}PS_3$ structure with change in Co[37]. **e** Change in hydrogen evolution reaction behavior based on P–P distance[37]. **f** Binding energy of the S $2p_{3/2}$ and P $2p_{3/2}$ peak as measured via X-ray photoelectron spectroscopy (XPS). **d–f** Reproduced with permission from ref. [37] (copyright American Chemical Society, ACS 2022).

lattice distortion[46–48]. Similarly, entropy stabilization can also be achieved through mixing in the X sites, leading to bulk single-phase materials forming, as shown in Fig. 1d[49,50].

Various characterization methods are required to confirm the high configurational entropy of the system. X-ray/neutron diffraction[51], and scanning transmission electron microscopy combined with energy-dispersive X-ray spectroscopy, and high-angle annular dark-field methods have been used to delineate and map the principal elements[52]. Atomic scale tomographic techniques may also be explored to accentuate these methods[53,54]. Altering the stoichiometric ratio beyond the equimolar ratio can be used as a qualitative method to evaluate the effect of entropy in stabilizing the structure[34]. In addition, spectroscopy methods, such as X-ray photoelectron spectroscopy, are currently being implemented to understand the complex oxidation states and their effect on properties in high-entropy nanomaterials[55].

The elements and their coordination states affect these materials' interaction with surrounding species in the lattice. The compatibility of transition metals and post-transition metals in different coordination states can be examined to understand the role of charge transfer between the cations in a high-entropy material structure. In Fig. 2a,

the compatibility of multi-valent metals in a cubic rock-salt lattice is demonstrated with their compatibility factor, labeled as the normalized temperature of mixing, or $T_{mix, normalized}$[56]. The compatibility, in this case, measures the propensity of a metal to transfer charge from one metal to another and maintain stability in a singular lattice. The green color, such as $Fe^{3+}$ or $V^{3+}$ with a $T_{mix, normalized} = 0.0$, is considered more compatible than the red elements, such as $Zn^{2+}$ or $Al^{3+}$ with a $T_{mix, normalized} = 1.0$[56]. In high-entropy materials, this charge transfer between the mixed metals plays a significant role in their inherent structural and electronic characteristics and their subsequent material properties.

## 2D high-entropy structures

The charge transfer process and changing local coordination states of metals within a high-entropy structure to create stable disordered lattice structures also impact the local strain within a lattice. The occupancy of multiple metal or non-metal sites in a 2D high-entropy material results in localized tensile and compressive strains on the lattice structure[57]. This strain results from the mixed atomic sizes of multi-valent distinct elements, as shown in Fig. 2b.

Using scanning transmission electron microscopy, the effect of five transition metals on the lattice can be seen by viewing the 2D structure perpendicular to the basal plane. By measuring the average distortion of the hexagonal lattice structure, the strain (red for tensile, blue for compressive) can be mapped onto the basal plane as seen in Fig. 1c for $(TiVZrNbTa)_2CT_x$ MXene[38], which demonstrates the local distortion caused by elements with various atomic radii in a single 2D material.

At the 2D nanosheet level, since most of the atoms are either on the surface or at the neighboring sites to the basal plane, localized strain and changes in electronic structure will have dominant effects on the material's properties. In a study on high-entropy 2D phosphorous trichalcogenides, $Co_x(VMnNiZn)_{1-x}PS_3$, the strain in the structure and localized changes in the electronic structure with their relative effects on the material's electrocatalysis behavior were explored[37]. A five-fold increase in the lattice strain was reported using powder X-ray diffraction on the bulk-layered phosphorous trichalcogenides. The high-entropy mixtures of $Co_x(VMnNiZn)_{1-x}PS_3$ also altered the X–X bond length (P–P bond here), and an increment-decrement relationship between the cobalt content and P–P bond length was observed (Fig. 2d). The effect of this P–P bond length change based on Co composition can be seen in Fig. 2e, where the highest hydrogen evolution reactivity is around a Co molar ratio of ~0.5. Because of these tunable P–P bonds, the authors speculate that a high-entropy structure could redistribute the electron density at each P atom and make it more active for electrocatalysis reactions. The authors also conducted X-ray photoelectron spectroscopy on $Co_{0.6}(VMnNiZn)_{0.4}PS_3$ and compared it with the corresponding single-metal phosphorous trichalcogenides ($CoPS_3$, $VPS_3$, $MnPS_3$, $NiPS_3$, and $ZnPS_3$). The results indicated the lowest binding energy states for both P and S, confirming a higher electron-donating character for the $[P_2S_6]^{4-}$ sites, which leads to better hydrogen adsorption in hydrogen evolution reactions (HER)[37]. The changes in the HER activity of $Co_x(VMnNiZn)_{1-x}PS_3$[37] demonstrate the effects of multiple elements on the electronic structure localized changes around cation and anion sites which can further control potential binding sites for energy storage or catalytic activity. However, further studies are necessary to fully investigate the effect of high entropy on the energy storage and conversion behavior of these 2D materials.

## 2D high-entropy materials in energy storage and conversion

There has been a growing research focus using the concept of high entropy in all components of an energy storage device, the electrodes (anode and cathode)[46,58], as well as solid-[59,60], and liquid-state electrolytes[61] (Fig. 3a, b). The possibility of tuning the bond length, electronic structure, and charge transfer in high-entropy materials coupled with the high surface area of 2D materials makes high-entropy 2D materials attractive candidates for energy storage and conversion. Current studies in high-entropy 2D systems have focused primarily on electrode materials.

The MXenes family has been explored extensively as electrode materials with research on their various synthesis techniques and modification strategies over the past decade[62,63]. However, it was not until recently that the high-entropy MXenes with four or more transition metal elements were reported[34,36,64]. These high-entropy MXenes are derived from their bulk precursors: the high-entropy MAX phases. While solid-solution double transition metal MAX phases have been studied for several decades, phase pure high-entropy MAX phases were not explored or reported independently of their 2D MXene counterparts.

As an outcome of the top-down synthesis approach, the MXenes' basal planes are decorated with functional moieties (such as –OH, = O, –F, –Cl, –S) bonded to the surface transition metal. The termination compositions depend highly on the synthesis route, providing another degree of tunability aside from

the principal M and X elements[65]. The surface functional groups further control the electronic properties (metallic conductors to semiconductors, and superconductivity)[66,67], and stability.

So far, five compositions of high-entropy MXenes have been reported since 2021, and a few of them are being studied in energy storage applications. Those include $Ti_{1.1}V_{0.7}Cr_xNb_{1.0}Ta_{0.6}CT_x$ used as Li-ion battery (LIB) anode, Zn-ion[64], and $H_2SO_4$ supercapacitor electrodes[36], $(TiZrNbTa)_2CT_x$ and $(Ti_{0.2}V_{0.2}Zr_{0.2}Nb_{0.2}Ta_{0.2})_2C$ as LIB anodes[38], and $(TiVZrNbTa)_2CN$ as lithium–sulfur battery cathode[68]. When used as a LIB anode, delaminated $Ti_{1.1}V_{0.7}Cr_xNb_{1.0}Ta_{0.6}C_3T_x$ MXene film exhibited a first-cycle capacity of 126 mAh g$^{-1}$ at 0.01 A g$^{-1}$, and a long-term stable capacitance of 40 mAh g$^{-1}$ at 1 A g$^{-1}$ for over 1000 cycles[64]. Although the charge storage capacities of high-entropy MXene are lower than (regular) $Ti_3C_2T_x$ MXene (410 mAh g$^{-1}$ at 1 °C)[69], the high-entropy MXene exhibits an interesting cycle stability behavior: the steady-state capacity for high-entropy MXene increases two-fold after 300 cycles. This is while it decreases almost two-fold for $Ti_3C_2T_x$ MXene. When used as electrodes for Zn-ion[64] and $H_2SO_4$ electrolyte supercapacitors[36], a ~90% capacitance retention was seen after ~10,000 cycles. This demonstrates the increased cyclical stability of the system due to the implementation of a high-entropy 2D electrode.

The charge storage capacity of 2D materials, such as LIB electrodes, is generally limited by the extent of Li intercalation into the available space between the layers[70]. Consequently, simply by employing a high-entropy 2D electrode, the charge storage capacities will not necessarily be improved, and a more systematic design is required for high-entropy 2D electrodes. For example, Du et al.[68] showed how a high-entropy carbonitride MXene could capitalize on the ultra-high theoretical capacity of sulfur (1672 mAh g$^{-1}$)[71] besides intercalation[72]. Benefiting from the high affinity and catalytic activity between the five different M–C/N bonds and polysulfides and the high mechanical strains in their carbonitride MXene layers, multistep sulfur conversion processes were shown to take place without the loss of active material. This has resulted in higher capacities (~900 mAh g$^{-1}$ at 1 °C) and rate capabilities (702 mAh g$^{-1}$ at 4 °C) with good cycling stability. Figure 3c summarizes the performance metrics of MXenes and layered transition metal oxides as models of high-entropy 2D materials used as battery electrodes in half-cell configurations.

The concept of high entropy in energy conversion has recently been introduced in other 2D materials, such as high-entropy transition metal chalcogenides. Wang et al. have recently reported >15-fold enhanced catalytic activity of $Co_{0.6}(VMnNiZn)_{0.4}PS_3$ toward HER compared to that of $CoPS_3$[37]. Owing to the composition-dependent electrocatalytic activities of the latter high-entropy material, it was found that by varying the Co content relative to other components, the following favorable properties are achieved: the material could be arbitrarily shifted left or right on the volcano plot[73]. This results in the highest population of active P and S sites for water dissociation and hydrogen adsorption with enhanced kinetics while minimizing the desorption energy barrier for adsorbed hydrogen intermediates to ensure a bond breakage and release of gaseous hydrogen (Fig. 3d). A similar mechanistic study has been reported earlier for ammonia decomposition using a series of bulk $Co_xMo_yFeNiCu$ ($x + y = 7$) nanoparticles (non-2D) by tuning the Co/Mo ratios[74].

Given the earth-abundant non-precious elements employed in the fabrication of 2D-electrocatalysts and the high level of compositional tunability, their application in (non-2D) catalysis is an emerging field of research[75–78]. In the 2D space, a recent study synthesized and used a high-entropy 2D transition metal dichalcogenide $(MoWVNbTa)S_2$ for electrocatalytic $CO_2$ capture
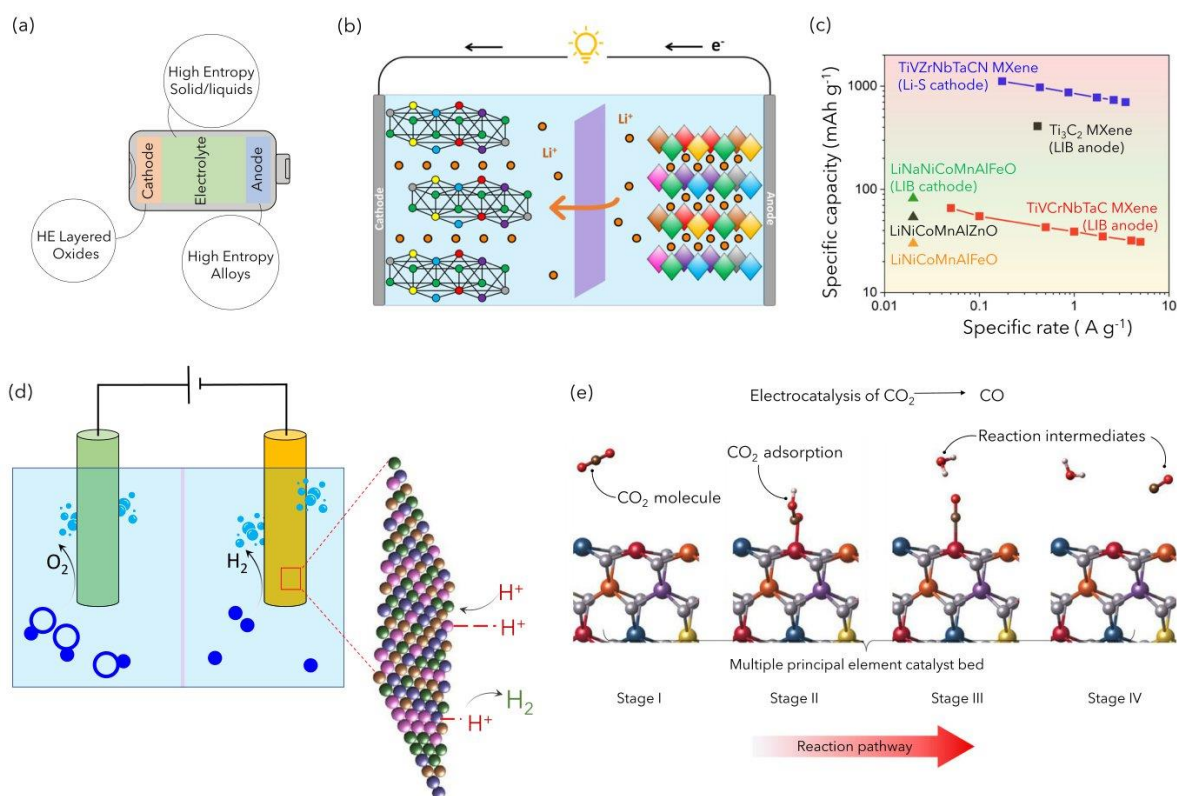
**Fig. 3 High-entropy 2D materials for energy storage and conversion.** Schematic representation of **a** a 'high-entropy battery' where anode, cathode, and electrolyte are all made of high-entropy materials; **b** Li-ion batteries composed of a high-entropy 2D intercalation material (such as MXene) and a 3D conversion material (oxides/sulfides) with improved cycle-stability owing to their high configurational entropy; **c** summary of capacities and rate handling capabilities of different high-entropy materials, marked by color codes denoting how recent each material was introduced to the community; **d** high-entropy 2D electrocatalysts used for hydrogen and oxygen evolution reactions, magnifying microscopic interactions of protons with different elements from the surface of the high-entropy electrode and their ultimate conversion into hydrogen molecule. **d** Adapted with permission from ref. [74] (copyright Springer Nature, 2019); **e** electrocatalysis reaction steps of $CO_2$ conversion into CO at a transition metal site of a (Mo, W, V, Nb, Ta)$S_2$ nanoribbon. **e** Reproduced with permission from ref. [42] (copyright Wiley, 2021).

and its conversion into CO[42]. Aided by computational studies, this high-entropy 2D material with equimolar transition metal composition is first screened and verified regarding miscibility, enthalpic and entropic stabilities and then synthesized and tested for electrochemical performance. Figure 3e schematically shows the stepwise process (from I to IV) of the $CO_2$ reduction reaction at a transition metal site in (MoWVNbTa)$S_2$[42]. The following steps are hypothesized based on the simulation and experiments: (I and II) as a $CO_2$ molecule approaches the surface, it adsorbs on the transition metal with strong binding affinity, resulting in the formation of COOH* and CO* reaction intermediates; (III and IV) the reduced desorption energy barrier caused by the disordered (because of the high-entropy system) and neighboring coordinated metal atoms facilitate the bond breakage of the product (CO)[76,79]. There is also the possibility of CO* hopping from stronger binding elements (W and Mo) to weaker binding elements (for example, vanadium).

## Outlook

Fundamentally, many questions are yet to be answered in this new field of high-entropy 2D materials. Mechanisms that explain the stability and performance of bulk high-entropy materials can aid in providing insights. For example, the cocktail effect, which is prominent in bulk materials and contributes significantly toward

property enhancement, may not be dominant in a 2D system as demonstrated in high-entropy MXenes, which have been computationally predicted to exhibit some short-range order of atoms in different atomic planes[37], which still requires experimental verifications. In addition, those 2D systems synthesized via top-down approaches have the presence of surface terminal groups which can affect the electronic structure of the surface or edge-site metallic species[80].

Another challenge is to identify stable compositions tailored to specific applications. One approach to mitigate instability can be introducing disorder in the non-metal sub-lattices, as a substitutional disorder in these sites will increase the entropy of mixing. For example, adding fluoride salts to high-entropy oxides led to greater stabilities and higher working potentials (3.4 V vs. $Li^+$/Li) for cathode materials[81]. Similar mixing, in principle, is adaptable to other systems such as 2D chalcogenides. Mixing in non-metal such as in 2D transition metal borocarbonitrides ($B_xC_yN_z$) with B, C, and N, all forming an alloy in the non-metallic sublattice can be functionalized toward efficient hydrogen storage and carbon sequestering[82]. A potential avenue for high-entropy 2D materials is envisioned for selective ion-sieving and sensing applications. Specifically, with tailorable basal atomic plane activity, the effects of fermi energy and spillover phenomena observed in high-entropy alloys can be better understood at the nanoscale to develop highly efficient sensing devices[83]. The

5

high-entropy 2D compounds can provide a platform to understand better the correlation of electronic structure and the improvement of mechanical properties reported in some bulk high-entropy carbides[84].

Studies on composition–structure–property relationships in 2D high-entropy systems are at a nascent stage. Models such as entropy descriptors[20], valence electron concentration[85] atomic radii, and electronegativity can be adapted for identifying stable compositions. In addition, using paired experimental and computational approaches can assist in the characterization and understanding of localized interactions. However, more development is necessary to handle the increased computational complexity due to these structures' size and facet dependency[86]. Yet, considering an immense number of possible 2D high-entropy compositions, modeling and predictive material science (in combination with high-throughput surveying) will play critical roles in advancing the research field[87].

Future development of high entropy principles at the nanoscale will be the most direct pairing of 2D materials' unique electronic structure with the high surface area toward energy storage, catalytic activity, magnetic behavior, mechanical properties, and other applications. As continued development of these materials moves into the current decade and beyond, we believe that high-entropy 2D materials will provide a wide degree of tunability and control, unlike other composition–structure–property techniques in materials science for the fundamental study of the high-entropy concept and address energy, catalytic, electronic, and structural challenges of our world.

## References

1. Zolotukhin, I. V. & Kalinin, Y. E. Amorphous metallic alloys. *Sov. Phys. Usp.* **33**, 720 (1990).
2. Eylon, D., Fujishiro, S., Postans, P. J. & Froes, F. H. High-temperature titanium alloys—a review. *JOM* **36**, 55–62 (1984).
3. Murty, B. S., Yeh, J. W., Ranganathan, S. & Bhattacharjee, P. P. A brief history of alloys and the birth of high-entropy alloys. In *High-Entropy Alloys* 2nd edn (eds Murty, B. S., Yeh, J. W., Ranganathan, S. & Bhattacharjee, P. P.) (Elsevier, 2019).
4. George, E. P., Raabe, D. & Ritchie, R. O. High-entropy alloys. *Nat. Rev. Mater.* **4**, 515–534 (2019).
5. Cantor, B., Chang, I. T. H., Knight, P. & Vincent, A. J. B. Microstructural development in equiatomic multicomponent alloys. *Mater. Sci. Eng.: A* **375–377**, 213–218 (2004). **Seminal work on high-entropy alloys.**
6. Gao, M. C., Yeh, J.-W., Liaw, P. K. & Zhang, Y. *High-entropy Alloys.* (Springer International Publishing, Cham, 2016).
7. Yeh, J. W. et al. Nanostructured high-entropy alloys with multiple principal elements: novel alloy design concepts and outcomes. *Adv. Eng. Mater.* **6**, 299–303 (2004). **Among the first reports on high-entropy alloys.**
8. Miracle, D. High entropy alloys as a bold step forward in alloy development. *Nat. Commun.* **10**, 1–3 (2019).
9. Li, J., Fang, Q. & Liaw, P. K. Microstructures and properties of high-entropy materials: modeling, simulation, and experiments. *Adv. Eng. Mater.* **23**, 2001044 (2021).
10. Lei, Z. et al. Enhanced strength and ductility in a high-entropy alloy via ordered oxygen complexes. *Nature* **563**, 546–550 (2018).
11. Huang, T. et al. Effect of carbon addition on the microstructure and mechanical properties of CoCrFeNi high entropy alloy. *Sci. China Technol. Sci.* **61**, 117–123 (2018).
12. Wu, M., Li, Z., Gault, B., Munroe, P. & Baker, I. The effects of carbon on the phase stability and mechanical properties of heat-treated FeNiMnCrAl high entropy alloys. *Mater. Sci. Eng. A* **748**, 59–73 (2019).
13. Luo, H. et al. Beating hydrogen with its own weapon: nano-twin gradients enhance embrittlement resistance of a high-entropy alloy. *Mater. Today* **21**, 1003–1009 (2018).
14. Chen, T. K., Shun, T. T., Yeh, J. W. & Wong, M. S. Nanostructured nitride films of multi-element high-entropy alloys by reactive DC sputtering. *Surf. Coat. Technol.* **188-189**, 193–200 (2004).
15. Moskovskikh, D. et al. Extremely hard and tough high entropy nitride ceramics. *Sci. Rep.* **10**, 19874 (2020).
16. Sarkar, A. et al. High entropy oxides for reversible energy storage. *Nat. Commun.* **9**, 3400 (2018).
17. Rost, C. M. et al. Entropy-stabilized oxides. *Nat. Commun.* **6**, 1–8 (2015). **Among the first reports on high-entropy oxide ceramics.**
18. Gild, J. et al. High-entropy fluorite oxides. *J. Eur. Ceram. Soc.* **38**, 3578–3584 (2018).
19. Zhang, J. et al. High-entropy oxides $10La_2O_3-20TiO_2-10Nb_2O_5-20WO_3-20ZrO_2$ amorphous spheres prepared by containerless solidification. *Mater. Lett.* **244**, 167–170 (2019).
20. Sarker, P. et al. High-entropy high-hardness metal carbides discovered by entropy descriptors. *Nat. Commun.* **9**, 4980 (2018).
21. Castle, E., Csanádi, T., Grasso, S., Dusza, J., & Reece, M. Processing and properties of high-entropy ultra-high temperature carbides. *Sci. Rep.* **8**, 1–12 (2018).
22. Gild, J. et al. High-entropy metal diborides: a new class of high-entropy materials and a new type of ultrahigh temperature ceramics. *Sci. Rep.* **6**, 37946 (2016).
23. Gild, J. et al. A high-entropy silicide: $(Mo_{0.2}Nb_{0.2}Ta_{0.2}Ti_{0.2}W_{0.2})Si_2$. *J. Materiom.* **5**, 337–343 (2019).
24. Qin, Y. et al. A high entropy silicide by reactive spark plasma sintering. *J. Adv. Ceram.* **8**, 148–152 (2019).
25. Jiang, B. et al. High-entropy-stabilized chalcogenides with high thermoelectric performance. *Science* **371**, 830–834 (2021).
26. Yang, J. X. et al. Rapid fabrication of high-entropy ceramic nanomaterials for catalytic reactions. *ACS Nano* **15**, 12324–12333 (2021).
27. Ding, S. et al. Plasma-regulated two-dimensional high entropy oxide arrays for synergistic hydrogen evolution: from theoretical prediction to electrocatalytic applications. *J Power Sources* **520**, 230873 (2022).
28. Dudnik, O. V. et al. High-entropy ceramics for thermal barrier coatings produced from $ZrO_2$ doped with rare-earth metal oxides. *Powder Metall. Metal Ceram.* **59**, 556–563 (2021).
29. Li, F., Zhou, L., Liu, J.-X., Liang, Y. & Zhang, G.-J. High-entropy pyrochlores with low thermal conductivity for thermal barrier coating materials. *J. Adv. Ceram.* **8**, 576–582 (2019).
30. Zhai, S. et al. The use of poly-cation oxides to lower the temperature of two-step thermochemical water splitting. *Energy Environ. Sci.* **11**, 2172–2178 (2018).
31. Wright, A. J. & Luo, J. A step forward from high-entropy ceramics to compositionally complex ceramics: a new perspective. *J. Mater. Sci.* **55**, 9812–9827 (2020).
32. Niu, B. et al. Sol–gel autocombustion synthesis of nanocrystalline high-entropy alloys. *Sci. Rep.* **7**, 3421 (2017). **Amongst the first reports on nanocrystalline high-entropy alloys.**
33. Miura, A., Ishiyama, S., Kubo, D., Rosero-Navarro, N. C., & Tadanaga, K. Synthesis and ionic conductivity of a high-entropy layered hydroxide. *J. Ceram. Soc. Jpn.* **128**, 336–339 (2020).
34. Nemani, S. K. et al. High-entropy 2D carbide MXenes: $TiVNbMoC_3$ and $TiVCrMoC_3$. *ACS Nano* **15**, 12815–12825 (2021). **Among the first papers on high-entropy 2D MXenes and the first on $M_4C_3T_x$ MXenes.**
35. Li, F. et al. Bottom-up synthesis of 2D layered high-entropy transition metal hydroxides. *Nanoscale Adv.* **4**, 2468–2478 (2022). **Among the first papers on high-entropy 2D transition metal hydroxides.**
36. Zhou, J. et al. High-entropy laminate metal carbide (MAX Phase) and its two-dimensional derivative MXene. *Chem. Mater.* **34**, 2098–2106 (2022).
37. Wang, R. et al. Two-dimensional high-entropy metal phosphorus trichalcogenides for enhanced hydrogen evolution reaction. *ACS Nano* **16**, 3593–3603 (2022).
38. Du, Z. et al. High-entropy atomic layers of transition-metal carbides (MXenes). *Adv. Mater.* **33**, 2101473 (2021). **Among the first papers on high-entropy 2D MXenes and the first on an $M_2CT_x$ high-entropy MXene.**
39. Cui, Y. et al. A perspective on high-entropy two-dimensional materials. *SusMat* **2**, 65–75 (2022).
40. Wu, L. et al. Electrocatalysts toward oxygen evolution reaction. *Adv. Funct. Mater.* **33**, 2208170 (2023).
41. Teplonogova, M. A., Yapryntsev, A. D., Baranchikov, A. E. & Ivanov, V. K. High-entropy layered rare earth hydroxides. *Inorg. Chem.* **61**, 19817–19827 (2022).
42. Cavin, J. et al. 2D High-entropy transition metal dichalcogenides for carbon dioxide electrocatalysis. *Adv. Mater.* **33**, 2100347 (2021). **Among the first reports on high-entropy 2D transition metal dichalcogenides.**
43. Ying, T. et al. High-entropy van der Waals materials formed from mixed metal dichalcogenides, halides, and phosphorus trisulfides. *J. Am. Chem. Soc.* **143**, 7042–7049 (2021).
44. Rao, Z. et al. Beyond solid solution high-entropy alloys: tailoring magnetic properties via spinodal decomposition. *Adv. Funct. Mater.* **31**, 2007668 (2021).
45. Wu, Y. et al. Short-range ordering and its effects on mechanical properties of high-entropy alloys. *J. Mater. Sci. Technol.* **62**, 214–220 (2021).

46. Oses, C., Toher, C. & Curtarolo, S. High-entropy ceramics. *Nat. Rev. Mater.* **5**, 295–309 (2020).

47. Rost, C. M., Rak, Z., Brenner, D. W. & Maria, J. P. Local structure of the $Mg_xNi_xCo_xCu_xZn_xO$ ($X = 0.2$) entropy-stabilized oxide: an EXAFS study. *J. Am. Ceram. Soc.* **100**, 2732–2738 (2017).

48. Berardan, D., Meena, A., Franger, S., Herrero, C. & Dragoe, N. Controlled Jahn–Teller distortion in (MgCoNiCuZn) O-based high entropy oxides. *J. Alloys Compd.* **704**, 693–700 (2017).

49. Li, F. et al. Synthesis of single-phase metal oxycarbonitride ceramics. *Scr. Mater.* **176**, 17–22 (2020).

50. Wen, T., Liu, H., Ye, B., Liu, D. & Chu, Y. High-entropy alumino-silicides: a novel class of high-entropy ceramics. *Sci. China Mater.* **63**, 300–306 (2020).

51. Wang, F. et al. The effect of submicron grain size on thermal stability and mechanical properties of high-entropy carbide ceramics. *J. Am. Ceram. Soc.* **103**, 4463–4472 (2020).

52. Dusza, J. et al. Microstructure of (Hf–Ta–Zr–Nb)C high-entropy carbide at micro and nano/atomic level. *J. Eur. Ceram. Soc.* **38**, 4303–4307 (2018).

53. Hu, R., Jin, S. & Sha, G. Application of atom probe tomography in understanding high entropy alloys: 3D local chemical compositions in atomic scale analysis. *Prog. Mater. Sci.* **123**, 100854 (2022).

54. Pradeep, K. G. et al. Atomic-scale compositional characterization of a nanocrystalline AlCrCuFeNiZn high-entropy alloy using atom probe tomography. *Acta Mater.* **61**, 4696–4706 (2013).

55. Wang, D. et al. Low-temperature synthesis of small-sized high-entropy oxides for water oxidation. *J. Mater. Chem. A* **7**, 24211–24216 (2019).

56. Lun, Z. et al. Cation-disordered rocksalt-type high-entropy cathodes for Li-ion batteries. *Nat. Mater.* **20**, 214–221 (2021).

57. Hedman, D., Feltrin, A. C., Miyamoto, Y. & Akhtar, F. Ab-initio aided design of novel quaternary, quinary and senary high-entropy borocarbides. *J. Mater. Sci.* **57**, 422–443 (2022).

58. Fu, M., Ma, X., Zhao, K., Li, X. & Su, D. High-entropy materials for energy-related applications. *Iscience* **24**, 102177 (2021).

59. Wu, B. et al. High-entropy NASICON phosphates ($Na_3M_2$ ($PO_4$)$_3$ and $NaMPO_4O_x$, M = Ti, V, Mn, Cr, and Zr) for sodium electrochemistry. *Inorg. Chem.* **61**, 4092–4101 (2022).

60. Guo, R. & He, T. High-entropy Perovskite electrolyte for protonic ceramic fuel cells operating below 600 °C. *ACS Mater. Lett.* **4**, 1646–1652 (2022).

61. Zhang, W. et al. Decimal solvent-based high-entropy electrolyte enabling the extended survival temperature of lithium-ion batteries to −130 °C. *CCS Chem.* **3**, 1245–1255 (2021).

62. Gogotsi, Y. & Anasori, B. The rise of MXenes. *ACS Nano* **13**, 8491–8494 (2019).

63. Anasori, B. & Gogotsi, Y. MXenes: trends, growth, and future directions. *Graphene 2D Mater.* **7**, 75–79 (2022).

64. Etman, A. S., Zhou, J. & Rosen, J. Ti$_{1.1}$V$_{0.7}$Cr$_x$Nb$_{1.0}$Ta$_{0.6}$C$_3$T$_z$ high-entropy MXene freestanding films for charge storage applications. *Electrochem. Commun.* **137**, 107264 (2022).

65. Lim, K. R. G. et al. Fundamentals of MXene synthesis. *Nat. Synth.* **1**, 601–614 (2022).

66. Li, X. et al. MXene chemistry, electrochemistry and energy storage applications. *Nat. Rev. Chem.* **6**, 1–16 (2022).

67. Kamysbayev, V. et al. Covalent surface modifications and superconductivity of two-dimensional metal carbide MXenes. *Science* **369**, 979–983 (2020).

68. Du, Z. et al. High-entropy carbonitride MAX phases and their derivative MXenes. *Adv. Energy Mater.* **12**, 2103228 (2022).

69. Mashtalir, O. et al. Intercalation and delamination of layered carbides and carbonitrides. *Nat. Commun.* **4**, 1716 (2013).

70. Kanno R. Secondary batteries—lithium rechargable systems | electrolytes: solid sulfide. In *Encyclopedia of Electrochemical Power Sources* (ed Garche, J.) (Elsevier, 2009).

71. Kim, J. H. et al. Encapsulation of S/SWNT with PANI Web for enhanced rate and cycle performance in lithium sulfur batteries. *Sci. Rep.* **5**, 8946 (2015).

72. Zhao, T. et al. Electrochemical lithiation mechanism of two-dimensional transition-metal dichalcogenide anode materials: intercalation versus conversion reactions. *J. Phys. Chem. C* **123**, 2139–2146 (2019).

73. Kakaei, K., Esrafili, M. D., & Ehsani, A. Alcohol oxidation and hydrogen evolution. In *Interface Science and Technology* (eds Kakaei, K., Esrafili, M. D., & Ehsani, A.) (Elsevier, 2019).

74. Xie, P. et al. Highly efficient decomposition of ammonia using high-entropy alloy catalysts. *Nat. Commun.* **10**, 4011 (2019).

75. Sun, Y. & Dai, S. High-entropy materials for catalysis: a new frontier. *Sci. Adv.* **7**, 1600 (2021).

76. Batchelor, T. A. A. et al. High-entropy alloys as a discovery platform for electrocatalysis. *Joule* **3**, 834–845 (2019).

77. Yu, L. et al. High-entropy alloy catalysts: from bulk to nano toward highly efficient carbon and nitrogen catalysis. *Carbon Energy* **4**, 731–761 (2022).

78. Sun, Y. et al. Battery-driven $N_2$ electrolysis enabled by high-entropy catalysts: from theoretical prediction to prototype model. *Small* **18**, 2106358 (2022).

79. Wang, S. & Xin, H. Predicting catalytic activity of high-entropy alloys for electrocatalysis. *Chem* **5**, 502–504 (2019).

80. Xie, Y. et al. Role of surface structure on Li-ion energy storage capacity of two-dimensional transition-metal carbides. *J. Am. Chem. Soc.* **136**, 6385–6394 (2014).

81. Wang, Q. et al. Multi-anionic and cationic compounds: new high entropy materials for advanced Li-ion batteries. *Energy Environ. Sci.* **12**, 2433–2442 (2019).

82. Muraleedharan, M. G. & Kent, P. R. C. Novel boron nitride MXenes as promising energy storage materials. *Nanoscale* **14**, 9086–9096 (2022).

83. Schweizer-Berberich, M. et al. The effect of Pt and Pd surface doping on the response of nanocrystalline tin dioxide gas sensors to CO. *Sensors Actuators B Chem.* **31**, 71–75 (1996).

84. Harrington, T. J. et al. Phase stability and mechanical properties of novel high entropy transition metal carbides. *Acta Mater.* **166**, 271–280 (2019).

85. Zhang, R.-Z., Gucci, F., Zhu, H., Chen, K. & Reece, M. J. Data-driven design of ecofriendly thermoelectric high-entropy sulfides. *Inorg. Chem.* **57**, 13027–13033 (2018).

86. Löffler, T. et al. Toward a paradigm shift in electrocatalysis using complex solid solution nanoparticles. *ACS Energy Lett.* **4**, 1206–1214 (2019).

87. Wang, Q., Velasco, L., Breitung, B. & Presser, V. High-entropy energy materials in the age of big data: a critical guide to next-generation synthesis and applications. *Adv. Energy Mater.* **11**, 2102355 (2021).

88. Liu, R. et al. Entropy as a gene-like performance indicator promoting thermoelectric materials. *Adv. Mater.* **29**, 1702712 (2017).

## Acknowledgements

## Author contributions

S.K.N., M.T., and B.C.W. conducted the literature search and prepared the first draft of the paper and the figures. V.P. proposed the idea. V.P. and B.A. supervised, reviewed, edited the paper, and acquired the funding. All authors revised and discussed the final manuscript.

## Competing interests

The authors declare no competing interests.

## Additional information

**Supplementary information** The online version contains supplementary material available at https://doi.org/10.1038/s43246-023-00341-y.

**Correspondence** and requests for materials should be addressed to Volker Presser or Babak Anasori.

**Peer review information** *Communications Materials* thanks the anonymous reviewers for their contribution to the peer review of this work. Primary Handling Editor: John Plummer. Peer reviewer reports are available.

**Reprints and permission information** is available at http://www.nature.com/reprints

**Publisher's note** Springer Nature remains neutral with regard to jurisdictional claims in published maps and institutional affiliations.

## 5. Conclusions and Outlook

The current Ph.D. thesis has focused on the exploration and potential applications of 2D nanolamellar materials in the context of the water-energy nexus. Specifically, we have investigated using select 2D layered materials as electrode materials for electrochemical water desalination, energy storage, and conversion.

After briefly introducing major desalination technologies currently employed worldwide, namely, thermal and membrane processes, the thesis has focused on electrochemical water desalination. The latter technology, which was first conceptualized in 1960, has ever since undergone major modifications both in terms of the electrode materials employed as well as the cell geometries developed. The electrode materials employed in electrochemical desalination research can be broadly categorized into three generations: (1st) carbon materials, (2nd) battery materials, and (3rd) electrocatalytic materials. Cell geometries, likewise, have evolved over the past few decades: from stagnant simple solid electrodes in a single-channel cell to flowing slurry electrodes in a multi-channel cell. Such a diverse menu of options then allows one to choose the right electrode materials, cell geometries, and operational conditions depending on the application in mind.

Once the foundation of the thesis is laid by reviewing a brief history of different electrode material types in electrochemical desalination research, a typical desalination setup, and its workings are introduced together with key performance metrics commonly reported in literature. Specifically, the desalination capacity, charge efficiency, energy consumption, and selectivity metrics are defined and expressed in the form of mathematical relationships. The thesis then turns to 2D materials as electrodes for electrochemical desalination. By focusing on MXene, a pseudocapacitive material, we demonstrated its unique capacitor-like electrochemical response achieved through ion intercalation. Through systematic investigations, this work evaluates the salt removal capacity, long-term stability, and structural changes of MXene during electrochemical cycling.

Further exploration of the 2D layered MXene material, this time in a multi-ionic electrolyte instead of a single-salt aqueous environment, sheds light on the ion intercalation dynamics in the layered MXene material. The time-dependent selective behavior of MXene in the desalination of a select group of alkaline and alkaline earth cations has shown how the cations give way to one another over the course of a desalination half-cycle, giving rise to 'kinetic'

selectivity. By use of a powerful in-situ online monitoring instrument, we provide insights into the relationship between MXene properties and its electrochemical desalination behavior.

We then expanded the scope beyond MXene and explored the potential of its sibling materials, such as MBene (transition metal boride) and transition metal dichalcogenides. We show-cased how these materials exhibited promise as electrodes for energy storage: MBene for lithium-ion battery and energy conversion and MXene-transition metal dichalcogenide hybrids as electrocatalysts for hydrogen production from water. The latter hybrid material was obtained through sulfidation heat treatment of MXene to sacrificially convert it into transition metal dichalcogenides, resulting in unique heterostructure morphologies. Future research can focus on optimizing the synthesis and structural engineering of 2D nanolamellar materials to enhance their performance and stability. The emerging field of functional two-dimensional high-entropy materials offers a great degree of structural tunability which can lead to significant advancements in electrochemical water desalination systems, energy storage, and energy conversion applications.

At the time of writing the current thesis, the electrochemical desalination research has advanced far beyond the once-envisioned 'desalination' application, meaning, mere sodium chloride removal from aqueous media. The electrochemical desalination technology indeed becomes economically more viable in salt removal from feedwaters of low salinity levels than thermal or membrane desalination processes. However, the entry-level costs to shut down the thermal or membrane desalination plants already in operation, and to replace them with new desalination plants based on electrochemical methods, might well outweigh the economic benefits of the latter in any short- or medium-term analysis. As a result, the water desalination policy-making might be reluctant to move toward the large-scale deployment of electrochemical desalination plants and instead be inclined more toward maintaining the status quo.

In the eyes of the author, the niche market for electrochemical methods of water treatment lies, therefore, in the realm of selective capture of target species. The latter could be either the selective removal of toxic ionic species such as lead, arsenic, and uranium, among others, or the value-added elements such as lithium, cobalt, or rare earth elements. Lithium, in particular, is of great economic value and strategic importance for the decades to come, given the rate of spread of electric vehicles and portable electronics. While lithium reserves in terrestrial sources are estimated to be 98 million tons, marine sources offer a virtually

unlimited supply estimated to be 260 billion tons. Given the lithium content in the latter source is very dilute (around 0.2 ppm) and co-exists with numerous competing ions, highly selective electrochemical methods need to be developed to extract lithium in significant concentrations that make the process economically feasible as well as environmentally sustainable. **Figure 29** schematically illustrates such a selective electrochemical method to capture value-added ionic species from different sources. Lithium sources with higher lithium content can be found in salt lakes, mining wastewaters, or in the leaching solution of spent lithium-ion batteries. The aqueous solutions from the latter sources are often far from neutral pH and also contain many other competing ions. As such, the development of robust electrode materials with long service lives that can handle such harsh conditions is of utmost importance.
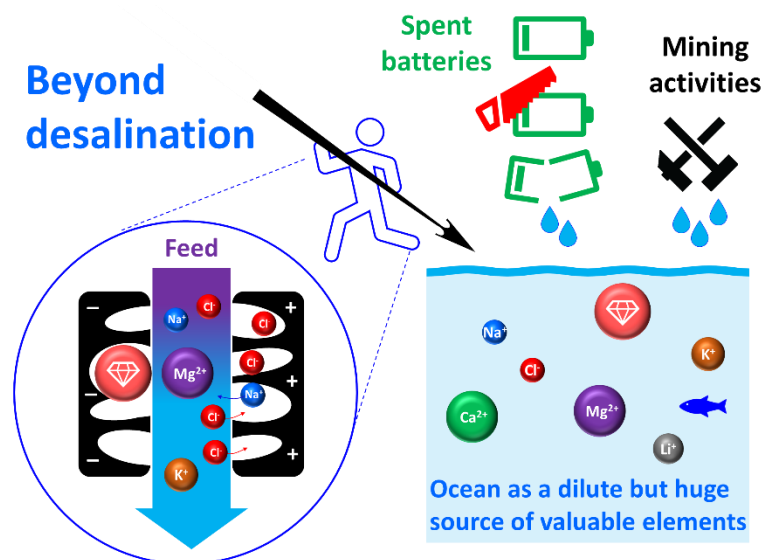


**Figure 29:** Schematic illustration of selective recovery of value-added elements from different aqueous sources.

A huge untapped potential also lies in the so-called 'fuel cell desalination' system, where hydrogen is used as a fuel to drive the salt ions away from the seawater, resulting in water desalination and generation of electricity at the same time. This concept can help mitigate the intermittent nature of renewable energy generation by peak shaving and load shifting. That is, the excess electricity generated during the day is converted into hydrogen fuel using an electrolyzer. The hydrogen fuel is later consumed by a fuel cell desalination unit during peak energy demand hours to generate clean water and electricity. Challenges associated with such a concept would be the costly platinum-based electrodes in a fuel cell desalination setup, as well as the electrodes' susceptibility to being poisoned by impurities in the fuel. As such, the

development of versatile electrocatalysts beyond platinum, which are cheap and are capable of processing fuels beyond hydrogen, such as syngas (mixture of hydrogen and carbon monoxide) or methane, is imperative toward the successful deployment of such sustainable water-energy nexus solutions.

# 6. Abbreviations

| | |
|---|---|
| AEM | Anion exchange membrane |
| CE | Charge efficiency |
| CEM | Cation exchange membrane |
| CNT | Carbon nanotube |
| CDI | Capacitive deionization |
| DC | Desalination capacity |
| DMSO | Dimethyl sulfoxide |
| E | Electrode potential |
| ED | Electrodialysis |
| EDX | Energy-dispersive X-ray spectroscopy |
| e | Elementary charge, $1.60217663 \times 10^{-19}$ C |
| F | Faraday constant, 96485 C mol$^{-1}$ |
| HER | Hydrogen evolution reaction |
| HCl | Hydrochloric acid |
| HF | Hydrofluoric acid |
| IUPAC | International Union of Pure and Applied Chemistry |
| I | Current |
| $I_{Leak}$ | Leakage current |
| $k_B$ | Boltzmann constant, $1.380649 \times 10^{-23}$ m$^2$ kg s$^{-2}$ K$^{-2}$ |
| MED | Multiple-effect distillation |
| MSF | Multi-stage flash distillation |
| mM | Millimolar, $1 \times 10^{-3}$ mol L$^{-1}$ |
| $M_{NaCl}$ | NaCl molar mass, 58.44 g mol$^{-1}$ |
| $m_{total}$ | Total mass of both negative and positive electrodes combined |
| $N_A$ | Avogadro constant, $6.02214076 \times 10^{23}$ mol$^{-1}$ |
| OER | Oxygen evolution reaction |
| OLC | Onion-like carbon |
| q | Electrical charge |
| RO | Reverse osmosis |
| RED | Reverse electrodialysis |
| SEC | Specific energy consumption |
| SEM | Scanning electron microscopy |
| TBAOH | Tetrabutylammonium hydroxide |
| TMD | Transition metal dichalcogenide |
| VCD | Vapor compression distillation |
| w | With |
| w/o | Without |
| XRD | X-ray diffraction |
| $\nu$ | Flow rate |

# 7. References

[1] N.K. Arora, I. Mishra, United Nations Sustainable Development Goals 2030 and environmental sustainability: race against time, Environmental Sustainability, 2 (2019) 339-342.

[2] H.B. Li, L.D. Zou, L.K. Pan, Z. Sun, Novel Graphene-Like Electrodes for Capacitive Deionization, Environmental Science & Technology, 44 (2010) 8692-8697.

[3] P.Y. Liu, T.T. Yan, L.Y. Shi, H.S. Park, X.C. Chen, Z.G. Zhao, D.S. Zhang, Graphene-based materials for capacitive deionization, Journal of Materials Chemistry A, 5 (2017) 13907-13943.

[4] P. Srimuk, J. Lee, S. Fleischmann, S. Choudhury, N. Jäckel, M. Zeiger, C. Kim, M. Aslan, V. Presser, Faradaic deionization of brackish and sea water via pseudocapacitive cation and anion intercalation into few-layered molybdenum disulfide, Journal of Materials Chemistry A, 5 (2017) 15640-15649.

[5] P. Srimuk, J. Lee, A. Tolosa, C. Kim, M. Aslan, V. Presser, Titanium disulfide: a promising low-dimensional electrode material for sodium ion intercalation for seawater desalination, Chemistry of Materials, 29 (2017) 9964-9973.

[6] P. Srimuk, J. Lee, S. Fleischmann, M. Aslan, C. Kim, V. Presser, Potential-dependent, switchable ion selectivity in aqueous media using titanium disulfide, ChemSusChem, 11 (2018) 2091-2100.

[7] K. Rasool, R.P. Pandey, P.A. Rasheed, S. Buczek, Y. Gogotsi, K.A. Mahmoud, Water treatment and environmental remediation applications of two-dimensional metal carbides (MXenes), Materials Today, 30 (2019).

[8] P. Srimuk, J. Halim, J. Lee, Q.Z. Tao, J. Rosen, V. Presser, Two-dimensional molybdenum carbide (MXene) with divacancy ordering for brackish and seawater desalination via cation and anion intercalation, ACS Sustainable Chemistry & Engineering, 6 (2018) 3739-3747.

[9] P. Sharan, T.J. Yoon, S.M. Jaffe, T. Ju, R.P. Currier, A.T. Findikoglu, Can capacitive deionization outperform reverse osmosis for brackish water desalination?, Cleaner Engineering and Technology, 3 (2021) 100102.

[10] M. Metzger, M.M. Besli, S. Kuppan, S. Hellstrom, S. Kim, E. Sebti, C.V. Subban, J. Christensen, Techno-economic analysis of capacitive and intercalative water deionization, Energy & Environmental Science, 13 (2020) 1544-1560.

[11] J.G. Gamaethiralalage, K. Singh, S. Sahin, J. Yoon, M. Elimelech, M.E. Suss, P. Liang, P.M. Biesheuvel, R.L. Zornitta, L.C.P.M. de Smet, Recent advances in ion selectivity with capacitive deionization, Energy & Environmental Science, 14 (2021) 1095-1120.

[12] C. Dang, A.S. Helal, L. Zhu, G. Xu, M. Zhu, Industrial pathways to lithium extraction from seawater: Challenges and perspectives, Nano Research Energy, 2 (2023) e9120059.

[13] P.G. Youssef, R.K. Al-Dadah, S.M. Mahmoud, Comparative Analysis of Desalination Technologies, Energy Procedia, 61 (2014) 2604-2607.

[14] A.D. Khawaji, I.K. Kutubkhanah, J.M. Wie, Advances in seawater desalination technologies, Desalination, 221 (2008) 47-69.

[15] D. Curto, V. Franzitta, A. Guercio, A review of the water desalination technologies, Applied Sciences, 11 (2021) 670.

[16] J. Kucera, Reverse Osmosis Principles, in: Reverse Osmosis, John Wiley & Sons, 2015, pp. 19-24.

[17] D.U. Lawal, M.A. Antar, K.G. Ismaila, A. Khalifa, S.M. Alawad, Hybrid multi-stage flash (MSF) and membrane distillation (MD) desalination system for energy saving and brine minimization, Desalination, 548 (2023) 116231.

[18] D.M.K. Al-Gobaisi, A. Hassan, G.P. Rao, A. Sattar, A. Woldai, R. Borsani, Towards improved automation for desalination processes, Part I: Advanced control, Desalination, 97 (1994) 469-506.

[19] G.P. Rao, D.M.K. Al-Gobaisi, A. Hassan, A. Kurdali, R. Borsani, M. Aziz, Towards improved automation for desalination processes, Part II: Intelligent control, Desalination, 97 (1994) 507-528.

[20] I. Khoshrou, M.R. Jafari Nasr, K. Bakhtari, New opportunities in mass and energy consumption of the Multi-Stage Flash Distillation type of brackish water desalination process, Solar Energy, 153 (2017) 115-125.

[21] P.R. Bom, Selection of Alloys For Multi-Stage Flash Distillation Plant, British Corrosion Journal, 5 (1970) 258-263.

[22] S.H. Chae, J.H. Kim, Chapter Four - Integration of PRO into Desalination Processes, in: K. Touati, F. Tadeo, S.H. Chae, J.H. Kim, O. Alvarez-Silva (Eds.) Pressure Retarded Osmosis, Academic Press, 2017, pp. 129-151.

[23] R. Semiat, Water Purification: Materials and Technologies, in: K.H.J. Buschow, R.W. Cahn, M.C. Flemings, B. Ilschner, E.J. Kramer, S. Mahajan, P. Veyssière (Eds.) Encyclopedia of Materials: Science and Technology, Elsevier, Oxford, 2010, pp. 1-4.

[24] A. Mansour, N. Müller, A review of flash evaporation phenomena and resulting shock waves, Experimental Thermal and Fluid Science, 107 (2019) 146-168.

[25] H.T. El-Dessouky, H.M. Ettouney, Y. Al-Roumi, Multi-stage flash desalination: present and future outlook, Chemical Engineering Journal, 73 (1999) 173-190.

[26] X. Yan, H. Noguchi, H. Sato, Y. Tachibana, K. Kunitomi, R. Hino, Study of an incrementally loaded multistage flash desalination system for optimum use of sensible waste heat from nuclear power plant, International Journal of Energy Research, 37 (2013) 1811-1820.

[27] A.G. Olabi, K. Elsaid, M.K.H. Rabaia, A.A. Askalany, M.A. Abdelkareem, Waste heat-driven desalination systems: Perspective, Energy, 209 (2020) 118373.

[28] V.G. Gude, Energy storage for desalination processes powered by renewable energy and waste heat sources, Applied Energy, 137 (2015) 877-898.

[29] M. Al-Shammiri, M. Safar, Multi-effect distillation plants: state of the art, Desalination, 126 (1999) 45-59.

[30] A. Ophir, F. Lokiec, Advanced MED process for most economical sea water desalination, Desalination, 182 (2005) 187-198.

[31] H.T. El-Dessouky, H.M. Ettouney, F. Al-Juwayhel, Multiple Effect Evaporation—Vapour Compression Desalination Processes, Chemical Engineering Research and Design, 78 (2000) 662-676.

[32] O.A. Hamed, A.M. Zamamiri, S. Aly, N. Lior, Thermal performance and exergy analysis of a thermal vapor compression desalination system, Energy Conversion and Management, 37 (1996) 379-387.

[33] M.A. Jamil, S.M. Zubair, On thermoeconomic analysis of a single-effect mechanical vapor compression desalination system, Desalination, 420 (2017) 292-307.

[34] M.A. Darwish, Thermal analysis of vapor compression desalination system, Desalination, 69 (1988) 275-295.

[35] R. Paulen, M. Fikar, R. Paulen, M. Fikar, Membrane processes, Optimal Operation of Batch Membrane Processes, (2016) 1-25.

[36] M. Park, J. Park, E. Lee, J. Khim, J. Cho, Application of nanofiltration pretreatment to remove divalent ions for economical seawater reverse osmosis desalination, Desalination and Water Treatment, 57 (2016) 20661-20670.

[37] A.B. Nasr, C. Charcosset, R.B. Amar, K. Walha, Defluoridation of water by nanofiltration, Journal of Fluorine Chemistry, 150 (2013) 92-97.

[38] Z. Yang, Y. Zhou, Z. Feng, X. Rui, T. Zhang, Z. Zhang, A review on reverse osmosis and nanofiltration membranes for water purification, Polymers, 11 (2019) 1252.

[39] Working principle of cross-flow filtration, Membrane Technology, published in 2019 https://www.ps-prozesstechnik.com/en/membrane-technology/membrane-process-development/membrane-technology-principle.html.

[40] Y. Yoon, R.M. Lueptow, Removal of organic contaminants by RO and NF membranes, Journal of Membrane Science, 261 (2005) 76-86.

[41] K. Kezia, J. Lee, A.J. Hill, S.E. Kentish, Convective transport of boron through a brackish water reverse osmosis membrane, Journal of Membrane Science, 445 (2013) 160-169.

[42] A. Alexiadis, J. Bao, D.F. Fletcher, D.E. Wiley, D.J. Clements, Analysis of the Dynamic Response of a Reverse Osmosis Membrane to Time-Dependent Transmembrane Pressure Variation, Industrial & Engineering Chemistry Research, 44 (2005) 7823-7834.

[43] M.A. Anderson, A.L. Cudero, J. Palma, Capacitive deionization as an electrochemical means of saving energy and delivering clean water. Comparison to present desalination practices: Will it compete?, Electrochimica Acta, 55 (2010) 3845-3856.

[44] S. Yang, S.-i. Jeon, H. Kim, J. Choi, J.-g. Yeo, H.-r. Park, D.K. Kim, Stack Design and Operation for Scaling Up the Capacity of Flow-Electrode Capacitive Deionization Technology, ACS Sustainable Chemistry & Engineering, 4 (2016) 4174-4180.

[45] L. Xu, Y. Mao, Y. Zong, D. Wu, Scale-up desalination: Membrane-current collector assembly in flow-electrode capacitive deionization system, Water Research, 190 (2021) 116782.

[46] J. Nordstrand, J. Dutta, Design principles for enhanced up-scaling of flow-through capacitive deionization for water desalination, Desalination, 500 (2021) 114842.

[47] J.J. Lado, E. García-Quismondo, I. Almonacid, G. García, G. Castro, J. Palma, A successful transition from a vanadium redox flow battery stack to an energy efficient electrochemical desalination module, Journal of Environmental Chemical Engineering, 9 (2021) 106875.

[48] J. Lee, P. Srimuk, S. Carpier, J. Choi, R.L. Zornitta, C. Kim, M. Aslan, V. Presser, Confined Redox Reactions of Iodide in Carbon Nanopores for Fast and Energy-Efficient Desalination of Brackish Water and Seawater, ChemSusChem, 11 (2018) 3460-3472.

[49] C. Tsouris, R. Mayes, J. Kiggans, K. Sharma, S. Yiacoumi, D. DePaoli, S. Dai, Mesoporous Carbon for Capacitive Deionization of Saline Water, Environmental Science & Technology, 45 (2011) 10243-10249.

[50] S.-Y. Pan, A.Z. Haddad, A. Kumar, S.-W. Wang, Brackish water desalination using reverse osmosis and capacitive deionization at the water-energy nexus, Water Research, 183 (2020) 116064.

[51] Y. Zhang, C. Prehal, H. Jiang, Y. Liu, G. Feng, V. Presser, Ionophobicity of carbon sub-nanometer pores enables efficient desalination at high salinity, Cell Reports Physical Science, 3 (2021) 100689.

[52] S. Bi, Y. Zhang, L. Cervini, T. Mo, J.M. Griffin, V. Presser, G. Feng, Permselective ion electrosorption of subnanometer pores at high molar strength enables capacitive deionization of saline water, Sustainable Energy & Fuels, 4 (2020) 1285-1295.

[53] A. Kalfa, B. Shapira, A. Shopin, I. Cohen, E. Avraham, D. Aurbach, Capacitive deionization for wastewater treatment: Opportunities and challenges, Chemosphere, 241 (2020) 125003.

[54] D.I. Kim, G. Gwak, P. Dorji, D. He, S. Phuntsho, S. Hong, H. Shon, Palladium Recovery through Membrane Capacitive Deionization from Metal Plating Wastewater, ACS Sustainable Chemistry & Engineering, 6 (2018) 1692-1701.

[55] P. Simon, Y. Gogotsi, Charge storage mechanism in nanoporous carbons and its consequence for electrical double layer capacitors, Philosophical Transactions of the Royal Society A, 368 (2010) 3457-3467.

[56] P.M. Biesheuvel, S. Porada, M. Elimelech, J.E. Dykstra, Tutorial review of reverse osmosis and electrodialysis, Journal of Membrane Science, 647 (2022) 120221.

[57] M. Sadrzadeh, T. Mohammadi, Sea water desalination using electrodialysis, Desalination, 221 (2008) 440-447.

[58] M. Tedesco, H.V.M. Hamelers, P.M. Biesheuvel, Nernst-Planck transport theory for (reverse) electrodialysis: I. Effect of co-ion transport through the membranes, Journal of Membrane Science, 510 (2016) 370-381.

[59] T.M. Mubita, S. Porada, P.M. Biesheuvel, A. van der Wal, J.E. Dykstra, Strategies to increase ion selectivity in electrodialysis, Separation and Purification Technology, 292 (2022) 120944.

[60] D.A. Vermaas, S. Bajracharya, B.B. Sales, M. Saakes, B. Hamelers, K. Nijmeijer, Clean energy generation using capacitive electrodes in reverse electrodialysis, Energy & Environmental Science, 6 (2013) 643-651.

[61] Y. Mei, C.Y. Tang, Recent developments and future perspectives of reverse electrodialysis technology: A review, Desalination, 425 (2018) 156-174.

[62] C. Tang, M.L. Bruening, Ion separations with membranes, Journal of Polymer Science, 58 (2020) 2831-2856.

[63] K.S. Spiegler, Y.M. El-Sayed, The energetics of desalination processes, Desalination, 134 (2001) 109-128.

[64] L. Wang, C. Violet, R.M. DuChanois, M. Elimelech, Derivation of the Theoretical Minimum Energy of Separation of Desalination Processes, Journal of Chemical Education, 97 (2020) 4361-4369.

[65] K.N. Knust, D. Hlushkou, U. Tallarek, R.M. Crooks, Electrochemical Desalination for a Sustainable Water Future, ChemElectroChem, 1 (2014) 850-857.

[66] E. Nagy, Chapter 21 - Pressure-Retarded Osmosis (PRO) Process, in: E. Nagy (Ed.) Basic Equations of Mass Transport Through a Membrane Layer (Second Edition), Elsevier, 2019, pp. 505-531.

[67] GROUNDWATER SALINITY, Department of Water, Land and Biodiversity Conservation of Australia, published in 2019 https://underdaledrillers.com.au/wp-content/uploads/2019/09/groundwater-salinity-chart.pdf.

[68] C. Harb, J. Pan, S. DeVilbiss, B. Badgley, L.C. Marr, D.G. Schmale III, H. Foroutan, Increasing freshwater salinity impacts aerosolized bacteria, Environmental Science & Technology, 55 (2021) 5731-5741.

[69] Measuring Salinity of Water, HORIBA-Group, published in 2016 https://www.horiba.com/int/water-quality/applications/water-wastewater/measuring-salinity-of-water/.

[70] Saline Water and Salinity, Water Science School, published in 2018 https://www.usgs.gov/special-topics/water-science-school/science/saline-water-and-salinity.

[71] T.D. Jickells, R. Chester, Marine geochemistry, John Wiley & Sons, 2012.

[72] A.J. Karabelas, C.P. Koutsou, M. Kostoglou, D.C. Sioutopoulos, Analysis of specific energy consumption in reverse osmosis desalination processes, Desalination, 431 (2018) 15-21.

[73] B. Suphanit, A. Bischert, P. Narataruksa, Exergy loss analysis of heat transfer across the wall of the dividing-wall distillation column, Energy, 32 (2007) 2121-2134.

[74] M.A. Darwish, F.A. Yousef, N.M. Al-Najem, Energy consumption and costs with a multi-stage flashing (MSF) desalting system, Desalination, 109 (1997) 285-302.

[75] M. Alhaj, A. Mabrouk, S.G. Al-Ghamdi, Energy efficient multi-effect distillation powered by a solar linear Fresnel collector, Energy Conversion and Management, 171 (2018) 576-586.

[76] J. Veza, Mechanical vapour compression desalination plants — A case study, Desalination, 101 (1995) 1-10.

[77] Z. Triki, M. Bouaziz, M. Boumaza, Techno-economic feasibility of wind-powered reverse osmosis brackish water desalination systems in southern Algeria, Desalination and Water Treatment, 52 (2014) 1745-1760.

[78] A. von Gottberg, A. Pang, J.L. Talavera, Optimizing water recovery and energy consumption for seawater RO systems, GE Water & Process Technologies, 510 (2005) 1-5.

[79] B. van Limpt, A. van der Wal, Water and chemical savings in cooling towers by using membrane capacitive deionization, Desalination, 342 (2014) 148-155.

[80] E. Jones, M. Qadir, M.T.H. van Vliet, V. Smakhtin, S.-m. Kang, The state of desalination and brine production: A global outlook, Science of The Total Environment, 657 (2019) 1343-1356.

[81] L. Wang, Y. Zhang, K. Moh, V. Presser, From capacitive deionization to desalination batteries and desalination fuel cells, Current Opinion in Electrochemistry, 29 (2021) 100758.

[82] M. Torkamanzadeh, C. Kök, P.R. Burger, P. Ren, Y. Zhang, J. Lee, C. Kim, V. Presser, Best practice for electrochemical water desalination data generation and analysis, Cell Reports Physical Science, (2023) 101661.

[83] P. Długołęcki, A. van der Wal, Energy recovery in membrane capacitive deionization, Environmental Science & Technology, 47 (2013) 4904-4910.

[84] J. Kang, T. Kim, H. Shin, J. Lee, J.-I. Ha, J. Yoon, Direct energy recovery system for membrane capacitive deionization, Desalination, 398 (2016) 144-150.

[85] A. Rommerskirchen, C.J. Linnartz, D. Muller, L.K. Willenberg, M. Wessling, Energy Recovery and Process Design in Continuous Flow Electrode Capacitive Deionization Processes, ACS Sustainable Chemistry & Engineering, 6 (2018) 13007-13015.

[86] S. Porada, L. Weinstein, R. Dash, A. Van Der Wal, M. Bryjak, Y. Gogotsi, P. Biesheuvel, Water desalination using capacitive deionization with microporous carbon electrodes, ACS Applied Materials & Interfaces, 4 (2012) 1194-1199.

[87] P. Ren, M. Torkamanzadeh, X. Zhang, M. Twardoch, C. Kim, V. Presser, Conductive carbon additives: Friend or foe of capacitive deionization with activated carbon?, Carbon, 213 (2023) 118191.

[88] J. Rouquerol, D. Avnir, C.W. Fairbridge, D.H. Everett, J.M. Haynes, N. Pernicone, J.D.F. Ramsay, K.S.W. Sing, K.K. Unger, Recommendations for the characterization of porous solids (Technical Report), Pure and Applied Chemistry, 66 (1994) 1739-1758.

[89] K. Kaneko, Determination of pore size and pore size distribution: 1. Adsorbents and catalysts, Journal of Membrane Science, 96 (1994) 59-89.

[90] R.J. White, V. Budarin, R. Luque, J.H. Clark, D.J. Macquarrie, Tuneable porous carbonaceous materials from renewable resources, Chemical Society Reviews, 38 (2009) 3401-3418.

[91] M. Ruike, T. Kasu, N. Setoyama, T. Suzuki, K. Kaneko, Inaccessible pore characterization of less-crystalline microporous solids, The Journal of Physical Chemistry, 98 (1994) 9594-9600.

[92] J.W. Blair, G.W. Murphy, Electrochemical demineralization of water with porous electrodes of large surface area, in: ACS (Ed.) Saline Water Conversion, American Chemical Society, Washington DC, 1960, pp. 206-223.

[93] S. Porada, R. Zhao, A. van der Wal, V. Presser, P.M. Biesheuvel, Review on the science and technology of water desalination by capacitive deionization, Progress in Materials Science, 58 (2013) 1388-1442.

[94] M.E. Suss, S. Porada, X. Sun, P.M. Biesheuvel, J. Yoon, V. Presser, Water desalination via capacitive deionization: what is it and what can we expect from it?, Energy & Environmental Science, 8 (2015) 2296-2319.

[95] M.-W. Ryoo, J.H. Kim, G. Seo, Role of titania incorporated on activated carbon cloth for capacitive deionization of NaCl solution, Journal of Colloid and Interface Science, 264 (2003) 414-419.

[96] C. Kim, J. Lee, S. Kim, J. Yoon, $TiO_2$ sol-gel spray method for carbon electrode fabrication to enhance desalination efficiency of capacitive deionization, Desalination, 342 (2014) 70-74.

[97] P. Srimuk, L. Ries, M. Zeiger, S. Fleischmann, N. Jäckel, A. Tolosa, B. Krüner, M. Aslan, V. Presser, High performance stability of titania decorated carbon for desalination with capacitive deionization in oxygenated water, Rsc Advances, 6 (2016) 106081-106089.

[98] J.-B. Lee, K.-K. Park, H.-M. Eum, C.-W. Lee, Desalination of a thermal power plant wastewater by membrane capacitive deionization, Desalination, 196 (2006) 125-134.

[99] R. McNair, L. Cseri, G. Szekely, R. Dryfe, Asymmetric Membrane Capacitive Deionization Using Anion-Exchange Membranes Based on Quaternized Polymer Blends, ACS Applied Polymer Materials, 2 (2020) 2946-2956.

[100] R. McNair, G. Szekely, R.A.W. Dryfe, Ion-Exchange Materials for Membrane Capacitive Deionization, ACS ES&T Water, 1 (2021) 217-239.

[101] P.M. Biesheuvel, A. van der Wal, Membrane capacitive deionization, Journal of Membrane Science, 346 (2010) 256-262.

[102] M. Pasta, C.D. Wessells, Y. Cui, F. La Mantia, A Desalination Battery, Nano Letters, 12 (2012) 839-843.

[103] J. Lee, S. Kim, J. Yoon, Rocking Chair Desalination Battery Based on Prussian Blue Electrodes, ACS Omega, 2 (2017) 1653-1659.

[104] M.R. Lukatskaya, O. Mashtalir, C.E. Ren, Y. Dall'Agnese, P. Rozier, P.L. Taberna, M. Naguib, P. Simon, M.W. Barsoum, Y. Gogotsi, Cation Intercalation and High Volumetric Capacitance of Two-Dimensional Titanium Carbide, Science, 341 (2013) 1502-1505.

[105] M. Naguib, J. Halim, J. Lu, K.M. Cook, L. Hultman, Y. Gogotsi, M.W. Barsoum, New Two-Dimensional Niobium and Vanadium Carbides as Promising Materials for Li-Ion Batteries, Journal of the American Chemical Society, 135 (2013) 15966-15969.

[106] P. Srimuk, F. Kaasik, B. Krüner, A. Tolosa, S. Fleischmann, N. Jäckel, M.C. Tekeli, M. Aslan, M.E. Suss, V. Presser, MXene as a novel intercalation-type pseudocapacitive cathode and anode for capacitive deionization, Journal of Materials Chemistry A, 4 (2016) 18265-18271.

[107] B. Liu, L. Yu, F. Yu, J. Ma, In-situ formation of uniform $V_2O_5$ nanocuboid from $V_2C$ MXene as electrodes for capacitive deionization with higher structural stability and ion diffusion ability, Desalination, 500 (2021) 114897.

[108] W.Z. Bao, X. Tang, X. Guo, S. Choi, C.Y. Wang, Y. Gogotsi, G.X. Wang, Porous Cryo-Dried MXene for Efficient Capacitive Deionization, Joule, 2 (2018) 778-787.

[109] B.W. Chen, Y.F. Wang, Z. Chang, X.W. Wang, M.X. Li, X. Liu, L.X. Zhang, Y.P. Wu, Enhanced capacitive desalination of $MnO_2$ by forming composite with multi-walled carbon nanotubes, Rsc Advances, 6 (2016) 6730-6736.

[110] B.W. Byles, B. Hayes-Oberst, E. Pomerantseva, Ion Removal Performance, Structural/Compositional Dynamics, and Electrochemical Stability of Layered Manganese Oxide Electrodes in Hybrid Capacitive Deionization, ACS Applied Materials & Interfaces, 10 (2018) 32313-32322.

[111] P. Srimuk, S. Husmann, V. Presser, Low voltage operation of a silver/silver chloride battery with high desalination capacity in seawater, Rsc Advances, 9 (2019) 14849-14858.

[112] J. Ahn, J. Lee, S. Kim, C. Kim, J. Lee, P. Biesheuvel, J. Yoon, High performance electrochemical saline water desalination using silver and silver-chloride electrodes, Desalination, 476 (2020) 114216.

[113] D.-H. Nam, K.-S. Choi, Bismuth as a New Chloride-Storage Electrode Enabling the Construction of a Practical High Capacity Desalination Battery, Journal of the American Chemical Society, 139 (2017) 11055-11063.

[114] D.-H. Nam, K.-S. Choi, Electrochemical Desalination Using Bi/BiOCl Electrodialysis Cells, ACS Sustainable Chemistry & Engineering, 6 (2018) 15455-15462.

[115] J. Lee, P. Srimuk, K. Aristizabal, C. Kim, S. Choudhury, Y.C. Nah, F. Mucklich, V. Presser, Pseudocapacitive Desalination of Brackish Water and Seawater with Vanadium-Pentoxide-Decorated Multiwalled Carbon Nanotubes, ChemSusChem, 10 (2017) 3611-3623.

[116] P. Srimuk, X. Su, J. Yoon, D. Aurbach, V. Presser, Charge-transfer materials for electrochemical water desalination, ion separation and the recovery of elements, Nature Reviews Materials, 5 (2020) 517-538.

[117] M. Torkamanzadeh, L. Wang, Y. Zhang, O. Budak, P. Srimuk, V. Presser, MXene/activated-carbon hybrid capacitive deionization for permselective ion removal at low and high salinity, ACS Applied Materials & Interfaces, 12 (2020) 26013-26025.

[118] J. Lee, S. Kim, C. Kim, J. Yoon, Hybrid capacitive deionization to enhance the desalination performance of capacitive techniques, Energy & Environmental Science, 7 (2014) 3683-3689.

[119] W. Zhao, M. Ding, L. Guo, H.Y. Yang, Dual-Ion Electrochemical Deionization System with Binder-Free Aerogel Electrodes, Small, 0 (2019) 1805505.

[120] L. Guo, R. Mo, W. Shi, Y. Huang, Z.Y. Leong, M. Ding, F. Chen, H.Y. Yang, A Prussian blue anode for high performance electrochemical deionization promoted by the faradaic mechanism, Nanoscale, 9 (2017) 13305-13312.

[121] T. Kim, C.A. Gorski, B.E. Logan, Low energy desalination using battery electrode deionization, Environmental Science & Technology Letters, 4 (2017) 444-449.

[122] S. Arnold, L. Wang, Ö. Budak, M. Aslan, P. Srimuk, V. Presser, Antimony alloying electrode for high-performance sodium removal: how to use a battery material not stable in aqueous media for saline water remediation, Journal of Materials Chemistry A, 9 (2021) 585-596.

[123] P. Srimuk, L. Wang, Ö. Budak, V. Presser, High-performance ion removal via zinc–air desalination, Electrochemistry Communications, 115 (2020) 106713.

[124] A. Mahmood, J.H. Kim, J.-W. Park, Development of an effective operation system in a magnesium-air desalination cell for electricity production with nitrogen and phosphorus removal, Desalination, 545 (2023) 116164.

[125] S.M. Shariatpannahi, M.S. Hatamipour, S. Rashid-Nadimi, M.K. Amini, Simultaneous saltwater desalination and power generation using an aluminum-powered cell, Journal of Environmental Chemical Engineering, 9 (2021) 104802.

[126] M. Ghahari, S. Rashid-Nadimi, H. Bemana, Metal-air desalination battery: Concurrent energy generation and water desalination, Journal of Power Sources, 412 (2019) 197-203.

[127] A.G. Olabi, E.T. Sayed, T. Wilberforce, A. Jamal, A.H. Alami, K. Elsaid, S.M.A. Rahman, S.K. Shah, M.A. Abdelkareem, Metal-Air Batteries—A Review, Energies, 14 (2021) 7373.

[128] Y. Zhang, L. Wang, V. Presser, Electrocatalytic fuel cell desalination for continuous energy and freshwater generation, Cell Reports Physical Science, 2 (2021) 100416.

[129] L. Wang, S. Arnold, P. Ren, Q. Wang, J. Jin, Z. Wen, V. Presser, Redox flow battery for continuous and energy-effective lithium recovery from aqueous solution, ACS Energy Letters, 7 (2022) 3539-3544.

[130] Y. Zhang, P. Ren, Y. Liu, V. Presser, Particle size distribution influence on capacitive deionization: Insights for electrode preparation, Desalination, 525 (2022) 115503.

[131] M.A. Alkhadra, X. Su, M.E. Suss, H. Tian, E.N. Guyes, A.N. Shocron, K.M. Conforti, J.P. de Souza, N. Kim, M. Tedesco, Electrochemical methods for water purification, ion separations, and energy conversion, Chemical Reviews, (2022).

[132] X. Huang, X. Guo, Q. Dong, L. Liu, R. Tallon, J. Chen, Zero-wastewater capacitive deionization: selective removal of heavy metal ions in tap water assisted by phosphate ions, Environ. Sci. Nano, 6 (2019) 3225-3231.

[133] L. Wang, L. Deligniere, S. Husmann, R. Leiner, C. Bahr, S. Zhang, C. Dun, M.M. Montemore, M. Gallei, J.J. Urban, C. Kim, V. Presser, Selective $Pb^{2+}$ removal and electrochemical regeneration of fresh and recycled FeOOH, Nano Res., 16 (2023) 9352–9363.

[134] Q. Dong, X. Guo, X. Huang, L. Liu, R. Tallon, B. Taylor, J. Chen, Selective removal of lead ions through capacitive deionization: Role of ion-exchange membrane, Chemical Engineering Journal, 361 (2019) 1535-1542.

[135] Q. Peng, L. Liu, Y. Luo, Y. Zhang, W. Tan, F. Liu, S.L. Suib, G. Qiu, Cadmium removal from aqueous solution by a deionization supercapacitor with a birnessite electrode, ACS Applied Materials & Interfaces, 8 (2016) 34405-34413.

[136] N. Vieceli, C. Vonderstein, T. Swiontekc, S. Stopić, C. Dertmann, R. Sojka, N. Reinhardt, C. Ekberg, B. Friedrich, M. Petranikova, Recycling of Li-ion batteries from industrial processing: upscaled hydrometallurgical treatment and recovery of high purity manganese by solvent extraction, Solvent Extraction and Ion Exchange, 41 (2023) 205-220.

[137] D. Mo, G. Yu, Z. Zeng, S. Ni, S. Zhang, X. Sun, Separation of lithium and transition metals in leaching solution of used lithium ion battery with Sec-octylphenoxyacetic acid, ChemistrySelect, 8 (2023) e202301036.

[138] E. Asadi Dalini, G. Karimi, S. Zandevakili, Treatment of valuable metals from leaching solution of spent lithium-ion batteries, Minerals Engineering, 173 (2021) 107226.

[139] R. Trocoli, G.K. Bidhendi, F. La Mantia, Lithium recovery by means of electrochemical ion pumping: a comparison between salt capturing and selective exchange, Journal of Physics: Condensed Matter, 28 (2016) 114005.

[140] R. Trócoli, C. Erinmwingbovo, F. La Mantia, Optimized lithium recovery from brines by using an electrochemical ion-pumping process based on $\lambda$-$MnO_2$ and nickel hexacyanoferrate, ChemElectroChem, 4 (2017) 143-149.

[141] R. Trócoli, A. Battistel, F.L. Mantia, Selectivity of a lithium-recovery process based on $LiFePO_4$, Chemistry – A European Journal, 20 (2014) 9888-9891.

[142] L. Wang, M. Torkamanzadeh, A. Majed, Y. Zhang, Q. Wang, B. Breitung, G. Feng, M. Naguib, V. Presser, Time-dependent cation selectivity of titanium carbide MXene in aqueous solution, Advanced Sustainable Systems, 6 (2022) 2100383.

[143] S.-J. Seo, H. Jeon, J.K. Lee, G.-Y. Kim, D. Park, H. Nojima, J. Lee, S.-H. Moon, Investigation on removal of hardness ions by capacitive deionization (CDI) for water softening applications, Water Research, 44 (2010) 2267-2275.

[144] J.E. Dykstra, J. Dijkstra, A. van der Wal, H.V.M. Hamelers, S. Porada, On-line method to study dynamics of ion adsorption from mixtures of salts in capacitive deionization, Desalination, 390 (2016) 47-52.

[145] R. Zhao, M. van Soestbergen, H.H.M. Rijnaarts, A. van der Wal, M.Z. Bazant, P.M. Biesheuvel, Time-dependent ion selectivity in capacitive charging of porous electrodes, Journal of Colloid and Interface Science, 384 (2012) 38-44.

[146] J. Choi, P. Dorji, H.K. Shon, S. Hong, Applications of capacitive deionization: Desalination, softening, selective removal, and energy efficiency, Desalination, 449 (2019) 118-130.

[147] K. Singh, Z. Qian, P. Biesheuvel, H. Zuilhof, S. Porada, L.C. de Smet, Nickel hexacyanoferrate electrodes for high mono/divalent ion-selectivity in capacitive deionization, Desalination, 481 (2020) 114346.

[148] K. Singh, S. Porada, H.D. de Gier, P.M. Biesheuvel, L.C.P.M. de Smet, Timeline on the application of intercalation materials in Capacitive Deionization, Desalination, 455 (2019) 115-134.

[149] A. Gupta, T. Sakthivel, S. Seal, Recent development in 2D materials beyond graphene, Progress in Materials Science, 73 (2015) 44-126.

[150] G.R. Bhimanapati, Z. Lin, V. Meunier, Y. Jung, J. Cha, S. Das, D. Xiao, Y. Son, M.S. Strano, V.R. Cooper, L. Liang, S.G. Louie, E. Ringe, W. Zhou, S.S. Kim, R.R. Naik, B.G. Sumpter, H. Terrones, F. Xia, Y. Wang, J. Zhu, D. Akinwande, N. Alem, J.A. Schuller, R.E. Schaak, M. Terrones, J.A. Robinson, Recent Advances in Two-Dimensional Materials beyond Graphene, ACS Nano, 9 (2015) 11509-11539.

[151] X. Zhang, L. Hou, A. Ciesielski, P. Samorì, 2D Materials Beyond Graphene for High-Performance Energy Storage Applications, Advanced Energy Materials, 6 (2016) 1600671.

[152] B. Zheng, G.X. Gu, Tuning the graphene mechanical anisotropy via defect engineering, Carbon, 155 (2019) 697-705.

[153] K.S. Novoselov, A.K. Geim, S.V. Morozov, D. Jiang, Y. Zhang, S.V. Dubonos, I.V. Grigorieva, A.A. Firsov, Electric field effect in atomically thin carbon films, Science, 306 (2004) 666-669.

[154] Z. Ni, H. Bu, M. Zou, H. Yi, K. Bi, Y. Chen, Anisotropic mechanical properties of graphene sheets from molecular dynamics, Physica B: Condensed Matter, 405 (2010) 1301-1306.

[155] M.A. Timmerman, R. Xia, P.T. Le, Y. Wang, J.E. ten Elshof, Metal oxide nanosheets as 2D building blocks for the design of novel materials, Chemistry–A European Journal, 26 (2020) 9084-9098.

[156] A. Bakandritsos, M. Pykal, P. Błoński, P. Jakubec, D.D. Chronopoulos, K. Poláková, V. Georgakilas, K. Čépe, O. Tomanec, V. Ranc, A.B. Bourlinos, R. Zbořil, M. Otyepka, Cyanographene and Graphene Acid: Emerging Derivatives Enabling High-Yield and Selective Functionalization of Graphene, ACS Nano, 11 (2017) 2982-2991.

[157] O. Jankovský, M. Nováček, J. Luxa, D. Sedmidubský, V. Fila, M. Pumera, Z. Sofer, A new member of the graphene family: graphene acid, Chemistry–A European Journal, 22 (2016) 17416-17424.

[158] M. Stavrou, D. Panáček, A. Bakandritsos, S. Couris, N-Doped Graphene and N-Doped Graphene Acid: Heteroatom Doping for Very Efficient Broad-Band Optical Limiting Performance from UV to NIR, The Journal of Physical Chemistry C, 126 (2022) 14339-14345.

[159] J. Duan, S. Chen, M. Jaroniec, S.Z. Qiao, Heteroatom-Doped Graphene-Based Materials for Energy-Relevant Electrocatalytic Processes, ACS Catalysis, 5 (2015) 5207-5234.

[160] J. Liang, Y. Jiao, M. Jaroniec, S.Z. Qiao, Sulfur and nitrogen dual-doped mesoporous graphene electrocatalyst for oxygen reduction with synergistically enhanced performance, Angewandte Chemie, 124 (2012) 11664-11668.

[161] B. Xia, Y. Yan, X. Wang, X.W.D. Lou, Recent progress on graphene-based hybrid electrocatalysts, Materials Horizons, 1 (2014) 379-399.

[162] M. Pumera, Electrochemistry of graphene: new horizons for sensing and energy storage, The Chemical Record, 9 (2009) 211-223.

[163] M. Pumera, B. Šmíd, K. Veltruská, Influence of nitric acid treatment of carbon nanotubes on their physico-chemical properties, Journal of Nanoscience and Nanotechnology, 9 (2009) 2671-2676.

[164] C. Gómez-Navarro, M. Burghard, K. Kern, Elastic Properties of Chemically Derived Single Graphene Sheets, Nano Letters, 8 (2008) 2045-2049.

[165] P. He, J. Cao, H. Ding, C. Liu, J. Neilson, Z. Li, I.A. Kinloch, B. Derby, Screen-printing of a highly conductive graphene ink for flexible printed electronics, ACS Applied Materials & Interfaces, 11 (2019) 32225-32234.

[166] Y.G. Babak Anasori, 2D Metal Carbides and Nitrides (MXenes) Structure, Properties, and Applications, Springer, (2019).

[167] B. Anasori, M.R. Lukatskaya, Y. Gogotsi, 2D metal carbides and nitrides (MXenes) for energy storage, Nature Reviews Materials, 2 (2017) 16098.

[168] L. Ding, L. Li, Y. Liu, Y. Wu, Z. Lu, J. Deng, Y. Wei, J. Caro, H. Wang, Effective ion sieving with Ti 3 C 2 T x MXene membranes for production of drinking water from seawater, Nature Sustainability, 3 (2020) 296-302.

[169] G.Z. Liu, J. Shen, Y.F. Ji, Q. Liu, G.P. Liu, J. Yang, W.Q. Jin, Two-dimensional $Ti_2CT_x$ MXene membranes with integrated and ordered nanochannels for efficient solvent dehydration, Journal of Materials Chemistry A, 7 (2019) 12095-12104.

[170] C.E. Ren, K.B. Hatzell, M. Alhabeb, Z. Ling, K.A. Mahmoud, Y. Gogotsi, Charge- and Size-Selective Ion Sieving Through $Ti_3C_2T_x$ MXene Membranes, The Journal of Physical Chemistry Letters, 6 (2015) 4026-4031.

[171] M. Naguib, J. Come, B. Dyatkin, V. Presser, P.L. Taberna, P. Simon, M.W. Barsoum, Y. Gogotsi, MXene: A promising transition metal carbide anode for lithium-ion batteries, Electrochemistry Communications, 16 (2012) 61-64.

[172] K.R.G. Lim, M. Shekhirev, B.C. Wyatt, B. Anasori, Y. Gogotsi, Z.W. Seh, Fundamentals of MXene synthesis, Nature Synthesis, 1 (2022) 1-14.

[173] O. Mashtalir, M. Naguib, B. Dyatkin, Y. Gogotsi, M.W. Barsoum, Kinetics of aluminum extraction from $Ti_3AlC_2$ in hydrofluoric acid, Materials Chemistry and Physics, 139 (2013) 147-152.

[174] B. Anasori, Û.G. Gogotsi, 2D metal carbides and nitrides (MXenes), Springer, 2019.

[175] O. Mashtalir, M. Naguib, V.N. Mochalin, Y. Dall'Agnese, M. Heon, M.W. Barsoum, Y. Gogotsi, Intercalation and delamination of layered carbides and carbonitrides, Nature Communications, 4 (2013) 1716.

[176] M. Naguib, R.R. Unocic, B.L. Armstrong, J. Nanda, Large-scale delamination of multi-layers transition metal carbides and carbonitrides "MXenes", Dalton Transactions, 44 (2015) 9353-9358.

[177] Z. Ling, C.E. Ren, M.Q. Zhao, J. Yang, J.M. Giammarco, J. Qiu, M.W. Barsoum, Y. Gogotsi, Flexible and conductive MXene films and nanocomposites with high capacitance, Proceedings of the National Academy of Sciences of the United States of America, 111 (2014) 16676-16681.

[178] C. Zhang, L. McKeon, M.P. Kremer, S.-H. Park, O. Ronan, A. Seral-Ascaso, S. Barwich, C.Ó. Coileáin, N. McEvoy, H.C. Nerl, B. Anasori, J.N. Coleman, Y. Gogotsi, V. Nicolosi, Additive-free MXene inks and direct printing of micro-supercapacitors, Nature Communications, 10 (2019) 1795.

[179] C.J. Zhang, B. Anasori, A. Seral-Ascaso, S.H. Park, N. McEvoy, A. Shmeliov, G.S. Duesberg, J.N. Coleman, Y. Gogotsi, V. Nicolosi, Transparent, Flexible, and Conductive 2D Titanium Carbide (MXene) Films with High Volumetric Capacitance, Advanced Materials, 29 (2017) 1702678.

[180] Y. Xie, M. Naguib, V.N. Mochalin, M.W. Barsoum, Y. Gogotsi, X. Yu, K.-W. Nam, X.-Q. Yang, A.I. Kolesnikov, P.R.C. Kent, Role of Surface Structure on Li-Ion Energy Storage Capacity of Two-Dimensional Transition-Metal Carbides, Journal of the American Chemical Society, 136 (2014) 6385-6394.

[181] M. Hu, T. Hu, Z. Li, Y. Yang, R. Cheng, J. Yang, C. Cui, X. Wang, Surface Functional Groups and Interlayer Water Determine the Electrochemical Capacitance of $Ti_3C_2T_x$ MXene, ACS Nano, 12 (2018) 3578-3586.

[182] M.A. Hope, A.C. Forse, K.J. Griffith, M.R. Lukatskaya, M. Ghidiu, Y. Gogotsi, C.P. Grey, NMR reveals the surface functionalisation of $Ti_3C_2$ MXene, Physical Chemistry Chemical Physics, 18 (2016) 5099-5102.

[183] J. Li, X. Yuan, C. Lin, Y. Yang, L. Xu, X. Du, J. Xie, J. Lin, J. Sun, Achieving High Pseudocapacitance of 2D Titanium Carbide (MXene) by Cation Intercalation and Surface Modification, Advanced Energy Materials, 7 (2017) 1602725.

[184] X. Liang, L.F. Nazar, MXene Materials as Electrodes for Lithium-Sulfur Batteries, 2D Metal Carbides and Nitrides (Mxenes) Structure, Properties and Applications, (2019) 381-398.

[185] X. Liang, A. Garsuch, L.F. Nazar, Sulfur Cathodes Based on Conductive MXene Nanosheets for High-Performance Lithium-Sulfur Batteries, Angewandte Chemie International Edition, 54 (2015) 3907-3911.

[186] W. Bao, X. Xie, J. Xu, X. Guo, J. Song, W. Wu, D. Su, G. Wang, Confined sulfur in 3 D MXene/reduced graphene oxide hybrid nanosheets for lithium–sulfur battery, Chemistry–A European Journal, 23 (2017) 12613-12619.

[187] G. Du, M. Tao, W. Gao, Y. Zhang, R. Zhan, S. Bao, M. Xu, Preparation of $MoS_2/Ti_3C_2T_x$ composite as anode material with enhanced sodium/lithium storage performance, Inorganic Chemistry Frontiers, 6 (2019) 117-125.

[188] W. Liu, Y. Zheng, Z. Zhang, Y. Zhang, Y. Wu, H. Gao, J. Su, Y. Gao, Ultrahigh gravimetric and volumetric capacitance in Ti3C2Tx MXene negative electrode enabled by surface modification and in-situ intercalation, Journal of Power Sources, 521 (2022) 230965.

[189] Y. Zhao, B. Li, C. Tian, X. Han, Y. Qiu, H. Xiong, K. Li, C. Hou, Y. Li, H. Wang, Q. Zhang, Anhydrous organic etching derived fluorine-rich terminated MXene nanosheets for efficient and stable perovskite solar cells, Chemical Engineering Journal, 469 (2023) 143862.

[190] L. Jin, Z. Li, H. Huang, X. Chu, W. Deng, J. Zhang, Y. Ao, T. Xu, G. Tian, T. Yang, L. Tang, W. Yang, Surface Triboelectrification of MXenes with Fluorine Groups for Flexible Energy Harvesting and Sensing, Advanced Engineering Materials, (2023) 2300709.

[191] S. Li, P. Tuo, J. Xie, X. Zhang, J. Xu, J. Bao, B. Pan, Y. Xie, Ultrathin MXene Nanosheets with Rich Fluorine Termination Groups Realizing Efficient Electrocatalytic Hydrogen Evolution, Nano Energy, 47 (2018) 512-518.

[192] M. Naguib, M. Kortoglu, V. Presser, J. Lu, L. Hultman, J. Niu, M. Heon, Y. Gogotsi, M.W. Barsoum, Two-dimensional nanocrystals produced by exfoliation of $Ti_3AlC_2$, Advanced Materials, 23 (2011) 4248-4253.

[193] M. Ghidiu, M.R. Lukatskaya, M.Q. Zhao, Y. Gogotsi, M.W. Barsoum, Conductive two-dimensional titanium carbide 'clay' with high volumetric capacitance, Nature, 516 (2014) 78-81.

[194] M. Ghidiu, J. Halim, S. Kota, D. Bish, Y. Gogotsi, M.W. Barsoum, Ion-Exchange and Cation Solvation Reactions in $Ti_3C_2$ MXene, Chemistry of Materials, 28 (2016) 3507-3514.

[195] Y. Li, H. Shao, Z. Lin, J. Lu, L. Liu, B. Duployer, P.O. Persson, P. Eklund, L. Hultman, M. Li, A general Lewis acidic etching route for preparing MXenes with enhanced electrochemical performance in non-aqueous electrolyte, Nature Materials, 19 (2020) 894-899.

[196] M. Li, J. Lu, K. Luo, Y. Li, K. Chang, K. Chen, J. Zhou, J. Rosen, L. Hultman, P. Eklund, P.O.Å. Persson, S. Du, Z. Chai, Z. Huang, Q. Huang, Element Replacement Approach by Reaction with Lewis Acidic Molten Salts to Synthesize Nanolaminated MAX Phases and MXenes, Journal of the American Chemical Society, 141 (2019) 4730-4737.

[197] S. Husmann, Ö. Budak, H. Shim, K. Liang, M. Aslan, A. Kruth, A. Quade, M. Naguib, V. Presser, Ionic liquid-based synthesis of MXene, Chemical Communications, 56 (2020) 11082-11085.

[198] H. Shi, P. Zhang, Z. Liu, S. Park, M.R. Lohe, Y. Wu, A. Shaygan Nia, S. Yang, X. Feng, Ambient-Stable Two-Dimensional Titanium Carbide (MXene) Enabled by Iodine Etching, Angewandte Chemie International Edition, 60 (2021) 8689-8693.

[199] A. Jawaid, A. Hassan, G. Neher, D. Nepal, R. Pachter, W.J. Kennedy, S. Ramakrishnan, R.A. Vaia, Halogen Etch of $Ti_3AlC_2$ MAX Phase for MXene Fabrication, ACS Nano, 15 (2021) 2771-2777.

[200] W. Sun, S. Shah, Y. Chen, Z. Tan, H. Gao, T. Habib, M. Radovic, M. Green, Electrochemical etching of $Ti_2AlC$ to $Ti_2CT_x$ (MXene) in low-concentration hydrochloric acid solution, Journal of Materials Chemistry A, 5 (2017) 21663-21668.

[201] T. Li, L. Yao, Q. Liu, J. Gu, R. Luo, J. Li, X. Yan, W. Wang, P. Liu, B. Chen, W. Zhang, W. Abbas, R. Naz, D. Zhang, Fluorine-Free Synthesis of High-Purity $Ti_3C_2T_x$ (T=OH, O) via Alkali Treatment, Angewandte Chemie International Edition, 57 (2018) 6115-6119.

[202] K.L. Firestein, J.F.S. Fernando, C. Zhang, C.-E.M. Lewis, D.V. Golberg, Delaminated $V_2C$ MXene Nanostructures Prepared via LiF Salt Etching for Electrochemical Applications, ACS Applied Nano Materials, 5 (2022) 12117-12125.

[203] H. Dong, P. Xiao, N. Jin, B. Wang, Y. Liu, Z. Lin, Molten Salt Derived $Nb_2CT_x$ MXene Anode for Li-ion Batteries, ChemElectroChem, 8 (2021) 957-962.

[204] M. Naguib, M.W. Barsoum, Y. Gogotsi, Ten years of progress in the synthesis and development of MXenes, Advanced Materials, 33 (2021) 2103393.

[205] M. Alhabeb, K. Maleski, B. Anasori, P. Lelyukh, L. Clark, S. Sin, Y. Gogotsi, Guidelines for Synthesis and Processing of Two-Dimensional Titanium Carbide ($Ti_3C_2T_x$ MXene), Chemistry of Materials, 29 (2017) 7633-7644.

[206] M. Lu, H. Li, W. Han, J. Chen, W. Shi, J. Wang, X.-M. Meng, J. Qi, H. Li, B. Zhang, W. Zhang, W. Zheng, 2D titanium carbide (MXene) electrodes with lower-F surface for high performance lithium-ion batteries, Journal of Energy Chemistry, 31 (2019) 148-153.

[207] F. Kong, X. He, Q. Liu, X. Qi, Y. Zheng, R. Wang, Y. Bai, Improving the electrochemical properties of MXene $Ti_3C_2$ multilayer for Li-ion batteries by vacuum calcination, Electrochimica Acta, 265 (2018) 140-150.

[208] X. Zhu, B. Liu, H. Hou, Z. Huang, K.M. Zeinu, L. Huang, X. Yuan, D. Guo, J. Hu, J. Yang, Alkaline intercalation of $Ti_3C_2$ MXene for simultaneous electrochemical detection of Cd(II), Pb(II), Cu(II) and Hg(II), Electrochimica Acta, 248 (2017) 46-57.

[209] P.C. Lian, Y.F. Dong, Z.S. Wu, S.H. Zheng, X.H. Wang, S. Wang, C.L. Sun, J.Q. Qin, X.Y. Shi, X.H. Bao, Alkalized $Ti_3C_2$ MXene Nanoribbons with Expanded Interlayer Spacing for High-Capacity Sodium and Potassium Ion Batteries, Nano Energy, 40 (2017) 1-8.

[210] P.A. Maughan, S. Arnold, Y. Zhang, V. Presser, N. Tapia-Ruiz, N. Bimbo, In Situ Investigation of Expansion during the Lithiation of Pillared MXenes with Ultralarge Interlayer Distance, The Journal of Physical Chemistry C, 125 (2021) 20791-20797.

[211] K. Maleski, C.E. Ren, M.Q. Zhao, B. Anasori, Y. Gogotsi, Size-Dependent Physical and Electrochemical Properties of Two-Dimensional MXene Flakes, ACS Applied Materials & Interfaces, 10 (2018) 24491-24498.

[212] J. Xiang, X. Wang, M. Ding, X. Tang, S. Zhang, X. Zhang, Z. Xie, The role of lateral size of MXene nanosheets in membrane filtration of dyeing wastewater: Membrane characteristic and performance, Chemosphere, 294 (2022) 133728.

[213] M.D. Levi, M.R. Lukatskaya, S. Sigalov, M. Beidaghi, N. Shpigel, L. Daikhin, D. Aurbach, M.W. Barsoum, Y. Gogotsi, Solving the Capacitive Paradox of 2D MXene using Electrochemical Quartz-Crystal Admittance and In Situ Electronic Conductance Measurements, Advanced Energy Materials, 5 (2015) 1400815.

[214] M. Shekhirev, J. Busa, C.E. Shuck, A. Torres, S. Bagheri, A. Sinitskii, Y. Gogotsi, Ultralarge Flakes of $Ti_3C_2T_x$ MXene via Soft Delamination, ACS Nano, 16 (2022) 13695-13703.

[215] M. Naguib, V.N. Mochalin, M.W. Barsoum, Y. Gogotsi, 25th anniversary article: MXenes: a new family of two-dimensional materials, Advanced Materials, 26 (2014) 992-1005.

[216] B. Chen, A. Feng, R. Deng, K. Liu, Y. Yu, L. Song, MXene as a cation-selective cathode material for asymmetric capacitive deionization, ACS Applied Materials & Interfaces, 12 (2020) 13750-13758.

[217] B. Chen, A. Feng, K. Liu, J. Wu, Y. Yu, L. Song, High-performance capacitive deionization using 3D porous $Ti_3C_2T_x$ with improved conductivity, Journal of Electroanalytical Chemistry, 895 (2021) 115515.

[218] B. Chen, A. Feng, K. Liu, J. Wu, Y. Yu, L. Song, Subsize $Ti_3C_2T_x$ derived from molten-salt synthesized $Ti_3AlC_2$ for enhanced capacitive deionization, Ceramics International, 47 (2021) 3665-3670.

[219] A. Amiri, Y. Chen, C.B. Teng, M. Naraghi, Porous nitrogen-doped MXene-based electrodes for capacitive deionization, Energy Storage Materials, 25 (2019) 731-739.

[220] L. Guo, X. Wang, Z.Y. Leong, R. Mo, L. Sun, H.Y. Yang, Ar plasma modification of 2D MXene $Ti_3C_2T_x$ nanosheets for efficient capacitive desalination, FlatChem, 8 (2018) 17-24.

[221] J. Ma, Y. Cheng, L. Wang, X. Dai, F. Yu, Free-standing $Ti_3C_2T_x$ MXene film as binder-free electrode in capacitive deionization with an ultrahigh desalination capacity, Chemical Engineering Journal, 384 (2020) 123329.

[222] L. Agartan, K. Hantanasirisakul, S. Buczek, B. Akuzum, K.A. Mahmoud, B. Anasori, Y. Gogotsi, E.C. Kumbur, Influence of operating conditions on the desalination performance of a symmetric pre-conditioned $Ti_3C_2T_x$-MXene membrane capacitive deionization system, Desalination, 477 (2020) 114267.

[223] X. Shen, Y. Xiong, R. Hai, F. Yu, J. Ma, All-MXene-based integrated membrane electrode constructed using $Ti_3C_2T_x$ as an intercalating agent for high-performance desalination, Environmental Science & Technology, 54 (2020) 4554-4563.

[224] B. Chen, A. Feng, R. Deng, K. Liu, Y. Yu, L. Song, MXene as a Cation-selective Cathode Material for Asymmetric Capacitive Deionization, ACS Applied Materials & Interfaces, (2020).

[225] N.E. Mansoor, L.A. Diaz, C.E. Shuck, Y. Gogotsi, T.E. Lister, D. Estrada, Removal and recovery of ammonia from simulated wastewater using $Ti_3C_2T_x$ MXene in flow electrode capacitive deionization, npj Clean Water, 5 (2022) 26.

[226] Q. Li, X. Xu, J. Guo, J.P. Hill, H. Xu, L. Xiang, C. Li, Y. Yamauchi, Y. Mai, Two-dimensional MXene-polymer heterostructure with ordered in-plane mesochannels for high-performance capacitive deionization, Angewandte Chemie, 133 (2021) 26732-26738.

[227] S. Zhang, X. Xu, X. Liu, Q. Yang, N. Shang, X. Zhao, X. Zang, C. Wang, Z. Wang, J.G. Shapter, Heterointerface optimization in a covalent organic framework-on-MXene for high-performance capacitive deionization of oxygenated saline water, Materials Horizons, 9 (2022) 1708-1716.

[228] W. Xi, J. Jin, Y. Zhang, R. Wang, Y. Gong, B. He, H. Wang, Hierarchical MXene/transition metal oxide heterostructures for rechargeable batteries, capacitors, and capacitive deionization, Nanoscale, 14 (2022) 11923-11944.

[229] J. Liang, J. Yu, W. Xing, W. Tang, N. Tang, J. Guo, 3D interconnected network architectures assembled from $W_{18}O_{49}$ and $Ti_3C_2$ MXene with excellent electrochemical properties and CDI performance, Chemical Engineering Journal, 435 (2022) 134922.

[230] K. Wang, L. Chen, G. Zhu, X. Xu, L. Wan, T. Lu, L. Pan, Ferroferric oxide@titanium carbide MXene heterostructure with enhanced sodium storage ability for efficient hybrid capacitive deionization, Desalination, 522 (2022) 115420.

[231] S. Wang, Z. Li, G. Wang, Y. Wang, Z. Ling, C. Li, Freestanding $Ti_3C_2T_x$ MXene/Prussian Blue Analogues Films with Superior Ion Uptake for Efficient Capacitive Deionization by a Dual Pseudocapacitance Effect, ACS Nano, 16 (2022) 1239-1249.

[232] Y. Gogotsi, Q. Huang, MXenes: two-dimensional building blocks for future materials and devices, ACS Nano, 15 (2021) 5775-5780.

[233] S.K. Nemani, M. Torkamanzadeh, B.C. Wyatt, V. Presser, B. Anasori, Functional two-dimensional high-entropy materials, Communications Materials, 4 (2023) 16.

[234] M. Jakubczak, A. Szuplewska, A. Rozmysłowska-Wojciechowska, A. Rosenkranz, A.M. Jastrzębska, Novel 2D MBenes - Synthesis, structure, and biotechnological potential, Advanced Functional Materials, 31 (2021) 2103048.

[235] I. Higashi, Y. Takahashi, S. Okada, Crystal structure of $MoB_2$, Journal of the Less Common Metals, 123 (1986) 277-283.

[236] S. Okada, T. Atoda, I. Higashi, Y. Takahashi, Preparation of single crystals of $MoB_2$ by the aluminium-flux technique and some of their properties, Journal of Materials Science, 22 (1987) 2993-2999.

[237] J. Zhou, J. Palisaitis, J. Halim, M. Dahlqvist, Q. Tao, I. Persson, L. Hultman, P.O.A. Persson, J. Rosen, Boridene: Two-dimensional $Mo_{4/3}B_{2-x}$ with ordered metal vacancies obtained by chemical exfoliation, Science, 373 (2021) 801-805.

[238] N.F. Rosli, M.Z.M. Nasir, N. Antonatos, Z.k. Sofer, A. Dash, J. Gonzalez-Julian, A.C. Fisher, R.D. Webster, M. Pumera, MAX and MAB Phases: Two-dimensional layered carbide and boride nanomaterials for electrochemical applications, ACS Applied Nano Materials, 2 (2019) 6010-6021.

[239] V.G. Nair, M. Birowska, D. Bury, M. Jakubczak, A. Rosenkranz, A.M. Jastrzebska, 2D MBenes: A novel member in the flatland, Advanced Materials, 34 (2022) 202108840.

[240] M. Jakubczak, A. Szuplewska, A. Rozmysłowska-Wojciechowska, A. Rosenkranz, A.M. Jastrzębska, Novel 2D MBenes—Synthesis, Structure, and Biotechnological Potential, Advanced Functional Materials, 31 (2021) 2103048.

[241] H. Zhang, H. Xiang, F. Dai, Z. Zhang, Y. Zhou, First demonstration of possible two-dimensional MBene CrB derived from MAB phase $Cr_2AlB_2$, Journal of Materials Science & Technology, 34 (2018) 2022-2026.

[242] H. Zhang, F. Dai, H. Xiang, X. Wang, Z. Zhang, Y. Zhou, Phase pure and well crystalline $Cr_2AlB_2$: A key precursor for two-dimensional CrB, Journal of Materials Science & Technology, 35 (2019) 1593-1600.

[243] S. Husmann, M. Torkamanzadeh, K. Liang, A. Majed, C. Dun, J.J. Urban, M. Naguib, V. Presser, Layered nano-mosaic of niobium disulfide heterostructures by direct sulfidation of niobium carbide MXenes for hydrogen evolution, Advanced Materials Interfaces, 9 (2022) 2102185.

[244] L.T. Alameda, R.W. Lord, J.A. Barr, P. Moradifar, Z.P. Metzger, B.C. Steimle, C.F. Holder, N. Alem, S.B. Sinnott, R.E. Schaak, Multi-Step Topochemical Pathway to Metastable $Mo_2AlB_2$ and Related Two-Dimensional Nanosheet Heterostructures, Journal of the American Chemical Society, 141 (2019) 10852-10861.

[245] L.T. Alameda, P. Moradifar, Z.P. Metzger, N. Alem, R.E. Schaak, Topochemical deintercalation of Al from MoAlB: Stepwise etching pathway, layered intergrowth structures, and two-dimensional mbene, Journal of the American Chemical Society, 140 (2018) 8833-8840.

[246] L.T. Alameda, C.F. Holder, J.L. Fenton, R.E. Schaak, Partial Etching of Al from MoAlB Single Crystals To Expose Catalytically Active Basal Planes for the Hydrogen Evolution Reaction, Chemistry of Materials, 29 (2017) 8953-8957.

[247] C.E. Shuck, M.K. Han, K. Maleski, K. Hantanasirisakul, S.J. Kim, J. Choi, W.E.B. Reil, Y. Gogotsi, Effect of $Ti_3AlC_2$ MAX Phase on Structure and Properties of Resultant $Ti_3C_2T_x$ MXene, ACS Applied Nano Materials, 2 (2019) 3368-3376.

[248] G. Bhaskar, V. Gvozdetskyi, M. Batuk, K.M. Wiaderek, Y. Sun, R. Wang, C. Zhang, S.L. Carnahan, X. Wu, R.A. Ribeiro, S.L. Bud'ko, P.C. Canfield, W. Huang, A.J. Rossini, C.-Z. Wang, K.-M. Ho, J. Hadermann, J.V. Zaikina, Topochemical Deintercalation of Li from Layered LiNiB: toward 2D MBene, Journal of the American Chemical Society, 143 (2021) 4213-4223.

[249] A. Majed, M. Torkamanzadeh, C.F. Nwaokorie, K. Eisawi, C. Dun, A. Buck, J.J. Urban, M.M. Montemore, V. Presser, M. Naguib, Toward MBenes Battery Electrode Materials: Layered Molybdenum Borides for Li-Ion Batteries, Small Methods, n/a (2023) 2300193.

[250] A.S. Brouwer, M. van den Broek, A. Seebregts, A. Faaij, Impacts of large-scale Intermittent Renewable Energy Sources on electricity systems, and how these can be modeled, Renewable and Sustainable Energy Reviews, 33 (2014) 443-466.

[251] H. Zsiborács, N.H. Baranyai, A. Vincze, L. Zentkó, Z. Birkner, K. Máté, G. Pintér, Intermittent Renewable Energy Sources: The Role of Energy Storage in the European Power System of 2040, Electronics, 8 (2019) 729.

[252] J.R. Rostrup-Nielsen, T. Rostrup-Nielsen, Large-Scale Hydrogen Production, CATTECH, 6 (2002) 150-159.

[253] J.D. Holladay, J. Hu, D.L. King, Y. Wang, An overview of hydrogen production technologies, Catalysis Today, 139 (2009) 244-260.

[254] M. Wang, L. Chen, L. Sun, Recent progress in electrochemical hydrogen production with earth-abundant metal complexes as catalysts, Energy & Environmental Science, 5 (2012) 6763-6778.

[255] K. Scott, Electrochemical methods for hydrogen production, Royal Society of Chemistry, 2019.

[256] Z. Kang, M.A. Khan, Y. Gong, R. Javed, Y. Xu, D. Ye, H. Zhao, J. Zhang, Recent progress of MXenes and MXene-based nanomaterials for the electrocatalytic hydrogen evolution reaction, Journal of Materials Chemistry A, 9 (2021) 6089-6108.

[257] H. Wang, J.-M. Lee, Recent advances in structural engineering of MXene electrocatalysts, Journal of Materials Chemistry A, 8 (2020) 10604-10624.

[258] J. Liu, W. Peng, Y. Li, F. Zhang, X. Fan, 2D MXene-Based Materials for Electrocatalysis, Transactions of Tianjin University, 26 (2020) 149-171.

[259] A. Liu, X. Liang, X. Ren, W. Guan, M. Gao, Y. Yang, Q. Yang, L. Gao, Y. Li, T. Ma, Recent Progress in MXene-Based Materials: Potential High-Performance Electrocatalysts, Advanced Functional Materials, 30 (2020) 2003437.

[260] G. Gao, A.P. O'Mullane, A. Du, 2D MXenes: A New Family of Promising Catalysts for the Hydrogen Evolution Reaction, ACS Catalysis, 7 (2017) 494-500.

[261] H. Pan, Ultra-high electrochemical catalytic activity of MXenes, Scientific Reports, 6 (2016) 32531.

[262] Q. Fu, J. Han, X. Wang, P. Xu, T. Yao, J. Zhong, W. Zhong, S. Liu, T. Gao, Z. Zhang, L. Xu, B. Song, 2D Transition Metal Dichalcogenides: Design, Modulation, and Challenges in Electrocatalysis, Advanced Materials, 33 (2021) 1907818.

[263] H. Wang, H. Feng, J. Li, Graphene and Graphene-like Layered Transition Metal Dichalcogenides in Energy Conversion and Storage, Small, 10 (2014) 2165-2181.

[264] A.D. Handoko, K.D. Fredrickson, B. Anasori, K.W. Convey, L.R. Johnson, Y. Gogotsi, A. Vojvodic, Z.W. Seh, Tuning the basal plane functionalization of two-dimensional metal carbides (MXenes) to control hydrogen evolution activity, ACS Applied Energy Materials, 1 (2017) 173-180.

[265] C. Ling, L. Shi, Y. Ouyang, J. Wang, Searching for Highly Active Catalysts for Hydrogen Evolution Reaction Based on O-Terminated MXenes through a Simple Descriptor, Chemistry of Materials, 28 (2016) 9026-9032.

[266] Z.W. Seh, K.D. Fredrickson, B. Anasori, J. Kibsgaard, A.L. Strickler, M.R. Lukatskaya, Y. Gogotsi, T.F. Jaramillo, A. Vojvodic, Two-Dimensional Molybdenum Carbide (MXene) as an Efficient Electrocatalyst for Hydrogen Evolution, ACS Energy Letters, 1 (2016) 589-594.

[267] B. Hinnemann, P.G. Moses, J. Bonde, K.P. Jørgensen, J.H. Nielsen, S. Horch, I. Chorkendorff, J.K. Nørskov, Biomimetic Hydrogen Evolution: $MoS_2$ Nanoparticles as Catalyst for Hydrogen Evolution, Journal of the American Chemical Society, 127 (2005) 5308-5309.

[268] L. Li, Z. Qin, L. Ries, S. Hong, T. Michel, J. Yang, C. Salameh, M. Bechelany, P. Miele, D. Kaplan, M. Chhowalla, D. Voiry, Role of Sulfur Vacancies and Undercoordinated Mo Regions in $MoS_2$ Nanosheets toward the Evolution of Hydrogen, ACS Nano, 13 (2019) 6824-6834.

[269] Z.H. Tan, X.Y. Kong, B.-J. Ng, H.S. Soo, A.R. Mohamed, S.-P. Chai, Recent Advances in Defect-Engineered Transition Metal Dichalcogenides for Enhanced Electrocatalytic Hydrogen Evolution: Perfecting Imperfections, ACS Omega, 8 (2023) 1851-1863.

[270] P. Raybaud, J. Hafner, G. Kresse, S. Kasztelan, H. Toulhoat, Ab Initio Study of the $H_2$–$H_2S$/$MoS_2$ Gas–Solid Interface: The Nature of the Catalytically Active Sites, Journal of Catalysis, 189 (2000) 129-146.

[271] J. Ding, Y. Zhou, Y. Li, S. Guo, X. Huang, MoS2 Nanosheet Assembling Superstructure with a Three-Dimensional Ion Accessible Site: A New Class of Bifunctional Materials for Batteries and Electrocatalysis, Chemistry of Materials, 28 (2016) 2074-2080.

[272] T.F. Jaramillo, K.P. Jørgensen, J. Bonde, J.H. Nielsen, S. Horch, I. Chorkendorff, Identification of active edge sites for electrochemical $H_2$ evolution from $MoS_2$ nanocatalysts, Science, 317 (2007) 100-102.

[273] Y. Sun, F. Alimohammadi, D. Zhang, G. Guo, Enabling colloidal synthesis of edge-oriented $MoS_2$ with expanded interlayer spacing for enhanced HER catalysis, Nano Letters, 17 (2017) 1963-1969.

[274] M.J. Crane, M.B. Lim, X. Zhou, P.J. Pauzauskie, Rapid synthesis of transition metal dichalcogenide–carbon aerogel composites for supercapacitor electrodes, Microsystems & Nanoengineering, 3 (2017) 1-9.

[275] K. Chang, W. Chen, L-cysteine-assisted synthesis of layered $MoS_2$/graphene composites with excellent electrochemical performances for lithium ion batteries, ACS Nano, 5 (2011) 4720-4728.

[276] K. Chang, W. Chen, In situ synthesis of $MoS_2$/graphene nanosheet composites with extraordinarily high electrochemical performance for lithium ion batteries, Chemical Communications, 47 (2011) 4252-4254.

[277] B. Kartick, S.K. Srivastava, S. Mahanty, $TiS_2$-MWCNT hybrid as high performance anode in lithium-ion battery, Journal of Nanoparticle Research, 15 (2013) 1950.

[278] S. Ding, J.S. Chen, X.W. Lou, Glucose-assisted growth of $MoS_2$ nanosheets on CNT backbone for improved lithium storage properties, Chemistry–A European Journal, 17 (2011) 13142-13145.

[279] A.S. Zeraati, S.A. Mirkhani, P. Sun, M. Naguib, P.V. Braun, U. Sundararaj, Improved synthesis of $Ti_3C_2T_x$ MXenes resulting in exceptional electrical conductivity, high synthesis yield, and enhanced capacitance, Nanoscale, 13 (2021) 3572-3580.

[280] L. Huang, L. Ai, M. Wang, J. Jiang, S. Wang, Hierarchical $MoS_2$ nanosheets integrated $Ti_3C_2$ MXenes for electrocatalytic hydrogen evolution, International Journal of Hydrogen Energy, 44 (2019) 965-976.

[281] S. Luan, M. Han, Y. Xi, K. Wei, Y. Wang, J. Zhou, L. Hou, F. Gao, $MoS_2$-decorated 2D $Ti_3C_2$ (MXene): a high-performance anode material for lithium-ion batteries, Ionics, 26 (2020) 51-59.

[282] C. Wang, X.-D. Zhu, K.-X. Wang, L.-L. Gu, S.-Y. Qiu, X.-T. Gao, P.-J. Zuo, N.-Q. Zhang, A general way to fabricate transition metal dichalcogenide/oxide-sandwiched MXene nanosheets as flexible film anodes for high-performance lithium storage, Sustainable Energy & Fuels, 3 (2019) 2577-2582.

[283] Y. Wu, P. Nie, L. Wu, H. Dou, X. Zhang, 2D MXene/$SnS_2$ composites as high-performance anodes for sodium ion batteries, Chemical Engineering Journal, 334 (2018) 932-938.

[284] W. Su, S. Wang, L. Fu, F. Chen, K. Song, X. Huang, L. Yang, Growth of $WS_2$ flakes on $Ti_3C_2T_x$ MXene using vapor transportation routine, Coatings, 8 (2018) 281.

[285] M.S. Sokolikova, C. Mattevi, Direct synthesis of metastable phases of 2D transition metal dichalcogenides, Chemical Society Reviews, 49 (2020) 3952-3980.

[286] Z. Du, S. Yang, S. Li, J. Lou, S. Zhang, S. Wang, B. Li, Y. Gong, L. Song, X. Zou, Conversion of non-van der Waals solids to 2D transition-metal chalcogenides, Nature, 577 (2020) 492-496.

[287] X. Huang, J. Tang, B. Luo, R. Knibbe, T. Lin, H. Hu, M. Rana, Y. Hu, X. Zhu, Q. Gu, Sandwich-Like Ultrathin $TiS_2$ Nanosheets Confined within N, S Codoped Porous Carbon as an Effective Polysulfide Promoter in Lithium-Sulfur Batteries, Advanced Energy Materials, 9 (2019) 1901872.

[288] J. Tang, X. Huang, T. Lin, T. Qiu, H. Huang, X. Zhu, Q. Gu, B. Luo, L. Wang, MXene derived TiS$_2$ nanosheets for high-rate and long-life sodium-ion capacitors, Energy Storage Materials, 26 (2020) 550-559.

[289] N. Hemanth, T. Kim, B. Kim, A.H. Jadhav, K. Lee, N.K. Chaudhari, Transition metal dichalcogenide-decorated MXenes: promising hybrid electrodes for energy storage and conversion applications, Materials Chemistry Frontiers, 5 (2021) 3298-3321.

[290] C. Chen, X. Xie, B. Anasori, A. Sarycheva, T. Makaryan, M. Zhao, P. Urbankowski, L. Miao, J. Jiang, Y. Gogotsi, MoS$_2$-on-MXene heterostructures as highly reversible anode materials for lithium-ion batteries, Angewandte Chemie International Edition, 57 (2018) 1846-1850.

[291] K.R.G. Lim, A.D. Handoko, L.R. Johnson, X. Meng, M. Lin, G.S. Subramanian, B. Anasori, Y. Gogotsi, A. Vojvodic, Z.W. Seh, 2H-MoS$_2$ on Mo$_2$CT$_x$ MXene Nanohybrid for Efficient and Durable Electrocatalytic Hydrogen Evolution, ACS Nano, 14 (2020) 16140-16155.

[292] O.F. Dippo, K.S. Vecchio, A universal configurational entropy metric for high-entropy materials, Scripta Materialia, 201 (2021) 113974.

[293] J.-W. Yeh, Alloy Design Strategies and Future Trends in High-Entropy Alloys, JOM, 65 (2013) 1759-1771.

[294] J.-W. Yeh, Physical Metallurgy of High-Entropy Alloys, JOM, 67 (2015) 2254-2261.

[295] M.W. Glasscott, Classifying and Benchmarking High-Entropy Alloys and Associated Materials for Electrocatalysis: A Brief Review of Best Practices, Current Opinion in Electrochemistry, 34 (2022) 100976.

[296] S.K. Nemani, B. Zhang, B.C. Wyatt, Z.D. Hood, S. Manna, R. Khaledialidusti, W. Hong, M.G. Sternberg, S.K. Sankaranarayanan, B. Anasori, High-Entropy 2D Carbide MXenes: TiVNbMoC$_3$ and TiVCrMoC$_3$, ACS Nano, 15 (2021) 12815-12825.

[297] Q. Wang, L. Velasco, B. Breitung, V. Presser, High-Entropy Energy Materials in the Age of Big Data: A Critical Guide to Next-Generation Synthesis and Applications, Advanced Energy Materials, 11 (2021) 2102355.

[298] D.B. Miracle, O.N. Senkov, A critical review of high entropy alloys and related concepts, Acta Materialia, 122 (2017) 448-511.

[299] T.A.A. Batchelor, J.K. Pedersen, S.H. Winther, I.E. Castelli, K.W. Jacobsen, J. Rossmeisl, High-entropy Alloys as a Discovery Platform for Electrocatalysis, Joule, 3 (2019) 834-845.

[300] Y. Sun, S. Dai, High-entropy Materials for Catalysis: a New Frontier, Science Advances, 7 (2021) 1600.

[301] L. Yu, K. Zeng, C. Li, X. Lin, H. Liu, W. Shi, H.-J. Qiu, Y. Yuan, Y. Yao, High-entropy Alloy Catalysts: From Bulk to Nano Toward Highly Efficient Carbon and Nitrogen Catalysis, Carbon Energy, 4 (2022) 731-761.

[302] Y. Sun, L. Yu, S. Xu, S. Xie, L. Jiang, J. Duan, J. Zhu, S. Chen, Battery-Driven N$_2$ Electrolysis Enabled by High-entropy Catalysts: From Theoretical Prediction to Prototype Model, Small, 18 (2022) 2106358.

[303] Z.-Y. Yu, Y. Duan, X.-Y. Feng, X. Yu, M.-R. Gao, S.-H. Yu, Clean and Affordable Hydrogen Fuel from Alkaline Water Splitting: Past, Recent Progress, and Future Prospects, Advanced Materials, 33 (2021) 2007100.

[304] H. Chen, X. Liang, Y. Liu, X. Ai, T. Asefa, X. Zou, Active Site Engineering in Porous Electrocatalysts, Advanced Materials, 32 (2020) 2002435.

[305] J.D. Benck, T.R. Hellstern, J. Kibsgaard, P. Chakthranont, T.F. Jaramillo, Catalyzing the Hydrogen Evolution Reaction (HER) with Molybdenum Sulfide Nanomaterials, ACS Catalysis, 4 (2014) 3957-3971.

[306] R. Wang, J. Huang, X. Zhang, J. Han, Z. Zhang, T. Gao, L. Xu, S. Liu, P. Xu, B. Song, Two-Dimensional High-Entropy Metal Phosphorus Trichalcogenides for Enhanced Hydrogen Evolution Reaction, ACS Nano, 16 (2022) 3593-3603.

[307] J. Cavin, A. Ahmadiparidari, L. Majidi, A.S. Thind, S.N. Misal, A. Prajapati, Z. Hemmat, S. Rastegar, A. Beukelman, M.R. Singh, 2D high-entropy transition metal dichalcogenides for carbon dioxide electrocatalysis, Advanced Materials, 33 (2021) 2100347.

[308] M. Fu, X. Ma, K. Zhao, X. Li, D. Su, High-entropy materials for energy-related applications, Iscience, 24 (2021) 102177.

[309] C. Oses, C. Toher, S. Curtarolo, High-entropy ceramics, Nature Reviews Materials, 5 (2020) 295-309.

[310] B. Wu, G. Hou, E. Kovalska, V. Mazanek, P. Marvan, L. Liao, L. Dekanovsky, D. Sedmidubsky, I. Marek, C. Hervoches, High-entropy NASICON Phosphates ($Na_3M_2$ $(PO_4)_3$ and $NaMPO_4O_x$, M= Ti, V, Mn, Cr, and Zr) for Sodium Electrochemistry, Inorganic Chemistry, 61 (2022) 4092-4101.

[311] R. Guo, T. He, High-Entropy Perovskite Electrolyte for Protonic Ceramic Fuel Cells Operating below 600 °C, ACS Materials Letters, 4 (2022) 1646-1652.

[312] W. Zhang, H. Xia, Z. Zhu, Z. Lv, S. Cao, J. Wei, Y. Luo, Y. Xiao, L. Liu, X. Chen, Decimal solvent-based high-entropy electrolyte enabling the extended survival temperature of lithium-ion batteries to −130 °C, CCS Chemistry, 3 (2021) 1245-1255.

[313] O. Mashtalir, M. Naguib, V.N. Mochalin, Y. Dall'Agnese, M. Heon, M.W. Barsoum, Y. Gogotsi, Intercalation and Delamination of Layered Carbides and Carbonitrides, Nature communications, 4 (2013) 1716.

[314] A.S. Etman, J. Zhou, J. Rosen, $Ti_{1.1}V_{0.7}Cr_xNb_{1.0}Ta_{0.6}C_3T_z$ high-entropy MXene freestanding films for charge storage applications, Electrochemistry Communications, 137 (2022) 107264.

[315] R. Kanno, Secondary Batteries – Lithium Rechargable Systems | Electrolytes: Solid Sulfide, in: J. Garche (Ed.) Encyclopedia of Electrochemical Power Sources, Elsevier, Amsterdam, 2009, pp. 129-137.

[316] J.H. Kim, K. Fu, J. Choi, K. Kil, J. Kim, X. Han, L. Hu, U. Paik, Encapsulation of S/SWNT with PANI Web for Enhanced Rate and Cycle Performance in Lithium Sulfur Batteries, Scientific Reports, 5 (2015) 8946.

[317] Z. Du, C. Wu, Y. Chen, Q. Zhu, Y. Cui, H. Wang, Y. Zhang, X. Chen, J. Shang, B. Li, High-Entropy Carbonitride MAX Phases and Their Derivative MXenes, Advanced Energy Materials, 12 (2022) 2103228.

# Mohammad Torkamanzadeh

**Adress:** INM- Leibniz Institute for New Materials
Campus D2 2
66123 Saarbrücken
Germany
**Date of Birth:** 20.01.1993
**Email:** Torkamanzadeh.m@gmail.com
**LinkedIn** https://www.linkedin.com/in/mtorkaman
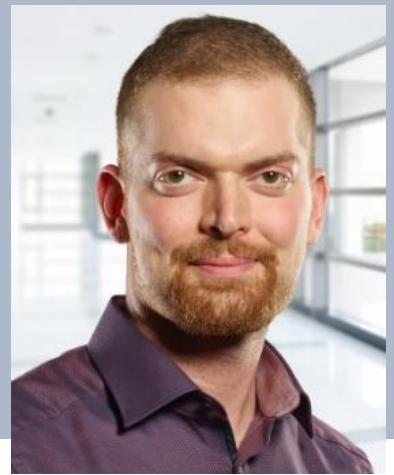
## Education

**Ph.D. in Materials Science and Engineering**          06/2019 – Present
Saarland University, Saarbrücken, Germany

  Project Title: MXene for Electrochemical Water Desalination
  Supervisor: Prof. Dr. Volker Presser
  Part of the Energy Materials group at INM - Leibniz Institute for New Materials

**MSc in Chemical Engineering**          09/2016 – 09/2018
University of Twente, Enschede, Netherlands

  Specialization: Materials and Molecular Engineering
  Project Title: Two-dimensional $MnO_2$ Nanosheets for Ink-jet Printing of Supercapacitors
  Supervisor: Prof. Dr. Andre ten Elshof
  Part of the Inorganic Materials Science group at MESA+ Institute for Nanotechnology

**BSc in Chemical Engineering**          09/2011 – 09/2015
Babol Noshirvani University of Technology, Babol, Iran

  Specialization: Chemical Process Engineering
  Project Title: MXene for Electrochemical Water Desalination
  Graduate Cum Laude

## Awards & Honors

- Awardee of Open Science Competition at Saarland University
- Awarded University of Twente Scholarship and Holland Scholarship
- Awarded Erasmus+ Traineeship Scholarship
- Awarded Partial Tuition Fee Waiver for the Duration of Masters Studies
- Graduated Ranking 4th in Chemical Engineering Department in Class of 2015

## Work Experience

**Research Assistant**          07/2021 – Present
INM- Leibniz Institute for New Materials, Saarbrücken, Germany

- Coordinating water desalination research activities of Energy Materials group
- Advising Master and junior PhD students in the lab on a daily basis
- Successfully led a water desalination project for a major industrial company

### Graduate Teaching Assistant                    05/2022 – 07/2023
Saarland University, Saarbrücken, Germany

- Teaching assistant to Prof. Dr. Volker Presser for the course 'Basic Thermodynamics'
- Solved problems for undergraduate students, 2 hours per week, spoken in German

### Undergraduate Teaching Assistant                    02/2015 – 01/2016
Babol Noshirvani University of Technology, Babol, Iran

- Taught 'Physics of Electricity & Magnetism' to undergraduate engineering students
- Implemented students' feedback to improve my teaching, and designed tests

# Publications ([Google Scholar](#))

**Torkamanzadeh, M.**, Kök, C., Burger, P. R., Ren, P., Zhang, Y., Lee, J, … & Presser, V. (2023). Best practice for electrochemical water desalination data generation and analysis. [Cell Reports Physical Science](#), 101661.

Nemani, S. K., **Torkamanzadeh, M.**, Wyatt, B. C., Presser, V., & Anasori, B. (2023). Functional two-dimensional high-entropy materials. [Communications Materials](#), 4(1), 16.

Wang, L., **Torkamanzadeh, M.**, Majed, A., Zhang, Y., Wang, Q., Breitung, B., … & Presser, V. (2022). *Time-Dependent Cation Selectivity of Titanium Carbide MXene in Aqueous Solution*. [Advanced Sustainable Systems](#), 6(3), 2100383.

Husmann, S., **Torkamanzadeh, M.**, Liang, K., Majed, A., Dun, C., Urban, J. J., … & Presser, V. (2022). *Layered Nano-Mosaic of Niobium Disulfide Heterostructures by Direct Sulfidation of Niobium Carbide MXenes for Hydrogen Evolution*. [Advanced Materials Interfaces](#), 2102185.

**Torkamanzadeh, M.**, Wang, L., Zhang, Y., Budak, O., Srimuk, P., & Presser, V. (2020). *MXene/activated-carbon hybrid capacitive deionization for permselective ion removal at low and high salinity*. [ACS applied materials & interfaces](#), 12(23), 26013-26025.

# Skills

**Lab skills:**
- Physicochemical characterizations of materials (SEM, EDX, XRD, Nitrogen gas sorption analysis, Raman, Boehm titration)
- Electrochemical characterizations (CV, charge/discharge, rate handling, etc.)
- Online monitoring of ion concentration changes in an electrochemical desalination cell (ICP-OES)

**Languages:**

Fluent in English. Native speaker of Persian. German (B2), Dutch (B1), Arabic (A1).

**Public Speaking and Presentation:**

Orally presented my PhD work at 15th International Ceramics Congress, June 20-24, Perugia, Italy, entitled: *MXene for Electrochemical Water Desalination.*